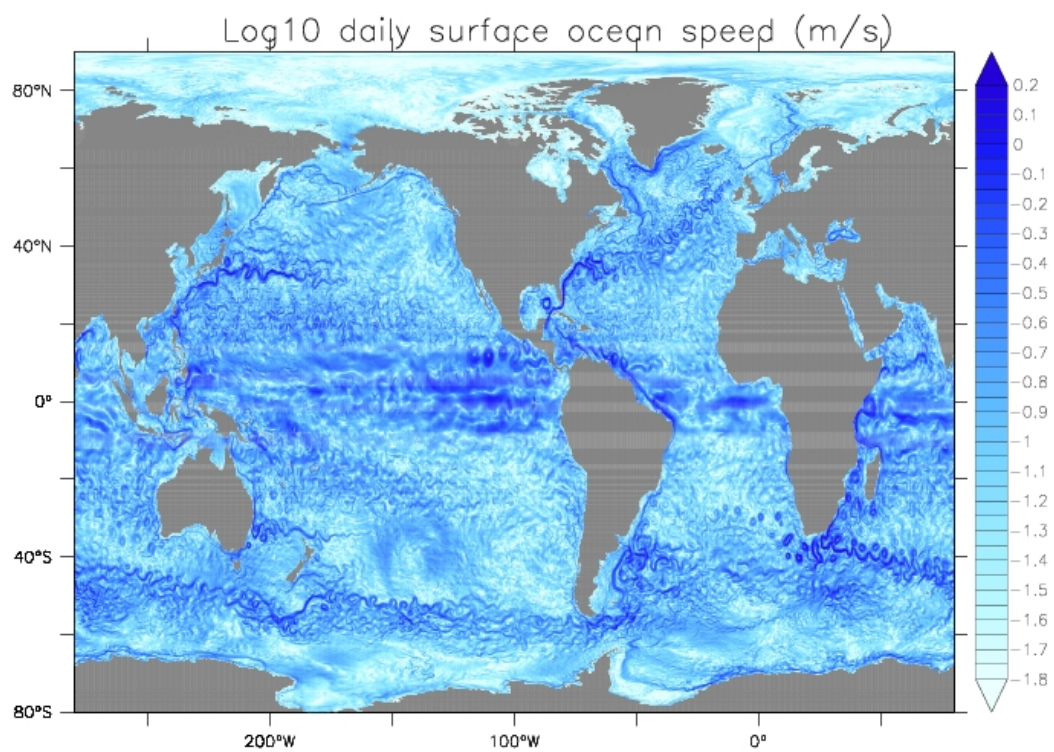


A HANDBOOK FOR THE GFDL CM2-O MODEL SUITE

GFDL Climate Processes and Sensitivity Group Technical Report #1

STEPHEN GRIFFIES
NOAA/GFDL
PRINCETON, USA
September 10, 2015



THE GFDL CM2-O SUITE OF GLOBAL COUPLED CLIMATE MODELS

This document describes elements of the CM2-O suite of climate models. This model suite is comprised of three GFDL coupled models that differ only in their ocean component. The atmosphere, land, sea ice, and iceberg model components are identical across the model suite, with details presented in [Delworth et al. \(2012\)](#). The ocean components are based on the following horizontal grid resolutions using the MOM5 ocean code:

- CM2-1deg uses a nominal one-degree horizontal grid spacing;
- CM2.5 uses a nominal quarter-degree spacing;
- CM2.6 uses a nominal tenth-degree CM2.6 spacing.

Each model uses the same vertical ocean grid resolution based on the Boussinesq z^* vertical coordinate. The mesoscale eddy admitting CM2.5 and CM2.6 models include no parameterization of mesoscale eddies in the tracer equation. In contrast, the mesoscale eddy lacking one-degree model CM2-1deg has a parameterization based on the ocean component of the ESM2M earth system model ([Dunne et al., 2012](#)). All other physical parameterizations are nearly identical across the model suite. As designed, the CM2-O suite provides a numerical framework to assess the role of ocean mesoscale eddies in climate, be they parameterized (CM2-1deg), partially admitted (CM2.5) or more vigorously admitted (CM2.6).

We present in this document physical and numerical aspects of the ocean components of the CM2-O model suite, and introduce certain of the physical diagnostics available from the simulations. Elements of this document formed working notes for the heat budget paper of [Griffies et al. \(2015\)](#), which made use of the 1990 radiatively forced simulations. The discussion is also relevant for the companion 1860 pre-industrial and idealized 2xCO₂ simulations.

The CM2-O simulations were hugely expensive in terms of human resources, computational resources, and archive space. Original plans proved overly ambitious, thus requiring scale-back as obstacles were encountered. Hence, we acknowledge the unfortunate reality that not all possible diagnostics were saved, and note that further simulations with CM2.6 are not planned. We nonetheless trust that many research questions can be addressed using output from this model suite. It is with an optimistic perspective that we offer this document for those aiming to understand details of the model suite, and hope that it serves as a useful entree into further analyses.

Contents

1 Fundamentals	1
1 FUNDAMENTAL MODEL EQUATIONS	3
1.1 Fluid kinematics	4
1.2 Mass conservation and the tracer equation	15
1.3 Thermodynamical tracers	18
1.4 Time changes over finite regions	20
1.5 Basics of the finite volume method	22
1.6 Mass and tracer budgets over finite regions	23
1.7 Special considerations for tracers	29
1.8 Forces from pressure	31
1.9 Linear momentum budget	36
1.10 The Boussinesq budgets	40
2 Numerical aspects of the ocean model	43
2.1 B-grid for the horizontal layout	43
2.2 The bipolar Arctic	44
2.3 The z^* vertical coordinate	45
2.4 Vertical grid cell thicknesses	46
2.5 Partial bottom cell representation of topography	48
2.6 Water fluxes crossing the ocean surface boundary	49
2.7 Time stepping the prognostic equations	50
2.8 The tracer advection scheme	51
3 Physical processes	55
3.1 Equation of state and seawater thermodynamics	56
3.2 Static background vertical viscosity and diffusivity	57
3.3 Parameterized mixing from gravitational instability	57
3.4 Mixing in the surface boundary layer from KPP	58
3.5 Parameterized mixing from shear induced instability	63
3.6 Parameterized mixing from double diffusive processes	64
3.7 Sample vertical diffusivities from the KPP module	66
3.8 Parameterized mixing from tide induced mechanical dissipation	69
3.9 Horizontal viscosity	79
3.10 Dimensionless bottom drag coefficient	79
3.11 Rayleigh drag in certain straits	81
3.12 Mixed layer submesoscale restratification	82
3.13 Mesoscale eddy parameterization in CM_O1.0_C180	86
3.14 Ocean optics and chlorophyll dataset	88
3.15 Icebergs	91

II Budgets and transport	93
4 Seawater mass budget and transport	95
4.1 Mass crossing the ocean surface boundary	96
4.2 Global ocean mass budget	99
4.3 Seawater mass budget for a tracer grid cell	101
4.4 Subgrid scale mass transport in ocean interior	102
4.5 MOM5 diagnostics for mass transport	103
4.6 Barotropic quasi-streamfunction	104
4.7 Mass transport through straits	106
4.8 Meridional overturning circulation	108
5 Ocean heat transport and heat budgets	119
5.1 Introduction	120
5.2 Heat crossing the ocean boundaries	121
5.3 Global ocean heat and global mean temperature	130
5.4 Tracer budget for a grid cell in MOM5	133
5.5 Sample ocean heat budgets	135
5.6 Depth integrated heat budget	139
5.7 Poleward heat transport	143
5.8 Heat budget for surface ocean grid cells	147
5.9 Zonal heat budget	157
6 Scalar budgets in the mixed layer	159
6.1 The mixed layer depth and mixed layer level	161
6.2 Budgets for extensive properties	161
6.3 Seawater mass budgets	164
6.4 Seawater tracer budgets	168
6.5 Subduction diagnostic with a continuous mixed layer base	171
6.6 Seawater mass and tracer budgets for a grid cell	173
6.7 Seawater mass and tracer budgets in the mixed layer	175
6.8 MOM5 mixed layer mass and tracer budgets	182
6.9 Sample mixed layer budget calculations	187
III Eddy-mean flow decomposition	189
7 Transient eddy contributions	191
7.1 Eddy-mean flow decomposition of tracer transport	192
7.2 Eddy decomposition with a seasonal cycle	194
7.3 Higher moments estimated from daily output	196
7.4 Horizontally averaged heat budget with eddy-mean flow decomposition	197
8 KINETIC ENERGY DIAGNOSTICS	199
8.1 Formulation of kinetic energy diagnostics	199
8.2 Eddy-mean flow decomposition	200
8.3 Diagnostics	200
BIBLIOGRAPHY	202

List of Figures

1.1 Schematic of a generalized surface interior to the ocean	8
1.2 Schematic of the ocean bottom surface	11
1.3 Schematic of the ocean upper surface	14
1.4 Schematic of an ocean grid cell	25
1.5 Schematic of an ocean grid cell next to bottom	27
1.6 Schematic of an ocean grid cell next to ocean surface	28
1.7 Schematic of mass convergence-divergence	32
1.8 Schematic of pressure acting on a cube	32
1.9 Schematic of pressure in two dimensions	34
2.1 Placement of fields onto the B-grid	44
2.2 Bipolar Arctic grid lines	45
2.3 Comparing geopotential and z^* vertical coordinates	47
2.4 Vertical grid cell thicknesses	47
2.5 Bottom topography comparing full and partial cells	49
2.6 Passive tracer profiles for the torus test case	54
3.1 KPP boundary layer schematic	60
3.2 Vertical diffusivity for temperature from KPP-plus	67
3.3 Horizontal averaged KPP diffusivity	68
3.4 Roughness amplitude and tide speed for tide mixing schemes	72
3.5 Vertical diffusivity from internal tide mixing scheme	76
3.6 Horizontal averaged internal tide diffusivity	77
3.7 Vertical diffusivity from coastal tide mixing scheme	79
3.8 Horizontal biharmonic viscosity	80
3.9 Dimensionless bottom drag coefficient	81
3.10 Power dissipation from Rayleigh drag	82
3.11 Submesoscale global overturning streamfunction	86
3.12 GM eddy diffusivity	88
3.13 Parameterized mesoscale global overturning streamfunction	89
3.14 Annual mean specified chlorophyll-a concentration	90
3.15 Annual mean latent heat of fusion given to melt icebergs	91
4.1 Net surface boundary mass fluxes	96
4.2 Surface air-sea mass fluxes	97
4.3 Surface mass fluxes	98
4.4 Global mean SSH and P-E+R	100
4.5 Global barotropic quasi-streamfunction	105
4.6 Map of straits through which measure transport	109

4.7 Sample choke point transports	110
4.8 Relating the overturning streamfunction to the transport	112
4.9 Global ocean overturning streamfunction	115
4.10 Atlantic ocean overturning streamfunction	116
4.11 Atlantic meridional overturning index	117
4.12 Indian-Pacific ocean overturning streamfunction	118
5.1 SST bias maps	121
5.2 Time series for horizontally averaged temperature drift	122
5.3 700m temperature bias maps	123
5.4 Zonal mean temperature drift	123
5.5 Surface ocean radiative heat fluxes	127
5.6 Surface ocean latent heat fluxes	128
5.7 Surface ocean heat fluxes	129
5.8 Net surface ocean heat fluxes	130
5.9 Global heat and averaged temperature	131
5.10 Vertically integrated heat budget	141
5.11 Vertically integrated heat budget	142
5.12 Vertically and zonally integrated heat budget	144
5.13 Vertically and zonally integrated heat budget	144
5.14 Meridional heat budget	145
5.15 Meridional heat budget	145
5.16 Meridional heat budget	146
5.17 Global mean surface ocean temperature	150
5.18 Global ocean net surface cell heating	151
5.19 Surface grid cell net heating and its decomposition	152
5.20 Surface grid cell net heating	153
5.21 Surface grid cell advective heating	154
5.22 Surface grid cell heating from non-advective boundary fluxes and from mixing	155
5.23 Surface grid cell mixing	156
6.1 Zonal-depth schematic of mixed layer depth budget	176

Fundamentals

This part discusses some of the fundamentals, with an aim towards identifying elements of the model formulations needed to develop analysis methods.

FUNDAMENTAL MODEL EQUATIONS

Contents

1.1	Fluid kinematics	4
1.1.1	Mass conserving fluid parcels	4
1.1.2	Volume conserving fluid parcels	6
1.1.3	Mass conservation for finite domains	6
1.1.4	dia-surface transport	7
1.1.4.1	Basic formulation	8
1.1.4.2	Alternative expressions for the dia-surface velocity component	9
1.1.5	Solid earth kinematic boundary condition	10
1.1.5.1	Orthogonal coordinates	10
1.1.5.2	Generalized vertical coordinates	11
1.1.6	Upper surface kinematic condition	13
1.1.6.1	Orthogonal coordinates	13
1.1.6.2	Generalized vertical coordinates	15
1.2	Mass conservation and the tracer equation	15
1.2.1	Eulerian form of mass conservation	15
1.2.2	Mass conservation for parcels	17
1.2.3	Mass conservation for constituents: the tracer equation	17
1.3	Thermodynamical tracers	18
1.3.1	Potential temperature	18
1.3.2	Potential enthalpy and conservative temperature	18
1.4	Time changes over finite regions	20
1.5	Basics of the finite volume method	22
1.6	Mass and tracer budgets over finite regions	23
1.6.1	General formulation	24
1.6.2	Budget for an interior grid cell	25
1.6.3	Cells adjacent to the ocean bottom	27
1.6.4	Cells adjacent to the ocean surface	28
1.7	Special considerations for tracers	29
1.7.1	Compatibility between mass and tracer budgets	30
1.7.2	Fresh water budget	30
1.7.3	The ideal age tracer	30
1.7.4	Budgets without dia-surface fluxes	31
1.8	Forces from pressure	31

1.8.1	The accumulation of contact pressure forces	33
1.8.2	Pressure gradient body force in hydrostatic fluids	35
1.9	Linear momentum budget	36
1.9.1	General formulation	37
1.9.2	An interior grid cell	37
1.9.3	Cell adjacent to the ocean bottom	38
1.9.4	Cell adjacent to the ocean surface	39
1.9.5	Horizontal momentum equations for hydrostatic fluids	40
1.10	The Boussinesq budgets	40

This chapter follows Chapter 2 in the MOM5 document of Griffies (2012). We here formulate the kinematic and dynamic equations that form the basis for MOM5, as well as any finite-volume ocean model code. Much of this material is derived from lectures of Griffies (2005) at the 2004 GODAE School on Operational Oceanography. The proceedings of this school have been put together by Chassignet and Verron (2005), and this book contains many pedagogical reviews of ocean modelling. Additional discussions can be found in the monograph of Griffies (2004), and the review article of Griffies and Adcroft (2008). The material here should be accessible to those having some exposure to the basics of mathematical physics, yet there is little assumed knowledge of fluid mechanics. This chapter can be readily skipped by those with a prior understanding of how to formulate the finite volume equations of an ocean model.

1.1 Fluid kinematics

Kinematics is the study of the intrinsic properties of motion, without concern for dynamical laws. The purpose of this section is to derive some of the basic equations of fluid kinematics applied to the ocean. As considered here, fluid kinematics is concerned with balances of mass for infinitesimal fluid parcels or finite regions of the ocean. It is also concerned with the behaviour of a fluid as it interacts with geometrical boundaries of the domain, such as the land-sea and air-sea boundaries of an ocean basin.

1.1.1 Mass conserving fluid parcels

Consider an infinitesimal parcel of seawater contained in a volume of size¹

$$dV = dx dy dz \quad (1.1)$$

with a mass given by

$$dM = \rho dV. \quad (1.2)$$

In these equations, ρ is the *in situ* mass density of the parcel and $\mathbf{x} = (x, y, z)$ is the Cartesian coordinate of the parcel with respect to an arbitrary origin. As the parcel moves through space-time, we measure its velocity

$$\mathbf{v} = \frac{dx}{dt} \quad (1.3)$$

by considering the time changes in its position.²

The time derivative d/dt introduced in equation (1.3) measures time changes of a fluid property as one follows the parcel. That is, we place ourselves in the parcel's moving frame of reference. This time

¹A parcel of fluid is macroscopically small yet microscopically large. That is, from a macroscopic perspective, the parcel's thermodynamic properties may be assumed uniform, and the methods of continuum mechanics are applicable to describing the mechanics of an infinite number of these parcels. However, from a microscopic perspective, these fluid parcels contain many molecules, and so it is safe to ignore the details of molecular interactions. Regions of a fluid with length scales on the order of 10^{-3} cm satisfy these properties of a fluid parcel. See Section 2.2 of Griffies (2004) for further discussion.

²The three dimensional velocity vector is written $\mathbf{v} = (\mathbf{u}, w)$ throughout these notes, with $\mathbf{u} = (u, v)$ the horizontal components and w the vertical component.

derivative is thus directly analogous to that employed in classical particle mechanics ([Landau and Lifshitz, 1976](#); [Marion and Thornton, 1988](#)). Describing fluid motion from the perspective of an observer moving with fluid parcels affords us with a *Lagrangian* description of fluid mechanics. For many purposes, it is useful to take a complementary perspective in which we measure fluid properties from a fixed space frame, and so allow fluid parcels to stream by the observer. The fixed space frame affords one with an *Eulerian* description of fluid motion. To relate the time tendencies of scalar properties measured in the moving and fixed frames, we perform a coordinate transformation, the result of which is (see Section 2.3.3 of [Griffies \(2004\)](#) for details)

$$\frac{d}{dt} = \partial_t + \mathbf{v} \cdot \nabla, \quad (1.4)$$

where

$$\partial_t = \frac{\partial}{\partial t} \quad (1.5)$$

measures time changes at a fixed space point. The *transport* term

$$\mathbf{v} \cdot \nabla = \mathbf{u} \cdot \nabla_s + w^{(s)} \partial_z \quad (1.6)$$

reveals the fundamentally nonlinear character of fluid dynamics. In this relation, ∇_s is the horizontal gradient operator taken on surfaces of constant generalized vertical coordinate s , and $w^{(s)}$ measures the transport of fluid crossing these surfaces. We provide further discussion of this expression in Section [1.1.4](#). In general, the operator $\mathbf{v} \cdot \nabla$ is known as the *advection* operator in geophysical fluids, whereas it is often termed *convection* in the classical fluids literature.³

It is convenient, and conventional, to formulate the mechanics of fluid parcels that conserve mass. Choosing to do so allows many notions from classical particle mechanics to transfer over to continuum mechanics of fluids, especially when formulating the equations of motion from a Lagrangian perspective. We thus focus on kinematics satisfied by mass conserving fluid parcels. In this case, the mass of a parcel changes only if there are sources within the continuous fluid, so that

$$\frac{d}{dt} \ln(dM) = \mathcal{S}^{(M)} \quad (1.7)$$

where $\mathcal{S}^{(M)}$ is the rate at which mass is added to the fluid, per unit mass. Mass sources are often assumed to vanish in textbook formulations of fluid kinematics. However, they can be nonzero in certain cases for ocean modelling in which mass is moved from one region to another through certain subgrid scale parameterizations, such as the cross land schemes discussed in Section 3.5 of [Griffies et al. \(2005\)](#). It is therefore convenient to carry mass sources around in our formulation of the equations used by MOM.

Equation (1.7) expresses mass conservation for fluid parcels in a Lagrangian form. To derive the Eulerian form of mass conservation, start by substituting the mass of a parcel given by equation (1.2) into the mass conservation equation (1.7) to derive

$$\frac{d}{dt} \ln \rho = -\nabla \cdot \mathbf{v} + \mathcal{S}^{(M)}. \quad (1.8)$$

That is, the density of a parcel increases when the velocity field converges onto the parcel. To reach this result, we first note the expression

$$\frac{d}{dt} \ln(dV) = \nabla \cdot \mathbf{v}, \quad (1.9)$$

which says that the infinitesimal volume of a fluid parcel increases in time if the velocity of the parcel diverges from the location of the parcel. Imagine the parcel expanding in response to the diverging velocity field.

Upon deriving the material evolution of density as given by equation (1.8), rearrangement renders the Eulerian form of mass conservation

$$\rho_{,t} + \nabla \cdot (\rho \mathbf{v}) = \rho \mathcal{S}^{(M)}. \quad (1.10)$$

³Convection in geophysical fluid dynamics generally refers to the rapid vertical motions that act to stabilize fluids that are gravitationally unstable (e.g., [Marshall and Schott, 1999](#)).

A comma is used here as shorthand for the partial time derivative taken at a fixed point in space

$$\rho_{,t} = \frac{\partial \rho}{\partial t}. \quad (1.11)$$

We use an analogous notation for other partial derivatives throughout these notes. Rewriting mass conservation in terms of the density time tendency

$$\rho_{,t} = -\nabla \cdot (\rho \mathbf{v}) + \rho \mathcal{S}^{(M)}, \quad (1.12)$$

reveals that at each point in the fluid, the mass density increases if the linear momentum per volume of the fluid parcel,

$$\mathbf{p} = \rho \mathbf{v}, \quad (1.13)$$

converges to the point.

1.1.2 Volume conserving fluid parcels

Fluids that are comprised of parcels that conserve their mass, as considered in the previous discussion, satisfy *non-Boussinesq* kinematics. In ocean climate modelling, it has been traditional to exploit the large degree to which the ocean fluid is incompressible, in which case the volume of fluid parcels is taken as constant. These fluids are said to satisfy *Boussinesq* kinematics.

For the Boussinesq fluid, conservation of volume for a fluid parcel leads to

$$\frac{d}{dt} \ln(dV) = \mathcal{S}^{(V)}, \quad (1.14)$$

where $\mathcal{S}^{(V)}$ is the volume source per unit volume present within the fluid. It is numerically the same as the mass source $\mathcal{S}^{(M)}$ defined in equation (1.7). This statement of volume conservation is equivalent to the mass conservation statement (1.7) if we assume the mass of the parcel is given by

$$dM = \rho_0 dV, \quad (1.15)$$

where ρ_0 is a constant reference density.

Using equation (1.9) in the Lagrangian volume conservation statement (1.14) leads to the following constraint for the Boussinesq velocity field

$$\nabla \cdot \mathbf{v} = \mathcal{S}^{(V)}. \quad (1.16)$$

Where the volume source vanishes, the three dimensional velocity field is non-divergent

$$\nabla \cdot \mathbf{v} = 0 \text{ for Boussinesq fluids with } \mathcal{S}^{(V)} = 0. \quad (1.17)$$

1.1.3 Mass conservation for finite domains

Now consider a finite sized region of ocean extending from the free surface at $z = \eta(x, y, t)$ to the solid earth boundary at $z = -H(x, y)$, and allow the fluid within this region to respect the mass conserving kinematics of a non-Boussinesq fluid. The total mass of fluid inside the region is given by

$$M = \int dx dy \int_{-H}^{\eta} \rho dz. \quad (1.18)$$

Conservation of mass for this region implies that the time tendency

$$\partial_t M = \int dx dy \partial_t \left(\int_{-H}^{\eta} dz \rho \right) \quad (1.19)$$

changes due to imbalances in the flux of seawater passing across the domain boundaries, and from sources within the region.⁴ For a region comprised of a vertical fluid column, the only means of affecting the mass are through fluxes crossing the ocean free surface, convergence of mass brought in by horizontal ocean currents through the vertical sides of the column, and sources within the column. These considerations lead to the balance

$$\partial_t M = \int dx dy \left(Q_m + \int_{-H}^{\eta} dz \rho S^{(M)} - \nabla \cdot \int_{-H}^{\eta} dz \rho \mathbf{u} \right). \quad (1.20)$$

The term $Q_m dx dy$ represents the mass flux of material (mass per unit time) crossing the free surface.⁵ We provide a more detailed accounting of this flux in Section 1.1.6. Equating the time tendencies given by equations (1.19) and (1.20) leads to a mass balance within each vertical column of fluid

$$\partial_t \left(\int_{-H}^{\eta} dz \rho \right) + \nabla \cdot \mathbf{U}^\rho = Q_m + \int_{-H}^{\eta} dz \rho S^{(M)}, \quad (1.21)$$

where

$$\mathbf{U}^\rho = \int_{-H}^{\eta} dz \rho \mathbf{u} \quad (1.22)$$

is a shorthand notation for the vertically integrated horizontal momentum per volume.

Setting density factors in the mass conservation equation (1.21) to the constant reference density ρ_o renders the volume conservation equation appropriate for a Boussinesq fluid

$$\partial_t \eta + \nabla \cdot \mathbf{U} = Q_m / \rho_o + \int_{-H}^{\eta} dz S^{(V)}. \quad (1.23)$$

In the Boussinesq fluid, parcels conserve volume rather than mass. In the column integrated volume equation equation (1.23), we introduced the vertically integrated horizontal velocity

$$\mathbf{U} = \int_{-H}^{\eta} dz \mathbf{u}. \quad (1.24)$$

1.1.4 Dia-surface transport

A surface of constant generalized vertical coordinate, s , is of importance when establishing the balances of mass, tracer, and momentum within a layer of fluid whose upper and lower bounds are determined by surfaces of constant s . Fluid transport through this surface is said to constitute the *dia-surface* transport. This transport plays a fundamental role in generalized vertical coordinate models such as MOM. Additionally, when considering the flow of fluid and tracer properties across the ocean surface and bottom, the notions of dia-surface transport are useful.

Generalized vertical coordinates provide the ocean theorist and modeler with a powerful set of tools to describe ocean flow, which in many situations is far more natural than the more traditional geopotential coordinates (x, y, z) that we have been using thus far. Therefore, it is important for the student to gain some exposure to the fundamentals of these coordinates, as they are ubiquitous in ocean modelling today.

⁴We assume no water enters the domain through the solid-earth boundaries.

⁵Water crossing the ocean surface is typically quite fresh, such as for precipitation or evaporation. However, rivers and ice melt can generally contain a nonzero salinity. Additionally, for most climate model applications, the mass of salt particles exchanged across the liquid ocean interface upon melting and freezing of sea ice is ignored when considering the mass balance of the liquid ocean fluid.

1.1.4.1 Basic formulation

At an arbitrary point on a surface of constant generalized vertical coordinate (see Figure 1.1), the flux of fluid in the direction normal to the surface is given by

$$\text{SEAWATER FLUX IN DIRECTION } \hat{\mathbf{n}} = \mathbf{v} \cdot \hat{\mathbf{n}}, \quad (1.25)$$

with

$$\hat{\mathbf{n}} = \frac{\nabla s}{|\nabla s|} \quad (1.26)$$

the surface unit normal direction. Introducing the material time derivative $ds/dt = s_{,t} + \mathbf{v} \cdot \nabla s$ leads to the equivalent expression

$$\mathbf{v} \cdot \hat{\mathbf{n}} = |\nabla s|^{-1} (d/dt - \partial_t) s. \quad (1.27)$$

That is, the normal component to a fluid parcel's velocity is proportional to the difference between the material time derivative of the surface and its partial time derivative.

Since the surface is generally moving, the net flux of seawater penetrating the surface is obtained by subtracting the velocity of the surface $\mathbf{v}^{(\text{ref})}$ in the $\hat{\mathbf{n}}$ direction from the velocity component $\mathbf{v} \cdot \hat{\mathbf{n}}$ of the fluid parcels. We thus define the dia-surface velocity component according to

$$\begin{aligned} w^{(s)} &\equiv \text{FLUX OF SEAWATER THROUGH SURFACE} \\ &= \hat{\mathbf{n}} \cdot (\mathbf{v} - \mathbf{v}^{(\text{ref})}). \end{aligned} \quad (1.28)$$

The velocity $\mathbf{v}^{(\text{ref})}$ is the velocity of a reference point fixed on the surface, which is defined so that

$$(\partial_t + \mathbf{v}^{(\text{ref})} \cdot \nabla) s = 0. \quad (1.29)$$

Consequently,

$$\hat{\mathbf{n}} \cdot \mathbf{v}^{(\text{ref})} = -s_{,t} |\nabla s|^{-1}, \quad (1.30)$$

so that the normal component of the surface's velocity vanishes when the surface is static.

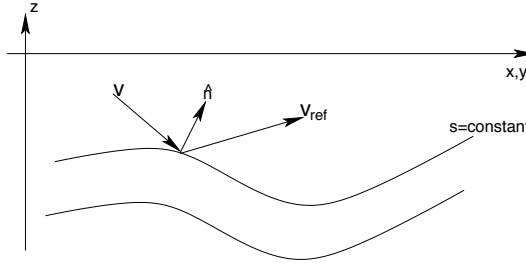


Figure 1.1: Surfaces of constant generalized vertical coordinate living interior to the ocean. An upward normal direction $\hat{\mathbf{n}}$ is indicated on one of the surfaces. Also shown is the orientation of a fluid parcel's velocity \mathbf{v} and the velocity $\mathbf{v}^{(\text{ref})}$ of a reference point living on the surface.

Expression (1.30) then leads to the following expression for the net flux of seawater crossing the surface

$$\begin{aligned} w^{(s)} &= \hat{\mathbf{n}} \cdot (\mathbf{v} - \mathbf{v}^{(\text{ref})}) \\ &= |\nabla s|^{-1} (\partial_t + \mathbf{v} \cdot \nabla) s \\ &= |\nabla s|^{-1} \frac{ds}{dt}. \end{aligned} \quad (1.31)$$

Hence, the material time derivative of the generalized surface vanishes if and only if no water parcels cross it. This important result is used throughout ocean theory and modelling. It measures the volume of seawater crossing a generalized surface, per time, per area. The area normalizing the volume flux is that

area $dA_{(\hat{n})}$ of an infinitesimal patch on the surface of constant generalized vertical coordinate with outward unit normal \hat{n} . When surfaces of constant generalized vertical coordinate are monotonically stacked in the vertical, this area factor can be written (see equation (6.58) of Griffies (2004))

$$dA_{(\hat{n})} = |z_s \nabla s| dA, \quad (1.32)$$

where

$$dA = dx dy \quad (1.33)$$

is the horizontal projection of the area element. Hence, the volume per time of fluid passing through the generalized surface is

$$\begin{aligned} (\text{VOLUME/TIME}) \text{ THROUGH SURFACE} &= \hat{n} \cdot (\mathbf{v} - \mathbf{v}^{(\text{ref})}) dA_{(\hat{n})} \\ &= |z_s| (ds/dt) dx dy, \end{aligned} \quad (1.34)$$

and the magnitude of this flux is

$$|\hat{n} \cdot (\mathbf{v} - \mathbf{v}^{(\text{ref})}) dA_{(\hat{n})}| \equiv |w^{(z)}| dx dy. \quad (1.35)$$

We introduced the expression

$$w^{(z)} = z_s \frac{ds}{dt}, \quad (1.36)$$

which measures the volume of fluid passing through the surface, per unit area $dA = dx dy$ of the horizontal projection of the surface, per unit time. That is,

$$\begin{aligned} w^{(z)} &\equiv \frac{\hat{n} \cdot (\mathbf{v} - \mathbf{v}^{(\text{ref})}) dA_{(\hat{n})}}{dA} \\ &= \frac{(\text{VOLUME/TIME}) \text{ OF FLUID THROUGH SURFACE}}{\text{AREA OF HORIZONTAL PROJECTION OF SURFACE}}. \end{aligned} \quad (1.37)$$

The quantity $w^{(z)}$ is the dia-surface velocity component that appears in the budget equations for mass, tracer, and momentum in the generalized level formulation of MOM.

1.1.4.2 Alternative expressions for the dia-surface velocity component

To gain some experience with the dia-surface velocity component, it is useful to write it in the equivalent forms

$$\begin{aligned} w^{(z)} &= z_s \frac{ds}{dt} \\ &= z_s \nabla s \cdot (\mathbf{v} - \mathbf{v}^{(\text{ref})}) \\ &= (\hat{z} - \nabla_s z) \cdot \mathbf{v} - z_t \\ &= w - (\partial_t + \mathbf{u} \cdot \nabla_s) z \end{aligned} \quad (1.38)$$

where the penultimate step used the identity (1.40), and where

$$\begin{aligned} \mathbf{S} &= \nabla_s z \\ &= -z_s \nabla_z s \end{aligned} \quad (1.39)$$

is the slope of the s surface as projected onto the horizontal directions. For example, if the slope vanishes, then the dia-surface velocity component measures the flux of fluid moving vertically relative to the motion of the generalized surface. When the surface is static and flat, then the dia-surface velocity component is simply the vertical velocity component $w = dz/dt$.

When interpreting the dia-surface velocity component below, we find it useful to note that relation (1.30) leads to

$$z_s \nabla s \cdot \mathbf{v}^{(\text{ref})} = z_t. \quad (1.40)$$

To reach this result, we used the identity $s_{,t} z_{,s} = -z_{,t}$, with $z_{,t}$ the time tendency for the depth of a particular constant s surface.

The expression (1.36) for $w^{(z)}$ brings the material time derivative (1.4) into the following equivalent forms

$$\frac{d}{dt} = \left(\frac{\partial}{\partial t} \right)_z + \mathbf{u} \cdot \nabla_z + w \left(\frac{\partial}{\partial z} \right) \quad (1.41)$$

$$= \left(\frac{\partial}{\partial t} \right)_s + \mathbf{u} \cdot \nabla_s + \frac{ds}{dt} \left(\frac{\partial}{\partial s} \right) \quad (1.42)$$

$$= \left(\frac{\partial}{\partial t} \right)_s + \mathbf{u} \cdot \nabla_s + w^{(z)} \left(\frac{\partial}{\partial z} \right), \quad (1.43)$$

where

$$\partial_s = z_{,s} \partial_z \quad (1.44)$$

relates the vertical coordinate partial derivatives. The form given by equation (1.43) motivates some to refer to $w^{(z)}$ as a vertical velocity component that measures the rate at which fluid parcels penetrate the surface of constant generalized coordinate (see Appendix A to McDougall (1995)). Indeed, such is part of the motivation for using the (z) superscript notation. However, we must be careful to distinguish $w^{(z)}$ from the generally different vertical velocity component $w = dz/dt$, which measures the water flux crossing constant geopotential surfaces.

We close with a few points of clarification for the case where no fluid parcels cross the generalized surface. Such occurs, in particular, in the case of adiabatic flows with $s = \rho$ an isopycnal coordinate. In this case, the material time derivative (1.43) only has a horizontal two-dimensional advective component $\mathbf{u} \cdot \nabla_s$. This result *should not* be interpreted to mean that the velocity of a fluid parcel is strictly horizontal. Indeed, it generally is not, as the form (1.41) should make clear. Rather, it means that the transport of fluid properties occurs along surfaces of constant s , and such transport is measured by the convergence of horizontal advective fluxes as measured along surfaces of constant s . We revisit this point in Section 1.6.2 when discussing tracer transport (see in particular Figure 1.7).

1.1.5 Solid earth kinematic boundary condition

We now apply the discussion of dia-surface transport from Section 1.1.4 to perhaps the simplest surface; namely, the time independent solid earth boundary. This surface is commonly assumed to be impenetrable to fluid.⁶ The expression for fluid transport at the lower surface leads to the *solid earth kinematic boundary condition*. In addition to deriving the bottom kinematic boundary condition, we introduce some mathematical techniques useful when working with non-orthogonal generalized vertical coordinates, as used in many ocean models such as MOM.

1.1.5.1 Orthogonal coordinates

As there is no fluid crossing the solid earth lower boundary, a no-normal flow condition is imposed at the solid earth boundary at the depth

$$z = -H(x, y). \quad (1.45)$$

To develop a mathematical expression for the boundary condition, note that the outward unit normal pointing from the ocean into the underlying rock is given by⁷ (see Figure 1.2)

$$\hat{\mathbf{n}}_H = - \left(\frac{\nabla(z + H)}{|\nabla(z + H)|} \right). \quad (1.46)$$

⁶This assumption may be broken in some cases. For example, when the lower boundary is a moving sedimentary layer in a coastal estuary, or when there is seeping ground water. We do not consider such cases here.

⁷The three dimensional gradient operator $\nabla = (\partial_x, \partial_y, \partial_z)$ reduces to the two dimensional horizontal operator $\nabla_z = (\partial_x, \partial_y, 0)$ when acting on functions that depend only on the horizontal directions. To reduce notation clutter, we do not expose the z subscript in cases where it is clear that the horizontal gradient is all that is relevant.

Furthermore, we assume that the bottom topography can be represented as a continuous function $H(x, y)$ that does not possess “overtures.” That is, we do not consider caves or overhangs in the bottom boundary where the topographic slope becomes infinite. Such would make it difficult to consider the slope of the bottom in our formulations. This limitation is common for ocean models.⁸

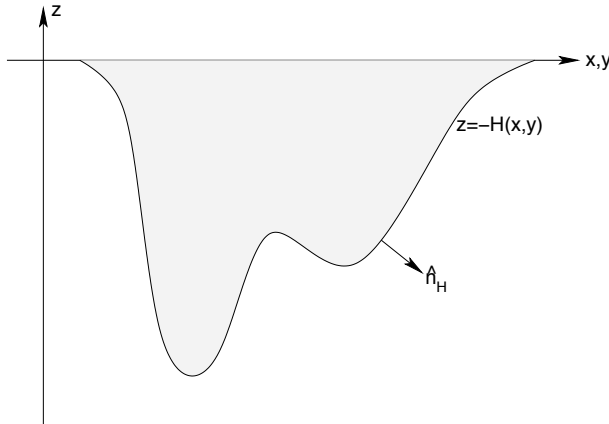


Figure 1.2: Schematic of the ocean’s bottom surface with a smoothed undulating solid earth topography at $z = -H(x, y)$ and outward normal direction \hat{n}_H . Undulations of the solid earth can reach from the ocean bottom at 5000m-6000m to the surface over the course of a few kilometers (slopes on the order of 0.1 to 1.0). These ranges of topographic variation are far greater than the surface height (see Figure 1.3). It is important for simulations to employ numerics that facilitate an accurate representation of the ocean bottom.

A no-normal flow condition on fluid flow at the ocean bottom implies

$$\mathbf{v} \cdot \hat{n}_H = 0 \quad \text{at } z = -H(x, y). \quad (1.47)$$

Expanding this constraint into its horizontal and vertical components yields

$$\mathbf{u} \cdot \nabla H + w = 0 \quad \text{at } z = -H(x, y). \quad (1.48)$$

Furthermore, introducing a material time derivative (1.4) allows us to write this boundary condition as

$$\frac{d(z + H)}{dt} = 0 \quad \text{at } z = -H(x, y). \quad (1.49)$$

Equation (1.49) expresses in a material or Lagrangian form the impenetrable nature of the solid earth lower surface, whereas equation (1.48) expresses the same constraint in an Eulerian form.

1.1.5.2 Generalized vertical coordinates

We now consider the form of the bottom kinematic boundary condition in generalized vertical coordinates. Chapter 6 of Griffies (2004) develops a calculus for generalized vertical coordinates. Experience with these methods is useful to nurture an understanding for ocean modelling in generalized vertical coordinates. Most notably, these coordinates, when used with the familiar horizontal coordinates (x, y) , form a non-orthogonal triad, and thus lead to some relationships that may be unfamiliar. To proceed in this section, we present some salient results of the mathematics of generalized vertical coordinates, and reserve many of the derivations for Griffies (2004).

⁸For hydrostatic models, the solution algorithms rely on the ability to integrate vertically from the ocean bottom to the top, uninterrupted by rock in between. Non-hydrostatic models do not employ such algorithms, and so may in principle allow for arbitrary bottom topography, including overhangs.

When considering generalized vertical coordinates for ocean models, we assume that the surfaces in question do not overturn on themselves. This constraint means that the Jacobian of transformation between the generalized vertical coordinate

$$s = s(x, y, z, t) \quad (1.50)$$

and the geopotential coordinate z , must be one signed. That is, the specific thickness

$$\frac{\partial z}{\partial s} = z_{,s} \quad (1.51)$$

is of the same sign throughout the ocean fluid. The name *specific thickness* arises from the property that

$$dz = z_{,s} ds \quad (1.52)$$

is an expression for the thickness of an infinitesimal layer of fluid bounded by two constant s surfaces.

Deriving the bottom kinematic boundary condition in s -coordinates requires a relation between the vertical velocity component used in geopotential coordinates, $w = dz/dt$, and the pseudo-velocity component ds/dt . For this purpose, we refer to some results from Section 6.5.5 of [Griffies \(2004\)](#). As in that discussion, we derive the isomorphic relations

$$\dot{z} = (\partial_t + \mathbf{u} \cdot \nabla_s + \dot{s} \partial_s) z \quad (1.53)$$

$$\dot{s} = (\partial_t + \mathbf{u} \cdot \nabla_z + \dot{z} \partial_z) s, \quad (1.54)$$

where

$$\dot{z} = \frac{dz}{dt} \quad (1.55)$$

$$\dot{s} = \frac{ds}{dt} \quad (1.56)$$

are useful shorthands for the vertical velocity components, motivated from similar notation used in classical particle mechanics. Note that the partial time derivative appearing in each of the expressions is taken with the corresponding space variables held fixed. That is, ∂_t in equation (1.53) is taken with s held fixed, whereas ∂_t in equation (1.54) is taken with z held fixed.

Rearrangement of equations (1.53) and (1.54) leads to

$$\dot{z} = z_{,s} (d/dt - \partial_t - \mathbf{u} \cdot \nabla_z) s. \quad (1.57)$$

This expression is relevant when measurements are taken on surfaces of constant geopotential, or depth. To reach this result, we made use of the triple product identities

$$z_{,t} = -s_{,t} z_{,s} \quad (1.58)$$

$$z_{,x} = -s_{,x} z_{,s} \quad (1.59)$$

$$z_{,y} = -s_{,y} z_{,s}. \quad (1.60)$$

A derivation of these identities is given in Section 6.5.4 of [Griffies \(2004\)](#). These relations should be familiar to those having studied thermodynamics, where the analogous expressions are known as the Maxwell relations (e.g., [Callen, 1985](#)).

We now apply relation (1.57) to the ocean bottom, which is generally not a surface of constant depth. It is thus necessary to transform the constant depth gradient ∇_z to a horizontal gradient taken along the bottom. To do so, proceed as in Section 6.5.3 of [Griffies \(2004\)](#) and consider the time-independent coordinate transformation

$$(\bar{x}, \bar{y}, \bar{z}, \bar{t}) = (x, y, -H(x, y), t). \quad (1.61)$$

The horizontal gradient taken on constant depth surfaces, ∇_z , and the horizontal gradient along the bottom, $\nabla_{\bar{z}}$, are thus related by

$$\nabla_{\bar{z}} = \nabla_z - (\nabla H) \partial_z. \quad (1.62)$$

Using this result in equation (1.57) yields

$$s_z(w + \mathbf{u} \cdot \nabla H) = (\partial_t - \partial_z - \mathbf{u} \cdot \nabla_{\bar{z}}) s \quad \text{at } z = -H. \quad (1.63)$$

The left hand side vanishes due to the kinematic boundary condition (1.48), which then leads to

$$ds/dt = (\partial_t + \mathbf{u} \cdot \nabla_{\bar{z}}) s \quad \text{at } s = s(x, y, z = -H, t). \quad (1.64)$$

The value of the generalized coordinate at the ocean bottom can be written in the shorthand form

$$s_{\text{bot}}(x, y, t) = s(x, y, z = -H, t) \quad (1.65)$$

which leads to

$$\frac{d(s - s_{\text{bot}})}{dt} = 0 \quad \text{at } s = s_{\text{bot}}. \quad (1.66)$$

This relation is analogous to equation (1.49) appropriate to z -coordinates. Indeed, it is actually a basic statement of the impenetrable nature of the solid earth lower boundary, which is true regardless the vertical coordinates.

The various mathematical steps that led to the very simple result (1.66) could have been dispensed with if we already understood some notions of generalized vertical coordinates. Nonetheless, the steps introduced some of the formalism required to work with generalized vertical coordinates, and as such provide a useful testing ground for later manipulations where the answer is less easy to anticipate. This strategy is highly recommended to the student working with new formalisms. That is, first test your mathematical skills with problems where the answer is either known, or can be readily judged correct with basic physical understanding. After garnering experience and confidence, one may then approach genuinely new problems using the methods.

1.1.6 Upper surface kinematic condition

To formulate budgets for mass, tracer, and momentum in the ocean, we consider the upper ocean surface to be a time dependent permeable membrane through which precipitation, evaporation, ice melt, and river runoff⁹ pass. The expression for fluid transport at the upper surface leads to the *upper ocean kinematic boundary condition*.

1.1.6.1 Orthogonal coordinates

To describe the kinematics of water transport into the ocean, it is useful to introduce an effective transport through a smoothed ocean surface, where smoothing is performed via an ensemble average. We assume that this averaging leads to a surface absent overturns or breaking waves, thus facilitating a mathematical description analogous to the ocean bottom just considered. The value of the geopotential at the ocean surface takes on the value

$$z = \eta(x, y, t) \quad (1.67)$$

at this idealized ocean surface. Correspondingly, the mass flux of material crossing the ocean surface is written

$$\begin{aligned} Q_m &= \frac{(\text{MASS/TIME}) \text{ THROUGH FREE SURFACE}}{\text{HORIZONTAL AREA UNDER FREE SURFACE}} \\ &= -\left(\frac{\rho dA(\hat{n}) \hat{n} \cdot (\mathbf{v} - \mathbf{v}^{\text{ref}})}{dA} \right) \quad \text{at } z = \eta. \end{aligned} \quad (1.68)$$

⁹River runoff generally enters the ocean at a nonzero depth rather than through the surface. Many global models, however, have traditionally inserted river runoff to the top model cell. Such can become problematic numerically and physically when the top grid cells are refined to levels common in coastal modelling. Hence, more applications are now considering the input of runoff throughout a nonzero depth. Likewise, sea ice can melt at depth, thus necessitating a mass transport to occur within the ocean between the liquid and solid water masses.

In this expression, the outward normal

$$\hat{\mathbf{n}} = \left(\frac{\nabla(z - \eta)}{|\nabla(z - \eta)|} \right) \quad \text{at } z = \eta \quad (1.69)$$

points from the ocean surface at $z = \eta$ into the overlying atmosphere (see Figure 1.3). The velocity \mathbf{v}^{ref} is taken from a point fixed on the free surface, so that

$$\partial_t(z - \eta) + \mathbf{v}^{\text{ref}} \cdot \nabla(z - \eta) = 0, \quad (1.70)$$

or equivalently

$$w^{\text{ref}} = (\partial_t + \nabla \cdot \mathbf{u}^{\text{ref}}) \eta \quad (1.71)$$

or

$$|\nabla(z - \eta)| \hat{\mathbf{n}} \cdot \mathbf{v}^{\text{ref}} = \partial_t \eta \quad \text{at } z = \eta. \quad (1.72)$$

Finally, the area element $dA_{(\hat{\mathbf{n}})}$ measures an infinitesimal area element on the ocean surface $z = \eta$, and it is given by (see Section 20.13.2 of [Griffies \(2004\)](#))

$$dA_{(\hat{\mathbf{n}})} = |\nabla(z - \eta)| dA \quad \text{at } z = \eta, \quad (1.73)$$

where $dA = dx dy$ is the horizontal area element. Use of these relations leads to the surface kinematic boundary condition written in material form

$$\rho \frac{d(z - \eta)}{dt} = -Q_m \quad \text{at } z = \eta. \quad (1.74)$$

Contrary to the solid earth condition (1.49), where $z + H$ is materially constant, permeability of the ocean surface leads to a nontrivial material evolution of $z - \eta$.

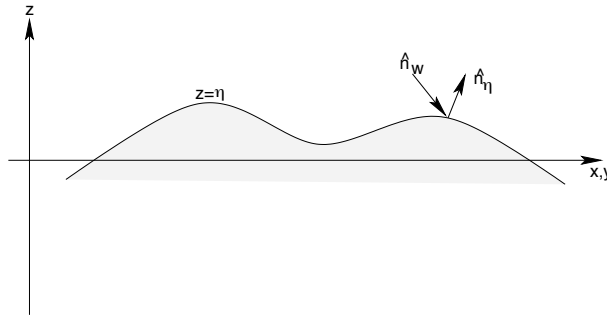


Figure 1.3: Schematic of the ocean's upper surface with a smoothed undulating surface at $z = \eta(x, y, t)$, outward normal direction $\hat{\mathbf{n}}_\eta$, and normal direction $\hat{\mathbf{n}}_w$ orienting the passage of water across the surface. Undulations of the surface height are on the order of a few metres due to tidal fluctuations in the open ocean, and order 10m-20m in certain embayments (e.g., Bay of Fundy in Nova Scotia). When imposing the weight of sea ice onto the ocean surface, the surface height can depress even further, on the order of 5m-10m, with larger values possible in some cases. It is important for simulations to employ numerical schemes facilitating such wide surface height undulations.

As an alternative means to develop the surface kinematic boundary condition, return to the expression (1.21) for mass conservation, rewritten here for completeness

$$\partial_t \left(\int_{-H}^{\eta} dz \rho \right) + \nabla \cdot \left(\int_{-H}^{\eta} dz \rho \mathbf{u} \right) = Q_m + \int_{-H}^{\eta} dz \rho \mathcal{S}^{(M)}. \quad (1.75)$$

Next, perform the derivative operations on the integrals, making use of Leibnitz's Rule when differentiating the integrals. The first step of the derivation leads to

$$[\rho(\partial_t + \mathbf{u} \cdot \nabla)\eta]_{z=\eta} + [\rho \nabla H \cdot \mathbf{u}]_{z=-H} + \int_{-H}^{\eta} dz [\rho_{,t} + \nabla \cdot (\rho \mathbf{u})] = Q_m + \int_{-H}^{\eta} S^{(M)} \rho dz. \quad (1.76)$$

The Eulerian mass conservation relation (1.10) and bottom kinematic boundary condition (1.48) render the Eulerian form of the surface kinematic boundary condition

$$\rho(\partial_t + \mathbf{u} \cdot \nabla)\eta = Q_m + \rho w \quad \text{at } z = \eta. \quad (1.77)$$

1.1.6.2 Generalized vertical coordinates

To derive the s -coordinate surface kinematic boundary condition, we proceed as for the bottom boundary condition in Section 1.1.5.2. Here, the coordinate transformation is time dependent

$$(\bar{x}, \bar{y}, \bar{z}, \bar{t}) = (x, y, \eta(x, y, t), t). \quad (1.78)$$

The horizontal gradient and time derivative operators are therefore related by

$$\nabla_{\bar{z}} = \nabla_z + (\nabla \eta) \partial_z \quad (1.79)$$

$$\partial_{\bar{t}} = \partial_t + (\partial_t \eta) \partial_z. \quad (1.80)$$

Hence, the relation (1.57) between vertical velocity components takes the following form at the ocean surface

$$w = z_{,s} (d/dt - \partial_{\bar{t}} - \mathbf{u} \cdot \nabla_{\bar{z}}) s + (\partial_t + \mathbf{u} \cdot \nabla)\eta \quad \text{at } z = \eta. \quad (1.81)$$

Substitution of the z -coordinate kinematic boundary condition (1.77) leads to

$$\rho z_{,s} (d/dt - \partial_{\bar{t}} - \mathbf{u} \cdot \nabla_{\bar{z}}) s = -Q_m \quad \text{at } s = s_{\text{top}} \quad (1.82)$$

where $s_{\text{top}} = s(x, y, z = \eta, t)$ is the value of the generalized vertical coordinate at the ocean surface. Reorganizing the result (1.82) leads to the material time derivative form

$$\rho z_{,s} \left(\frac{d(s - s_{\text{top}})}{dt} \right) = -Q_m \quad \text{at } s = s_{\text{top}} \quad (1.83)$$

which is analogous to the z -coordinate result (1.74). Indeed, it can be derived trivially by noting that $dz/dt = z_{,s} ds/dt$. Even so, just as for the bottom kinematic boundary condition considered in Section 1.1.5.2, it is useful to have gone through these manipulations to garner experience and confidence with the formalism.

1.2 Mass conservation and the tracer equation

We revisit here the mathematical description of a mass conserving fluid parcel for the purpose of introducing the evolution equation for trace material within a parcel. For brevity, we ignore the possibilities of mass sources in this discussion, though note as in Section 1.1 that mass sources may be of use for implementing certain subgrid scale schemes in MOM. This discussion here follows that in Section II.2 of DeGroot and Mazur (1984), Section 8.4 of Chaikin and Lubensky (1995), and Section 3.3 of Müller (2006). See also the discussion in Warren (2009).

1.2.1 Eulerian form of mass conservation

Seawater consists of many material constituents, such as freshwater, salts and biogeochemical components, with the possibility also for chemical reactions to take place. For brevity, we ignore chemical reactions, though note that the following discussion can be generalized to such cases (see, for example, Section II-2 in DeGroot and Mazur, 1984).

The mass density of each constituent within a parcel of seawater is given by

$$\rho_n = \frac{\text{mass of component } n}{\text{volume of seawater parcel}}, \quad (1.84)$$

with the total density in a parcel given by the sum over all N constituents

$$\begin{aligned} \rho &= \sum_{n=1}^N \left(\frac{\text{mass of component } n}{\text{volume of seawater parcel}} \right) \\ &= \sum_{n=1}^N \rho_n. \end{aligned} \quad (1.85)$$

Observe that the mass of a seawater parcel is the sum of individual constituent masses (numerator in equation (1.85)), whereas the volume of the parcel is a complicated function of the temperature, pressure, and material constituents.

For an arbitrary finite region within the fluid, conservation of mass for each constituent takes the form

$$\partial_t \left(\int \rho_n dV \right) = - \int \rho_n \mathbf{v}_n \cdot d\mathbf{A}, \quad (1.86)$$

where

$$d\mathbf{A} = \hat{\mathbf{n}} dA_{(\hat{\mathbf{n}})} \quad (1.87)$$

is the area element on the region boundary, with $\hat{\mathbf{n}}$ the outward normal, and \mathbf{v}_n is the velocity of constituent n . Equation (1.86) says that the mass of each constituent within a region is affected by the flow of that constituent through the region boundaries.

Now apply the mass budget (1.86) to a static volume, in which case we can bring the time derivative inside the integral, and use Gauss' Theorem on the boundary integral to render

$$\int dV (\partial_t \rho_n + \nabla \cdot (\rho_n \mathbf{v}_n)) = 0. \quad (1.88)$$

Since the volume is arbitrary, this relation leads to the local expression of mass balance for each constituent

$$\partial_t \rho_n = -\nabla \cdot (\rho_n \mathbf{v}_n). \quad (1.89)$$

Summing over all constituents then leads to the familiar Eulerian expression of mass conservation

$$\partial_t \rho = -\nabla \cdot (\rho \mathbf{v}), \quad (1.90)$$

where

$$\mathbf{v} = \rho^{-1} \sum_{n=1}^N \rho_n \mathbf{v}_n \quad (1.91)$$

is the velocity for the center of mass of the parcel.

The density of seawater is often well approximated by

$$\rho \approx \rho_{\text{salt}} + \rho_{\text{fresh}}, \quad (1.92)$$

where ρ_{salt} is the mass of ocean “salt” per mass of seawater, and ρ_{fresh} is the mass of fresh water per mass of seawater. Other material constituents occur in such small concentrations that their contributions to the seawater density are generally ignored for purposes of ocean modeling.

1.2.2 Mass conservation for parcels

The material time derivative

$$\frac{d}{dt} = \partial_t + \mathbf{v} \cdot \nabla, \quad (1.93)$$

measures time changes of a fluid property for an observer moving with the center of mass velocity \mathbf{v} . Mass conservation (1.90) in the moving, or *Lagrangian*, frame then takes the form

$$\frac{d\rho}{dt} = -\rho \nabla \cdot \mathbf{v}, \quad (1.94)$$

indicating that the density of a fluid parcel increases in regions where currents converge, and density decreases where currents diverge.

1.2.3 Mass conservation for constituents: the tracer equation

Introducing the material time derivative to the constituent mass balances (1.89) leads to the material budget

$$\frac{d\rho_n}{dt} = -\rho_n \nabla \cdot \mathbf{v} - \nabla \cdot [\rho_n (\mathbf{v}_n - \mathbf{v})]. \quad (1.95)$$

Now define the *relative mass flux*

$$\mathbf{J}_n = \rho_n (\mathbf{v}_n - \mathbf{v}) \quad (1.96)$$

to render an expression for the material evolution of the density for each constituent

$$\frac{d\rho_n}{dt} = -\rho_n \nabla \cdot \mathbf{v} - \nabla \cdot \mathbf{J}_n. \quad (1.97)$$

The flux \mathbf{J}_n is nonzero for those motions where the constituent n moves relative to the parcel's center of mass. This motion can be caused by many effects, with molecular diffusion the canonical example, in which case we parameterize \mathbf{J}_n as a downgradient diffusive flux.¹⁰ Notably, the total mass flux vanishes

$$\mathbf{J} = \sum_{n=1}^N \mathbf{J}_n = 0, \quad (1.98)$$

which follows since we choose to measure the parcel motion with respect to its center of mass. Hence, there is no subgrid scale flux for the full density ρ ; i.e., the mass conservation equation (1.90) is exact, even in the presence of subgrid scale processes.

As a final step in our development of mass conservation, introduce the concentration of a material constituent, defined by

$$\begin{aligned} C_n &= \frac{\text{mass of component } n}{\text{mass of seawater parcel}} \\ &= \frac{\rho_n}{\rho}. \end{aligned} \quad (1.99)$$

Substituting this *tracer concentration* into the constituent density equation (1.97) leads to the material form of the *tracer equation*

$$\rho \frac{dC_n}{dt} = -\nabla \cdot (\rho \mathbf{v} C_n + \mathbf{J}_n), \quad (1.100)$$

with the Eulerian form given by

$$\partial_t (\rho C_n) = -\nabla \cdot (\rho \mathbf{v} C_n + \mathbf{J}_n). \quad (1.101)$$

This is the Eulerian form of the tracer equation implemented in MOM. It applies to both the material tracers considered here, and the thermodynamical heat tracer described in Section 1.3.

¹⁰For an ocean model, whose grid spacing is far greater than that appropriate for molecular diffusion, the relative motion of a constituent is also affected by far larger subgrid scale processes, such as unresolved eddy advective and diffusive transport.

1.3 Thermodynamical tracers

Heating and cooling of the ocean, as well as mass exchange, predominantly occur near the ocean surface. In contrast, transport in the interior is nearly adiabatic and isohaline. Hence, the surface ocean experiences irreversible processes that set characteristics of the water masses moving quasi-isentropically within the ocean interior. Useful labels for these water masses maintain their values when moving within the largely ideal ocean interior. Salinity is a good tracer for such purposes since it is altered predominantly by mixing between waters of varying concentrations, and the resulting salinity after homogenization of two water parcels is the mass weighted mean of the salinities of the individual parcels. These two properties are basic to the material tracers considered in Section 1.2. We discuss here desirable properties of a thermodynamic tracer that tags the heat within a water parcel and evolves analogously to material tracers. Much of this material follows from Chapter 5 of [Griffies \(2004\)](#).

1.3.1 Potential temperature

Vertical adiabatic and isohaline motion in the ocean changes a fluid parcel's hydrostatic pressure, which thus causes its *in situ* temperature to change in proportion to the adiabatic lapse rate as given by

$$dT = \Gamma dp. \quad (1.102)$$

Consequently, *in situ* temperature is not a useful thermodynamic variable to label water parcels of common origin. Instead, it is more useful to remove the adiabatic pressure effects.

Removing adiabatic pressure effects from *in situ* temperature leads to the concept of *potential temperature*. Potential temperature is the *in situ* temperature that a water parcel of fixed composition would have if it were isentropically transported from its *in situ* pressure to a reference pressure p_r , with the reference pressure typically taken at the ocean surface. Mathematically, the potential temperature θ is the reference temperature obtained via integration of $dT = \Gamma dp$ for an isentropic *in situ* temperature change with respect to pressure (e.g., [Apel, 1987](#)):

$$T = \theta(s, T, p_r) + \int_{p_r}^p \Gamma(s, \theta, p') dp', \quad (1.103)$$

with Γ the lapse rate defined in terms of pressure changes. By definition, the *in situ* temperature T equals the potential temperature θ at the reference pressure $p = p_r$. Elsewhere, they differ by an amount determined by the adiabatic lapse rate. Beneath the diabatic surface mixed layer, a vertical profile of potential temperature is far more constant than *in situ* temperature.

As shown in Section 5.6.1 of [Griffies \(2004\)](#), the potential temperature of a parcel is constant when the parcel's specific entropy ζ and material composition are constant. Mathematically, this result follows by noting that when entropy changes at a fixed pressure and composition, $p = p_r$ so that temperature equals potential temperature. Equation (5.41) of [Griffies \(2004\)](#) then leads to

$$d\zeta = C_p d\ln \theta, \quad (1.104)$$

implying $d\zeta = 0$ if and only if $d\theta = 0$.

1.3.2 Potential enthalpy and conservative temperature

Potential temperature has proven useful for many oceanographic purposes. However, we have yet to ask whether it is a convenient variable to mark the heat content in a parcel of seawater. Traditionally, it is the potential temperature multiplied by the heat capacity that is used for this purpose. [Bacon and Fofonoff \(1996\)](#) provide a review with suggestions for this approach. In contrast, [McDougall \(2003\)](#) argues that potential temperature multiplied by heat capacity is less precise, by some two orders of magnitude, than an alternative thermodynamic tracer called *potential enthalpy*.

To understand this issue from a mathematical perspective, consider the evolution equation for potential temperature

$$\rho \frac{d\theta}{dt} = -\nabla \cdot \mathbf{J}_\theta + \Sigma_\theta, \quad (1.105)$$

where \mathbf{J}_θ is a flux due to molecular diffusion, and Σ_θ is a source. That potential temperature evolves in this manner is ensured by its being a scalar field. Consider the mixing of two seawater parcels at the same pressure where the parcels have different potential temperature and salinity. In the absence of the source term, the equilibrated state consists of a single parcel with mass equal to the sum of the two separate masses, and potential temperature and salinity determined by their respective mass weighted means. Does this actually happen in the real ocean? That is, can source terms be ignored? [Fofonoff \(1962\)](#) and [McDougall \(2003\)](#) note that it is indeed the case for salinity (and any other material tracer due to conservation of matter), yet it is not the case for potential temperature. Instead, potential temperature contains source terms that alter the mass weighted average equilibrated state. In contrast, potential enthalpy (discussed below) maintains the desired conservative behavior when mixing at constant reference pressure, and nearly maintains this behavior if mixing parcels at a different pressure. Hence, ocean models which set the source term to zero upon mixing potential temperature are in error. [McDougall \(2003\)](#) quantifies this error.

Potential enthalpy is defined analogously to potential temperature. What motivates the use of potential enthalpy is the observation that the fundamental relation between thermodynamic state variables takes a nearly conservative form when written in terms of potential enthalpy. To see this point, consider the evolution of internal energy (see equation (5.94) in [Griffies, 2004](#)), and introduce the enthalpy per mass (specific enthalpy)

$$\mathcal{H} = \mathcal{I} + p/\rho \quad (1.106)$$

leads to

$$\rho \frac{d\mathcal{H}}{dt} = -\nabla \cdot \mathbf{J}_q + \frac{dp}{dt} + \rho \epsilon. \quad (1.107)$$

Dropping the frictional dissipation term arising from molecular friction leads to the approximate statement

$$\rho \frac{d\mathcal{H}}{dt} - \frac{dp}{dt} \approx -\nabla \cdot \mathbf{J}_q. \quad (1.108)$$

To proceed, the fundamental thermodynamic relation (see equation (5.31) [Griffies, 2004](#), in) becomes

$$d\mathcal{H} = T d\zeta + \rho^{-1} dp + \mu dC \quad (1.109)$$

in terms of enthalpy. Thus, enthalpy can be written as a function of entropy, salt concentration, and pressure,

$$\mathcal{H} = \mathcal{H}(\zeta, C, p). \quad (1.110)$$

Transport of a seawater parcel without changing heat, salt, or momentum occurs without change in entropy, thus rendering

$$\left(\frac{\partial \mathcal{H}}{\partial p} \right)_{\zeta, C} = \rho^{-1}. \quad (1.111)$$

Keeping salinity and entropy fixed (or equivalently fixed salinity and potential temperature) leads to

$$\mathcal{H}(\theta, s, p) = \mathcal{H}^o(\theta, s, p_r) + \int_{p_r}^p \rho^{-1}(\theta, s, p') dp' \quad (1.112)$$

with $\mathcal{H}^o(\theta, s, p_r)$ defining the potential enthalpy of a parcel with potential temperature θ and salinity s . Taking the time derivative and using the approximate relation (1.108) yields

$$\frac{d\mathcal{H}^o}{dt} \approx -\rho^{-1} \nabla \cdot \mathbf{J}_q + \int_p^{p_r} dp' \frac{d\rho^{-1}(\theta, s, p')}{dt}. \quad (1.113)$$

[McDougall \(2003\)](#) shows that for the ocean, the integral

$$\begin{aligned} \int_p^{p_r} dp' \frac{d\rho^{-1}(\theta, s, p')}{dt} &= \int_p^{p_r} dp' \left(\frac{\partial \rho^{-1}}{\partial \theta} \frac{d\theta}{dt} + \frac{\partial \rho^{-1}}{\partial s} \frac{ds}{dt} \right) \\ &= \frac{d\theta}{dt} \int_p^{p_r} dp' \rho^{-1} \alpha - \frac{ds}{dt} \int_p^{p_r} dp' \rho^{-1} \beta \end{aligned} \quad (1.114)$$

has magnitude on the order of the ocean's tiny levels of dissipation arising from molecular viscosity. These expressions introduced the thermal expansion coefficient $\alpha = -\partial \ln \rho / \partial \theta$ and saline contraction coefficient $\beta = \partial \ln \rho / \partial s$. The time derivatives of potential temperature and salinity can be removed from the pressure integrals, since they are each independent of pressure. Given the smallness of $\int_p^{p_r} dp' d\rho^{-1}/dt$, one can write the approximate potential enthalpy equation

$$\rho \frac{d\mathcal{H}^o}{dt} \approx -\nabla \cdot \mathbf{J}_q. \quad (1.115)$$

Hence, potential enthalpy is a state function that approximately specifies the heat in a parcel of seawater, and it evolves analogously to a material tracer such as salinity. See [McDougall \(2003\)](#) for a proof that \mathcal{H}^o more accurately sets the heat for a parcel of seawater than does $C_p \theta$. Given that it does, [McDougall \(2003\)](#) suggests that *conservative temperature*

$$\Theta \equiv \frac{\mathcal{H}^o(\theta, s, p_r)}{C_p^o} \quad (1.116)$$

with $p_r = 0$ is more appropriate than potential temperature as a thermodynamic tracer for use in an ocean model, and generally for measuring heat in the ocean. In this equation

$$\begin{aligned} C_p^o &= \frac{\mathcal{H}(\theta = 25^\circ C, s = 35 \text{ psu}, p_r = 0)}{25^\circ C} \\ &= 3989.245 \text{ J kg}^{-1} \text{ K}^{-1} \end{aligned} \quad (1.117)$$

is a heat capacity chosen to minimize the difference between $C_p^o \theta$ and potential enthalpy $\mathcal{H}^o(\theta, s, p_r)$ when averaged over the sea surface.¹¹

Conservative temperature of [McDougall \(2003\)](#) has been recommended by [IOC et al. \(2010\)](#) as the preferred means to measure heat content in a seawater parcel. MOM has the ability to use conservative temperature as its prognostic temperature field. Conservative temperature is the preferred method rather than the older potential temperature, with potential temperature retained for legacy purposes. In the remainder of these notes, we maintain the notation θ to mean conservative temperature, but with all formulas remaining unchanged if interpreted as potential temperature.

1.4 Time changes over finite regions

In the following sections, we focus on the mass, tracer, and momentum budgets formulated over a finite domain. The domain, or control volume, of interest is that of an ocean model grid cell. The budget for a grid cell is distinct from budgets for infinitesimal mass conserving Lagrangian fluid parcels moving with the fluid. Mass conserving fluid parcels form the fundamental system for which the budgets of mass, tracer, momentum, and energy are generally formulated from first principles (see, for example, chapters 3-5 in [Griffies, 2004](#)). Grid cell budgets are then derived from the fundamental parcel budgets.

The grid cells of concern for MOM have vertical sides fixed in space-time, but with the top and bottom generally moving. In particular, the top and bottom either represent the ocean top, ocean bottom, or

¹¹The value quoted by [IOC et al. \(2010\)](#) is $c_p^o = 3991.86795711963 \text{ J kg}^{-1} \text{ K}^{-1}$.

a surface of constant generalized vertical coordinate. We furthermore assume that at no place in the fluid do the top or bottom surfaces of the grid cell become vertical. This assumption allows for a one-to-one relation to exist between geopotential depth z and the generalized vertical coordinate s introduced in Section 1.1.5.2 (i.e., the relation is invertible).

To establish the grid cell budget, we integrate the budget for mass conserving fluid parcels over the volume of the cell. This section is focused on the mathematics required for integrating the density weighted material time derivative acting on an arbitrary field ψ

$$\rho \frac{d\psi}{dt} = (\rho\psi)_{,t} + \nabla \cdot (\rho\mathbf{v}\psi). \quad (1.118)$$

We start with the partial time derivative on the right hand side, and introduce Cartesian coordinates (x, y, z) for the purpose of performing the grid cell integral

$$\begin{aligned} \int (\rho\psi)_{,t} dV &= \int (\rho\psi)_{,t} dx dy dz \\ &= \int dx dy \int_{z_1}^{z_2} dz (\rho\psi)_{,t} \\ &= \iint dx dy \left[-(\rho\psi)_2 \partial_t z_2 + (\rho\psi)_1 \partial_t z_1 + \partial_t \left(\int_{z_1}^{z_2} dz (\rho\psi) \right) \right]. \end{aligned} \quad (1.119)$$

The second equality follows by noting that the horizontal extent of a grid cell remains static, thus allowing for the horizontal integral to be brought outside of the time derivative. In contrast, the vertical extent has a time dependence, which necessitates the use of Leibniz's Rule. We now use equation (1.58)

$$z_{,t} = -s_{,t} z_{,s} \quad (1.120)$$

which relates time tendencies of the depth of a generalized surface to time tendencies of the surface itself. Equation (1.30) is next used to write

$$\begin{aligned} z_{,t} &= -s_{,t} z_{,s} \\ &= z_{,s} |\nabla s| \hat{\mathbf{n}} \cdot \mathbf{v}^{(\text{ref})}, \end{aligned} \quad (1.121)$$

in which we introduced the reference velocity $\mathbf{v}^{(\text{ref})}$ for a point sitting on the generalized surface. Finally, recall equation (1.32), which relates the area element on the surface to the horizontal projection $dA = dx dy$ of the surface

$$dA_{(\hat{\mathbf{n}})} = |z_{,s} \nabla s| dA. \quad (1.122)$$

Introducing this area then renders

$$z_{,t} dA = \hat{\mathbf{n}} \cdot \mathbf{v}^{(\text{ref})} dA_{(\hat{\mathbf{n}})}. \quad (1.123)$$

This equation relates the time tendency of the depth of the generalized surface to the normal component of the velocity at a point on the surface. The two are related through the ratio of the area elements. This result is now used for the top and bottom boundary terms in relation (1.119), yielding

$$\int dV (\rho\psi)_{,t} = \partial_t \left(\int \rho dV \psi \right) - \int dA_{(\hat{\mathbf{n}})} \hat{\mathbf{n}} \cdot \mathbf{v}^{(\text{ref})} (\rho\psi). \quad (1.124)$$

Hence, the domain integrated Eulerian time tendency of the density weighted field equals the time tendency of the density weighted field integrated over the domain, minus an integral over the domain boundary associated with transport of material across that domain, with proper account taken for time dependence of the domain boundary.

The next step needed for volume integrating the density weighted material time derivative in equation (1.118) involves the divergence of the density weighted field

$$\int \nabla \cdot (\rho \mathbf{v} \psi) dV = \int \hat{\mathbf{n}} \cdot \mathbf{v} (\rho \psi) dA_{(\hat{\mathbf{n}})}, \quad (1.125)$$

which follows from Gauss' Law. Combining this result with equation (1.124) leads to the relation

$$\int \frac{d\psi}{dt} \rho dV = \partial_t \left(\iiint \rho dV \psi \right) + \iint dA_{(\hat{\mathbf{n}})} \hat{\mathbf{n}} \cdot (\mathbf{v} - \mathbf{v}^{(\text{ref})}) (\rho \psi). \quad (1.126)$$

Hence, the mass weighted grid cell integral of the material time derivative of a field is given by the time derivative of the mass weighted field integrated over the domain, plus a boundary term that accounts for the transport across the domain boundaries, with allowance made for moving domain boundaries. The manipulations leading to this result focused on an interior grid cell. The result, however, holds in general for a cell that abuts either the ocean surface or ocean bottom. For the ocean bottom, the boundary term vanishes since the bottom has a zero reference velocity, and there is no normal flow of fluid across the bottom. For the ocean surface, we employ relation (1.68) that defines the dia-surface transport of mass across the ocean surface in a manner analogous to the dia-surface transport (1.37) across an interior surface.

1.5 Basics of the finite volume method

The finite volume method for formulating the discrete equations of an ocean model has been incorporated to the ocean modelling literature only since the late 1990's. The work of [Adcroft et al. \(1997\)](#) is a canonical example of how this method can be used to garner a better representation of the solid earth boundary. In this section, we briefly outline the basis for this method. The interested reader may wish to look at chapter 6 of the book by [Hirsch \(1988\)](#), or the chapter by [Machenauer et al. \(2009\)](#) for a more thorough introduction, or one of the growing number of monographs devoted exclusively to the method.

The general equations of fluid mechanics can be represented as conservation equations for scalar quantities (e.g., seawater mass and tracer mass) and vector quantities (e.g., linear momentum). As just detailed in Section 1.4, the conservation law for a scalar Ψ over an arbitrary fluid region can be put in the form

$$\partial_t \left(\int \Psi dV \right) = - \int dA_{(\hat{\mathbf{n}})} \hat{\mathbf{n}} \cdot \mathbf{F} + \int \mathcal{S} dV. \quad (1.127)$$

The volume integral is taken over an arbitrary fluid region, and the area integral is taken over the bounding surface to that volume, with outward normal $\hat{\mathbf{n}}$. The flux \mathbf{F} penetrates the surface and acts to alter the scalar, whereas internal sources \mathcal{S} contribute to changes in the scalar throughout the interior of the domain. The budget for the vector linear momentum can be written in this form, with the addition of body forces that act similar to the source term written here (see Section 1.9). Fundamental to the finite volume method is that the fluxes contribute *only* at the boundary to the domain, and not within the interior as well. Hence, the domain can be subdivided into arbitrary shapes, with budgets over the subdivisions summing to recover the global budget.

A discrete finite volume analog to equation (1.127), for a region labeled with the integer J , takes the form

$$\partial_t (V_J \Psi_J) = - \sum_{\text{sides}} (A_{(\hat{\mathbf{n}})} \hat{\mathbf{n}} \cdot \mathbf{F}) + \mathcal{S}_J V_J. \quad (1.128)$$

Quantities with the integer J subscript refer to the discrete analogs to the continuum fields and the geo-

metric factors in equation (1.127). In particular, we define the discrete finite volume quantities

$$V_J \equiv \int dV \quad (1.129)$$

$$\Psi_J \equiv \frac{\int \Psi dV}{\int dV} \quad (1.130)$$

$$\mathcal{S}_J \equiv \frac{\int \mathcal{S} dV}{\int dV}. \quad (1.131)$$

Again, it is due to the conservation form of the fundamental fluid dynamic equation (1.127) that allows for a straightforward finite volume interpretation of the discrete equations. Notably, once formulated as such, the problem shifts from fundamentals to details, with details differing on how one represents the subgrid scale behaviour of the continuum fields. This shift leads to the multitude of discretization methods available for such processes as transport, time stepping, etc. In the following, we endeavour to write the fluid equations of the ocean in the conservation form (1.127). Doing so then renders a finite volume framework for the resulting discrete or semi-discrete equations.

When working with non-Boussinesq budgets, the finite volume interpretation applies directly to the tracer mass per volume, ρC , rather than to the tracer concentration C . The same applies to the linear momentum per volume, $\rho \mathbf{v}$, rather than to the velocity \mathbf{v} . That is, the finite volume model carries the discrete fields ρ_J , $(\rho C)_J$ and $(\rho \mathbf{v})_J$, defined as

$$\rho_J \equiv \frac{\int \rho dV}{\int dV} \quad (1.132)$$

$$(\rho C)_J \equiv \frac{\int \rho C dV}{\int dV} \quad (1.133)$$

$$(\rho \mathbf{v})_J \equiv \frac{\int \rho \mathbf{v} dV}{\int dV}. \quad (1.134)$$

As we will see in the discussions in Sections 1.6 and 1.9, we actually work with a slightly modified finite volume suite of variables, whereby the finite volume interpretation applies to the seawater mass per horizontal area, the tracer mass per horizontal area and linear momentum per horizontal area

$$(dz\rho)_J \equiv \frac{\int dA \int \rho dz}{\int dA} \quad (1.135)$$

$$(dz\rho C)_J \equiv \frac{\int dA \int \rho C dz}{\int dA} \quad (1.136)$$

$$(dz\rho \mathbf{v})_J \equiv \frac{\int dA \int \rho \mathbf{v} dz}{\int dA}, \quad (1.137)$$

where dz is the thickness of a grid cell, and

$$dA = dx dy \quad (1.138)$$

is the horizontal projection of its area. The inclusion of thickness facilitates the treatment of grid cells whose thickness is a function of time, such as in MOM. Note that to reduce notational clutter, we employ the same symbol for the continuum field as for the discrete, so we drop the J subscript in the following.

1.6 Mass and tracer budgets over finite regions

The purpose of this section is to extend the kinematics discussed in the previous sections to the case of mass and tracer budgets for finite domains within the ocean fluid. In the formulation of ocean models, these domains are thought of as discrete model grid cells.

1.6.1 General formulation

As described in Section 1.2, the tracer concentration C represents a mass of tracer per mass of seawater for *material tracers* such as salt or biogeochemical tracers. Mathematically, this definition means that for each fluid parcel,

$$\begin{aligned} C &= \frac{\text{mass of tracer}}{\text{mass of seawater}} \\ &= \frac{\rho_C dV}{\rho dV}, \end{aligned} \quad (1.139)$$

where ρ_C is the mass density of tracer within the fluid parcel. In addition to material tracers, we are concerned with a thermodynamical tracer that measures the heat within a fluid parcel. In this case, C is typically taken to be the potential temperature. However, the work of McDougall (2003) prompts us to consider a modified temperature known as *conservative temperature*, which more accurately measures the heat within a fluid parcel and is transported, to within a very good approximation, in a manner directly analogous to material tracers. We discussed these temperature variables in Section 1.3.

Given these considerations, the total tracer mass within a finite region of seawater is given by the integral.

$$\begin{aligned} \text{tracer mass in a region} &= \int \rho_C dV \\ &= \int C \rho dV. \end{aligned} \quad (1.140)$$

Correspondingly, the evolution of tracer mass within a Lagrangian parcel of mass conserving fluid is given by (see Section 5.1 of Griffies, 2004)

$$\rho \frac{dC}{dt} = -\nabla \cdot \mathbf{J} + \rho S^{(C)}, \quad (1.141)$$

where $S^{(C)}$ is a tracer source in the region, with units of tracer concentration per time. The tracer flux \mathbf{J} arises from subgrid scale transport of tracer in the absence of mass transport. Such transport in MOM consists of diffusion and/or unresolved advection. As discussed in Section 1.2.3, this flux is computed with respect to the center of mass of a fluid parcel. It therefore vanishes when the tracer concentration is uniform, in which case the tracer budget reduces to the mass budget (1.7).

We now develop a regional budget for tracer mass over a grid cell. For this purpose, apply the general result (1.126) relating the material time derivative to a regional budget, to render

$$\partial_t \left(\int C \rho dV \right) = \int S^{(C)} \rho dV - \int dA_{(\hat{n})} \hat{n} \cdot [(\mathbf{v} - \mathbf{v}^{\text{ref}}) \rho C + \mathbf{J}]. \quad (1.142)$$

Again, the left hand side of this equation is the time tendency for tracer mass within the finite sized grid cell region. When the tracer concentration is uniform, the SGS flux vanishes, in which case the tracer budget (1.142) reduces to the finite domain mass budget

$$\partial_t \left(\int \rho dV \right) = \int S^{(M)} \rho dV - \int dA_{(\hat{n})} \hat{n} \cdot [(\mathbf{v} - \mathbf{v}^{\text{ref}}) \rho]. \quad (1.143)$$

In addition to the tracer flux \mathbf{J} , it is convenient to define the *tracer concentration flux* \mathbf{F} via

$$\mathbf{J} = \rho \mathbf{F}, \quad (1.144)$$

where the dimensions of \mathbf{F} are velocity \times tracer concentration.

In a manner analogous to our definition of a dia-surface velocity component in Section 1.1.4, it is useful to introduce the dia-surface SGS flux component. For this purpose, consider the tracer mass per time

crossing a surface of constant generalized vertical coordinate, where this transport arises from SGS processes. Manipulations similar to those used to derive the dia-surface velocity component lead to

$$\begin{aligned} (\text{SGS tracer mass through surface})/(\text{time}) &= dA_{(\hat{\mathbf{n}})} \hat{\mathbf{n}} \cdot \mathbf{J} \\ &= z_s \nabla s \cdot \mathbf{J} dx dy \\ &= (\hat{\mathbf{z}} - \mathbf{S}) \cdot \mathbf{J} dx dy, \end{aligned} \quad (1.145)$$

where \mathbf{S} is the slope vector for the generalized surface defined in equation (1.39). We are therefore led to introduce the dia-surface SGS tracer flux

$$\begin{aligned} J^{(z)} &\equiv \frac{dA_{(\hat{\mathbf{n}})} \hat{\mathbf{n}} \cdot \mathbf{J}}{dA} \\ &= z_s \nabla s \cdot \mathbf{J} \\ &= (\hat{\mathbf{z}} - \mathbf{S}) \cdot \mathbf{J}, \end{aligned} \quad (1.146)$$

where $dA = dx dy$ is the horizontal cross-sectional area. In words, $J^{(z)}$ is the tracer mass per time per horizontal area penetrating surfaces of constant generalized vertical coordinate via processes that are unresolved by the dia-surface velocity component $w^{(z)}$.

1.6.2 Budget for an interior grid cell

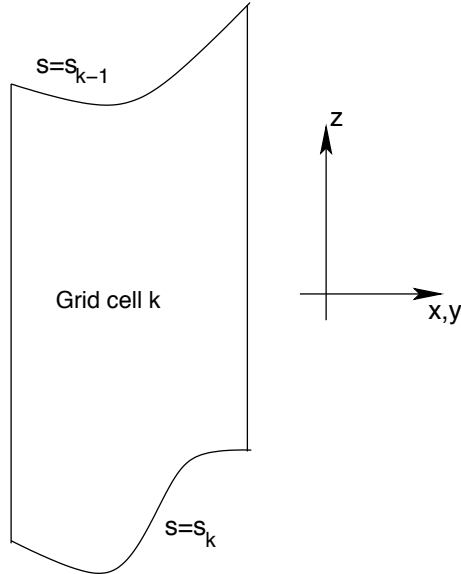


Figure 1.4: Schematic of an ocean grid cell labeled by the vertical integer k . Its sides are vertical and oriented according to $\hat{\mathbf{x}}$ and $\hat{\mathbf{y}}$, and its horizontal position is fixed in time. The top and bottom surfaces are determined by constant generalized vertical coordinates s_{k-1} and s_k , respectively. Furthermore, the top and bottom are assumed to always have an outward normal with a nonzero component in the vertical direction $\hat{\mathbf{z}}$. That is, the top and bottom are never vertical. We take the convention that the discrete vertical label k increases as moving downward in the column, and grid cell k is bounded at its upper face by $s = s_{k-1}$ and lower face by $s = s_k$.

Consider the budget for a region bounded away from the ocean surface and bottom, such as that shown in Figure 1.4. We have in mind here a grid cell within a discrete numerical model. There are two assumptions that define a grid cell for our purposes.

- The sides of the cell are vertical, so they are parallel to \hat{z} and aligned with the horizontal coordinate directions (\hat{x}, \hat{y}). Their horizontal positions are fixed in time.
- The top and bottom of the cell are defined by surfaces of constant generalized vertical coordinate $s = s(x, y, z, t)$. The generalized surfaces do not overturn, which means that $s_{,z}$ is single signed throughout the ocean.

These assumptions lead to the following results for the sides of the grid cell

$$\text{TRACER MASS ENTERING CELL WEST FACE} = \int_{x=x_1} (u \rho C + \rho F^x) dy dz \quad (1.147)$$

$$\text{TRACER MASS LEAVING CELL EAST FACE} = - \int_{x=x_2} (u \rho C + \rho F^x) dy dz \quad (1.148)$$

where $x_1 \leq x \leq x_2$ defines the domain boundaries for the east-west coordinates.¹² Similar results hold for the tracer mass crossing the cell in the north-south directions. At the top and bottom of the grid cell

$$\text{TRACER MASS ENTERING CELL BOTTOM FACE} = \int_{s=s_k} (w^{(z)} C + F^{(z)}) \rho dx dy \quad (1.149)$$

$$\text{TRACER MASS LEAVING CELL TOP FACE} = - \int_{s=s_{k-1}} (w^{(z)} C + F^{(z)}) \rho dx dy. \quad (1.150)$$

To reach this result, we used a result from Section 1.1.4 to write the volume flux passing through the top face of the grid cell

$$dA_{(\hat{n})} \hat{n} \cdot (\mathbf{v} - \mathbf{v}^{\text{ref}}) = w^{(z)} dx dy, \quad (1.151)$$

with $w^{(z)} = z_{,s} ds/dt$ the dia-surface velocity component from Section 1.1.4. A similar relation holds for the bottom face of the cell. The form of the SGS flux passing across the top and bottom is correspondingly given by

$$dA_{(\hat{n})} \hat{n} \cdot \mathbf{J} = J^{(z)} dx dy, \quad (1.152)$$

which follows from the general expression (1.146) for the dia-surface tracer flux.

In a model using the generalized coordinate s for the vertical, it is sometimes convenient to do the vertical integrals over s instead of z . For this purpose, recall that with $z_{,s}$ single signed, the vertical thickness of a grid cell is given by equation (1.52), repeated here for completeness

$$dz = z_{,s} ds. \quad (1.153)$$

Bringing these results together, and taking the limit as the volume of the cell in (x, y, s) space goes to zero (i.e., $dx dy ds \rightarrow 0$) leads to

$$\partial_t (z_{,s} \rho C) = z_{,s} \rho \mathcal{S}^{(C)} - \nabla_s \cdot [z_{,s} \rho (\mathbf{u} C + \mathbf{F})] - \partial_s [\rho (w^{(z)} C + F^{(z)})] \quad (1.154)$$

Notably, the horizontal gradient operator ∇_s is computed on surfaces of constant s , and so it is distinct generally from the horizontal gradient ∇_z taken on surfaces of constant z .

As indicated at the end of Section 1.5, we prefer to work with thickness weighted quantities, given the general time dependence of a model grid cell in MOM. Hence, as an alternative to taking the limit as $dx dy ds \rightarrow 0$, consider instead the limit as the time independent horizontal area $dx dy$ goes to zero, thus maintaining the time dependent thickness $dz = z_{,s} ds$ inside the derivative operators. In this case, the thickness weighted tracer mass budget takes the form

$$\partial_t (C \rho dz) = \mathcal{S}^{(C)} \rho dz - \nabla_s \cdot [(\mathbf{u} C + \mathbf{F}) \rho dz] - [\rho (w^{(z)} C + F^{(z)})]_{s=s_{k-1}} + [\rho (w^{(z)} C + F^{(z)})]_{s=s_k}. \quad (1.155)$$

¹²We use generalized horizontal coordinates, such as those discussed in Griffies (2004). Hence, the directions east, west, north, and south may not correspond to the usual geographic directions. Nonetheless, this terminology is useful for establishing the budgets, whose validity is general.

Similarly, the thickness weighted mass budget is

$$\partial_t(\rho dz) = \mathcal{S}^{(M)} \rho dz - \nabla_s \cdot (\mathbf{u} \rho dz) - (\rho w^{(z)})_{s=s_{k-1}} + (\rho w^{(z)})_{s=s_k}. \quad (1.156)$$

For clarity, note that the horizontal divergence operator acting on the mass transport takes the form

$$\nabla_s \cdot (\mathbf{u} \rho dz) = \frac{1}{dy} \frac{\partial}{\partial x} (dy u \rho dz) + \frac{1}{dx} \frac{\partial}{\partial y} (dx v \rho dz). \quad (1.157)$$

The mass source $\mathcal{S}^{(M)}$ has units of inverse time that, for self-consistency, must be related to the tracer source via

$$\mathcal{S}^{(M)} = \mathcal{S}^{(C)} (C = 1). \quad (1.158)$$

Additionally, the SGS tracer flux vanishes with a uniform tracer

$$\mathbf{F}(C = 1) = 0. \quad (1.159)$$

Note that by setting the tracer concentration in equation (1.155) to a uniform constant, SGS transort fluxes vanish, thus revealing the mass conservation budget. This procedure for deriving the mass budget from the tracer budget follows trivially from the definition of the tracer concentration given by equation (1.139). It represents a *compatibility condition* between the discrete budgets, and this condition is critical to maintain within a numerical model in order to respect tracer and mass conservation in the simulation. We have more to say about the compatibility condition in Section 1.7.1.

One reason that the thickness weighted budget given by equation (1.155) is more convenient than equation (1.154) is that equation (1.155) expresses the budget in terms of the grid cell thickness dz , rather than the specific thickness z_s . Nonetheless, this point is largely one of style and convenience, as there is no fundamental reason to prefer one form over the other for purposes of developing the discrete equations of an ocean model.

1.6.3 Cells adjacent to the ocean bottom

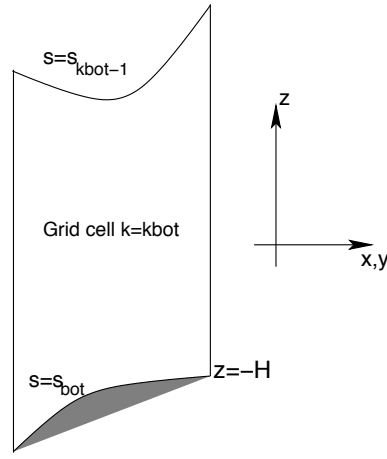


Figure 1.5: Schematic of an ocean grid cell next to the ocean bottom labeled by $k = k_{\text{bot}}$. Its top face is a surface of constant generalized vertical coordinate $s = s_{k_{\text{bot}}-1}$, and the bottom face is determined by the ocean bottom topography at $z = -H$ where $s_{\text{bot}}(x, y, t) = s(x, y, z = -H, t)$.

For a grid cell adjacent to the ocean bottom (Figure 1.5), we assume that just the bottom face of this cell abuts the solid earth boundary. The outward normal $\hat{\mathbf{n}}_H$ to the bottom is given by equation (1.46), and the area element along the bottom is

$$dA_H = |\nabla(z + H)| dx dy. \quad (1.160)$$

Hence, the transport across the solid earth boundary is

$$-\int dA_H \hat{n}_H \cdot (\mathbf{v} \rho C + \mathbf{J}) = \int (\nabla H + \hat{\mathbf{z}}) \cdot (\mathbf{v} \rho C + \mathbf{J}) dx dy. \quad (1.161)$$

We assume that there is zero advective mass flux across the bottom, in which case the advective flux drops out since $\mathbf{v} \cdot (\nabla H + \hat{\mathbf{z}}) = 0$ (equation (1.48)). However, the possibility of a nonzero geothermal tracer transport warrants a nonzero SGS tracer flux at the bottom, in which case the bottom tracer flux is written

$$Q_{(\text{bot})}^{(C)} = (\nabla H + \hat{\mathbf{z}}) \cdot \mathbf{J}. \quad (1.162)$$

The corresponding thickness weighted budget is given by

$$\partial_t (C \rho dz) = \mathcal{S}^{(C)} \rho dz - \nabla_s \cdot [(\mathbf{u} C + \mathbf{F}) \rho dz] - [\rho (w^{(z)} C + z_s \nabla s \cdot \mathbf{F})]_{s=s_{kbot-1}} + Q_{(\text{bot})}^{(C)}, \quad (1.163)$$

and the corresponding mass budget is

$$\partial_t (\rho dz) = \mathcal{S}^{(M)} \rho dz - \nabla_s \cdot (\mathbf{u} \rho dz) - (\rho w^s)_{s=s_{kbot-1}} + Q_{(\text{bot})}^{(M)}, \quad (1.164)$$

where $Q_{(\text{bot})}^{(M)}$ allows for the possibility of mass entering through geothermal boundary sources. For brevity, we drop this term in the following, since it generally is ignored for ocean climate modeling.

1.6.4 Cells adjacent to the ocean surface

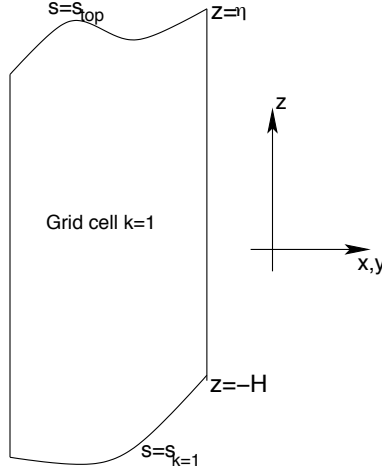


Figure 1.6: Schematic of an ocean grid cell next to the ocean surface labeled by $k = 1$. Its top face is at $z = \eta$, and the bottom is a surface of constant generalized vertical coordinate $s = s_{k=1}$.

For a grid cell adjacent to the ocean surface (Figure 1.6), we assume that just the upper face of this cell abuts the boundary between the ocean and the atmosphere or sea ice. The ocean surface is a time dependent boundary with $z = \eta(x, y, t)$. The outward normal $\hat{\mathbf{n}}_\eta$ is given by equation (1.69), and its area element dA_η is given by equation (1.73).

As the surface can move, we must measure the advective transport with respect to the moving surface. Just as in the dia-surface transport discussed in Section 1.1.4, we consider the velocity of a reference point on the surface

$$\mathbf{v}^{\text{ref}} = \mathbf{u}^{\text{ref}} + \hat{\mathbf{z}} w^{\text{ref}}. \quad (1.165)$$

Since $z = \eta$ represents the vertical position of the reference point, the vertical component of the velocity for this point is given by

$$w^{\text{ref}} = (\partial_t + \mathbf{u}^{\text{ref}} \cdot \nabla) \eta \quad (1.166)$$

which then leads to

$$\mathbf{v}^{\text{ref}} \cdot \nabla(z - \eta) = \eta_{,t}. \quad (1.167)$$

Hence, the advective transport leaving the ocean surface is

$$\begin{aligned} \int_{z=\eta} \rho C (\mathbf{v} - \mathbf{v}^{\text{ref}}) \cdot \hat{\mathbf{n}} dA_{(\hat{\mathbf{n}})} &= \int_{z=\eta} \rho C (-\eta_{,t} + w - \mathbf{u} \cdot \nabla \eta) dx dy \\ &= - \int_{z=\eta} Q_m C dx dy, \end{aligned} \quad (1.168)$$

where the surface kinematic boundary condition (1.77) was used. The negative sign on the right hand side arises from our convention that $Q_m > 0$ represents an input of mass to the ocean domain. In summary, the tracer flux leaving the ocean free surface is given by

$$\int_{z=\eta} [(\mathbf{v} - \mathbf{v}^{\text{ref}}) \rho C + \mathbf{J}] \cdot \hat{\mathbf{n}} dA_{(\hat{\mathbf{n}})} = \int_{z=\eta} [-Q_m C + \nabla(z - \eta) \cdot \mathbf{J}] dx dy. \quad (1.169)$$

In equation (1.169), we formally require the tracer concentration precisely at the ocean surface $z = \eta$. However, as mentioned at the start of Section 1.1.6, it is actually a fiction that the ocean surface is a smooth mathematical function. Furthermore, seawater properties precisely at the ocean surface, known generally as *skin properties*, are generally not what an ocean model carries as its prognostic variable in its top grid cell. Instead, the model carries a bulk property averaged over roughly the upper few tens of centimeters.

To proceed in formulating the boundary condition for an ocean climate model, we consider there to be a boundary layer model that provides us with the total tracer flux passing through the ocean surface. Developing such a model is a nontrivial problem in air-sea and ice-sea interaction theory and phenomenology. For present purposes, we do not focus on these details, and instead just introduce this flux in the form

$$Q^{(C)} = -Q_m C_m + Q_{(\text{turb})}^{(C)} \quad (1.170)$$

where C_m is the tracer concentration within the incoming water. The first term on the right hand side represents the advective transport of tracer through the surface with the fresh water (i.e., ice melt, rivers, precipitation, evaporation). The term $Q_{(\text{turb})}^{(C)}$ arises from parameterized turbulence and/or radiative fluxes, such as sensible, latent, shortwave, and longwave heating appropriate for the temperature equation. A positive value for $Q_{(\text{turb})}^{(C)}$ signals tracer leaving the ocean through its surface. In the special case of zero fresh water flux, then

$$\nabla(z - \eta) \cdot \mathbf{J} = Q_{(\text{turb})}^{(C)} \quad \text{if } Q_m = 0. \quad (1.171)$$

In general, it is not possible to make this identification. Instead, we must settle for the general expression

$$\int_{z=\eta} [(\mathbf{v} - \mathbf{v}^{\text{ref}}) \rho C + \mathbf{J}] \cdot \hat{\mathbf{n}} dA_{(\hat{\mathbf{n}})} = \int_{z=\eta} (-Q_m C_m + Q_{(\text{turb})}^{(C)}) dx dy. \quad (1.172)$$

The above results lead to the thickness weighted tracer budget for the ocean surface grid cell

$$\partial_t (C \rho dz) = \mathcal{S}^{(C)} \rho dz - \nabla_s \cdot [(\mathbf{u} C + \mathbf{F}) \rho dz] + [\rho (w^{(z)} C + z_{,s} \nabla s \cdot \mathbf{F})]_{s=s_{k=1}} + (Q_m C_m - Q_{(C)}^{(\text{turb})}), \quad (1.173)$$

and the corresponding mass budget

$$\partial_t (\rho dz) = \mathcal{S}^{(M)} \rho dz - \nabla_s \cdot (\mathbf{u} \rho dz) + (\rho w^{(z)})_{s=s_{k=1}} + Q_m. \quad (1.174)$$

1.7 Special considerations for tracers

We now describe some special considerations for tracers in a numerical ocean model.

1.7.1 Compatability between mass and tracer budgets

In Section 1.6.2, we considered issues of compatibility between the tracer and mass budgets within a grid cell. Such compatibility follows trivially from the definition of tracer concentration given in Section 1.6.1. We briefly revisit compatibility here, by focusing on the vertically integrated tracer and mass budgets.

Combining the surface tracer budget (1.174), the bottom budget (1.163), and interior budget (1.155), renders the vertically integrated tracer budget

$$\partial_t \left(\sum_k C \rho dz \right) = \sum_k S^{(C)} \rho dz - \nabla_s \cdot \left(\sum_k (\mathbf{u} C + \mathbf{F}) \rho dz \right) + \left(Q_m C_m - Q_{(C)}^{(\text{turb})} + Q_{(C)}^{(\text{bott})} \right). \quad (1.175)$$

As expected, the only contributions from vertical fluxes come from the top and bottom boundaries. Furthermore, by setting the tracer concentration to a uniform constant, in which case the SGS turbulent terms vanish, the tracer budget reduces to the vertically integrated mass budget

$$\partial_t \left(\sum_k \rho dz \right) = \sum_k S^{(M)} \rho dz - \nabla_s \cdot \mathbf{U}^\rho + Q_m, \quad (1.176)$$

where

$$\mathbf{U}^\rho = \sum_k \mathbf{u} \rho dz \quad (1.177)$$

is the discrete form of the vertically integrated horizontal momentum per volume defined by equation (1.22). As for the individual grid cells, this vertically integrated compatibility between tracer and mass budgets must be carefully maintained by the space and time discretizations used in an ocean model. Otherwise, conservation properties of the model will be compromised (Griffies et al., 2001).

1.7.2 Fresh water budget

Seawater is comprised of fresh water with a relatively fixed ratio of various salts. It is common to consider the budget for the concentration of these salts, which is described by the tracer equation (1.155). As a complement, it may be of interest to formulate a budget for fresh water. In this case, we consider the mass of fresh water within a fluid parcel

$$\text{mass of fresh water} = \text{mass of seawater} - \text{mass of salt} \quad (1.178a)$$

$$= (1 - S) \rho dV \quad (1.178b)$$

$$= W \rho dV, \quad (1.178c)$$

where S is the salinity (mass of salt per mass of seawater), and

$$W \equiv 1 - S \quad (1.179)$$

is the mass of fresh water per mass of seawater. Results from the tracer budget considered in Section 1.6.2 allow us to derive the following budget for fresh water within an interior ocean model grid cell

$$\partial_t (W \rho dz) = (S^{(M)} - S^{(S)}) \rho dz - \nabla_s \cdot [(\mathbf{u} W - \mathbf{F}) \rho dz] - [\rho (w^{(z)} W - F^{(z)})]_{s=s_{k-1}} + [\rho (w^{(z)} W - F^{(z)})]_{s=s_k}. \quad (1.180)$$

In these relations, the SGS tracer flux components \mathbf{F} and $F^{(z)}$ are those for salt, and $S^{(S)}$ is the salt source. Equation (1.180) is very similar to the tracer equation (1.155), with modified source term and negative signs on the SGS flux components.

1.7.3 The ideal age tracer

Thiele and Sarmiento (1990) and England (1995) consider an ideal age tracer for Boussinesq fluids. We consider the generalization here to non-Boussinesq fluids, in which

$$\rho \frac{dA}{dt} + \nabla \cdot \mathbf{J} = \rho \mathcal{S}^{(A)}, \quad (1.181)$$

where the age tracer A has dimensions of time and it is initialized globally to zero. It is characterized by the dimensionless *clock source* $S^{(A)}$, which takes the values

$$S^{(A)} = \begin{cases} 0 & \text{if } z = \eta \\ 1 & \text{if } z < \eta, \end{cases} \quad (1.182)$$

In a finite difference model, the boundary condition at $z = \eta$ is applied at the top grid cell $k = 1$. In MOM, various age tracers can be defined that differ by the region that their boundary condition is set to zero. Given these prescriptions, A measures the age, in units of time, that a water parcel has spent away from the region where it was set to zero. Therefore, visual maps of A are useful to deduce such physically interesting properties as ventilation times.

From equation (1.155), the budget for ideal age tracer mass per area in a grid cell is given by

$$\partial_t(A\rho dz) = S^{(A)}\rho dz - \nabla_s \cdot [(\mathbf{u}A + \mathbf{F})\rho dz] - [\rho(w^{(z)}A + F^{(z)})]_{s=s_{k-1}} + [\rho(w^{(z)}A + F^{(z)})]_{s=s_k}. \quad (1.183)$$

In practice, the clock source is added to the age tracer at the very end of the time step, so that it is implemented as an adjustment process. In this way, we remove the ambiguity regarding the time step to evaluate the ρdz factor that multiplies the age source.

1.7.4 Budgets without dia-surface fluxes

To garner some experience with tracer budgets, it is useful to consider the special case of zero dia-surface transport, either via advection or SGS fluxes, and zero tracer/mass sources. In this case, the thickness weighted mass and tracer mass budgets take the simplified form

$$\partial_t(\rho dz) = -\nabla_s \cdot (\mathbf{u}\rho dz) \quad (1.184)$$

$$\partial_t(C\rho dz) = -\nabla_s \cdot [(\mathbf{u}C + \mathbf{F})\rho dz]. \quad (1.185)$$

The first equation says that the time tendency of the thickness weighted density (mass per area) at a point between two surfaces of constant generalized vertical coordinate is given by the horizontal convergence of mass per area onto that point. The transport is quasi-two-dimensional in the sense that it is only a two-dimensional convergence that determines the evolution. The tracer equation has an analogous interpretation. We illustrate this situation in Figure 1.7. As emphasized in our discussion of the material time derivative (1.43), this simplification of the transport equation does not mean that fluid parcels are strictly horizontal. Indeed, such is distinctly not the case when the surfaces are moving.

A further simplification of the mass and tracer mass budgets ensues when considering adiabatic and Boussinesq flow in isopycnal coordinates. We consider ρ now to represent the constant potential density of the finitely thick fluid layer. In this case, the mass and tracer budgets reduce to

$$\partial_t(dz) = -\nabla_\rho \cdot (\mathbf{u}dz) \quad (1.186)$$

$$\partial_t(Cdz) = -\nabla_\rho \cdot [(\mathbf{u}C + \mathbf{F})dz]. \quad (1.187)$$

Equation (1.186) provides a relation for the thickness of the density layers, and equation (1.187) is the analogous relation for the tracer within the layer. These expressions are commonly used in the construction of adiabatic isopycnal models, which are often used in the study of geophysical fluid mechanics of the ocean.

1.8 Forces from pressure

Pressure is a contact force per area that acts in a compressive manner on the boundary of a finite fluid domain (e.g., see Figure 1.8). Mathematically, we have

$$\mathbf{F}_{\text{press}} = - \int \hat{\mathbf{n}} p dA_{(\hat{\mathbf{n}})}, \quad (1.188)$$

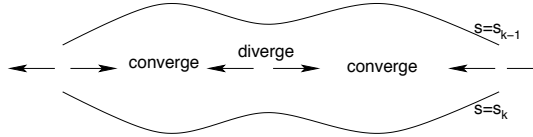


Figure 1.7: Schematic of the horizontal convergence of mass between two surfaces of constant generalized vertical coordinates. As indicated by equation (1.184), when there is zero dia-surface transport, it is just the horizontal convergence that determines the time evolution of mass between the layers. Evolution of thickness weighted tracer concentration in between the layers is likewise evolved just by the horizontal convergence of the thickness weighted advective and diffusive tracer fluxes (equation (1.185)). In this way, the transport is quasi-two-dimensional when the dia-surface transports vanish. A common example of this special system is an adiabatic ocean where the generalized surfaces are defined by isopycnals.

where p is the pressure (with units of a force per area) acting on the boundary of the domain with outward normal \hat{n} and area element $dA(\hat{n})$. The minus sign accounts for the compressive behaviour of pressure. The accumulation of contact pressure forces acting over the bounding area of the domain leads to a net pressure force acting on the domain.

Through use of the Green-Gauss theorem of vector calculus, we can equivalently consider pressure to exert a body force per area at each point within the domain, so that

$$\mathbf{F}_{\text{press}} = - \int \nabla p dV, \quad (1.189)$$

where dV is the volume element. That is, the volume integral of the pressure gradient body force over the domain yields the net pressure force.

In the continuum, the two formulations (1.188) and (1.189) yield identical pressure forces. Likewise, in a finite volume discretization, the two forms are identical (e.g., Section 6.2.2 of Hirsch, 1988). But with finite differences, as used in earlier versions of MOM for pressure forces, the two forms can lead to different numerical methods. In the remainder of this section, we further explore the computation of pressure forces according to the two different formulations.

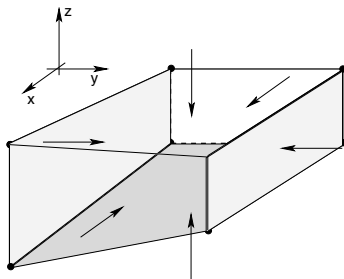


Figure 1.8: Schematic of a grid cell bounded at its top and bottom in general by sloped surfaces and vertical side walls. The top and bottom surfaces can represent linear piecewise approximations to surfaces of constant generalized vertical coordinates, with $s = s_1$ at the top surface and $s = s_2$ at the bottom surface. They could also represent the ocean surface (for the top face) or the ocean bottom (for the bottom face). The arrows represent the pressure contact forces that act in a compressive manner along the boundaries of the grid cell and in a direction normal to the boundaries. These forces arise from contact between the shown fluid volume and adjacent regions. Due to Newton's Third Law, the pressure acting on an arbitrary fluid parcel A due to contact with a parcel B is equal and opposite to the pressure acting on parcel B due to contact with parcel A. If coded according to finite volume budgets, as in Lin (1997) or Adcroft et al. (2008), this law extends to the pressure forces acting between grid cells in an ocean model.

1.8.1 The accumulation of contact pressure forces

Pressure acts as a contact or interfacial stress on the sides of a finite region of fluid. In particular, the total pressure force acting on the grid cell in Figure 1.8 is given by summing the pressure forces acting on the six cell faces

$$\mathbf{F}_{\text{pressure}} = \mathbf{F}_{x=x_1} + \mathbf{F}_{x=x_2} + \mathbf{F}_{y=y_1} + \mathbf{F}_{y=y_2} + \mathbf{F}_{s=s_1} + \mathbf{F}_{s=s_2}. \quad (1.190)$$

The pressure acting on faces with a zonal normal can be written

$$\mathbf{F}_{x=x_1} = \hat{\mathbf{x}} \left(\int dy \int_{z_2}^{z_1} p dz \right)_{x=x_1} \quad (1.191)$$

$$\mathbf{F}_{x=x_2} = -\hat{\mathbf{x}} \left(\int dy \int_{z_2}^{z_1} p dz \right)_{x=x_2} \quad (1.192)$$

where the vertical integral extends from the bottom face at $z_2 = z(x, y, s = s_2, t)$ to the top face at $z_1 = z(x, y, s = s_1, t)$. Likewise, the meridional pressure forces are

$$\mathbf{F}_{y=y_1} = \hat{\mathbf{y}} \left(\int dx \int_{z_2}^{z_1} p dz \right)_{y=y_1} \quad (1.193)$$

$$\mathbf{F}_{y=y_2} = -\hat{\mathbf{y}} \left(\int dx \int_{z_2}^{z_1} p dz \right)_{y=y_2}. \quad (1.194)$$

On the top face, the pressure force is given by

$$\begin{aligned} \mathbf{F}_{s=s_1} &= - \left(\int dy \int p z_s \nabla_s dx \right)_{s=s_1} \\ &= - \left(\int dy \int p (-\nabla_s z + \hat{\mathbf{z}}) dx \right)_{s=s_1}. \end{aligned} \quad (1.195)$$

Note the contribution from the generally non-horizontal top face as represented by the two dimensional vector

$$\nabla_s z = \mathbf{S}, \quad (1.196)$$

which is the slope of the surface of constant generalized vertical coordinate relative to the horizontal plane. The pressure force on the bottom face has a similar appearance

$$\mathbf{F}_{s=s_2} = \left(\int dy \int p (-\nabla_s z + \hat{\mathbf{z}}) dx \right)_{s=s_2}. \quad (1.197)$$

If the top and bottom faces are horizontal, as for z -models, the pressure force acting at $s = s_1$ and $s = s_2$ acts solely in the vertical direction. More generally, the pressure force per area on the top and bottom faces is oriented according to the slope of the faces and so has a nontrivial projection into all three directions.

To garner a sense for how pressure acts on the face of a grid cell, consider the case where the top surface of a grid cell rises to the east as shown in Figure 1.9. In this case, the pressure force per area in the $x-z$ plane takes the form

$$\text{PRESSURE FORCE PER AREA ON TOP FACE} = -p [\hat{\mathbf{z}} - (\partial z / \partial x)_s \hat{\mathbf{x}}]. \quad (1.198)$$

Since $(\partial z / \partial x)_s > 0$ for this example, the pressure force per area has a positive component in the $\hat{\mathbf{x}}$ direction, as indicated by the arrow normal to the top surface in Figure 1.9.

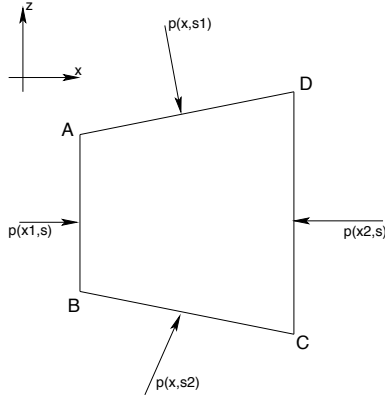


Figure 1.9: The sides of the grid cell, with the slopes top and bottom surfaces more enhanced here than in Figure 1.9. The corners are denoted A, B, C, and D, and oriented in a counterclockwise manner. This is the orientation appropriate for performing a contour integral in order to compute the pressure force acting on the area.

When the top surface represents the surface of the ocean at $z = \eta$, the pressure p is the applied pressure p_a arising from any media above the ocean, such as the atmosphere and sea ice. In this case,

$$\begin{aligned} \text{PRESSURE FORCE PER AREA ON OCEAN SURFACE} &= -p_a \nabla(z - \eta) \\ &= -p_a (\hat{z} - \nabla\eta), \end{aligned} \quad (1.199)$$

where $\nabla\eta$ is the slope of the ocean surface. Likewise, if the bottom of the grid cell is bounded by the solid earth boundary,

$$\begin{aligned} \text{PRESSURE FORCE PER AREA ON OCEAN BOTTOM} &= p_b \nabla(z + H) \\ &= p_b (\hat{z} + \nabla H), \end{aligned} \quad (1.200)$$

where ∇H is the bottom slope.

A sum of the pressure forces acting on the six faces of the grid cell determines the acceleration due to pressure acting on a grid cell. Organizing the forces into the three directions leads to

$$F_{\text{pressure}}^x = \left(\int dy \int_{z_2}^{z_1} p dz \right)_{x=x_1} - \left(\int dy \int_{z_2}^{z_1} p dz \right)_{x=x_2} \quad (1.201)$$

$$+ \left(\int dy \int_{x_1}^{x_2} z_x p dx \right)_{s=s_1} - \left(\int dy \int_{x_1}^{x_2} z_x p dx \right)_{s=s_2} \quad (1.202)$$

$$F_{\text{pressure}}^y = \left(\int dx \int_{z_2}^{z_1} p dz \right)_{y=y_1} - \left(\int dx \int_{z_2}^{z_1} p dz \right)_{y=y_2} \quad (1.203)$$

$$+ \left(\int dx \int_{y_1}^{y_2} z_y p dy \right)_{s=s_1} - \left(\int dx \int_{y_1}^{y_2} z_y p dy \right)_{s=s_2} \quad (1.204)$$

$$F_{\text{pressure}}^z = \left(\int p dx dy \right)_{s=s_2} - \left(\int p dx dy \right)_{s=s_1}. \quad (1.205)$$

Making the hydrostatic approximation, whereby the vertical momentum equation maintains the inviscid hydrostatic balance, allows us to note that the difference in pressure between the top and bottom surfaces

of the region is determined by the weight of fluid between the surfaces,

$$\int_{s=s_2} p dx dy - \int_{s=s_1} p dx dy = g \int \rho dV. \quad (1.206)$$

It is notable that this expression relates the difference in contact forces acting on the domain boundaries to the integral of a body force (the gravitational force) acting throughout the domain interior.

We now work on reformulating the horizontal pressure forces into a manner amenable to finite volume discretization. Referring to Figure 1.9, we can write the horizontal forces in a manner than builds in the orientation of pressure via a counterclockwise contour integral

$$\begin{aligned} F_{\text{pressure}}^x &= - \left(\int dy \int_{z_1}^{z_2} p dz \right)_{x=x_1} - \left(\int dy \int_{x_1}^{x_2} z_x p dx \right)_{s=s_2} \\ &\quad - \left(\int dy \int_{z_2}^{z_1} p dz \right)_{x=x_2} - \left(\int dy \int_{x_2}^{x_1} z_x p dx \right)_{s=s_1} \\ &= - \left(\int dy \int_{z_1}^{z_2} p dz \right)_{x=x_1} - \left(\int dy \int_{x_1}^{x_2} p dz \right)_{s=s_2} \\ &\quad - \left(\int dy \int_{z_2}^{z_1} p dz \right)_{x=x_2} - \left(\int dy \int_{x_2}^{x_1} p dz \right)_{s=s_1} \\ &= - \int dy \oint_{ABCD} p dz. \end{aligned} \quad (1.207)$$

In the penultimate step, we set $z_x dx = dz$, which is an relation valid along the particular contour $ABCD$. That is, in all the integrals, the differential increment dz is taken along the contour surrounding the cell. The counter-clockwise orientation of the integral follows from the compressive nature of pressure. Since the contour of integration is closed, we have the identity

$$\begin{aligned} F_{\text{pressure}}^x &= - \int dy \oint_{ABCD} p dz \\ &= \int dy \oint_{ABCD} z dp. \end{aligned} \quad (1.208)$$

The contour integral form of the pressure force is key to providing a finite volume discretization that is consistent with Newton's Third Law ([Lin, 1997](#); [Adcroft et al., 2008](#)). What is needed next is an assumption about the subgrid profiles for pressure and geopotential $\Phi = gz$ in order to evaluate the contour integral.

1.8.2 Pressure gradient body force in hydrostatic fluids

In the early finite difference formulations of the pressure force, modelers discretized the gradient of pressure and performed certain grid averages so that the gradient occurs at the appropriate grid point. Guidance to the discretization details was provided by concerns of energetic consistency (see Chapter 14 of [Griffies \(2012\)](#)), whereby work done by pressure in the discrete algorithm is balanced by buoyancy work ([Bryan, 1969](#)). This general philosophy *still* guides the formulation of the pressure force in MOM.

As with the contact forces formulation, in a hydrostatic fluid we are only concerned with horizontal pressure gradients, since the vertical momentum equation is reduced to the inviscid hydrostatic balance.

Hence, we are concerned with the horizontal acceleration arising from pressure differences in a hydrostatic and non-Boussinesq fluid, and this acceleration can be written¹³

$$\rho^{-1} \nabla_z p = \rho^{-1} (\nabla_s - \nabla_s z \partial_z) p \quad (1.209a)$$

$$= \rho^{-1} \nabla_s p + g \nabla_s z \quad (1.209b)$$

$$= \rho^{-1} \nabla_s p + \nabla_s \Phi, \quad (1.209c)$$

where the hydrostatic relation $p_{,z} = -\rho g$ was used to reach the second equality, and

$$\Phi = g z \quad (1.210)$$

is the geopotential. To reach this result, we used the expression

$$\nabla_z = \nabla_s - \nabla_s z \partial_z, \quad (1.211)$$

which relates the lateral gradient operator acting on constant depth surfaces, ∇_z , to the lateral operator acting on surfaces of constant generalized vertical coordinate, ∇_s .

Depending on the choice for the vertical coordinate s , discretizations of the pressure gradient body force can result in both terms in equation (1.209) being large and of opposite sign in many regions. This issue is especially pernicious for terrain following coordinates in regions of nontrivial topographic slope (e.g., Griffies et al., 2000). Hence, this calculation exposes the discrete pressure gradient force to non-trivial numerical truncation errors which can lead to spurious numerical pressure gradients and thus to incorrect simulated currents. Significant effort has gone into reducing such *pressure gradient errors*, especially in terrain following models where undulations of the coordinate surfaces can be large with realistic topography. Some of these issues are summarized in Section 2 of Griffies et al. (2000).

The pressure gradient force acting at a point represents the infinitesimal limit of a body force. We see this fact by multiplying the pressure gradient acceleration by the mass of a fluid parcel, which leads to the pressure force acting at a point in the continuum

$$\text{PRESSURE GRADIENT FORCE} = -(\rho dV) \rho^{-1} \nabla_z p \quad (1.212a)$$

$$= -dV \nabla_z p \quad (1.212b)$$

$$= -dV (\nabla_s p + \rho \nabla_s \Phi). \quad (1.212c)$$

Hence, the pressure force acting on a finite region is given by the integral over the extent of the region

$$\text{PRESSURE GRADIENT FORCE OVER REGION} = - \int \frac{1}{\rho} \nabla_z p \rho dV \quad (1.213a)$$

$$= - \int \nabla_z p dV. \quad (1.213b)$$

As stated earlier, a finite volume discretization of this force will take the same form as the finite volume discretization of the pressure contact force discussed in Section 1.8.1, as it should due to the Green-Gauss Theorem invoked to go from equation (1.188) to (1.189). However, these formulations generally *do not* provide for a clear energetic interpretation as promoted by the finite difference formulation of Bryan (1969).

1.9 Linear momentum budget

The purpose of this section is to formulate the budget for linear momentum over a finite region of the ocean, with specific application to ocean model grid cells. The material here requires many of the same elements as in Section 1.6, but with added richness arising from the vector nature of momentum, and the additional considerations of forces from pressure, friction, gravity, and planetary rotation. Note that we initially formulate the equations using the pressure contact force, as this provides a general formulation. Afterwards, we specialize to hydrostatic fluids, and thus write the pressure force as a gradient (Section 1.8.2), as commonly done in primitive equation ocean models

¹³For a Boussinesq fluid, equation (1.209) is modified by a factor of ρ/ρ_0 .

1.9.1 General formulation

The budget of linear momentum for a finite region of fluid is given by the following relation based on Newton's second and third laws

$$\partial_t \left(\int \mathbf{v} \rho dV \right) = \int \mathcal{S}^{(\mathbf{v})} dV - \int [\hat{\mathbf{n}} \cdot (\mathbf{v} - \mathbf{v}^{\text{ref}})] \rho \mathbf{v} dA_{(\hat{\mathbf{n}})} + \int (\hat{\mathbf{n}} \cdot \boldsymbol{\tau} - \hat{\mathbf{n}} p) dA_{(\hat{\mathbf{n}})} - \int [g \hat{\mathbf{z}} + (f + \mathcal{M}) \hat{\mathbf{z}} \wedge \mathbf{v}] \rho dV. \quad (1.214)$$

The left hand side is the time tendency of the region's linear momentum. The first term on the right hand side, $\mathcal{S}^{(\mathbf{v})}$, is a momentum source, with units momentum per volume per time. This term is nonzero if, for example, the addition of mass to the ocean via a source occurs with a nonzero momentum. Often, it is assumed that mass is added with zero velocity, and so does not appear as a momentum source. The second term is the advective transport of linear momentum across the boundary of the region, with recognition that the region's boundaries are generally moving with velocity \mathbf{v}^{ref} . The third term is the integral of the contact stresses due to friction and pressure. These stresses act on the boundary of the fluid domain. We already discussed the forces from pressure in Section 1.8. The stress tensor $\boldsymbol{\tau}$ is a symmetric second order tensor that parameterizes subgrid scale transport of momentum. The final term on the right hand side is the volume integral of body forces due to gravity and the Coriolis force.¹⁴ In addition, there is a body force arising from the nonzero curvature of the spherical space. This curvature leads to the advection metric frequency (see equation (4.49) of Griffies (2004))

$$\mathcal{M} = v \partial_x \ln dy - u \partial_y \ln dx. \quad (1.215)$$

In spherical coordinates where

$$dx = (r \cos \phi) d\lambda \quad (1.216)$$

$$dy = r d\phi, \quad (1.217)$$

with r the distance from the earth's center, λ the longitude, and ϕ the latitude, the advective metric frequency takes the form

$$\mathcal{M} = (u/r) \tan \phi. \quad (1.218)$$

The advection metric frequency arises since linear momentum is not conserved on the sphere.¹⁵ Hence, the linear momentum budget picks up this extra term that is a function of the chosen lateral coordinates.

1.9.2 An interior grid cell

At the west side of a grid cell, $\hat{\mathbf{n}} = -\hat{\mathbf{x}}$ whereas $\hat{\mathbf{n}} = \hat{\mathbf{x}}$ on the east side. Hence, the advective transport of linear momentum entering through the west side of the grid cell and that which is leaving through the east side are given by

$$\text{TRANSPORT ENTERING FROM WEST} = \int_{x=x_1} z_s u (\rho \mathbf{v}) dy ds \quad (1.219)$$

$$\text{TRANSPORT LEAVING THROUGH EAST} = - \int_{x=x_2} z_s u (\rho \mathbf{v}) dy ds. \quad (1.220)$$

¹⁴The wedge symbol \wedge represents a vector cross product, also commonly written as \times . The wedge is typically used in the physics literature, and is preferred here to avoid confusion with the horizontal coordinate x .

¹⁵Linear momentum is not conserved for ideal flow on a sphere. Instead, angular momentum is conserved for ideal fluid flow on the sphere in the absence of horizontal boundaries (see Section 4.11.2 of Griffies (2004)).

Similar results hold for momentum crossing the cell boundaries in the north and south directions. Momentum crossing the top and bottom surfaces of an interior cell is given by

$$\text{TRANSPORT ENTERING FROM THE BOTTOM} = \int_{s=s_2} w^{(z)} (\rho \mathbf{v}) dx dy \quad (1.221)$$

$$\text{TRANSPORT LEAVING FROM THE TOP} = - \int_{s=s_1} w^{(z)} (\rho \mathbf{v}) dx dy. \quad (1.222)$$

Forces due to the contact stresses at the west and east sides are given by

$$\text{CONTACT FORCE ON WEST SIDE} = - \int_{x=x_1} z_{,s} (\hat{\mathbf{x}} \cdot \boldsymbol{\tau} - \hat{\mathbf{x}} p) dy ds \quad (1.223)$$

$$\text{CONTACT FORCE ON EAST SIDE} = \int_{x=x_2} z_{,s} (\hat{\mathbf{x}} \cdot \boldsymbol{\tau} - \hat{\mathbf{x}} p) dy ds \quad (1.224)$$

with similar results at the north and south sides. At the top of the cell, $dA_{(\hat{\mathbf{n}})} \hat{\mathbf{n}} = \nabla s dx dy$ whereas $dA_{(\hat{\mathbf{n}})} \hat{\mathbf{n}} = -\nabla s dx dy$ at the bottom. Hence,

$$\text{CONTACT FORCE ON CELL TOP} = \int_{s=s_{k-1}} z_{,s} (\nabla s \cdot \boldsymbol{\tau} - p \nabla s) dx dy \quad (1.225)$$

$$\text{CONTACT FORCE ON CELL BOTTOM} = - \int_{s=s_k} z_{,s} (\nabla s \cdot \boldsymbol{\tau} - p \nabla s) dy ds. \quad (1.226)$$

Bringing these results together, and taking limit as the time independent horizontal area $dx dy \rightarrow 0$, leads to the thickness weighted budget for the momentum per horizontal area of an interior grid cell

$$\begin{aligned} \partial_t (\mathbf{v} \rho dz) &= \mathcal{S}^{(\mathbf{v})} dz - \nabla_s \cdot [\mathbf{u}(\mathbf{v} \rho dz)] + (w^{(z)} \rho \mathbf{v})_{s=s_k} - (w^{(z)} \rho \mathbf{v})_{s=s_{k-1}} \\ &\quad + \partial_x [(\hat{\mathbf{x}} \cdot \boldsymbol{\tau} - \hat{\mathbf{x}} p) dz] + \partial_y [(\hat{\mathbf{y}} \cdot \boldsymbol{\tau} - \hat{\mathbf{y}} p) dz] \\ &\quad + [z_{,s} (\nabla s \cdot \boldsymbol{\tau} - p \nabla s)]_{s=s_{k-1}} - [z_{,s} (\nabla s \cdot \boldsymbol{\tau} - p \nabla s)]_{s=s_k} \\ &\quad - [g \hat{\mathbf{z}} + (f + \mathcal{M}) \hat{\mathbf{z}} \wedge \mathbf{v}] \rho dz. \end{aligned} \quad (1.227)$$

Note that both the time and horizontal partial derivatives are for positions fixed on a constant generalized vertical coordinate surface. Also, the pressure force as written here is a shorthand for the more complete contour integral formulation provided in Section 1.8 (e.g., equation (1.208)). Additionally, we have yet to take the hydrostatic approximation, so these equations are written for the three components of the velocity.

The first term on the right hand side of the thickness weighted momentum budget (1.227) is the momentum source, and the second is the convergence of advective momentum fluxes occurring within the layer. We discussed the analogous flux convergence for the tracer and mass budgets in Section 1.7.4. The third and fourth terms arise from the transport of momentum across the upper and lower constant s interfaces. The fifth and sixth terms arise from the horizontal convergence of pressure and viscous stresses. The seventh and eighth terms arise from the frictional and pressure stresses acting on the constant generalized surfaces. These forces provide an interfacial stress between layers of constant s . Note that even in the absence of frictional stresses, interfacial stresses from pressure acting on the generally curved s surface can transmit momentum between vertically stacked layers. The final term arises from the gravitational force, the Coriolis force, and the advective frequency.

1.9.3 Cell adjacent to the ocean bottom

As for the tracer and mass budgets, we assume zero mass flux through the ocean bottom at $z = -H(x, y)$. However, there is generally a nonzero stress at the bottom due to both the pressure between the fluid

and the bottom, and unresolved features in the flow which can correlate or anti-correlate with bottom topographic features (Holloway (1999)). The area integral of the stresses lead to a force on the fluid at the bottom

$$\mathbf{F}_{\text{bottom}} = - \int_{z=-H} [\nabla(z+H) \cdot \boldsymbol{\tau} - p \nabla(z+H)] dx dy. \quad (1.228)$$

Details of the stress term requires fine scale information that is generally unavailable. For present purposes we assume that some boundary layer model provides information that is schematically written

$$\boldsymbol{\tau}^{\text{bot}} = \nabla(z+H) \cdot \boldsymbol{\tau} \quad (1.229)$$

where $\boldsymbol{\tau}^{\text{bot}}$ is a vector bottom stress. Taking the limit as the horizontal area vanishes leads to the thickness weighted budget for momentum per horizontal area of a grid cell next to the ocean bottom

$$\begin{aligned} \partial_t (\mathbf{v} \rho dz) &= \mathcal{S}^{(\mathbf{v})} dz - \nabla_s \cdot [\mathbf{u}(\mathbf{v} \rho dz)] - (w^{(z)} \rho \mathbf{v})_{s=s_{kbot-1}} \\ &\quad + \partial_x [(\hat{\mathbf{x}} \cdot \boldsymbol{\tau} - \hat{\mathbf{x}} p) dz] + \partial_y [(\hat{\mathbf{y}} \cdot \boldsymbol{\tau} - \hat{\mathbf{y}} p) dz] \\ &\quad + [z_s (\nabla s \cdot \boldsymbol{\tau} - p \nabla s)]_{s=s_{kbot-1}} \\ &\quad - \boldsymbol{\tau}^{\text{bot}} + p_b \nabla(z+H) \\ &\quad - [g \hat{\mathbf{z}} + (f + \mathcal{M}) \hat{\mathbf{z}} \wedge \mathbf{v}] \rho dz. \end{aligned} \quad (1.230)$$

1.9.4 Cell adjacent to the ocean surface

There is a nonzero mass and momentum flux through the upper ocean surface at $z = \eta(x, y, t)$, and contact stresses are applied from resolved and unresolved processes involving interactions with the atmosphere and sea ice. Following the discussion of the tracer budget at the ocean surface in Section 1.6.4 leads to the expression for the transport of momentum into the ocean due to mass transport at the surface

$$-\int_{z=\eta} \hat{\mathbf{n}} \cdot [(\mathbf{v} - \mathbf{v}^{\text{ref}}) \rho \mathbf{v} dA_{(\hat{\mathbf{n}})}] = \int_{z=\eta} Q_m \mathbf{v} dx dy. \quad (1.231)$$

The force arising from the contact stresses at the surface is written

$$\mathbf{F}_{\text{contact}} = \int_{z=\eta} [\nabla(z - \eta) \cdot \boldsymbol{\tau} - p \nabla(z - \eta)] dx dy. \quad (1.232)$$

Bringing these results together leads to the force acting at the ocean surface

$$\mathbf{F}_{\text{surface}} = \int_{z=\eta} [\nabla(z - \eta) \cdot \boldsymbol{\tau} - p \nabla(z - \eta) + Q_m \mathbf{v}] dx dy. \quad (1.233)$$

Details of the various terms in this force are generally unknown. Therefore, just as for the tracer at $z = \eta$ in Section 1.6.4, we assume that a boundary layer model provides information about the total force, and that this force is written

$$\mathbf{F}_{\text{surface}} = \int_{z=\eta} [\boldsymbol{\tau}^{\text{top}} - p_a \nabla(z - \eta) + Q_m \mathbf{v}_m] dx dy, \quad (1.234)$$

where \mathbf{v}_m is the velocity of the water crossing the ocean surface. This velocity is typically taken to be equal to the velocity of the ocean currents in the top cells of the ocean model, but such is not necessarily the case when considering the different velocities of, say, river water and precipitation. The stress $\boldsymbol{\tau}^{\text{top}}$ is that arising from the wind, as well as interactions between the ocean and sea ice. Letting the horizontal area

vanish leads to the thickness weighted budget for a grid cell next to the ocean surface

$$\begin{aligned} \partial_t (\mathbf{v} \rho dz) = & \mathcal{S}^{(\mathbf{v})} dz - \nabla_s \cdot [\mathbf{u} (\mathbf{v} \rho dz)] + (w^{(z)} \rho \mathbf{v})_{s=s_{k=1}} \\ & + \partial_x [(\hat{\mathbf{x}} \cdot \boldsymbol{\tau} - \hat{\mathbf{x}} p) dz] + \partial_y [(\hat{\mathbf{y}} \cdot \boldsymbol{\tau} - \hat{\mathbf{y}} p) dz] \\ & - [z_s (\nabla s \cdot \boldsymbol{\tau} - p \nabla s)]_{s=s_{k=1}} \\ & + [\boldsymbol{\tau}^{\text{top}} - p_a \nabla (z - \eta) + Q_m \mathbf{v}_m] \\ & - [g \hat{\mathbf{z}} + (f + M) \hat{\mathbf{z}} \wedge \mathbf{v}] \rho dz. \end{aligned} \quad (1.235)$$

1.9.5 Horizontal momentum equations for hydrostatic fluids

We now assume the fluid to maintain a hydrostatic balance, which is the case for primitive equation ocean general circulation models. In this case, we exploit the pressure gradient body force as discussed in Section 1.8.2. Specializing the momentum budgets from Sections 1.9.2, 1.9.3, and 1.9.4 to use the hydrostatic pressure gradient force (again, interpreted according to the finite volume form given in Section 1.8) leads to the horizontal linear momentum budget for interior, bottom, and surface grid cells

$$\begin{aligned} [\partial_t + (f + M) \hat{\mathbf{z}} \wedge] (\mathbf{u} \rho dz) = & \mathcal{S}^{(\mathbf{u})} dz - \nabla_s \cdot [\mathbf{u} (\mathbf{u} \rho dz)] \\ & - (\nabla_s p + \rho \nabla_s \Phi) dz \\ & + \partial_x (\hat{\mathbf{x}} \cdot \boldsymbol{\tau} dz) + \partial_y (\hat{\mathbf{y}} \cdot \boldsymbol{\tau} dz) \\ & - [w^{(z)} \rho \mathbf{u} - z_s \nabla s \cdot \boldsymbol{\tau}]_{s=s_{k=1}} \\ & + [w^{(z)} \rho \mathbf{u} - z_s \nabla s \cdot \boldsymbol{\tau}]_{s=s_k}. \end{aligned} \quad (1.236)$$

$$\begin{aligned} [\partial_t + (f + M) \hat{\mathbf{z}} \wedge] (\mathbf{u} \rho dz) = & \mathcal{S}^{(\mathbf{u})} dz - \nabla_s \cdot [\mathbf{u} (\mathbf{u} \rho dz)] \\ & - (\nabla_s p + \rho \nabla_s \Phi) dz \\ & + \partial_x (\hat{\mathbf{x}} \cdot \boldsymbol{\tau} dz) + \partial_y (\hat{\mathbf{y}} \cdot \boldsymbol{\tau} dz) \\ & - [w^{(z)} \rho \mathbf{u} - z_s \nabla s \cdot \boldsymbol{\tau}]_{s=s_{kbot-1}} \\ & - \boldsymbol{\tau}_{\text{bottom}} \end{aligned} \quad (1.237)$$

$$\begin{aligned} [\partial_t + (f + M) \hat{\mathbf{z}} \wedge] (\mathbf{u} \rho dz) = & \mathcal{S}^{(\mathbf{u})} dz - \nabla_s \cdot [\mathbf{u} (\mathbf{u} \rho dz)] \\ & - (\nabla_s p + \rho \nabla_s \Phi) dz \\ & + \partial_x (\hat{\mathbf{x}} \cdot \boldsymbol{\tau} dz) + \partial_y (\hat{\mathbf{y}} \cdot \boldsymbol{\tau} dz) \\ & + [\boldsymbol{\tau}^{\text{wind}} + Q_m \mathbf{u}_w] \\ & + [w^{(z)} \rho \mathbf{u} - z_s \nabla s \cdot \boldsymbol{\tau}]_{s=s_1}. \end{aligned} \quad (1.238)$$

1.10 The Boussinesq budgets

Depth-based vertical coordinates are used to discretize the Boussinesq model equations where the volume of a parcel is conserved rather than the mass. A detailed discussion of the interpretation of the Boussinesq equations in terms of density weighted fields is given by McDougall et al. (2002) and Griffies (2004). For now, we gloss over those details by quoting the Boussinesq equations for volume, tracer, and momentum as arising from setting all density factors to the constant ρ_o , except when multiplied by the gravitational acceleration in the hydrostatic balance (i.e., for calculation of pressure and geopotential, the full density is used). The density ρ_o is a representative density of the ocean fluid. In MOM5 we set

$$\rho_o = 1035 \text{ kg m}^{-3}, \quad (1.239)$$

although this value can be changed via altering a parameter statement and thus recompiling the code). For much of the ocean, the *in situ* density deviates less than 3% from 1035 kg m^{-3} (see page 47 of Gill (1982)).

The replacement of density in the mass, tracer, and linear momentum budgets over a grid cell in the ocean interior leads to the following budgets for the hydrostatic model

$$\begin{aligned}
 \partial_t(dz) &= dz\mathcal{S}^{(V)} - \nabla_s \cdot (\mathbf{u} dz) - (w^{(z)})_{s=s_{k-1}} + (w^{(z)})_{s=s_k} \\
 \partial_t(C dz) &= \mathcal{S}^{(C)} dz - \nabla_s \cdot [dz(\mathbf{u} C + \mathbf{F})] \\
 &\quad - (w^{(z)} C + F^{(z)})_{s=s_{k-1}} \\
 &\quad + (w^{(z)} C + F^{(z)})_{s=s_k} \\
 [\partial_t + (f + M)\hat{\mathbf{z}} \wedge](\mathbf{u} \rho_o dz) &= \mathcal{S}^{(u)} dz - \nabla_s \cdot [\mathbf{u}(\mathbf{u} \rho_o dz)] \\
 &\quad - dz(\nabla_s p + \rho \nabla_s \Phi) \\
 &\quad + \partial_x(\hat{\mathbf{x}} \cdot \boldsymbol{\tau} dz) + \partial_y(\hat{\mathbf{y}} \cdot \boldsymbol{\tau} dz) \\
 &\quad - [w^{(z)} \rho_o \mathbf{u} - z_{,s} \nabla s \cdot \boldsymbol{\tau}]_{s=s_{k-1}} \\
 &\quad + [w^{(z)} \rho_o \mathbf{u} - z_{,s} \nabla s \cdot \boldsymbol{\tau}]_{s=s_k}.
 \end{aligned} \tag{1.240}$$

The first equation reduces to a volume budget rather than a mass budget found for the non-Boussinesq system. In this equation, $\mathcal{S}^{(V)}$ is a volume source with units of inverse time. Likewise, $\mathcal{S}^{(u)}$ is a velocity source (with units of acceleration). The Boussinesq equations for a grid cell adjacent to the ocean bottom are given by

$$\begin{aligned}
 \partial_t(dz) &= dz\mathcal{S}^{(V)} - \nabla_s \cdot (dz\mathbf{u}) - (w^{(z)})_{s=s_{kbot-1}} \\
 \partial_t(C dz) &= \mathcal{S}^{(C)} dz - \nabla_s \cdot [(\mathbf{u} C + \mathbf{F}) dz] \\
 &\quad - (w^{(z)} C + F^{(z)})_{s=s_{kbot-1}} \\
 &\quad + Q_{(bot)}^{(C)} \\
 [\partial_t + (f + M)\hat{\mathbf{z}} \wedge](\mathbf{u} \rho_o dz) &= \mathcal{S}^{(u)} dz - \nabla_s \cdot [\mathbf{u}(\mathbf{u} \rho_o dz)] \\
 &\quad - dz(\nabla_s p + \rho \nabla_s \Phi) \\
 &\quad + \partial_x(\hat{\mathbf{x}} \cdot \boldsymbol{\tau} dz) + \partial_y(\hat{\mathbf{y}} \cdot \boldsymbol{\tau} dz) \\
 &\quad - [w^{(z)} \rho_o \mathbf{u} - z_{,s} \nabla s \cdot \boldsymbol{\tau}]_{s=s_{kbot-1}} \\
 &\quad - \boldsymbol{\tau}^{\text{bottom}}
 \end{aligned} \tag{1.241}$$

and the equations for a cell next to the ocean surface are

$$\begin{aligned}
 \partial_t(dz) &= \mathcal{S}^{(V)} dz - \nabla_s \cdot (\mathbf{u} dz) + (w^{(z)})_{s=s_{k+1}} + Q_m/\rho_o \\
 \partial_t(C dz) &= \mathcal{S}^{(C)} dz - \nabla_s \cdot [(\mathbf{u} C + \mathbf{F}) dz] \\
 &\quad + (w^{(z)} C + F^{(z)})_{s=s_{k+1}} \\
 &\quad + ((Q_m/\rho_o) C_m - Q_{(C)}^{(\text{turb})}) \\
 [\partial_t + (f + M)\hat{\mathbf{z}} \wedge](\mathbf{u} \rho_o dz) &= \mathcal{S}^{(u)} dz - \nabla_s \cdot [\mathbf{u}(\mathbf{u} \rho_o dz)] \\
 &\quad - (\nabla_s p + \rho \nabla_s \Phi) dz \\
 &\quad + \partial_x(\hat{\mathbf{x}} \cdot \boldsymbol{\tau} dz) + \partial_y(\hat{\mathbf{y}} \cdot \boldsymbol{\tau} dz) \\
 &\quad + [\boldsymbol{\tau}^{\text{wind}} + Q_m \mathbf{u}_w] \\
 &\quad + [w^{(z)} \rho_o \mathbf{u} - z_{,s} \nabla s \cdot \boldsymbol{\tau}]_{s=s_1}.
 \end{aligned} \tag{1.242}$$

Chapter 2

Numerical aspects of the ocean model

Contents

2.1	B-grid for the horizontal layout	43
2.2	The bipolar Arctic	44
2.3	The z^* vertical coordinate	45
2.4	Vertical grid cell thicknesses	46
2.5	Partial bottom cell representation of topography	48
2.5.1	Characteristics of partial bottom cells	48
2.5.2	How to plot partial bottom cells in Ferret	48
2.6	Water fluxes crossing the ocean surface boundary	49
2.7	Time stepping the prognostic equations	50
2.8	The tracer advection scheme	51
2.8.1	Torus test case	51
2.8.2	Summary of the CM2-O tracer scheme choices	53

In this chapter, we discuss various numerical methods available in MOM5 that are used in the CM2-O suite.

2.1 B-grid for the horizontal layout

We configurate MOM5 using the Arakawa B-grid layout for discrete grid variables in the horizontal. Full details of both the B-grid and C-grid versions of MOM5 are given in Chapter 9 of Griffies (2012). We summaize here some of the salient points.

Figure 2.1 illustrates the horizontal arrangement of prognostic model fields used with the B-grid. The B-grid places both horizontal prognostic velocity components at the same point, the corner of the tracer cell. This placement is natural when computing the Coriolis Force. However, it is unnatural for computation of advective tracer transport or the horizontal pressure gradient force acting on velocity. The need to perform an averaging operation when computing the horizontal pressure gradient leads to the computational mode associated with gravity waves on the B-grid (see Section 31.1 of Griffies (2012) and references cited there).

MOM follows a *northeast convention*, whereby the velocity is positioned at the northeast corner of the corresponding tracer cell. With half-integer notation, the velocity U-point lives at $(i+1/2, j+1/2)$ with the T-point at (i, j) . There are good reasons to employ the half-integer convention when representing discrete quantities on a grid. However, we choose to avoid such notation, preferring instead to keep the grid variable placements implied by use of the *northeast convention*.

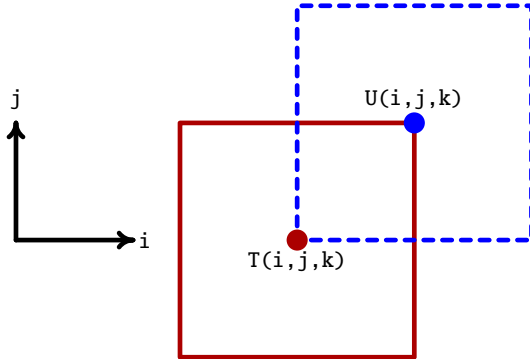


Figure 2.1: Illustration of how fields are placed on the horizontal B-grid used in MOM using a *northeast convention*. Velocity points $U(i, j, k)$ are placed to the northeast of tracer points $T(i, j, k)$. Both horizontal velocity components $u_{i,j,k}$ and $v_{i,j,k}$ are placed at the velocity point $U(i, j, k)$. Both the tracer point and velocity point have a corresponding grid cell region, denoted by the solid and dashed squares.

The B-grid placement leads to the following placements for the discrete fields realized in MOM on the grid.

- As density is a function of temperature, salinity, and pressure, density is naturally defined at the tracer point. Correspondingly, so is hydrostatic pressure and the surface ocean height.
- For each tracer cell there is a corresponding velocity cell, as depicted in Figure 2.1. Fluxes through the faces of the velocity cell are related to those through the faces of the tracer cell via remapping operations as detailed in Chapter 15 of [Griffies \(2012\)](#).
- The vertical velocity component is defined according to the requirements of continuity across the tracer and velocity cells. Hence, the vertical velocity component lives at the bottom face of the corresponding tracer or velocity cell. Once the horizontal grid placement is defined, the vertical position is specified for both the grid point and the vertical velocity position. Chapter 16 of [The MOM3 Manual \(Pacanowski and Griffies, 1999\)](#) provides further details of the vertical grid.

2.2 The bipolar Arctic

Code for reading in the grid and defining MOM specific grid factors is found in the module

`mom5/ocean_core/ocean_grids.`

MOM4.0 and later releases of MOM are written using generalized horizontal coordinates, with the coordinates assumed to be locally orthogonal. For global ocean climate modeling, a common global grid is the tripolar grid of [Murray \(1996\)](#), which contains a bipolar Arctic as depicted in Figure 2.2. By hiding the coordinate singularities over land, we remove problems associated with the convergence of the spherical meridians. MOM comes with preprocessing code suitable for generating grid specification files of various complexity, including the [Murray \(1996\)](#) tripolar grid that has a bipolar Arctic region (see Figure 2.2). Note that the horizontal grid in MOM is static (time independent), whereas the vertical grid is generally time dependent (Section 2.3). Hence, there is utility in separating the horizontal from the vertical grids.

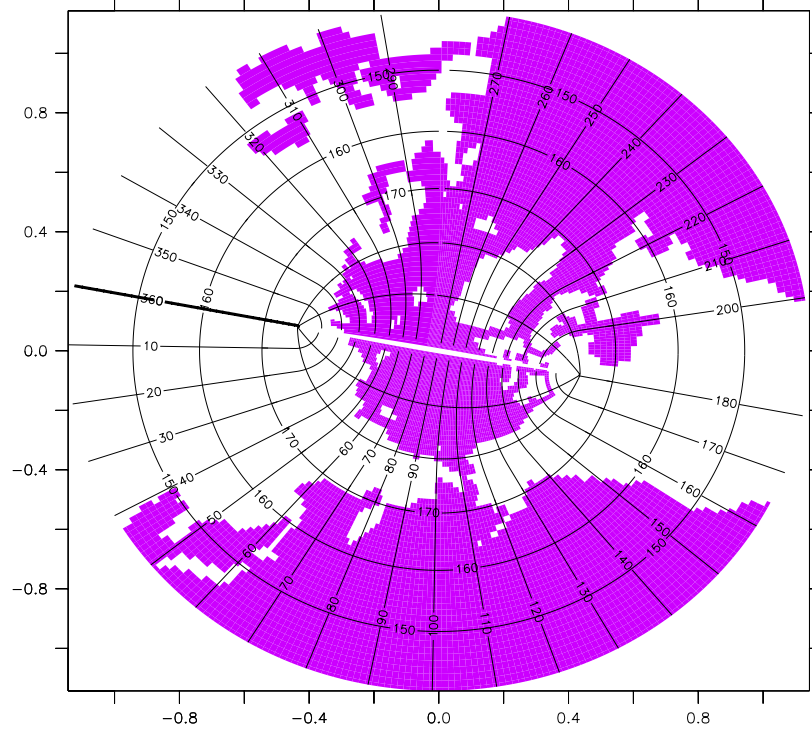


Figure 2.2: Illustration of the bipolar Arctic as prescribed by Murray (1996) (see his Figure 7) and realized in the one-degree ocean component of CM2-O, as well as CM2.1, CM3, and ESM2M. The transition from the bipolar Arctic to the spherical grid occurs at 65°N. We denote horizontal grid cells by (i, j) indices. As in the spherical coordinate region of the grid, lines of constant i -index move in a generalized eastward direction within the bipolar region. They start from the bipolar south pole at $i = 0$, which is identified with $i = ni$, where ni is the number of points along a latitude circle and $ni = 360$ for a one degree horizontal resolution. The bipolar north pole is at $i = ni/2$, which necessitates that ni be an even number. Both poles are centered at a velocity point when using the B-grid in MOM. Lines of constant j move in a generalized northward direction. The bipolar prime-meridian is situated along the j -line with $j = nj$, where $nj = 200$ in CM2.1. This line defines the *bipolar fold* that bisects the tracer grid. Care must be exercised when mapping fields across this fold. As noted by Griffies et al. (2004), maintaining the exact identity of fields computed redundantly along the fold is essential for model stability. Note that the cut across the bipolar fold is a limitation of the graphics package, and does not represent a land-sea boundary in the model domain. This figure is taken after Figure 1 of Griffies et al. (2005). See Chapter 9 in Griffies (2012) for more details.

2.3 The z^* vertical coordinate

Code associated with vertical coordinates is located in the module

`mom5/ocean_core/ocean_thickness.F90.`

Various vertical coordinates have been implemented in MOM5 (see Chapter 5 in Griffies (2012)) which are based on functions of depth or pressure, which means in particular that MOM does not support thermodynamic or isopycnal based vertical coordinates. For the CM2-O ocean component, we use the quasi-horizontal rescaled height coordinate of Stacey et al. (1995) and Adcroft and Campin (2004)

$$z^* = H \left(\frac{z - \eta}{H + \eta} \right). \quad (2.1)$$

This is the vertical coordinate used in the ocean component of the GFDL IPCC AR5 coupled climate model

CM3 documented by Griffies et al. (2011) and Donner et al. (2011). It is also the vertical coordinate used in the earth system model ESM2M documented by Dunne et al. (2012, 2013). Note that tests at GFDL indicate that CM2.1 with the z^* vertical coordinate exhibits the same climate as CM2.1 with geopotential vertical coordinate.

In equation (2.1), $z = \eta(x, y, t)$ is the deviation of the ocean free surface from a state of rest at $z = 0$, and $z = -H(x, y)$ is the ocean bottom. Whereas a geopotential ocean model places all free surface undulations into the top model grid cell, a z^* model distributes the undulations throughout the ocean column. All grid cells thus have a time dependent thickness with z^* . Surfaces of constant z^* differ from geopotential surfaces according to the ratio η/H , which is generally quite small. Hence, surfaces of constant z^* are quasi-horizontal, thus minimizing difficulties of accurately computing the horizontal pressure gradient otherwise present with terrain following sigma coordinate z^*/H of Blumberg and Mellor (1987) (see Griffies et al., 2000, for a review). The z^* vertical coordinate is analogous to the “eta” coordinate sometimes used for atmospheric models (Black, 1994).

The thickness of a grid cell using the z^* vertical coordinate is given by

$$dz = \left(\frac{\partial z}{\partial z^*} \right) dz^* \quad (2.2a)$$

$$= (1 + \eta/H) dz^*, \quad (2.2b)$$

where dz^* is the static grid cell thickness in the z^* coordinate frame, and dz is the grid cell thickness in the geopotential coordinate frame. Consequently, the thickness dz of a grid cell is generally a function of time, and it deviates from that in a resting ocean according to the ratio η/H . As in CM2.1, the shallowest ocean depth in CM2-O is

$$H_{\text{shallowest}} = 40 \text{ m}, \quad (2.3)$$

so that the ratio η/H is generally quite small.

We chose z^* because of the enhanced flexibility when considering two key applications of climate models. The first application concerns large surface height deviations associated with tides and/or increased loading from sea ice (e.g., a global cooling simulation). The z^* model allows for the free surface to fluctuate to values as large as the local ocean depth, $|\eta| < H$, whereas the geopotential model is subject to the more stringent constraint $|\eta| < \Delta z_1$, with Δz_1 the thickness of the top grid cell with a resting ocean. The ocean models in CM2.1 and CM3 set a minimum depth to $H \geq 40\text{m}$, whereas $\Delta z_1 = 10\text{m}$ (note that there is no wetting and drying algorithm in MOM). This flexibility with z^* is further exploited if considering even finer vertical grid resolution. Figure 2.3 illustrates this flexibility.

The second application where z^* is useful concerns increased land ice melt that adds substantially to the sea level, as in the idealized studies of Stouffer et al. (2006), Kopp et al. (2010), and Yin et al. (2010). Placing all of the surface expansion into the top model grid cell, as with the free surface geopotential model, greatly coarsens the vertical grid resolution in this important portion of the ocean, whereas the z^* model does not suffer from this problem since the expansion is distributed throughout the column.

2.4 Vertical grid cell thicknesses

In the development of CM2.1, attention was given to the vertical resolution of the tropical thermocline in order to enhance the representation of ENSO. Following from the work of Rosati and Miyakoda (1988), the CM2.1 vertical grid spacing was held constant at 10 m throughout the upper 220 m of the ocean, with cells then getting thicker with depth. This vertical grid spacing was also used in the ocean component of ESM2M (Dunne et al., 2012) and CM3 (Griffies et al., 2011). We exhibit this grid spacing in Figure 2.4. Note that for cells next to the bottom, the grid cell thickness adjusts to match the bottom topography, according to the partial cell methods of Pacanowski and Gnanadesikan (1998) (see Figure 2.5).

There is a problem with the CM2.1 grid at the transition depth of 220 m, since the derivative of the grid spacing has a jump at that depth. In the development of CM2.5, we discovered an instability associated with large vertical velocities in the Denmark Strait region, with the instability resolved only by reducing the time step to a rather small value. We thus decided to smooth the grid transition in order to avoid the jump in the derivative in hopes of allowing for a larger time step. The result is the CM2-O vertical grid shown

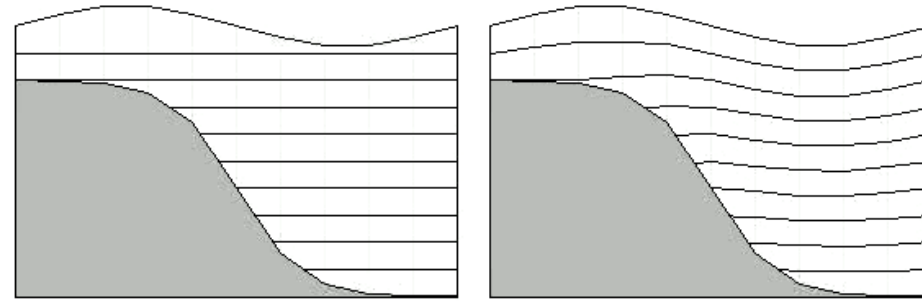


Figure 2.3: Illustrating the differences between geopotential vertical coordinate (left panel) and z^* vertical coordinate (right panel). In the upper ocean grid cell, the free surface with the geopotential vertical coordinate can generally penetrate through the bottom of the top cell lower boundary, in which case there is a problem with the simulation. In contrast, for the z^* vertical coordinate, all vertical cells undulate in time, with motion of the free surface spread throughout the ocean depth. Note that the undulations of the cell interfaces with z^* are scaled according to η/H , which is generally quite small. The undulations shown in this schematic are thus highly exaggerated for visualization purposes.

in Figure 2.4. This grid change indeed removed the unstable behaviour in the Denmark Strait region, thus motivating its adoption for CM2-O.

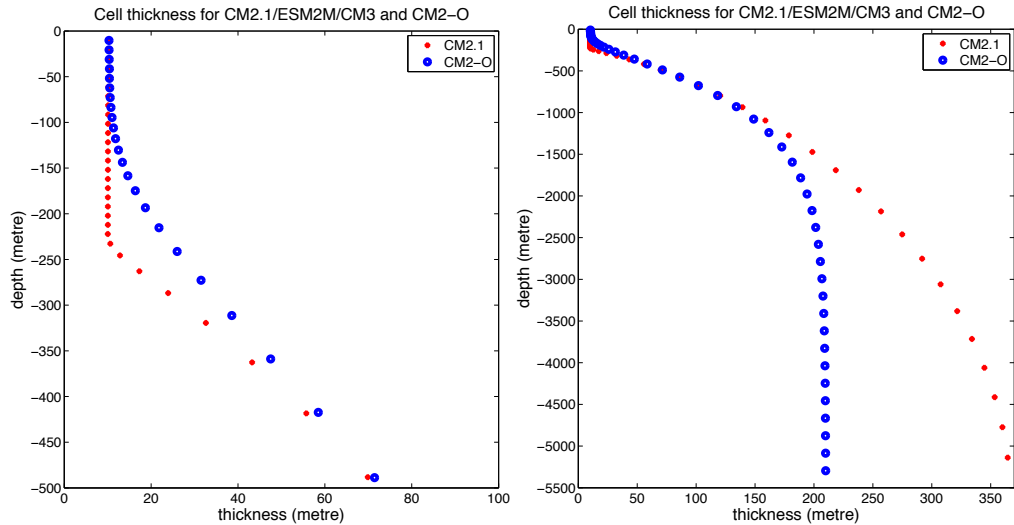


Figure 2.4: Comparison of the cell thicknesses used for the CM2.1/ESM2M/CM3 configuration, and that used for the CM2-O suite. The right panel shows just the upper ocean, whereas the left panel is the full depth. Note the kink in the CM2.1 vertical grid around 220 m. The thinnest cells in the upper ocean are roughly 10 m thick for both models. For CM2.1, the thickest cells next to the bottom are roughly 365 m, whereas CM2-O bottom cells are no larger than 210 m. Note that these are the grid cell thicknesses appropriate when the model is at rest with a zero surface height undulation. There are slight modifications for a non-zero sea surface height due to the use of the z^* vertical coordinate (see equation (2.2b)). Additionally, grid cells abutting the bottom have thicknesses modified according to the partial bottom cell methods discussed in Section 2.5.

2.5 Partial bottom cell representation of topography

MOM4.0 and later releases employ the partial bottom step technology of ([Pacanowski and Gnanadesikan, 1998](#)) to facilitate the representation of bottom topography. Each of the generalized level coordinates in MOM make use of this technology. Code associated with partial bottom steps is located in the module

mom5/ocean_core/ocean_topog.

2.5.1 Characteristics of partial bottom cells

It is common in older (those dating from before 1997) *z*-models for model grid cells at a given discrete level to have the same thickness. In these models, it is difficult to resolve weak topographic slopes without including uncommonly fine vertical and horizontal resolution. This limitation can have important impacts on the model's ability to represent topographically influenced advective and wave processes. The partial step methods of ([Adcroft et al., 1997](#)) and ([Pacanowski and Gnanadesikan, 1998](#)) have greatly remedied this problem via the implementation of more realistic representations of the solid earth lower boundary. Here, the vertical thickness of a grid cell at a particular discrete level does not need to be the same. This added freedom allows for a smoother, and more realistic, representation of topography by adjusting the bottom grid cell thickness to more faithfully contour the topography. Figure 2.5 illustrates the bottom realized with the ocean component of CM2.1, CM3, and ESM2M along the equator. Also shown is a representation using an older *full step* method with the same horizontal and vertical resolution. The most visible differences between full step and partial step topography are in regions where the topographic slope is not large, whereas the differences are minor in steeply sloping regions.

2.5.2 How to plot partial bottom cells in Ferret

The following algorithm is of use when aiming to exhibit the partial bottom cell nature of the topography. This is the algorithm used to generate the images in Figure 2.5.

```

! for partial bottom cells
! ht = bottom depth on T-cells
! temp = temperature or another tracer

define axis/z=0:5500:10/units=m/depth newz
define grid/like=temp/z=newz newg
let htp      = missing(ht,0)
let htpartial = if z[g=newg] ge htp then 0 else 1
let htfull   = if temp gt -2 then 1 else 0

let mask1   = htfull/htfull
let mask2   = missing(mask1,-1000)
let mask3   = htpartial/htpartial
let mask4   = missing(mask3,-1000)

set v upper
shade/nokey/nolab/lev=(-1000 0 1000)/pal=gray/y=0 ignore0(mask2)
set v lower
shade/nokey/nolab/lev=(-1000 0 1000)/pal=gray/y=0 ignore0(mask4)

```

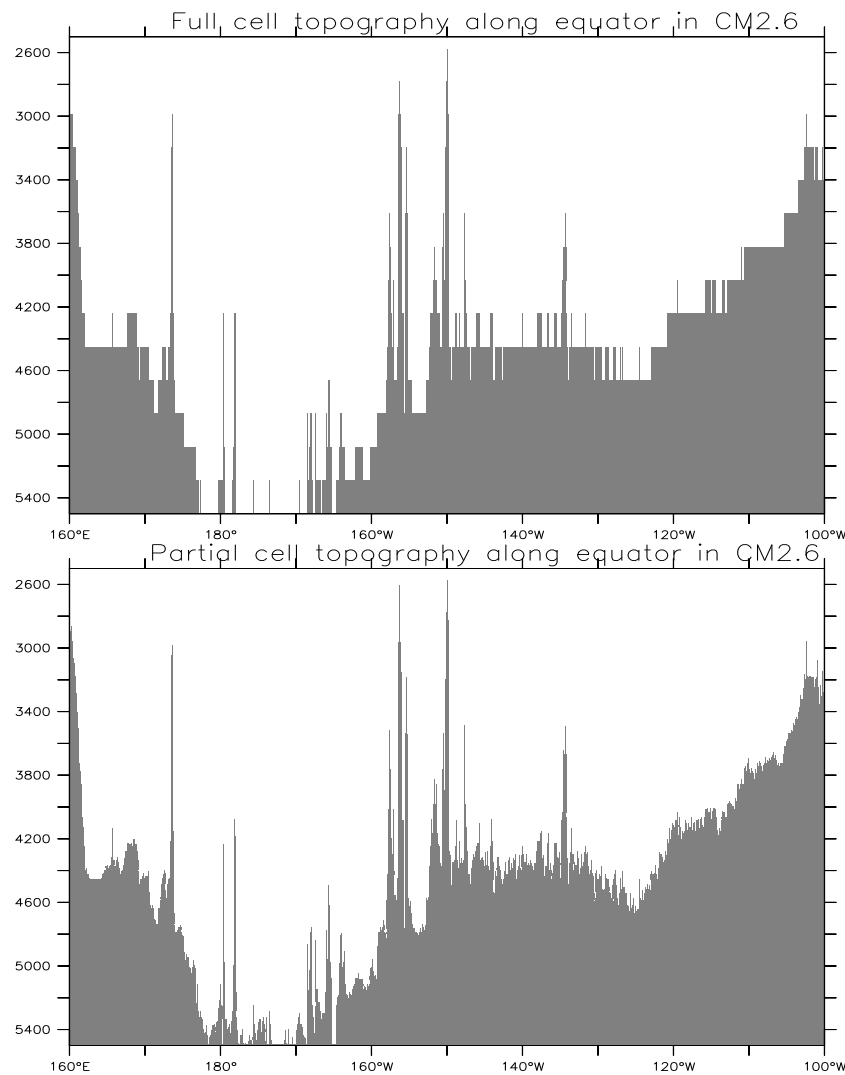


Figure 2.5: Bottom topography along the equator for the tracer cells in CM2.6. This figure illustrates the difference between the older full step representation of the bottom topography (upper) and the partial step representation (lower). Note the large differences especially in regions where the topographic slope is modest and small. The partial bottom cell representation allows for a more realistically rough representation of the bottom. This figure is analogous to Figure 4 of [Griffies et al. \(2005\)](#) shown for the one-degree configuration. The partial bottom cell representation of topography is used for all MOM configurations of the CM2-O suite of models.

2.6 Water fluxes crossing the ocean surface boundary

Ever since the CM2.1 climate model of [Delworth et al. \(2006\)](#), the GFDL climate oceans employ a true freshwater flux boundary condition for the ocean. Hence, the transport of water across the ocean boundary is associated with a change in ocean volume (as per the volume conserving Boussinesq approximation), or bottom pressure (as per the non-Boussinesq mass conserving models). As discussed in [Huang \(1993\)](#), [Griffies et al. \(2001\)](#), [Griffies et al. \(2005\)](#), and [Yin et al. \(2010\)](#), the real water boundary condition provides for the following improvements in model formulation and behavior:

- Total salt content within the ocean is constant, except for the small amounts exchanged with the sea ice model, which assumes a constant salinity of 5ppt.
- There are more realistic feedbacks associated with rivers, precipitation, and evaporation.
- The Goldsborough-Stommel circulation is admitted, as it is driven by hydrological forcing.
- There are barotropic signals and mass redistributions associated with the exchange of water with other climate components. As highlighted by [Kopp et al. \(2010\)](#), the ability to exchange mass with other climate components facilitates studies of how mass redistributions in the climate system impact the earth's gravity field and rotation, both of which are critical for understanding and quantifying sea level change.

Many climate models do not use the real water boundary condition, even those that employ a free surface in which the introduction of water is algorithmically trivial. Instead, they use the virtual salt flux commonly used in rigid lid ocean models ([Huang, 1993](#); [Griffies et al., 2001](#)). The above listed reasons in favor of the real water boundary condition serve as strong motivation to favor it over virtual tracer fluxes.

2.7 Time stepping the prognostic equations

Time stepping in MOM5 depends on the particular terms in the dynamical and tracer equations, with the following list of methods used in CM2-O.

- The tracer and baroclinic momentum use a staggered two-time level scheme whereby the tracer and baroclinic momentum fields are staggered one-half time step apart. This scheme was introduced for MOM in Section 3.2 of the CM2.1 ocean documentation paper [Griffies et al. \(2005\)](#). More details are available in Chapter 11 of [Griffies \(2012\)](#) or Chapter 12 of [Griffies \(2004\)](#). Previous to the two-level staggered scheme, MOM utilized a three-level leap-frog scheme for the inviscid dynamics and forward time stepping for the dissipative dynamics. Advantages of the two-level staggered scheme include the following.
 - There is no need to employ explicit time filters (e.g., Robert-Asselin filter) with the staggered scheme, thus enhancing temporal accuracy over the time filtered leap-frog scheme.
 - The time staggered scheme conserves seawater volume/mass and tracer mass to within computational roundoff, whereas the leap-frog based methods, due to the use of explicit time filtering, fail to conserve.
 - The time staggered scheme updates the state of the ocean one time step by employing tendencies based on that one time step. In contrast, leap-frog based schemes update the state over one time step by using tendencies based on two time steps. Hence, the leap-frog based schemes have a CFL stability constraint based on the two time step tendencies, and so can in many cases be run at only one-half the time step of the staggered scheme. Thus, the staggered scheme is for some configurations only one half the computational cost of the leap-frog based schemes.
- Momentum advection is time stepped using a 3rd order Adams-Bashforth scheme, as described in Section 12.6.3 of [Griffies \(2012\)](#) (see Section 2.3 of [Durran \(1999\)](#) for more details). We cannot use the centred second order momentum advection of [Bryan \(1969\)](#), since centred advection for momentum or tracer is unstable with a forward time stepping scheme; it is only stable with the older leap-frog approach of MOM.
- The vertically integrated momentum and volume equations (the “barotropic system”) are time stepped using a predictor-corrector scheme as detailed in Section 11.5 of [Griffies \(2012\)](#) or Section 12.7 of [Griffies \(2004\)](#).
- A semi-implicit approach is used to time step the Coriolis Force, as detailed in Chapter 12 of [Griffies \(2012\)](#).

- Vertical diffusion for both tracer and momentum are time stepped using a fully implicit scheme, as detailed in Chapter 13 of [Griffies \(2012\)](#).

The particular time steps taken for the CM-O suite of models is shown in Table 2.1. There are many constraints that contribute to the precise setting of the model time steps, with both short and extended integrations generally required to settle on a choice. One of the most onerous constraints is associated with vertical motion in regions of fine grid spacing, especially that near to topography. In general, the model may be able to support stable simulations with larger time steps. However, we chose to retain slightly smaller time steps to reduce the potential for model crashes. This conservative practice is partly motivated by the use of a relatively energetic 50 km atmosphere model (far more energetic than the 200 km atmosphere used in CM2.1/ESM2M or CM3) with diurnal flux variations. In particular, the synoptic atmospheric storms can sporadically input a tremendous amount of inertial energy to the ocean, which can induce model instabilities when trying to push the ocean time step to values that may be suitable for less realistic forcing, such as for an ocean forced CORE simulation ([Griffies et al., 2009b](#)).

MODEL	TRACER	BAROCLINIC	BAROTROPIC	AIR-SEA AND ICE-SEA COUPLING
CM2-1deg	3600	3600	3600/80	3600
CM2.5	1800	1800	1800/80	3600
CM2.6	300	300	300/35	1200

Table 2.1: Time steps (seconds) taken in the ocean component of the CM2-O models. Also listed is the coupling time step, which is the time between which fluxes are passed between the ocean and other model components. The tracer and baroclinic momentum time steps are the same, whereas the split-explicit method takes a smaller time step for the barotropic, or vertically integrated, momentum. Note that the ocean time step is equated to the tracer time step. Also note that the coupling time step is sufficiently small for each of the models to represent a diurnal cycle in all boundary fluxes, including radiation and turbulent fluxes of buoyancy and momentum.

2.8 The tracer advection scheme

The CM2-O suite uses the MDPPM (multi-dimensional piece-wise parabolic method), with flux limiters based on [Suresh and Huynh \(1997\)](#), for advecting ocean tracers. In this subsection, we compare the performance of MDPPM versus other schemes available in MOM5.

The following MOM module is directly connected to the material in this section:

```
mom5/ocean_tracers/ocean_tracer_advect.F90.
```

2.8.1 Torus test case

To test the tracer advection schemes, we consider the MOM5 torus test case, consisting of a flat bottom square domain on the F-plane with doubly periodic boundary conditions. It provides an idealized test bed for implementing various numerical schemes, with applications to tracer advection frequently exercised at GFDL.

The flow field can be specified to have uniform horizontal velocity. For the illustration considered here, we consider a zonal flow with $(u, v) = (0.25\text{ms}^{-1}, 0)$. We consider two initial profiles shown in the top panel of Figure 2.6. The first profile is a square wave or pulse, and the second is a smooth Gaussian bump. The initial tracer concentrations all live within the range $[0, 1]$. Numerical solutions that fall outside this range constitute spurious unphysical results arising from errors in the advection scheme. A perfect advection scheme would advect the profiles without alteration.

The tracer profiles are advected with the following Courant number

$$\begin{aligned} C &= \frac{u \Delta t}{\Delta x} \\ &= \frac{0.25 \text{ ms}^{-1} \times 10800 \text{ s}}{1.04 \times 10^5 \text{ m}} \\ &\approx 0.5 \end{aligned} \quad (2.4)$$

using the staggered time stepping scheme standard in MOM. For the centred 2nd order and 4th order advection schemes, however, stability requires leap-frog time stepping, in which case the Courant number is ≈ 1 since the time step for advection is $2\Delta t$. We consider the following centered advection schemes:

- **2nd:** The second order centred differences scheme has been the traditional scheme employed in earlier versions of MOM. It is available only with the leap-frog version of MOM, since it is unstable with a forward time step used with the forward-backward method.
- **4th:** The fourth order centred scheme also is available only for the leap-frog version of MOM. This scheme assumes the grid is uniformly spaced (in metres), and so is less than fourth order accurate when the grid is stretched, in either the horizontal or vertical.
- **Upwind:** This is a first order upwind scheme, which is highly diffusive yet monotonic.
- **Quicker:** The quicker scheme is third order upwind biased and based on the work of [Leonard \(1979\)](#). [Holland et al. \(1998\)](#) and [Pacanowski and Griffies \(1999\)](#) discuss implementations in ocean climate models. This scheme does not have flux limiters, so it is not monotonic.
- **MDPPM:** The piece-wise parabolic method with flux limiters.
- **Super B:** Multi-dimensional third order upwind biased approach of [Hundsdorfer and Trompert \(1994\)](#), with Super-B flux limiters.¹
- **Sweby:** Multi-dimensional third order upwind biased approach of [Hundsdorfer and Trompert \(1994\)](#), with flux limiters of [Sweby \(1984\)](#).²
- **PSOM unlimited:** The second order moment scheme of [Prather \(1986\)](#).
- **PSOM limited:** The second order moment scheme of [Prather \(1986\)](#) with flux limiters from [Merryfield and Holloway \(2003\)](#). The impacts on spurious mixing from this scheme were considered in the study of [Hill et al. \(2012\)](#).

After 100 days, the tracer concentration profiles have evolved to those in the second, third, and fourth panels of Figure 2.6. There are nontrivial differences between the various schemes, to which we now comment.

- The 2nd and 4th order schemes exhibit nontrivial extrema for the square pulse. Extrema arise from the dispersion errors intrinsic to these schemes. The errors are especially large when advecting profiles with strong gradients, such as the square pulse. In contrast, they perform much better for the Gaussian pulse, due to the pulse's much more smooth initial profile.
- The first order upwind scheme produces no extrema, yet it is highly dissipative, with the square pulse nearly as damped as the Gaussian pulse after 100 days.
- The Quicker scheme is somewhat of a compromise between the first order upwind scheme and the 2nd and 4th order schemes. It contains diffusion intrinsic to the algorithm, which smooths the profile to help maintain a more reasonable level of boundedness. However, its performance for the square pulse remains unsatisfying, as there remain some nontrivial unphysical extrema.

¹This scheme was ported to MOM by Alistair Adcroft, based on his implementation in the MITgcm. The online documentation of the MITgcm at <http://mitgcm.org> contains useful discussions and details about this advection scheme.

²This scheme was ported to MOM by Alistair Adcroft, based on his implementation in the MITgcm. The online documentation of the MITgcm at <http://mitgcm.org> contains useful discussions and details about this advection scheme.

- In the third panel, the Sweby, Super B, and MDPPM schemes all show similar behaviour to each other. In particular, each maintains the tracer within its physical bounds, since these schemes are flux limited. More detailed analysis reveals that MDPPM is a bit less dissipative than the other two schemes, thus allowing for a slightly better maintenance of the square pulse shape. It is interesting that each scheme converts the initially smooth Gaussian pulse into a more square feature over time. Such is a property common to many advection schemes with flux limiters.
- The fourth panel shows results for the limited and unlimited PSOM schemes. The unlimited PSOM scheme produces extrema for the square pulse, but with far smaller amplitude than Quicker, 2nd, or 4th order advection. Even so, it does a wonderful job maintaining the shape of the square pulse. The limited PSOM scheme also maintains the square pulse, but clips the extrema thus retaining tracer concentrations within their physically relevant bounds.

2.8.2 Summary of the CM2-O tracer scheme choices

Based on performance in the square pulse test, the limited PSOM scheme appears to be the best if we insist on maintaining boundedness of the tracer, with the unlimited PSOM scheme preferable if extrema are allowed. The unlimited PSOM scheme is favoured by [Hill et al. \(2012\)](#) in order to reduce spurious mixing in eddying simulations.

However, use of the PSOM schemes come at the price of adding 10 extra three-dimensional arrays for each tracer. Additionally, when flux limited, its performance is only marginally better than the flux limited MDPPM scheme. As flux limiting is essential for realistic applications such as CM2-O, we find little motivation to use the PSOM-limited scheme. We thus chose the MDPPM scheme for CM2-O, with this scheme having been developed by Alistair Adcroft at GFDL. Furthermore, we use the MDPPM flux limiter based on the approach of [Suresh and Huynh \(1997\)](#), which is implemented in the MOM5 code using the `field_table` setting

$$\text{ppm_limiter} = 3 \quad \text{CM2-O}. \quad (2.5)$$

Note that this is *not* the same limiter as that used in the ESM2M simulation of [Dunne et al. \(2012, 2013\)](#), which instead used

$$\text{ppm_limiter} = 2 \quad \text{ESM2M}, \quad (2.6)$$

with this limiter based on the *Improved Full Constraint* method of [Lin \(2004\)](#) (see his Appendix B). The reason for using `ppm_limiter = 3` in the CM2-O suite is that this limiter is more strictly monotonic than `ppm_limiter = 2`, so that the CM2-O simulations are less likely to incur extrema in the presence of strong gradients.

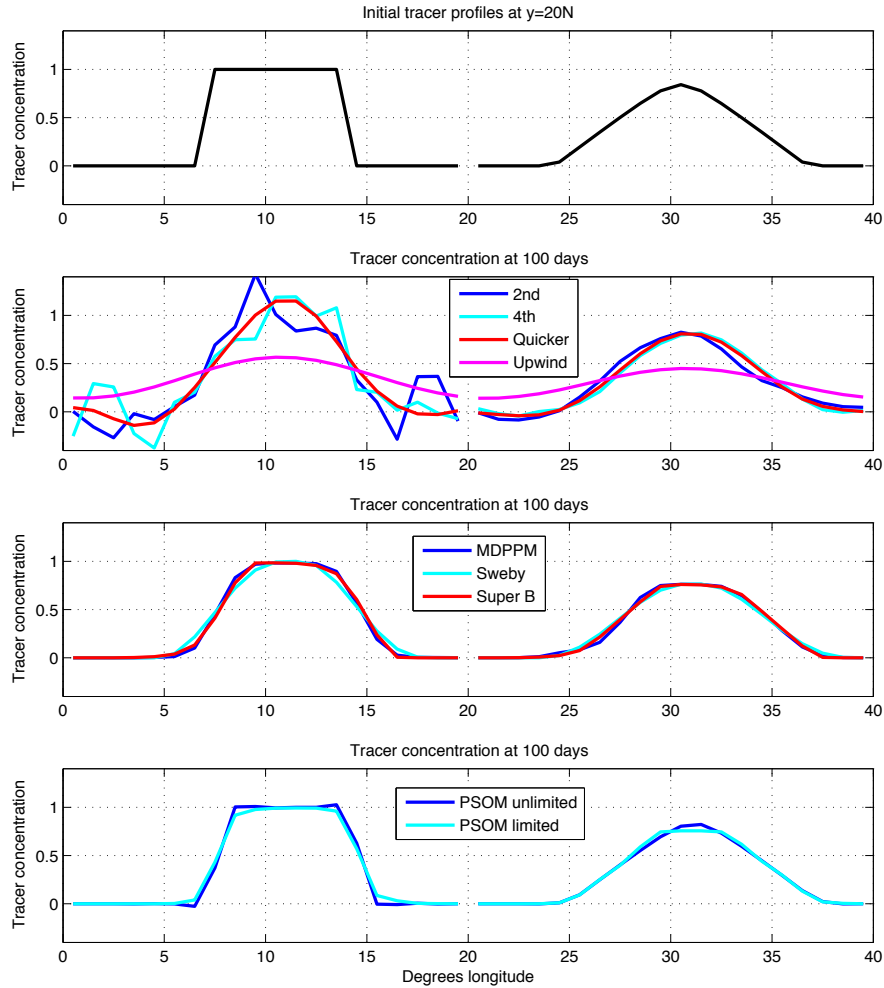


Figure 2.6: Top panel: Initial passive tracer profile for the torus test case. The two profiles are artificially offset in the zonal direction for purposes of clarity in presentation. Shown here is a plot through $y = 20^{\circ}\text{N}$. Second panel: passive tracer profiles after 100 days of integration using 2nd, 4th, Quicker, and Upwind advection schemes. Third panel: Results using MDPPM, Sweby, and Super B. Fourth panel: Results from the limited and unlimited PSOM scheme.

Chapter **3**

Physical processes

Contents

3.1	Equation of state and seawater thermodynamics	56
3.2	Static background vertical viscosity and diffusivity	57
3.3	Parameterized mixing from gravitational instability	57
3.4	Mixing in the surface boundary layer from KPP	58
3.4.1	General form of the KPP parameterization	58
3.4.2	The vertical diffusivity	59
3.4.3	Boundary layer thickness	59
3.4.4	Measuring vertical distances within the OBL	59
3.4.5	Vertical turbulent velocity scale w_λ	60
3.4.6	Non-dimensional vertical shape function $G_\lambda(\sigma)$	61
3.4.7	The non-local transport γ_λ	61
3.4.8	Surface boundary condition	62
3.4.9	Convergence into a surface grid cell	63
3.5	Parameterized mixing from shear induced instability	63
3.6	Parameterized mixing from double diffusive processes	64
3.6.1	Salt fingering regime	65
3.6.2	Diffusive convective regime	65
3.7	Sample vertical diffusivities from the KPP module	66
3.8	Parameterized mixing from tide induced mechanical dissipation	69
3.8.1	General considerations	69
3.8.2	How the roughness amplitude was computed	70
3.8.3	How the tide amplitude was computed	73
3.8.4	Parameterized mixing from internal tide dissipation	73
3.8.4.1	Energy flux	73
3.8.4.2	Mixing efficiency	74
3.8.4.3	Ratio of local to nonlocal dissipation	74
3.8.4.4	Background diffusivity and viscosity	75
3.8.4.5	Vertical deposition function	75
3.8.4.6	Cutoff in shallow seas	75
3.8.4.7	Sample diffusivities from internal tide mixing parameterization	76
3.8.5	Parameterized mixing from coastal tide induced dissipation	78
3.9	Horizontal viscosity	79
3.10	Dimensionless bottom drag coefficient	79

3.11	Rayleigh drag in certain straits	81
3.12	Mixed layer submesoscale restratification	82
3.12.1	Basics of the scheme and choices for CM2-O	83
3.12.2	Eddy induced transport	84
3.12.3	Overturning circulation	85
3.12.4	CM2-O submesoscale global overturning streamfunction	86
3.13	Mesoscale eddy parameterization in CM_O1.0_C180	86
3.13.1	Details of the chosen neutral physics scheme	86
3.13.2	Overturning from the parameterized mesoscale transport	87
3.14	Ocean optics and chlorophyll dataset	88
3.14.1	General considerations and model implementation	88
3.14.2	Chlorophyll-a climatology	90
3.14.3	Diagnosing the impacts of shortwave heating in MOM	90
3.15	Icebergs	91

The MOM ocean code used for the CM2-O suite of models is based on the hydrostatic primitive equations. MOM4p1 and MOM5 allow for a mass conserving non-Boussinesq formulation, as available using a pressure-based vertical coordinate. However, the CM2-O suite retains the volume conserving Boussinesq formulation available with the stretched geopotential vertical coordinate z^* (Section 2.3). The main reason for choosing z^* is that it is far more mature in various MOM applications than pressure-based vertical coordinates. For example, it was used for the ocean component of the CM3 climate model (Donner et al., 2011; Griffies et al., 2011) and ESM2M earth system model (Dunne et al., 2012, 2013), both of which contributed to CMIP5. This chapter further details physical assumptions and subgrid scale parameterizations used in the CM2-O suite.

3.1 Equation of state and seawater thermodynamics

The following MOM modules are directly connected to the material in this section:

```
mom5/ocean_core/ocean_density.F90
mom5/ocean_tracers/ocean_tempsalt.F90.
```

The prognostic active tracers in the CM2-O ocean component are practical salinity, S , and potential temperature, θ . The CM2-O ocean component thus uses an equation of state written as a function of the hydrostatic pressure, practical salinity, and potential temperature

$$\rho = \rho(p, S, \theta). \quad (3.1)$$

The functional form of $\rho(p, S, \theta)$ is based on the work of Jackett et al. (2006). A more accurate equation of state, TEOS-10, has become the standard in the observational and modeling communities (IOC et al., 2010). This equation of state is written as a function of pressure, absolute salinity, S_A , and conservative temperature Θ . TEOS-10 is available in MOM5; however, we do not use it for the CM2-O ocean, since initial development of CM2-O preceded implementation of TEOS-10 in MOM.

As noted by McDougall (2003), one awkward consequence of working with potential temperature in CM2-O is that the heat capacity of seawater is a function of space, whereas the use of conservative temperature allows one to make use of the constant heat capacity

$$C_p^o \approx 3992.1 \text{ J kg}^{-1} \text{ K}^{-1}. \quad (3.2)$$

Nonetheless, for purposes of performing a heat budget in the CM2-O suite, and for passing enthalpy across the air-sea interface, we ignore the distinction between potential temperature and conservative temperature. We thus make use of the constant heat capacity C_p^o to convert between potential temperature and enthalpy.

3.2 Static background vertical viscosity and diffusivity

The CM2-O models use a non-zero static background viscosity

$$\text{background_viscosity} = 10^{-4} \text{ m}^2 \text{ s}^{-1}, \quad (3.3)$$

which is a traditional value used in global ocean climate models. In contrast, the CM2-O models use a zero static background tracer diffusivity

$$\text{background_diffusivity} = 0. \quad (3.4)$$

The choice of zero static background tracer diffusivity is uncommon, with most modelers choosing a background diffusivity that is either spatially constant, such as $10^{-5} \text{ m}^2 \text{ s}^{-1}$ as suggested by the measurements of [Ledwell et al. \(1993\)](#), or spatially dependent as in [Jochum \(2009\)](#). For example, the ESM2M simulations from [Dunne et al. \(2012\)](#) use the static background diffusivity that is depth independent, and is set to $1 \times 10^{-5} \text{ m}^2 \text{ s}^{-1}$ in the tropics and transitions exponentially to $1.5 \times 10^{-5} \text{ m}^2 \text{ s}^{-1}$ poleward of 35° .

The magnitude and geography of the static background diffusivity remains uncertain, and is the topic of active research (e.g., [MacKinnon et al., 2010](#)). Given the sometimes large sensitivity of the simulations to details of the static background diffusivity ([Jochum, 2009](#)), particularly in the tropics ([Meehl et al., 2001](#)), we set to zero the static background vertical diffusivity in the CM2-O suite. Various other sources for vertical diffusive mixing are certainly included in CM2-O, with this list including surface boundary layer processes (Section 3.4), shear instability (Section 3.5), double diffusive processes (Section 3.6), convective mixing in regions of gravitational instability (Section 3.3), and dissipation of tidal energy (Section 3.8). We detail each of these methods in the following sections.

3.3 Parameterized mixing from gravitational instability

The following MOM module is directly connected to the material in this section:

`mom5/ocean_param/vertical/ocean_vert_kpp_mom4p1.F90.`

The hydrostatic approximation necessitates the use of a parameterization of vertical overturning processes arising from gravitationally unstable water parcels. The original parameterization used by Bryan in the 1960's was motivated largely from ideas then used for modeling convection in stars ([Bryan \(1969\)](#)). Work by Marshall and collaborators ([Klinger et al. \(1996\)](#), [Marshall et al. \(1997\)](#)) have largely supported the basic ideas of vertical adjustment for purposes of large-scale ocean circulation.

The [Cox \(1984\)](#) implementation of convective adjustment (the "NCON" scheme) may leave columns unstable after completing the code's adjustment loop. Various full convective schemes have come on-line, with that from [Rahmstorf \(1993\)](#) implemented in MOM. An alternative to the traditional form of convective adjustment is to increase the vertical mixing coefficient to a large value, thus quickly diffusing vertically unstable water columns. Indeed, it is this form recommended from the study of [Klinger et al. \(1996\)](#), and it is the approach commonly used in boundary layer schemes such as [Pacanowski and Philander \(1981\)](#) and [Large et al. \(1994\)](#). It is this vertical convective mixing approach that is used in CM2-O, in which the vertical diffusivity and viscosity are set to the values

$$\text{diff_con_limit} = 0.1 \text{ m}^2 \text{ s}^{-1} \quad (3.5a)$$

$$\text{visc_con_limit} = 0.1 \text{ m}^2 \text{ s}^{-1}, \quad (3.5b)$$

which are the defaults chosen in MOM5's implementation of the KPP scheme.

A time-explicit treatment of vertical diffusion, especially with fine vertical grid resolution, places an unreasonable limitation on the size of the time step associated with vertical mixing processes. The use of fine vertical resolution with sophisticated mixed layer and/or neutral physics schemes has prompted the near universal time-implicit treatment of vertical mixing in ocean climate models. MOM5 takes that approach, with details of the numerics provided in Chapter 13 of [Griffies \(2012\)](#).

3.4 Mixing in the surface boundary layer from KPP

The following MOM module is directly connected to the material in this section:

`mom5/ocean_param/vertical/ocean_vert_kpp_mom4p1.F90.`

The ocean surface boundary layer (OBL) mediates the exchange of properties between the ocean and other components of the climate system. Hence, parameterization of processes active in the OBL are fundamental to the integrity of a climate simulation. The K-profile parameterization (KPP) is a widely used method for parameterizing boundary layer processes in both the atmosphere and ocean, and it is used in the CM2-O suite. The paper by [Large et al. \(1994\)](#) introduced this scheme to the ocean community for use in parameterizing processes in the surface ocean boundary layer. The pedagogical lectures by [Large \(1998\)](#) and [Large \(2012\)](#) provide added insight into the scheme that complements some of the material in [Large et al. \(1994\)](#). We here present a very abbreviated version of the discussion provided in Chapter 18 of [Griffies \(2012\)](#).

The KPP scheme has been used by many ocean climate studies for parameterizing mixing in the OBL, with examples discussed in [Large et al. \(1997\)](#), [Holland et al. \(1998\)](#), [Gent et al. \(1998\)](#), [Umlauf et al. \(2005\)](#), [Li et al. \(2001\)](#), [Smyth et al. \(2002\)](#), [Durski et al. \(2004\)](#), and [Chang et al. \(2005\)](#)). We consider here only the implementation of KPP for the surface ocean boundary layer, as implementations for the bottom do not exist in MOM.

3.4.1 General form of the KPP parameterization

Ignoring all terms except vertical advective transport in the prognostic equation for the mean field Λ , its time tendency is determined by

$$\frac{\partial \Lambda}{\partial t} = - \left(\frac{\partial (W \Lambda)}{\partial z} \right) - \left(\frac{\partial (\overline{w \lambda})}{\partial z} \right). \quad (3.6)$$

The advective flux by the mean vertical velocity, $W \Lambda$, is represented via a numerical advection operator. In contrast, the turbulent correlation, $w \lambda$, is a subgrid scale flux that must be parameterized in order to close the equation for Λ . Here, the overbar signifies an Eulerian averaging operator over unresolved turbulent motions occurring within the OBL.

The KPP scheme provides a first order closure for $\overline{w \lambda}$ within the OBL. It does so by introducing two terms in the following manner

$$\overline{w \lambda} = -K_\lambda \left(\frac{\partial \Lambda}{\partial z} - \gamma_\lambda \right). \quad (3.7)$$

In effect, the KPP parameterization (3.7) splits the vertical turbulent flux into two terms

$$\overline{w \lambda} = \overline{w \lambda}^{\text{local}} + \overline{w \lambda}^{\text{non-local}}. \quad (3.8)$$

The first term provides for the familiar downgradient vertical diffusion determined by a vertical diffusivity and the local vertical derivative of the mean field. This term is referred to as the local portion of the parameterization

$$\overline{w \lambda}^{\text{local}} = -K_\lambda \left(\frac{\partial \Lambda}{\partial z} \right), \quad (3.9)$$

even though the diffusivity is a non-local function of boundary layer properties. The second term, γ_λ , accounts for non-local transport that is not directly associated with local vertical gradients of Λ , in which

$$\overline{w \lambda}^{\text{non-local}} = K_\lambda \gamma_\lambda. \quad (3.10)$$

We next provide a general discussion of these two contributions to the KPP parameterization.

3.4.2 The vertical diffusivity

The vertical diffusivity arising from KPP in the OBL is determined as a non-local function of boundary layer properties. It is written in the following form

$$K_\lambda(\sigma) = h w_\lambda(\sigma) G_\lambda(\sigma). \quad (3.11)$$

The diffusivity is constructed as the product of three terms: the boundary layer thickness h , the vertical turbulent velocity scale $w_\lambda(\sigma)$, and the vertical shape function $G_\lambda(\sigma)$. Note that we introduce a dependence of the shape function on the field diffused. This dependence arises from matching to interior diffusivities, which are generally a function of λ .

3.4.3 Boundary layer thickness

The boundary layer thickness is denoted by

$$h \geq 0 \text{ is the boundary layer thickness.} \quad (3.12)$$

This is the thickness of the OBL prescribed by the KPP scheme. It is determined by locating where in the vertical a bulk Richardson number rises above a critical value, chosen in the CM2-O models as

$$\text{Ricr} = 0.3. \quad (3.13)$$

The direct dependence of the vertical diffusivity in equation (3.11) on the OBL thickness manifests the common property of boundary layers, whereby thicker layers generally arise from stronger eddy motions and are thus associated with more rapid mixing of tracer concentration and momentum. Figure 3.1 provides a schematic of the KPP boundary layer, the Monin-Obukhov surface layer, and the associated momentum, mass, and buoyancy fluxes impacting these layers.

3.4.4 Measuring vertical distances within the OBL

When measuring distances within the boundary layer, it is the thickness of the water as measured from the ocean surface that is important. Free surface undulations can be a nontrivial fraction of the boundary layer thickness, particularly under conditions of stable buoyancy forcing. Hence, we make explicit note that the ocean has an undulating free surface at $z = \eta(x, y, t)$, which contrasts to [Large et al. \(1994\)](#) and [Large \(1998\)](#), who assumed that $z = 0$ sets the upper ocean surface.

Following [Large et al. \(1994\)](#), we introduce the non-dimensional depth, σ , given by

$$\sigma = \frac{d}{h}. \quad (3.14)$$

In this definition, $d \geq 0$ is the distance from the ocean surface at $z = \eta$ to a point within the boundary layer

$$d = -z + \eta. \quad (3.15)$$

Likewise, $h \geq 0$ is the distance from the free surface to the bottom of the boundary layer

$$h = h_{\text{obl}} + \eta, \quad (3.16)$$

where h_{obl} is the depth of the boundary layer as measured from $z = 0$. That is, h is the thickness of the OBL, and it is this thickness, not h_{obl} , that is predicted by KPP. Regions within the boundary layer are given by the non-dimensional depth range

$$0 \leq \sigma \leq 1 \quad \text{within boundary layer,} \quad (3.17)$$

with $\sigma = 0$ the ocean surface and $\sigma = 1$ the bottom of the boundary layer.

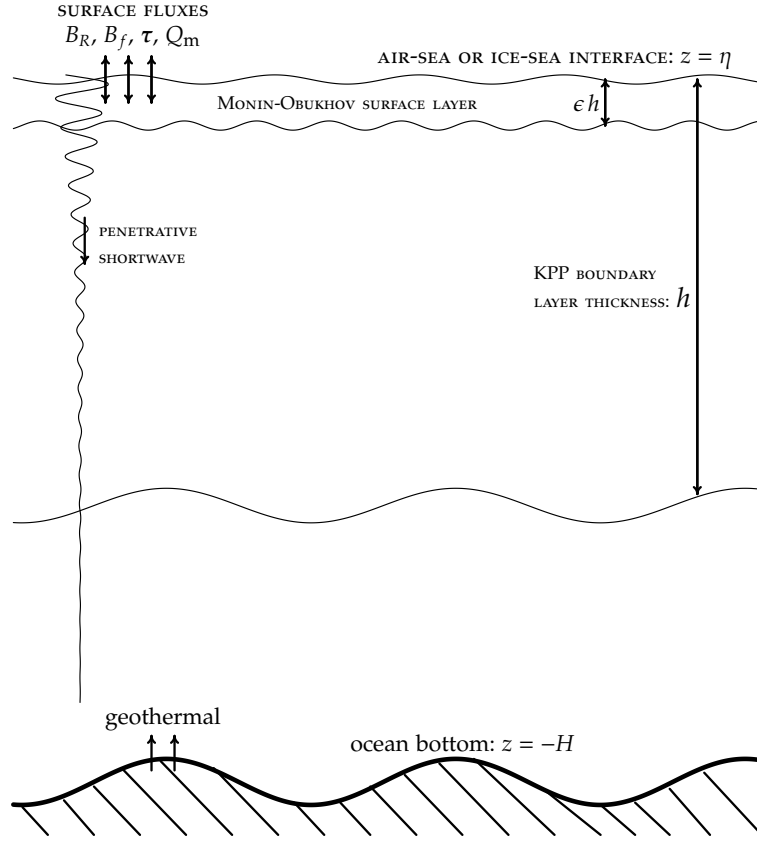


Figure 3.1: Schematic of the upper ocean boundary layer regions associated with the KPP boundary layer parameterization. The upper ocean is exposed to non-penetrative air-sea and ice-sea fluxes of momentum τ , mass Q_m , and buoyancy B_f . In addition, there is penetrative shortwave radiation, $-\overline{w\theta}_R$, indicated by the exponentially decaying vertical sinusoidal. The Monin-Obukhov surface layer has a thickness ϵh , with $\epsilon \approx 0.1$. The surface layer is where turbulence delivers fluxes to the molecular skin layer for transfer to the atmosphere or ice. The surface layer starts from just beneath the surface roughness elements at the upper ocean interface. Since neither these roughness elements, nor the molecular viscous sublayer, are resolved in ocean models, we assume in practice that the Monin-Obukhov surface layer extends to the sea surface at $z = \eta(x, y, t)$. The KPP boundary layer includes the surface layer, and it has a thickness $h(x, y, t)$ determined by the KPP parameterization. The ocean bottom at $z = -H(x, y)$ is rigid and is exposed to geothermal heating. Presently, the KPP boundary layer scheme has not been implemented in MOM or POP to parameterize bottom boundary layer physics, though nothing fundamental precludes such. In fact, Durski et al. (2004) provide just such an implementation.

3.4.5 Vertical turbulent velocity scale w_λ

The velocity scale

$$w_\lambda \geq 0 \quad (3.18)$$

is a function of depth within the boundary layer, and a function of the field to which it refers.

3.4.6 Non-dimensional vertical shape function $G_\lambda(\sigma)$

Non-dimensional vertical shape function $G_\lambda(\sigma)$ is used to smoothly transition from the ocean surface to the bottom of the boundary layer. [Large et al. \(1994\)](#) chose a cubic polynomial

$$G_\lambda(\sigma) = a_0 + a_1 \sigma + a_2 \sigma^2 + a_3 \sigma^3. \quad (3.19)$$

Since turbulent eddies do not cross the ocean surface at $\sigma = 0$, we should correspondingly have a vanishing diffusivity at $\sigma = 0$. This constraint is satisfied by setting

$$a_0 = 0. \quad (3.20)$$

3.4.7 The non-local transport γ_λ

Section 2 of [Large et al. \(1994\)](#) notes the presence of many processes in the boundary layer that lead to nonlocal transport. This behaviour leads to a diffusivity K_λ that is a function of the surface fluxes and boundary layer thickness h . Furthermore, under convective forcing (negative surface buoyancy forcing; $B_f < 0$), fluxes can penetrate into stratified interior. This characteristic then motivates the introduction of a non-local transport term γ_λ to the KPP parameterization (equation (3.7)) when $B_f < 0$.

As part of the KPP parameterization, the non-local transport, γ_λ , aims to account for such processes as boundary layer eddies whose transport may be unrelated to the local vertical gradient of the mean field, and whose impacts may penetrate within the stratified ocean interior. In general, [Large et al. \(1994\)](#) prescribe the following characteristics to γ_λ .

- Page 371 of ([Large et al., 1994](#)) notes that there is no theory for non-local momentum transport, and so the non-local transport directly affects only the tracer fields:

$$\gamma_\lambda = \begin{cases} 0 & \text{if } \lambda = (u, v, w) \text{ a velocity component} \\ \neq 0 & \text{nonzero if } \lambda = \theta, s \text{ or another tracer.} \end{cases} \quad (3.21)$$

However, [Smyth et al. \(2002\)](#) consider a non-local term for momentum, thus motivating further research to see whether it is suitable for climate modeling.

- The non-local transport is non-zero only within the OBL:

$$\gamma_\lambda = \begin{cases} 0 & \text{if } \sigma > 1 \\ \neq 0 & \text{if } 0 \leq \sigma \leq 1. \end{cases} \quad (3.22)$$

- The non-local transport is non-zero only in the presence of destabilizing negative surface ocean buoyancy flux, whose presence gives rise to convective mixing:

$$\gamma_\lambda = \begin{cases} 0 & \text{for positive (stabilizing) surface buoyancy forcing} \\ \neq 0 & \text{for negative (destabilizing) surface buoyancy forcing.} \end{cases} \quad (3.23)$$

- The non-local transport can give rise, under certain conditions, to either down-gradient or up-gradient transport of the mean tracer field. Hence, it can either act to smooth gradients of mean fields (down-gradient non-local fluxes) or enhance gradients (upgradient non-local fluxes).

The non-local transport for temperature and arbitrary scalars is parameterized by [Large et al. \(1994\)](#) according to the following expression, again valid just for destabilizing negative surface ocean buoyancy fluxes:

$$\gamma_\theta = C_s \left(\frac{\overline{w\theta}^\eta - Q_R / (\rho_0 C_p^o)}{h w_\theta(\sigma)} \right) \quad (3.24)$$

$$\gamma_s = C_s \left(\frac{\overline{ws}^\eta}{h w_s(\sigma)} \right). \quad (3.25)$$

In these expressions, we have

$$C_s = C_* \kappa (c_s \kappa \epsilon)^{1/3}, \quad (3.26)$$

with Large et al. (1994) suggesting the value of

$$C_* = 10, \quad (3.27)$$

whereas $C_* = 5$ in Smyth et al. (2002). The von Karman constant

$$\kappa = 0.41 \quad (3.28)$$

appears in this expression, as well as the fraction of the boundary layer assumed to be occupied by the Monin-Obukov surface layer

$$\epsilon = 0.1. \quad (3.29)$$

The coefficient c_s is set according to the similarity function ϕ_s discussed in Large et al. (1994).

The flux $Q_R > 0$ appearing in the γ_θ expression for equation (3.24) is the heat flux crossing the ocean surface from shortwave radiation. We split this penetrative shortwave flux from the non-penetrative heat flux $\overline{w\theta}^q$ (i.e., longwave, sensible, and latent), which is positive for cases where heat leaves the ocean surface. The net heat flux crossing the ocean surface is given by

$$Q^{\text{heat}} = Q_R - \rho_o C_p^o \overline{w\theta}^q, \quad (3.30)$$

where $Q^{\text{heat}} > 0$ for heat entering the ocean. The parameterized non-local transport term thus takes the following form for temperature

$$\gamma_\theta = - \left(\frac{C_s}{\rho_o C_p^o} \right) \frac{Q^{\text{heat}}}{h w_\theta(\sigma)}. \quad (3.31)$$

Generally the negative buoyancy forcing that gives rise to the non-local transport is associated with cooling ($Q^{\text{heat}} < 0$), so that

$$\gamma_\theta > 0 \quad \text{surface cooling.} \quad (3.32)$$

Combining the parameterizations (3.24) and (3.25) for the non-local term γ_λ , with that for the vertical diffusivity K_λ in equation (3.11) renders the non-local flux parameterization in the form

$$\overline{w\theta}^{\text{non-local}} = K_\lambda \gamma_\theta = -G_\theta(\sigma) C_s \left(\frac{Q^{\text{heat}}}{\rho_o C_p^o} \right) \quad (3.33)$$

$$\overline{ws}^{\text{non-local}} = K_\lambda \gamma_s = G_s(\sigma) C_s (\overline{ws}^q). \quad (3.34)$$

Notice how explicit dependence on both the turbulent velocity scale, w_λ , and boundary layer depth, h , drop out from the parameterization of the non-local flux. Consequently, we see that the non-local flux is parameterized by KPP as a redistribution through the boundary layer of the surface boundary flux.

3.4.8 Surface boundary condition

The non-local turbulent flux appearing in equation (3.8) satisfies a no-flux boundary condition at the ocean surface, so that

$$\overline{w\lambda}^{\text{non-local}} = K_\lambda \gamma_\lambda = 0 \quad \text{at } z = \eta. \quad (3.35)$$

This boundary condition is satisfied by ensuring that the non-dimensional vertical shape function $G(\sigma)$ vanishes at $\sigma = 0$ (see equation (3.11)), which means that

$$K_\lambda = 0 \quad \text{at } z = \eta. \quad (3.36)$$

We also set the local closure portion of the flux to zero at the surface

$$\overline{w\lambda}^{\text{local}} = -K_\lambda \left(\frac{\partial \Lambda}{\partial z} \right) = 0 \quad \text{at } z = \eta, \quad (3.37)$$

which again follows since $K_\lambda = 0$ at $z = \eta$. However, to incorporate the non-advection surface boundary fluxes (e.g., shortwave, longwave, latent, and sensible heat fluxes), we follow the usual convention these fluxes enter through the vertical diffusion equation surface flux boundary condition, so that in effect we have

$$\overline{w\lambda}^\eta = Q^\lambda \quad \text{at } z = \eta. \quad (3.38)$$

3.4.9 Convergence into a surface grid cell

At the surface boundary, the parameterized local and non-local flux components vanish. However, these flux components are generally quite large at the bottom interface of the $k = 1$ cell. Hence, there is a sizable convergence of the parameterized fluxes into the $k = 1$ cell. We can furthermore account for the predominance of a tendency for the parameterized local fluxes to cool the $k = 1$ cell, whereas the parameterized non-local fluxes generally warm this cell.

In a region stably stratified in temperature, we have temperature increasing upwards in the column, $\partial\Theta/\partial z > 0$. Assuming such stratification for the upper ocean, the downgradient diffusive flux

$$\overline{w\theta}^{\text{local}} = -K_\theta \left(\frac{\partial\Theta}{\partial z} \right) < 0, \quad (3.39)$$

is then negative at the lower face of the $k = 1$ cell. With the no-flux boundary condition (3.37) at the ocean surface, the parameterized local diffusive flux will thus cool the top model grid cell. For $k > 1$ interior cells, the diffusive flux either cools or warms, depending on curvature in the temperature field. Figure 5.23 illustrates this behaviour for the CM2-O simulations.

The non-local transport is non-zero only for cases of negative buoyancy forcing. Assuming such forcing occurs due to a cooling surface heat flux, we already showed in Section 3.4.8 that $\gamma_\theta > 0$ for cooling (equation (3.32)). With the no-flux surface boundary condition (3.35), we thus have a positive convergence of heat into the $k = 1$ cell due to the parameterized non-local flux. Hence, the parameterized non-local fluxes tend to warm the $k = 1$ cells whereas the parameterized downgradient diffusive fluxes tend to cool these cells. Figure 5.23 illustrates this behaviour for the CM2-O simulations.

3.5 Parameterized mixing from shear induced instability

The following MOM module is directly connected to the material in this section:

`mom5/ocean_param/vertical/ocean_vert_kpp_mom4p1.F90.`

Shear induced mixing occurs when vertical shears in the horizontal velocity overcome the stabilizing effects from vertical buoyancy stratification. Shear instability is governed by the local or gradient Richardson number

$$Ri = \frac{N^2}{|\partial_z \mathbf{u}|^2}. \quad (3.40)$$

In this expression, N^2 is the squared buoyancy frequency

$$N^2 = g \left(\alpha \frac{\partial\Theta}{\partial z} - \beta \frac{\partial S}{\partial z} \right). \quad (3.41)$$

We assume throughout that the water is stably stratified, so that $N^2 > 0$. With $N^2 < 0$, we set the diffusivity and viscosity to a large value to parameterize mixing associated with the gravitational instability (Section 3.3).

The denominator in the Richardson number in equation (3.40) is the squared vertical shear of the horizontal velocity vector as resolved by the model grid

$$|\partial_z \mathbf{u}|^2 = \left(\frac{\partial u}{\partial z} \right)^2 + \left(\frac{\partial v}{\partial z} \right)^2. \quad (3.42)$$

When the Richardson number is below a critical value, $Ri < Ri_c$, shear instabilities can grow to initiate turbulence, which in turn leads to enhanced mixing.

The canonical value of the critical gradient Richardson number is

$$Ri_c = 1/4 \quad \text{analytical value from shear layer instability.} \quad (3.43)$$

This value corresponds to the critical value for initiation of a Kelvin-Helmholz instability in a shear layer ([Miles, 1961](#)). However, as reviewed in Section 4b of [Jackson et al. \(2008\)](#), there are many reasons that 1/4 is not always the optimal value to use in numerical simulations. The key point is that global circulation models do not resolve all of the small scale shears, in which case $Ri_c = 1/4$ would lead to less mixing than in a real fluid or a direct numerical simulation. Thus, most mixing parameterizations choose noticeably larger values for the critical Richardson number. In effect, they do so in order for parameterized shear-induced mixing to be initiated in less unstable regions of the model's resolved flow.

For regions beneath the KPP boundary layer (see Figure 3.1), [Large et al. \(1994\)](#) and [Large and Gent \(1999\)](#) parameterized shear induced mixing using the following diffusivities

$$\kappa_{\text{kpp shear}} = \begin{cases} \kappa_0 & Ri < 0 \quad \text{gravitational instability regime} \\ \kappa_0 \left[1 - \left(\frac{Ri}{Ri_0} \right)^2 \right]^3 & 0 < Ri < Ri_0 \quad \text{shear instability regime} \\ 0 & Ri \geq Ri_0 \quad \text{stable regime.} \end{cases} \quad (3.44)$$

The form in the shear instability regime falls most rapidly near $Ri = 0.4Ri_0$, which aims to parameterize the onset of shear instability. In this neighborhood, rapid changes in Ri can cause gravitational instabilities to develop in the vertical, but these are largely controlled by vertically smoothing Ri profiles with a 1 – 2 – 1 smoother. For the CM2-O models, we choose a Richardson number parameter

$$Ri_{\text{infty}} = Ri_0 = 0.8, \quad (3.45)$$

which is the default in MOM5. We also choose the MOM5 default for the maximum diffusivity arising from shear instability

$$\text{diff_cbt_limit} = \kappa_0 = 5 \times 10^{-3} \text{ m}^2 \text{ s}^{-1}. \quad (3.46)$$

Unlike [Pacanowski and Philander \(1981\)](#), [Large et al. \(1994\)](#) chose a unit Prandtl number for shear induced mixing; i.e., the shear induced viscosity is the same as the shear induced diffusivity

$$\text{Pr}_{\text{kpp}} = \frac{\nu_{\text{kpp shear}}}{\kappa_{\text{kpp shear}}} \quad (3.47a)$$

$$= 1. \quad (3.47b)$$

3.6 Parameterized mixing from double diffusive processes

The following MOM module is directly connected to the material in this section:

`mom5/ocean_param/vertical/ocean_vert_kpp_mom4p1.F90.`

We detail here the double diffusive parameterization as implemented in the NCAR CESM. The MOM5 implementation used in CM2-O is slightly older, based on previous fits to data yet with similar functional forms.

Double diffusion processes ([Schmitt, 1994](#)) have the potential to significantly enhance vertical diffusivities. The key stratification parameter of use for double diffusive processes is

$$R_\rho = \frac{\alpha}{\beta} \left(\frac{\partial \Theta / \partial z}{\partial S / \partial z} \right), \quad (3.48)$$

where the thermal expansion coefficient is given by

$$\alpha = -\frac{1}{\rho} \left(\frac{\partial \rho}{\partial \Theta} \right), \quad (3.49)$$

and the haline contraction coefficient is

$$\beta = \frac{1}{\rho} \left(\frac{\partial \rho}{\partial S} \right). \quad (3.50)$$

Note that the effects from double diffusive processes on viscosity are ignored in CVMix for two reasons:

- The effects on viscosity are not well known.
- For most applications, the vertical Prandtl number is larger than unity (often 10) for background viscosities (e.g., Section 3.2, so that modifying the vertical viscosity according to double diffusion will not represent a sizable relative impact.

There are two regimes of double diffusive processes, with the parameterization different in the regimes. We now detail how CM2-O parameterizes vertical mixing in these two regimes, with the approach taken from an updated version of [Large et al. \(1994\)](#) as detailed in [Danabasoglu et al. \(2006\)](#).

3.6.1 Salt fingering regime

The salt fingering regime occurs when salinity is destabilizing the water column (salty water above fresh water) and when the stratification parameter R_ρ is within a particular range:

$$\frac{\partial S}{\partial z} > 0 \quad (3.51)$$

$$1 < R_\rho < R_\rho^0 = 2.55. \quad (3.52)$$

The parameterized vertical diffusivity in this regime is fit to observational estimates given by [Laurent and Schmitt \(1999\)](#), who propose the following form

$$\kappa_d = \kappa_d^0 \left[1 - \frac{R_\rho - 1}{R_\rho^0 - 1} \right]^3. \quad (3.53)$$

The default values for the parameter κ_d^0 are set to

$$\kappa_d^0 = \begin{cases} 1 \times 10^{-4} \text{ m}^2 \text{ s}^{-1} & \text{for salinity and other tracers} \\ 0.7 \times 10^{-4} \text{ m}^2 \text{ s}^{-1} & \text{for temperature.} \end{cases} \quad (3.54)$$

3.6.2 Diffusive convective regime

Diffusive convective instability occurs where the temperature is destabilizing (cold water above warm water) and with $0 < R_\rho < 1$

$$\frac{\partial \Theta}{\partial z} < 0 \quad (3.55)$$

$$0 < R_\rho < 1. \quad (3.56)$$

For temperature, the vertical diffusivity used in [Large et al. \(1994\)](#) is given by

$$\kappa_d = \nu_{\text{molecular}} \times 0.909 \exp \left(4.6 \exp \left[-54 \left(R_\rho^{-1} - 1 \right) \right] \right), \quad (3.57)$$

where

$$\nu_{\text{molecular}} = 1.5 \times 10^{-6} \text{ m}^2 \text{ s}^{-1} \quad (3.58)$$

is the molecular viscosity of water. Multiplying the diffusivity (3.57) by the factor

$$\text{factor} = \begin{cases} \left(1.85 - 0.85 R_\rho^{-1} \right) R_\rho & 0.5 \leq R_\rho < 1 \\ 0.15 R_\rho & R_\rho < 0.5, \end{cases} \quad (3.59)$$

gives the diffusivity for salinity and other tracers.

3.7 Sample vertical diffusivities from the KPP module

Figure 3.2 shows a sample vertical temperature diffusivity computed as the sum of the diffusivity associated with gravitational instability (Section 3.3), the KPP boundary layer scheme (Section 3.4), shear induced instability (Section 3.5), and double diffusive processes (Section 3.6). The diffusivity arising from these processes are all computed within the KPP module in MOM5. The largest diffusivities are near the ocean surface and in regions of deep water formation in the North Atlantic and Southern Ocean.

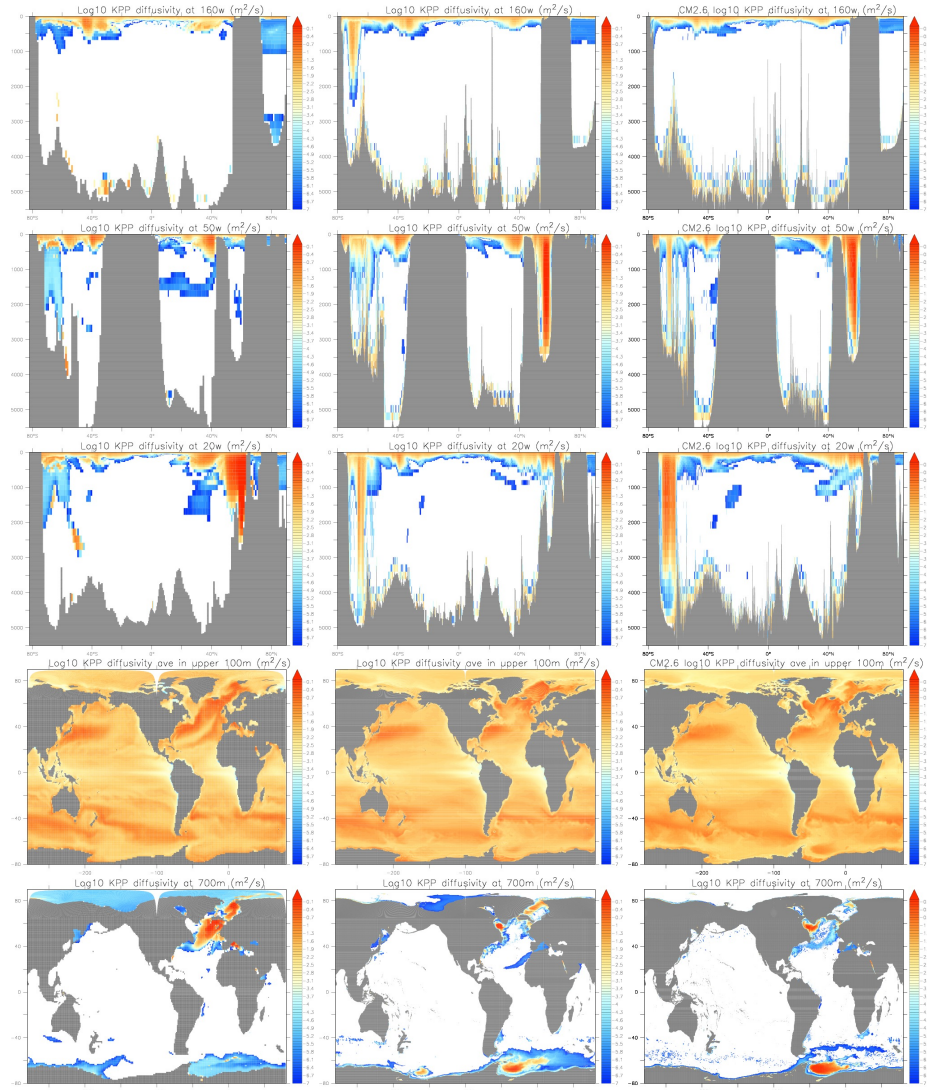


Figure 3.2: Vertical temperature diffusivities from the combined effects of gravitational instability (Section 3.3), the KPP boundary layer scheme (3.4), shear mixing (3.5), and double diffusive processes (3.6). These four schemes are computed as part of the KPP module in MOM5, so their sum is diagnosed in the field `diff_cbt_kpp_t` and `diff_cbt_kpp_s`. The left column is for CM_O1p0_C180, the middle column for CM2.5, and the right column for CM2.6. The KPP diffusivities are largest in the upper ocean, with notable diffusivities near the bottom due to the low stratification reducing the Richardson number. Shown are values computed at 160°W (Pacific sector through Ross Sea in the south), 50°W (Atlantic sector with Labrador Sea in the north), 20°W (Atlantic sector through GIN Sea in the north), averaged over the upper 100 m, and the map at 700 m. Note the particularly large diffusivities found in the Labrador Sea in the CM2.5 simulation, with the CM2.6 diffusivities somewhat smaller and the CM_O1p0_C180 even smaller still. CM_O1p0_C180 shows much larger diffusivities in the middle latitude central and eastern North Atlantic, extending northward into the GIN sea. Missing values represent points where the diffusivity is smaller than $10^{-7} \text{ m}^2 \text{ s}^{-1}$. Diffusivities are centered at the bottom face of a cell, which explains why there is a zero in the bottom-most cell. The top row is for the one-degree CM_O1p0_C180, middle row for CM2.5, and bottom row for CM2.6.

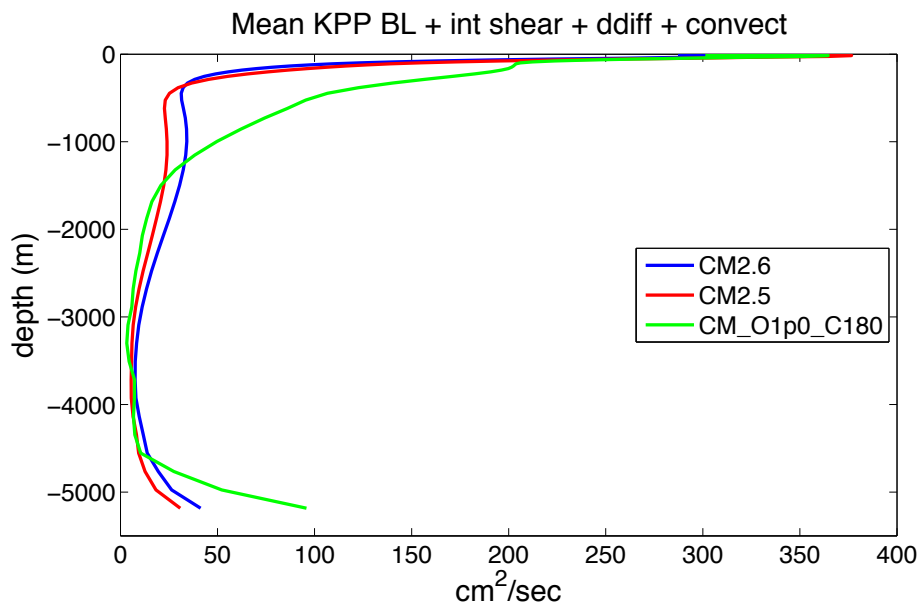


Figure 3.3: Horizontal averaged vertical temperature diffusivity from gravitational instability (Section 3.3), the KPP boundary layer scheme (3.4), shear mixing (3.5), and double diffusive processes (3.6). These four schemes are computed as part of the KPP module in MOM5, so their sum is diagnosed in the field `diff_cbt_kpp_t` and `diff_cbt_kpp_s`. Note the enhanced diffusivity in CM_O1p0_C180 throughout the middle depths. This diffusivity is largely associated with the strong vertical mixing in the central and eastern North Atlantic and GIN Sea region seen in Figure 3.2.

3.8 Parameterized mixing from tide induced mechanical dissipation

The following MOM module is directly connected to the material in this section:

`mom5/ocean_param/vertical/ocean_vert_tidal.F90.`

The CM2-O suite makes use of two tide mixing parameterizations: the coastal tide mixing scheme of [Lee et al. \(2006\)](#) and the interior tide mixing scheme of [Simmons et al. \(2004\)](#). The MOM5 implementation of these schemes is detailed in Chapter 20 in [Griffies \(2012\)](#). We summarize that discussion here with configuration details chosen for CM2-O. Note that the tide mixing parameterizations in MOM5 generally assume a unit Prandtl number, so the parameterized tracer diffusivity arising from dissipation of tidal energy is associated with the same value for a parameterized momentum viscosity.

3.8.1 General considerations

Dianeutral mixing of tracer and momentum arises when energy dissipates at the small scales. There are two sources of energy dissipation considered here:

- breaking internal gravity waves, where the gravity wave energy source is from barotropic tidal energy scattered into internal tidal energy occurring when tides interact with rough bottom topography;
- frictional bottom drag as tides encounter continental shelves (whose depths are generally 500m or less).

To resolve both of these dissipation processes in a numerical model requires grid resolution no coarser than meters in the vertical (throughout the water column), and 1-10 kilometers in the horizontal. This very fine resolution is not generally accessible to global climate models, in which case it is necessary to consider a parameterization.

Bottom drag is typically parameterized as

$$D_{\text{bottom drag}} = C_D \mathbf{u} |\mathbf{u}|, \quad (3.60)$$

where C_D is a dimensionless drag coefficient. The velocity dominating this drag is associated with energy input to the ocean via the barotropic tides as they encounter continental shelves and other shallow ocean regions. The energy dissipation (W m^{-2}) associated with this bottom drag is given by

$$E_{\text{bottom drag}} = C_D \rho_o \langle \mathbf{u}^2 \rangle |\mathbf{u}| \quad (3.61)$$

where the angle bracket symbolizes a time or ensemble average. We assume this time averaged squared velocity arises from the amplitude of barotropic tides as computed in a tide model

$$\langle \mathbf{u}^2 \rangle = U_{\text{tide}}^2. \quad (3.62)$$

This energy dissipation represents energy taken out of the barotropic tide and into small scale dissipation within the ocean bottom boundary layer. We assume that the dissipated energy due to bottom drag contributes to enhanced dianeutral mixing locally.

A wave drag associated with breaking internal gravity waves is written by [Jayne and St.Laurent \(2001\)](#) as

$$D_{\text{wave drag}} = (1/2) N_b \kappa_{\text{rough amp}} h_{\text{rough amp}}^2 \mathbf{u}, \quad (3.63)$$

where N_b is the buoyancy frequency at the ocean bottom, and $(\kappa_{\text{rough amp}}, h_{\text{rough amp}})$ are wavenumber and amplitude scales for the topography. The product $\kappa_{\text{rough amp}} h_{\text{rough amp}}^2$ has dimensions of length and thus defines a *roughness length*

$$L_{\text{rough length}} = \kappa_{\text{rough amp}} h_{\text{rough amp}}^2 \quad (3.64)$$

to be specified according to statistics of the observed ocean bottom topography. Figure 3.4 shows the roughness amplitude, $h_{\text{rough amp}}$, used in CM2.6. Note the larger values associated with gradients in the bottom topography.

The energy dissipation (W m^{-2}) associated with breaking internal gravity waves is given by

$$E_{\text{wave drag}} = (\rho_0/2) N_b L_{\text{rough length}} \langle \mathbf{u}^2 \rangle, \quad (3.65)$$

where again the scale for the ensemble mean of the squared speed, $\langle \mathbf{u}^2 \rangle$, is set according to the tide speed as per equation (3.62). Jayne and St.Laurent (2001) emphasize that $\kappa_{\text{rough amp}}$ is a tuning parameter, with the tide model tuned to give sea level values agreeing with observations. For the CM2-O model, we choose

$$\kappa_{\text{rough amp}} = \frac{2\pi}{\text{roughness_scale}} \quad (3.66)$$

where the namelist parameter is set as

$$\text{roughness_scale} = 1.2 \times 10^4 \text{ m}. \quad (3.67)$$

It is important to distinguish the spatially constant `roughness_scale`, which is used to specify the tuning parameter $\kappa_{\text{rough amp}}$, from the spatially dependent roughness length, $L_{\text{rough length}}$, which is proportional to the square of the spatially dependent roughness amplitude, $h_{\text{rough amp}}$, through equation (3.64).

Once chosen, the energy dissipation can be diagnosed from the tide model. As with the bottom drag, the wave drag energy dissipation represents energy taken out of the barotropic tides, with the energy here transferred into the baroclinic tides. Some of the energy transferred into the baroclinic tides dissipates locally due to local wave breaking, and this then leads to enhanced dianeutral mixing locally. The remaining baroclinic energy propagates away; i.e., it is nonlocal. The ratio of local to nonlocal energy is not well known, and is the focus of research.

Figure 3.4 shows the tide speed or tide amplitude, U_{tide} , used in the CM2.6 simulation. Note the larger amplitudes in certain shelf regions around the world, and generally smaller amplitude in the open ocean. There are some exceptions, such as the western tropical Pacific, where there are some large amplitudes associated with mid-ocean topography. This tide speed is used for both the Simmons et al. (2004) internal tide mixing scheme, and the Lee et al. (2006) coastal scheme.

3.8.2 How the roughness amplitude was computed

The first panel in Figure 3.4 shows the topographic roughness amplitude, $h_{\text{rough amp}}$, used for the tide mixing scheme. This roughness map was computed using the following steps.

- For latitudes between 70°S – 70°N , we take roughness amplitude, $h_{\text{rough amp}}$, from the Smith and Sandwell (1997) dataset (see also Gille et al. (2000)).
- For polar regions, we compute the roughness using the same algorithm as in Smith and Sandwell (1997), yet starting from the global topography dataset

`/archive/1hc/Topo/Gtopo30/padman2.nc`

which is on a $1/30^\circ \times 1/30^\circ$ grid (two minute). We compute the roughness $h_{\text{rough amp}}$ using the following algorithm

$$h_{\text{rough amp}}^2 = \frac{2\pi}{\kappa_o} \left[\left(\frac{d(H^2)}{dx} \right)^2 + \left(\frac{d(H^2)}{dy} \right)^2 \right]^{1/2}, \quad (3.68)$$

where $H(x, y)$ is the bottom two minute topography. Following Jayne and St.Laurent (2001), we choose $\kappa_o = 10^{-4} \text{ m}^{-1}$. We then interpolate the $h_{\text{rough amp}}$ data onto $1/4 \times 1/5$ grid of Smith and Sandwell (1997) and use it for regions poleward of 72° . For the two-degree wide region 70° – 72° , we take a linear combination between the two roughness estimates. Once interpolated (using a Gaussian interpolation method) onto the model grid, we perform a bilinear smoothing near the bipolar transition at 65°N .

- The combined global data is contained in the file

/archive/lhc/cm2/Tide_topo/rough_ascii_pm3.dat

- The bottom roughness for the CM2-O suite was derived sometime in the late 2000s. Subsequent to this work, [Goff and Arbic \(2010\)](#) proposed a new method to derive roughness for use with tide mixing schemes. Additionally, there has been no tuning of the wave number κ_o , or the related $\kappa_{\text{rough amp}}$. We have nonetheless retained the original bottom roughness largely to maintain consistency across updated versions of the models.

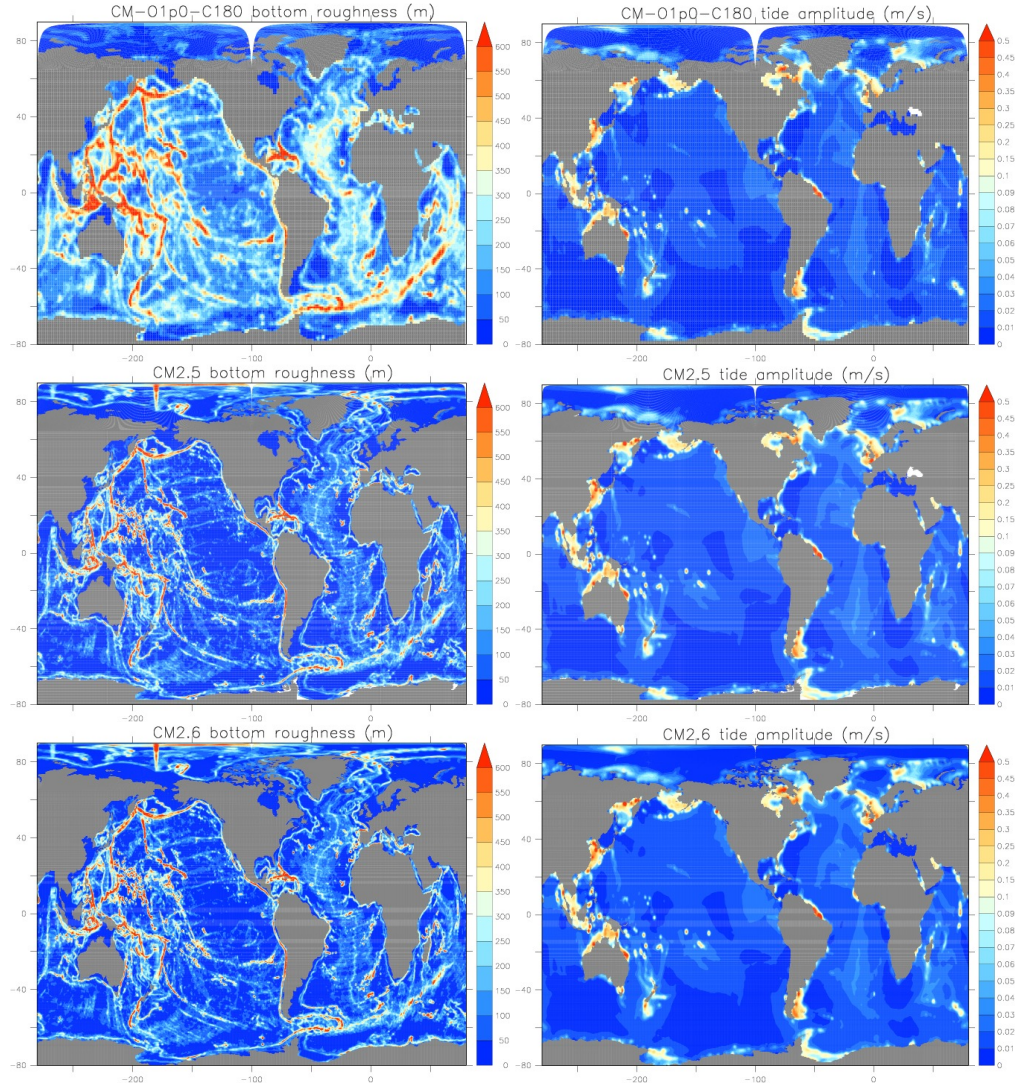


Figure 3.4: Tide mixing input files for the CM2-O suite of models, as created by Hyun-Chul.Lee@noaa.gov. Left panel: Topographic roughness amplitude, $h_{\text{rough amp}}$, used to generate the roughness length, $L_{\text{rough length}}$, according to equation (3.64). For latitudes between 70°S – 70°N , we take roughness amplitude from the [Smith and Sandwell \(1997\)](#) dataset. For higher latitude regions, we compute the roughness amplitude using a two minute bottom topography dataset and blend to the lower latitudes. It is unclear why the enhanced roughness in the Arctic poleward of the Bering strait found in CM2.5 and CM2.6 is missing from CM_O1p0_C180. Right panel: Tide amplitude (m s^{-1}) for the tide mixing parameterization schemes. Note the larger amplitudes in certain shelf regions around the world., and generally smaller amplitude in the open ocean. There are some exceptions, such as the western tropical Pacific, where there are some large amplitudes associated with mid-ocean topography.

3.8.3 How the tide amplitude was computed

The second panel in Figure 3.4 shows the tide amplitude U_{tide} used for the tide mixing parameterizations. This field is computed by starting from the first ten tide components of the [Egbert et al. \(1994\)](#); [Egbert and Erofeeva \(2002\)](#) tide model output, with these components containing more than 99% of the total tide energy. The raw data is contained in the file

/archive/lhc/cm2/Tidaleff/u_TPX0.6.0

Along with astronomical frequency and astronomical phase information, we use the amplitude and phase of the ten tidal components to approximate the full tide velocity \mathbf{u}_{tide} . We then compute the time mean for one year of the tide velocity

$$\overline{\mathbf{u}}_{\text{tide}} = \frac{1}{T} \int_0^T \mathbf{u}_{\text{tide}} dt \quad (3.69)$$

and use it to estimate the tide amplitude according to

$$U_{\text{tide}} = |\overline{\mathbf{u}}_{\text{tide}}|. \quad (3.70)$$

3.8.4 Parameterized mixing from internal tide dissipation

When mechanical energy is dissipated, it is associated with dianeutral mixing. The relation between energy dissipation and mixing is not known precisely, though some empirical formulations have proven useful. For energy dissipation due to breaking internal gravity waves, we follow [Simmons et al. \(2004\)](#), who compute a tracer diffusivity¹

$$\kappa_{\text{wave drag}} = \kappa_0 + \frac{q \Gamma E_{\text{wave drag}}(x, y) F(z)}{\rho N^2}, \quad (3.71)$$

where E_{waves} is the wave energy flux from scattered barotropic to baroclinic waves, given by equation (3.65). Vertical stratification is measured by the buoyancy frequency

$$N^2 = g(\alpha \partial_z \Theta - \beta \partial_z S), \quad (3.72)$$

where

$$\alpha = -\frac{1}{\rho} \frac{\partial \rho}{\partial \Theta} \quad (3.73)$$

$$\beta = \frac{1}{\rho} \frac{\partial \rho}{\partial S} \quad (3.74)$$

introduce the thermal expansion coefficient and haline contraction coefficient, respectively. In regions of large N^2 , vertical mixing is suppressed, hence its presence in the denominator of equation (3.71).

3.8.4.1 Energy flux

We make the following choices for evaluating the energy flux in equation (3.65).

- N_b is computed from the model's evolving buoyancy frequency at the top face of a bottom boundary layer (often just the bottom-most tracer cell). Note that the buoyancy frequency at the bottom face of the bottom-most cell is zero, by definition.

¹We assume a unit Prandtl number. This assumption means the vertical viscosity is enhanced along with the diffusivity when considering internal wave breaking. Note that [Simmons et al. \(2004\)](#) do not discuss vertical viscosity in their study.

- The roughness length $L_{\text{rough length}} = \kappa_{\text{rough amp}} h_{\text{rough amp}}^2$ requires an algorithm to compute $h_{\text{rough amp}}^2$ from observed bottom topography, and tide model to tune $\kappa_{\text{rough amp}}$. However, in practice what can be done is to take $h_{\text{rough amp}}$ given some variance of topography within a grid cell, and then tune $E_{\text{wave drag}}$ to be roughly 1TW in ocean deeper than 1000m, with $\kappa_{\text{rough amp}}$ as the tuning parameter. As discussed in Section 3.8.1, for CM2-O we choose

$$\kappa_{\text{rough amp}} = \frac{2\pi}{\text{roughness_scale}} \quad (3.75)$$

where

$$\text{roughness_scale} = 1.2 \times 10^4 \text{ m}. \quad (3.76)$$

- For purposes of regularization, the CM2-O models enforce a maximum mechanical energy flux from internal tides available for mixing

$$E_{\text{wave drag max}} = \text{wave_energy_flux_max} = 0.1 \text{ W m}^{-2}. \quad (3.77)$$

3.8.4.2 Mixing efficiency

The dimensionless parameter Γ in equation (3.71) measures the efficiency that wave energy dissipation translates into dianeutral mixing. This *mixing efficiency* parameter is often chosen as

$$\Gamma = 0.2 \quad (3.78)$$

based on the empirical results from [Osborn \(1980\)](#). However, in regions of very weak stratification, the mixing efficiency tends to zero according to

$$\Gamma = 0.2 \left(\frac{N^2}{N^2 + \Omega^2} \right) \quad (3.79)$$

where

$$\begin{aligned} \Omega &= \left(\frac{2\pi + 2\pi/365.24}{86400\text{s}} \right) \\ &= \left(\frac{\pi}{43082} \right) \text{s}^{-1} \\ &= 7.2921 \times 10^{-5} \text{s}^{-1}. \end{aligned} \quad (3.80)$$

is the angular rotation rate of the earth about its axis and about the sun. This modified mixing efficiency reduces the regions where spuriously large values of diffusivity may occur, especially next to the bottom, where low values of N^2 may appear. There is little physical reason to believe the huge diffusivities diagnosed from regions with $N^2 < \Omega^2$. Note that the mixing efficiency (3.79) was used by [Melet et al. \(2013\)](#) in their refinement of the [Simmons et al. \(2004\)](#) scheme.

3.8.4.3 Ratio of local to nonlocal dissipation

Another dimensionless parameter, q , in equation (3.71) measures the amount of mechanical energy dissipated locally, and thus contributes to local dianeutral mixing. [Simmons et al. \(2004\)](#) chose

$$q = 1/3 \quad (3.81)$$

based on the work of [St.Laurent et al. \(2002\)](#). The remaining 2/3 of the energy is assumed to propagate away and be dissipated nonlocally.

A global setting of $q = 1/3$ is incorrect. The actual value is related to the modal content of the excited internal tide, which is related to the roughness spectrum of topography. The redder the mode/roughness spectrum, the lower q . For example, Hawaii has been modelled as a knife-edge by [\(St.Laurent et al., 2003\)](#). This topography excites predominantly low modes, and these modes are stable, propagate quickly, and have long interaction times. That is, they propagate to the far field. [Klymak et al. \(2005\)](#) argue that $q = 0.1$ for Hawaii from the Hawaiian Ocean Mixing Experiment (HOME) data. For the mid-Atlantic ridge, the use of $q = 1/3$, as in [Simmons et al. \(2004\)](#), may be more suitable.

3.8.4.4 Background diffusivity and viscosity

The nonlocal dissipation of mechanical energy held by the internal tides, or more generally internal mode energy arising from other sources (e.g., wind energy), are typically accounted for in an *ad hoc* manner via the background diffusivity κ_0 (and background viscosity). A value within the range

$$\kappa_0 = (0.1 - 0.2) \times 10^{-4} \text{ m}^2 \text{ s}^{-1} \quad (3.82)$$

is recommended based on the measurements of [Ledwell et al. \(1993\)](#). Note that this diffusivity does not account for mixing in a planetary boundary layer, such as that discussed by [Large et al. \(1994\)](#) (see Section 3.4). However, as discussed in Section 3.2, the CM2-O models use a zero background diffusivity, which was chosen partly based on simplicity

$$\text{background_diffusivity} = 0. \quad (3.83)$$

However, the CM2-O models use a non-zero background viscosity

$$\text{background_viscosity} = 10^{-4} \text{ m}^2 \text{ s}^{-1}, \quad (3.84)$$

which is a traditional value used in global ocean climate models.

3.8.4.5 Vertical deposition function

The bottom intensified vertical profile, or *deposition function*, $F(z)$ is taken as

$$F = \frac{e^{-(D-d)/\zeta}}{\zeta(1-e^{-D/\zeta})} \quad (3.85a)$$

$$= \frac{e^{d/\zeta}}{\zeta(e^{D/\zeta}-1)}. \quad (3.85b)$$

In this expression,

$$D = H + \eta \quad (3.86)$$

is the time dependent thickness of water between the free surface at $z = \eta(x, y, t)$ and the ocean bottom at $z = -H(x, y)$, and

$$d = -z + \eta \quad (3.87)$$

is the time dependent distance from the free surface to a point within the water column.² The chosen form of the deposition function is motivated by the microstructure measurements of [St.Laurent et al. \(2001\)](#) in the abyssal Brazil Basin, and the continental slope measurements of [Moum et al. \(2002\)](#). This profile respects the observation that mixing from breaking internal gravity waves, generated by scattered barotropic tidal energy, is exponentially trapped within a distance ζ from the bottom. An *ad hoc* decay scale of

$$\zeta = 500 \text{ m} \quad (3.88)$$

is suggested by [Simmons et al. \(2004\)](#) for use with internal gravity wave breaking in the abyssal ocean. This choice is taken for CM2-O through the namelist setting

$$\zeta = \text{decay_scale} = 500 \text{ m}. \quad (3.89)$$

3.8.4.6 Cutoff in shallow seas

[Simmons et al. \(2004\)](#) did not apply their scheme in waters with ocean bottom shallower than 1000 m. In contrast, [Jayne \(2009\)](#) avoided this arbitrary cutoff by applying the scheme for all depths, including the continental shelves. Notably, use of a decay scale $\zeta = 500$ m globally presents no problems numerically, since the structure function (3.85b) will integrate to unity whether or not the ocean depth is greater or less than ζ . It is for these reasons that for CM2-O, we apply the [Simmons et al. \(2004\)](#) scheme without a shallow depth cutoff, thus avoiding the introduction of an arbitrary cutoff depth to the model.

²We emphasize that with a free surface, D and d are generally time dependent. Furthermore, with general vertical coordinates, d is time dependent for all grid cells.

3.8.4.7 Sample diffusivities from internal tide mixing parameterization

Figure 3.5 illustrates the diffusivities from the CM2-O suite that arise from the internal tide mixing scheme. As expected, the diffusivities exponentially decay upwards when moving away from the bottom, and they are largest near rough topography such as the mid-Atlantic ridge. Figure 3.6 shows the horizontal averaged diffusivity for the three models. Note the reduced diffusivity in CM2.6 throughout most of the column relative to the other models. Also note the much larger values for CM2.5 in the deeper ocean. The differences between these simulations may be due to differences in vertical stratification. A clearer comparison must be made over the same time period and same radiative forcing.

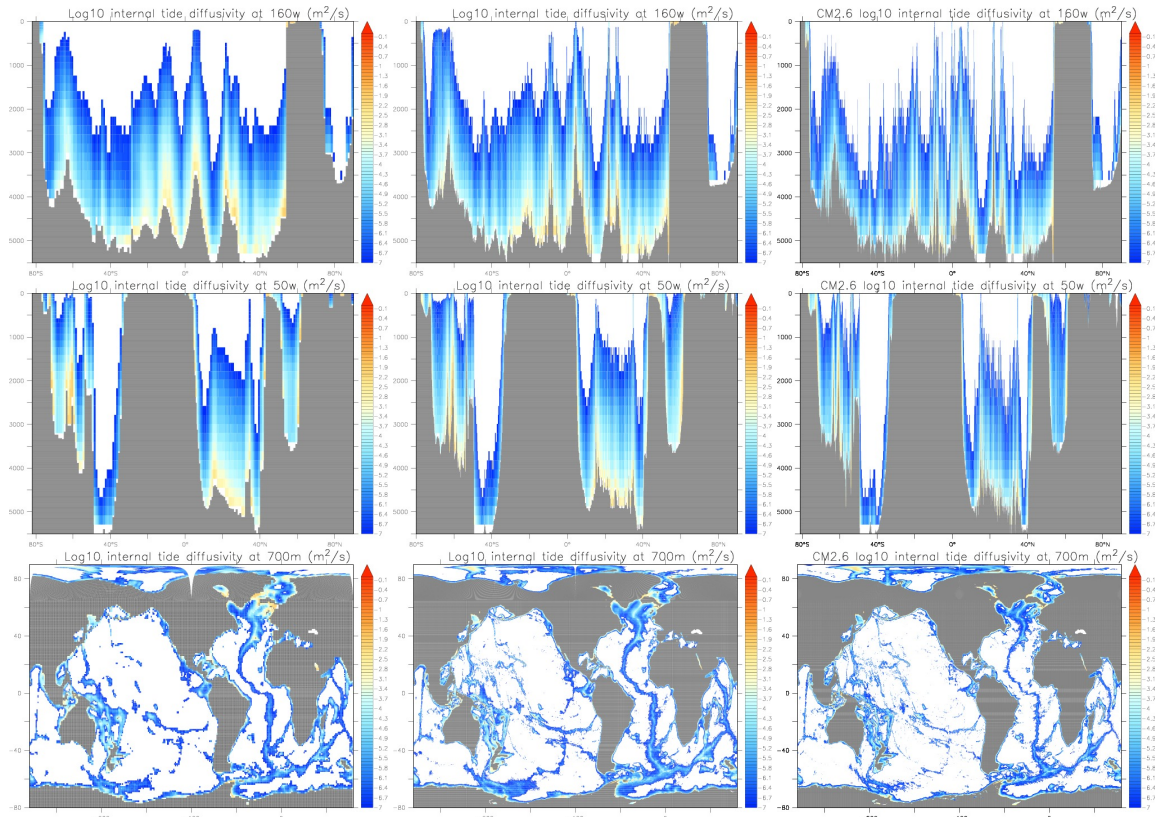


Figure 3.5: Vertical tracer diffusivities from the internal tide mixing parameterization (3.71). Shown are values computed at 160°W (Pacific sector), 50°W (Atlantic sector through Labrador Sea), and map for 700 m. Missing values represent points where the diffusivity is smaller than $10^{-7} \text{ m}^2 \text{ s}^{-1}$. Diffusivities are centered at the bottom face of a cell, which explains why there is a zero in the bottom-most cell. The left column is for the one-degree CM_O1p0_C180, middle column for CM2.5, and right column for CM2.6. The reduced diffusivities found in CM2.5 and CM2.6 relative to CM_O1p0_C180 may be related to the reduced bottom roughness seen in Figure 3.4.

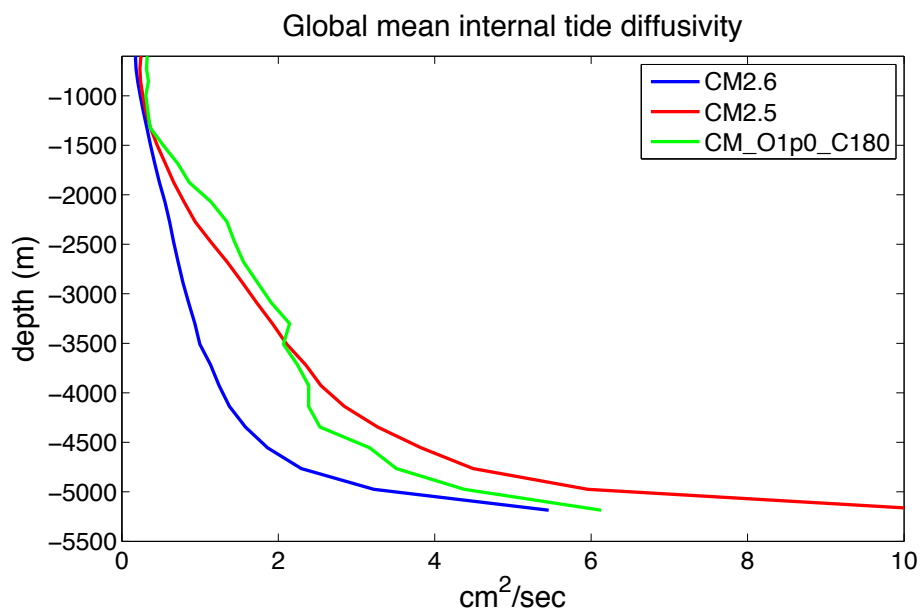


Figure 3.6: Horizontal averaged vertical tracer diffusivity from parameterized mixing due to breaking internal tides. CM2.6 shows less diffusivity than CM2.5 and CM_O1p0_C180, perhaps due to the stronger vertical stratification in CM2.6.

3.8.5 Parameterized mixing from coastal tide induced dissipation

The [Lee et al. \(2006\)](#) scheme provides a means to parameterize mixing from barotropic tides interacting with the continental shelf regions. Contrary to the energetic approach of [Simmons et al. \(2004\)](#), the [Lee et al. \(2006\)](#) scheme does not consider energetic arguments for determining the diffusivity associated with barotropic tides dissipated by the bottom boundary layer. Instead, it follows the ideas of [Munk and Anderson \(1948\)](#), whereby a dianeutral diffusivity is given by

$$\kappa_{\text{bottom drag}} = \kappa_{\max} (1 + \sigma \text{Ri})^{-p} \exp^{-(D-h)/z_{\text{tide}}}, \quad (3.90)$$

where the dimensionless parameters σ and p have the default values

$$\sigma = 3 \quad (3.91)$$

$$p = 1/4. \quad (3.92)$$

The Richardson number is given by

$$\text{Ri} = \frac{N^2}{|\partial_z \mathbf{u}|^2}. \quad (3.93)$$

Small Richardson numbers (e.g., regions of low stratification or strong vertical shear) will give larger vertical diffusivities, with the maximum diffusivity set by κ_{\max} . Following [Lee et al. \(2006\)](#), we set the default for the maximum diffusivity arising from bottom drag dissipation as

$$\kappa_{\max} = 5 \times 10^{-3} \text{ m}^2 \text{ s}^{-1}. \quad (3.94)$$

Since we do not generally resolve the bottom boundary layer in global models, we must approximate the vertical shear to compute the Richardson number, and here we use the form

$$2|\partial_z \mathbf{u}|^2 = \left(\frac{\tilde{U}_{\text{tide}}}{D-h} \right)^2, \quad (3.95)$$

with the scaled tidal speed \tilde{U}_{tide} given by

$$\tilde{U}_{\text{tide}} = U_{\text{tide}} \sqrt{Cd}/\kappa_{\text{von Karman}}. \quad (3.96)$$

Here, Cd is the bottom drag coefficient, taken as $Cd = 2.4 \times 10^{-3}$ by [Lee et al. \(2006\)](#),

$$\kappa_{\text{von Karman}} = 0.41 \quad (3.97)$$

is the von Karman constant, and U_{tide} is the tidal speed taken from a barotropic tidal model. These speeds are largest in the shallow regions.

The exponential decay appearing in equation (3.90) is not part of the original [Lee et al. \(2006\)](#) scheme, nor was it part of the MOM4.0 and MOM4p1 implementations. However, it is an essential element of the MOM5 implementation in CM2-O. Its presence ensures the resulting vertical diffusivities drop off exponentially when moving upward away from the ocean bottom. Absent this exponential decay, regions of small Richardson number, leading to large κ_{drag} , can move upwards in a column (see Figure 20.1 in [Griffies \(2012\)](#)). The chosen exponential decay length scale is given by

$$z_{\text{tide}} = \tilde{U}_{\text{tide}} \frac{\tau_{\text{tide}}}{2\pi} \quad (3.98)$$

where

$$\tau_{\text{tide}} = 12 \times 3600 \text{ s}, \quad (3.99)$$

corresponding to the M2 tide period. Another means for removing the spurious diffusivities from the [Lee et al. \(2006\)](#) scheme is to enable the scheme only in continental shelf regions, which is where it is physically appropriate. Such is the default for the MOM5 implementation and used for CM2-O.

Figure 3.7 shows a sample of the diffusivities from the CM2-O suite associated with the coastal tide mixing scheme. The values are zero in most regions, except next to the coasts.

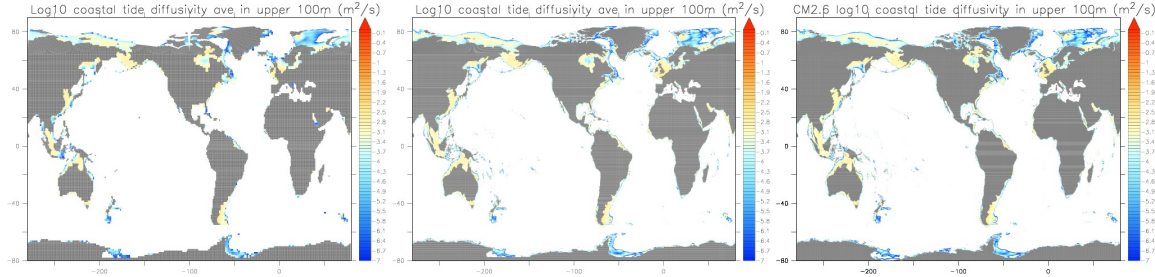


Figure 3.7: Vertical tracer diffusivities from the coastal tide mixing parameterization (3.90). Shown are values computed as an average of the upper 100 m of ocean. Missing values represent points where the diffusivity is smaller than $10^{-7} \text{ m}^2 \text{ s}^{-1}$. The left panel is for CM_O1p0_C180, middle for CM2.5, and right for CM2.6.

3.9 Horizontal viscosity

The horizontal viscosity in the CM2-O models is based on the biharmonic Smagorinsky scheme of Griffies and Hallberg (2000) (see also Section 18.3 of Griffies (2004)). With this approach, the biharmonic viscosity, B , is given by

$$B = A(\Delta)^2/8, \quad (3.100)$$

with A the Laplacian Smagorinsky viscosity given by

$$A = (\Upsilon \Delta/\pi)^2 |E|. \quad (3.101)$$

In this equation, we introduced the grid spacing

$$\Delta = \frac{2\Delta x \Delta y}{\Delta x + \Delta y}, \quad (3.102)$$

and the magnitude of the deformation rate E that measures horizontal tension and shear in the horizontal flow (see Sections 17.5.2, 17.7.1, and 18.3.2 of Griffies (2004)). The dimensionless parameter $\Upsilon > 0$ sets the scale for the viscosity, which we set in CM2-O to the value

$$\Upsilon = 2. \quad (3.103)$$

This value was suggested by Griffies and Hallberg (2000).

We use the Smagorinsky biharmonic approach for both CM2.5 and CM2.6. However, for the coarse model CM_O1.0_C180, we follow the ESM2M approach (Dunne et al., 2012), which uses a combination of Laplacian and biharmonic viscosities.

Figure 3.8 shows a sample of the horizontal biharmonic viscosity for CM2.5 and CM2.6. Note how the viscosity is generally larger near land, which is where the no-slip side boundary induces shear on the fluid thus enhancing the deformation rate and so producing a larger Smagorinsky viscosity. The viscosity is much smaller in the high latitudes and in the deep ocean, which are regions where the horizontal shears are smaller.

3.10 Dimensionless bottom drag coefficient

The following MOM module is directly connected to the material in this section:

`mom5/ocean_core/ocean_bbc.F90`

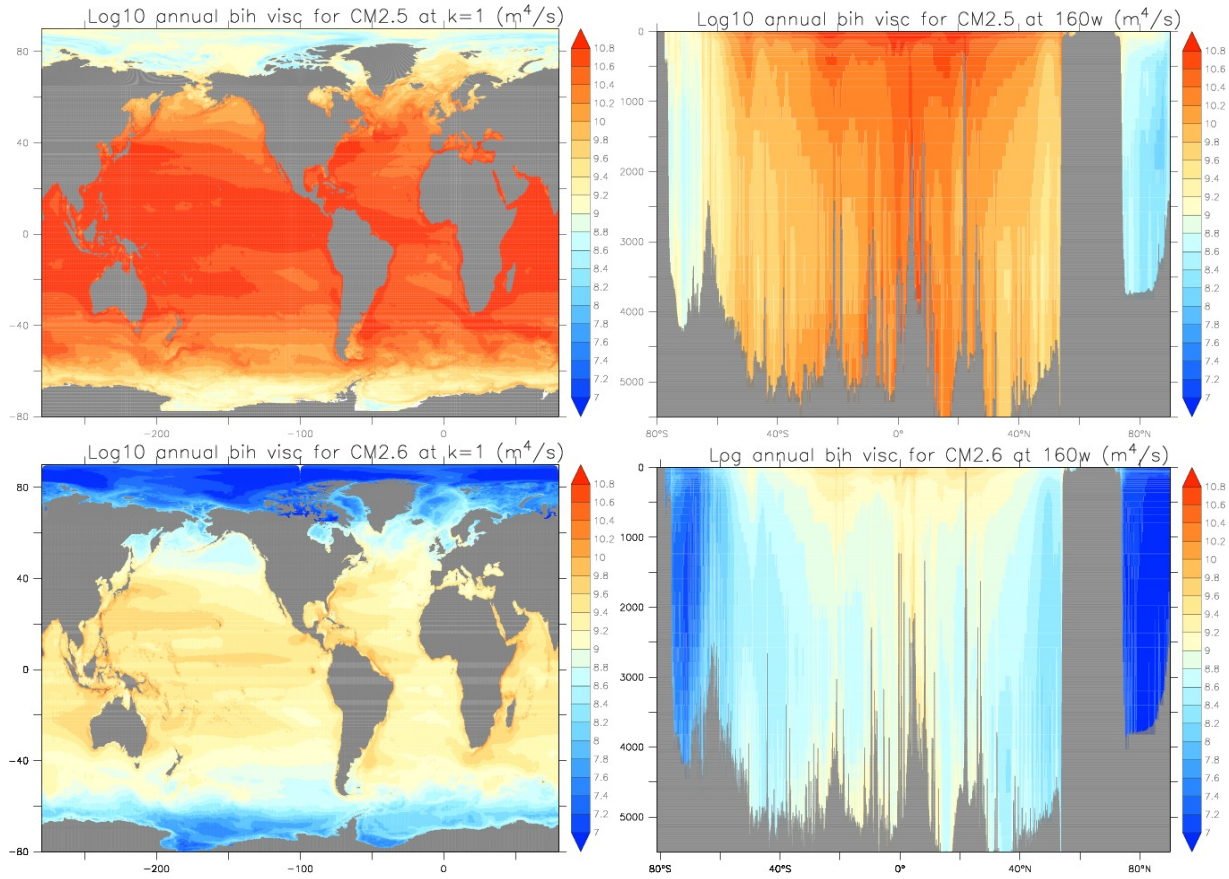


Figure 3.8: Smagorinsky horizontal biharmonic viscosity for CM2.5 and CM2.6 as computed according to equation (3.100). There is zero background horizontal viscosity. The viscosity in both models is computed as an annual mean, with the CM2.5 result from year 80 of the 1990 control simulation and the CM2.6 result from year 100 of the 1860 control simulation. The first panel is from the ocean surface level, and the second panel is along 160°W. The log scale shows the large range for the viscosity, from roughly $10^7 \text{ m}^4 \text{ s}^{-1}$ in the high latitudes and at depth, to nearly $10^{11} \text{ m}^4 \text{ s}^{-1}$ in the boundary regions of the upper ocean where horizontal shears are large. Note the values for CM2.6 are roughly 10 times smaller than for CM2.5, consistent with the smaller grid spacing and the scaling found in equation (3.100) for the Smagorinsky viscosity.

Bottom drag is meant to parameterized dissipative effects from unresolved bottom topography. We incorporate drag to the CM2-O suite via a quadratic bottom drag relation of the form (see Section 13.4 of Griffies (2004))

$$\mathbf{J}_{k=k\mu u}^z = -\rho_o C_d \mathbf{u} \sqrt{\mathbf{u}_{\text{res}}^2 + \mathbf{u}^2}. \quad (3.104)$$

The dimensionless drag coefficient, C_d , scales the drag, and residual bottom speed $|\mathbf{u}_{\text{res}}|$ is meant to incorporate effects from unresolved bottom velocities, such as from tides. The use of a residual tide speed was also incorporated to the OCCAM simulations of Webb et al. (1998). For the CM2-O suite, we set

$$|\mathbf{u}_{\text{res}}| = 0.05 \text{ m s}^{-1}. \quad (3.105)$$

The traditional approach to computing bottom drag is to use a spatially constant bottom drag coefficient. But doing so ignores spatial variations in bottom roughness, with such variations important for

parameterization of mixing from tides discussed in Section 3.8. We therefore consider for CM2-O a dimensionless bottom drag coefficient that is a function of both the tide amplitude, U_{tide} (Section 3.8.3), and roughness amplitude, $h_{\text{rough amp}}$ (Section 3.8.2). The functional form of the bottom drag coefficient is given by

$$C_d = \left(\frac{\kappa_{\text{von Karman}}}{\log\left(\frac{H_o}{h_{\text{rough amp}}} \frac{U_o}{U_{\text{tide}}}\right)} \right)^2, \quad (3.106)$$

with this form inspired by the Law of the Wall form. In this expression, we introduced the von Karman constant, $\kappa_{\text{von Karman}} = 0.41$ (equation (3.97)), and the dimensionful topography and speed scales, H_o and U_o , which take the following values in CM2-O

$$H_o = 1100 \text{ m} \quad (3.107)$$

$$U_o = 1 \text{ m s}^{-1}. \quad (3.108)$$

We furthermore limit the drag coefficient to the range

$$1 \times 10^{-3} \leq C_d \leq 7 \times 10^{-3}. \quad (3.109)$$

Figure 3.9 shows the bottom drag coefficient computed using this approach, based on the bottom roughness amplitude $h_{\text{rough amp}}$ and tide speed U_{tide} shown in Figure 3.4.

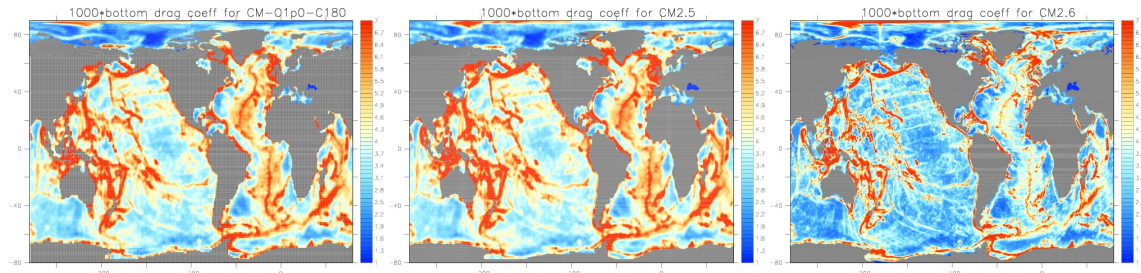


Figure 3.9: Map of the time independent dimensionless bottom drag coefficient (multiplied by 1000) used in the CM2-O suite, based on the expression (3.106) and using the bottom roughness amplitude $h_{\text{rough amp}}$ and tide speed U_{tide} shown in Figure 3.4. The range is $1 \times 10^{-3} \leq C_d \leq 7 \times 10^{-3}$. The drag coefficient is placed on the velocity point rather than the tracer point, since it directly impacts velocity. Notice how the drag coefficient for CM2.6 has smaller values over much of the ocean relative to CM2.5 and CM_O1p0_C180. It is unclear why there is this distinction in bottom drag coefficient, particularly since the bottom roughness in Figure 3.4 show CM2.5 and CM2.6 to be quite closely related.

A large dimensionless bottom drag coefficient, C_d , or large residual velocity, \mathbf{u}_{res} , require a time implicit solution to remain numerically stable. MOM5 provides such an approach (see Section 13.4 of Griffies (2004)) via a namelist option in `ocean.bbc.F90`, and it is used in CM2-O. As we make use of spatially dependent bottom drag coefficient, the time-implicit approach is necessary for model stability.

3.11 Rayleigh drag in certain straits

There are two features of MOM5 that limit its abilities to simulate flow through narrow and shallow straits. First, the B-grid requires two tracer points for each velocity point. Hence, in order to simulate flow through narrow straits, we must open the strait to two tracer points. Doing so generally coarses the representation of the land-sea boundary. Second, the model has a difficult time remaining stable in the presence of very shallow waters. Hence, for the CM2-O suite, we have set the minimum ocean depth to 40 m. This minimum

depth is adequate for much of the ocean, except near the coasts and continental shelves. In some cases, artificially deepening the ocean allows for overly large mass transports through regions.

To partially address both of the above limitations, we have found it useful to add extra frictional dissipation in order to reduce the mass transport through certain regions. We do so in MOM5 by adding Rayleigh drag term to the momentum equation, written in the form

$$\partial_t(\rho dz u)_{\text{Rayleigh}} = -\gamma \rho dz u \quad (3.110)$$

$$\partial_t(\rho dz v)_{\text{Rayleigh}} = -\gamma \rho dz v. \quad (3.111)$$

The damping coefficient γ_{Rayleigh} (units inverse seconds) is generally a function of space and time. However, for CM2-O we prescribe it based on an entry to a table, with nonzero values only in those places where transports were found to be too large absent the extra drag. Physically, the Rayleigh drag may be considered a parameterization for missing drag associated with breaking gravity waves near topography.

In fact, the Rayleigh drag has *only* been implemented in the CM2.5 component of the CM2-O suite. Figure 3.10 shows the energy dissipation associated with the drag in CM2.5, with this dissipation restricted to the Indonesian region and the Torres Strait north of Australia. We compute this dissipation by

$$\text{power dissipate from Rayleigh drag (Watt)} = -\gamma \rho dz (u^2 + v^2). \quad (3.112)$$

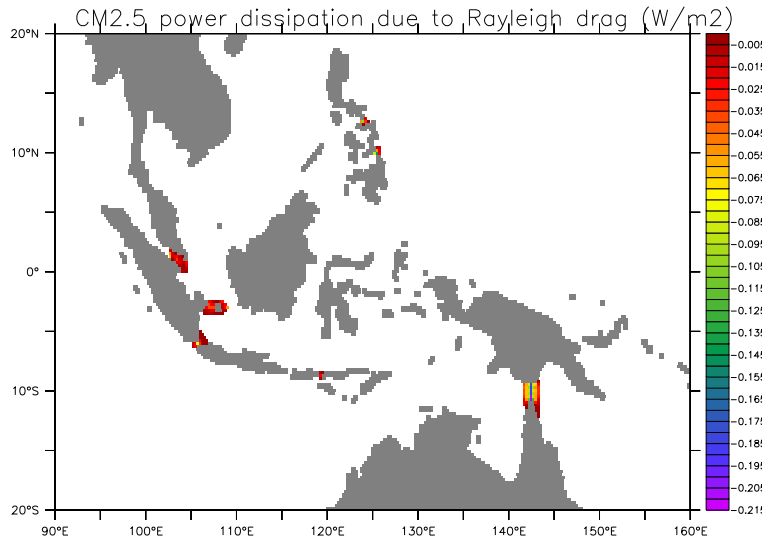


Figure 3.10: Power dissipation (W m^{-2}) due to the Rayleigh drag used in the Indonesian region. We compute this power dissipation from equation (3.112) and dividing by the horizontal area of a grid cell.

3.12 Mixed layer submesoscale restratification

The following MOM module is directly connected to the material in this section:

`mom5/ocean_param/lateral/ocean_submesoscale.F90.`

CM2-O makes use of the mixed layer submesoscale restratification parameterization scheme of [Fox-Kemper et al. \(2008\)](#) and [Fox-Kemper et al. \(2011\)](#). This scheme parameterizes the restratification effects of submesoscale eddies in the ocean surface mixed layer. These effects occur on a time scale much shorter than the mesoscale eddies parameterized via the neutral physics scheme of [Gent and McWilliams \(1990\)](#).

and Gent et al. (1995). Full details on the MOM5 implementation of the submesoscale parameterization are provided in Chapter 24 of Griffies (2012). Here, we summarize some salient points about the parameterization and its implementation in CM2-O.

This scheme was problematic in early implementations of CM2.5, as it was prone to introducing instabilities and/or unphysically cold water extrema production. Details of the problems are provided in Section 24.5 of Griffies (2012), where it is also shown how the scheme was reformulated to address the problems. As part of that development, we chose to set certain of the scheme's parameters towards a weaker end of their uncertainty range, to reduce the potential for further problems.

3.12.1 Basics of the scheme and choices for CM2-O

The parameterization is based on the calculation of a vector streamfunction Ψ (with units length² time⁻¹)

$$\Psi = \left(\frac{C_e \mu h^2 g \Delta}{L_f \sqrt{f^2 + \tau^{-2}}} \right) \hat{\mathbf{z}} \wedge \overline{(-\alpha \nabla \Theta + \beta \nabla S)}^z. \quad (3.113)$$

This expression introduces the following terms.

- g is the gravitational acceleration, f is the Coriolis parameter, ρ_o is the constant Boussinesq reference density, and Δ is the horizontal grid spacing as defined by equation (3.102).
- C_e is a dimensionless number that Fox-Kemper et al. (2008) suggest should live in the range $0.06 \leq C_e \leq 0.08$. It is set to the slightly smaller value of $C_e = 0.05$ in the CM2-O models through use of the namelist coefficient_ce=0.05.
- A non-negative vertical structure function

$$\mu = [1 - (1 - 2d/h)^2][1 + 5/21(1 - 2d/h)^2] \quad 0 \leq \mu \leq 1 \quad (3.114)$$

is used in the mixed layer ($d \leq 0$), with zero values beneath the mixed layer ($d \geq h$). Here, $d = -z + \eta$ is the vertical distance from the ocean free surface at $z = \eta(x, y, t)$.

- h is the mixed layer thickness determined according to the mixed layer depth diagnostic detailed in Section ???. In particular, we use the default critical buoyancy value of $\Delta B_{\text{crit}} = 0.0003 \text{ m s}^{-2}$ through use of the mom5/ocean_diag/ocean_tracer_diag.F90 namelist setting buoyancy_crit=0.0003.
- $\overline{-\alpha \nabla \Theta + \beta \nabla S}^z$ is the gradient of locally referenced potential density, averaged over the depth of the mixed layer, where

$$\alpha = -\frac{1}{\rho} \frac{\partial \rho}{\partial \Theta} \approx -\frac{1}{\rho_o} \frac{\partial \rho}{\partial \Theta} \quad (3.115)$$

$$\beta = \frac{1}{\rho} \frac{\partial \rho}{\partial S} \approx \frac{1}{\rho_o} \frac{\partial \rho}{\partial S} \quad (3.116)$$

are the thermal expansion and haline contraction coefficients, respectively.

- τ is a time scale for the submesoscale eddies, which corresponds to the MOM5 namelist time_constant found in the module ocean_submesoscale.F90. The CM2-O models set time_constant = 86400, which is a single day.
- L_f is a length scale for the width of the submesoscale eddies (order 5 km). We present the CM2-O choice for this length in equation (3.119).

Written in components, the streamfunction is given by

$$\Psi = \Gamma \mu (-\overline{-\alpha \partial_y \Theta + \beta \partial_y S}^z, \overline{-\alpha \partial_x \Theta + \beta \partial_x S}^z, 0), \quad (3.117)$$

where

$$\Gamma = \frac{C_e h^2 g \Delta}{L_f \sqrt{f^2 + \tau^{-2}}} \quad (3.118)$$

is shorthand for the non-negative contributions with physical dimensions of a volume transport, $\text{m}^3 \text{ s}^{-1}$. The dimensionless function $\mu(z)$ carries the only vertical dependence of the streamfunction Ψ . We make the following observations.

- The formulation of [Fox-Kemper et al. \(2008\)](#) is in terms of the mixed layer depth, rather than the planetary boundary layer depth. The reasoning is that the planetary boundary layer can be very small under stable buoyancy forcing. However, the submesoscale eddies remain even in these situations, so long as the mixed layer depth is nontrivial. MOM has an option for setting h according to either the mixed layer depth or the planetary boundary layer depth, with the mixed layer depth the recommended choice, and the approach used for CM2-O.
- The streamfunction (3.113) magnitude is inversely proportional to the submesoscale front length scale L_f , so that the streamfunction is larger in regions of tight fronts. For the MOM5 implementation of the submesoscale parameterization, we may choose the front length to be either a constant or a function of the flow. A constant is not appropriate for a global model. So for CM2-O, we determine the length scale according to the first baroclinic Rossby radius defined over the mixed layer. We compute this Rossby radius by

$$L_f = \frac{h \bar{N}^z}{f} \quad (3.119)$$

with \bar{N}^z the buoyancy frequency averaged over the depth of the mixed layer, and h the mixed layer thickness. Substitution of the length scale (3.119) into the streamfunction (3.113) leads to

$$\Psi = \left(\frac{C_e \mu h g \Delta}{\bar{N}^z} \right) \left(\frac{f}{\sqrt{f^2 + \tau^{-2}}} \right) \hat{\mathbf{z}} \wedge \overline{(-\alpha \nabla \Theta + \beta \nabla S)}^z. \quad (3.120)$$

The streamfunction thus gets larger in regions of weak vertical stratification (\bar{N}^z small), which correspond to regions of small front lengths (3.119). Conversely, the streamfunction goes to zero as the equator is approached ($f \rightarrow 0$). Note that it is not appropriate to compute the baroclinic Rossby radius near the equator according to equation (3.119). Nonetheless, we retain this formulation, as the parameterization has not been formulated in the equatorial region, so we consider its removal in that region to be desirable.

3.12.2 Eddy induced transport

The vector streamfunction (3.113) gives rise to an eddy induced velocity

$$\mathbf{v}^* = \nabla \wedge \Psi \quad (3.121a)$$

$$= (-\partial_z \Psi^{(y)}, \partial_z \Psi^{(x)}, \partial_x \Psi^{(y)} - \partial_y \Psi^{(x)}) \quad (3.121b)$$

and an associated volume transport within the mixed layer. There is zero net horizontal volume transport

$$\int_{-H}^H \mathbf{u}^* dz = 0, \quad (3.122)$$

since the vector streamfunction vanishes at the ocean surface and at the base of the mixed layer. A zero net volume transport is also the case for the eddy induced transport from the [Gent et al. \(1995\)](#) mesoscale parameterization, where the [Gent et al. \(1995\)](#) quasi-Stokes streamfunction vanishes at the ocean surface and bottom ([McDougall and McIntosh, 2001](#)) (see Section 3.13).

3.12.3 Overturning circulation

For a vertical position z within the mixed layer, the meridional volume transport passing beneath this depth z , zonally integrated within a basin or over the globe, is computed by the integral (see Section 4.8)

$$\mathcal{T}^{(y)}(y, z, t) = - \int dx \int_{-H}^z v^* dz' \quad (3.123a)$$

$$= - \int dx \int_{-h}^z \partial_{z'} \Psi^{(x)} dz' \quad (3.123b)$$

$$= - \int \Psi^{(x)}(x, y, z, t) dx \quad (3.123c)$$

$$= \int \Gamma \mu \overline{(-\alpha \partial_y \Theta + \beta \partial_y S)^z} dx \quad (3.123d)$$

since the streamfunction vanishes at $z \leq -h$ (beneath the mixed layer). Likewise, the zonal transport within the mixed layer is

$$\mathcal{T}^{(x)}(x, z, t) = - \int dy \int_{-H}^z u^* dz' \quad (3.124a)$$

$$= \int dy \int_{-h}^z \partial_{z'} \Psi^{(y)} dz' \quad (3.124b)$$

$$= \int \Psi^{(y)}(x, y, z, t) dy \quad (3.124c)$$

$$= \int \Gamma \mu \overline{(-\alpha \partial_x \Theta + \beta \partial_x S)^z} dy. \quad (3.124d)$$

Since $\Gamma \mu$ is single signed within the mixed layer, the sign of the horizontal transport in the mixed layer is given by the sign of the gradient of the locally referenced potential density. For example, with denser water towards the north, so that $\overline{(-\alpha \partial_y \Theta + \beta \partial_y S)^z} > 0$, the meridional transport passing beneath a depth z within the mixed layer will be negative, $\mathcal{T}^{(y)}(y, z, t) < 0$. This property of the transport provides a useful check that the scheme has been implemented in the model with the proper sign.

It is instructive to compare the volume transport from the submesoscale parameterization to that induced by the Gent et al. (1995) mesoscale scheme. For Gent et al. (1995), the horizontal component of the eddy-induced velocity is

$$\mathbf{u}^{gm} = -\partial_z(\kappa \mathbf{S}), \quad (3.125)$$

with

$$\mathbf{S} = - \left(\frac{-\alpha \nabla \Theta + \beta \nabla S}{-\alpha \partial_z \Theta + \beta \partial_z S} \right) \quad (3.126)$$

the neutral slope vector, and $\kappa > 0$ a diffusivity. The meridional transport is given by

$$\mathcal{T}_{gm}^{(y)} = - \int dx \int_{-H}^z v^{gm} dz' \quad (3.127a)$$

$$= - \int \kappa S^{(y)} dx \quad (3.127b)$$

$$= \int \kappa g N^{-2} (-\alpha \partial_y \Theta + \beta \partial_y S) dx \quad (3.127c)$$

where we set the streamfunction to zero at the ocean bottom, and introduced the squared buoyancy frequency

$$N^2 = g(\alpha \partial_z \Theta + \beta \partial_z S). \quad (3.128)$$

For a stable stratification with $N^2 > 0$, the volume transport is directed in the sign of the meridional density gradient, which is analogous to the case for the submesoscale transport (3.123d).

3.12.4 CM2-O submesoscale global overturning streamfunction

To evaluate the overturning streamfunction when implementing the submesoscale closure using skew fluxes, we perform the following step in Ferret

$$\mathcal{T}^{(y)}(y, z, t) = \text{ty_trans_submeso[i = @sum]} \quad \text{skew fluxes,} \quad (3.129)$$

which is just as for the skew flux implementation of Gent et al. (1995). Note that the vertically integrated seawater transport from the submesoscale parameterization scheme vanishes. We see this property analytically via equation (3.122), whereas Section 4.8.5 discusses how it manifests diagnostically in MOM5. So there is no contribution from this scheme to the column integrated volume/mass transport.

Figure 3.11 shows the annual mean overturning streamfunction from the submesoscale parameterization scheme as realized in the CM2-O suite of simulations. Note how the streamfunction vanishes beneath the mixed layer, with penetration into the deep only in the high latitudes. Also note how it gets smaller as the horizontal resolution is enhanced. The grid factor appearing as a multiplier in the streamfunction (equation (3.113)) causes the magnitude of the streamfunction to reduce as resolution is refined.

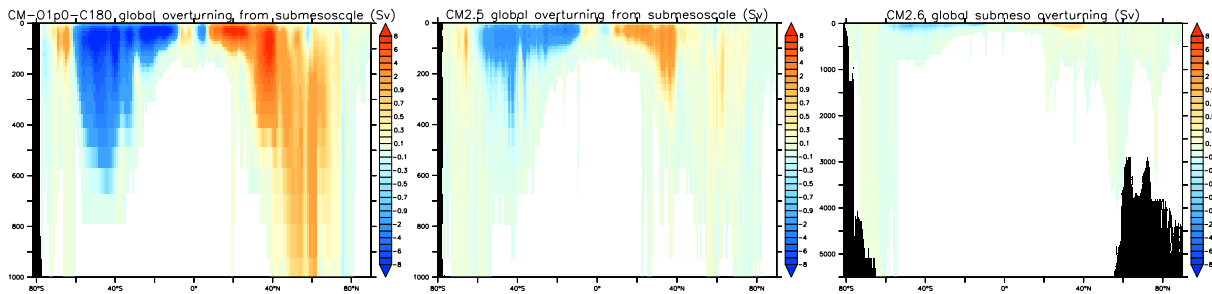


Figure 3.11: Time mean (years 101-140) overturning streamfunction from the submesoscale parameterization as realized in the CM2-O suite of simulations, shown here over just the upper 1000 m of ocean. Positive values indicate clockwise circulation, as predominantly occurs in the northern hemisphere, whereas negative values occur for counterclockwise circulation, as predominantly occurs in the southern hemisphere. Note how the streamfunction gets smaller as the resolution is refined, with this behaviour expected due to the grid scale factor in the submesoscale streamfunction (3.113).

3.13 Mesoscale eddy parameterization in CM_O1.0_C180

The ocean component in CM_O1.0_C180 uses the same horizontal grid spacing as that in CM2.1, CM3, and ESM2M. Consequently, we need to prescribe a parameterization of mesoscale eddies, since they are unresolved at the nominally one-degree resolution of this ocean. We follow the convention approach in which we employ the neutral diffusion and skew diffusion parameterizations in an aim to incorporate the mean effects from mesoscale eddies on the resolved flow.

3.13.1 Details of the chosen neutral physics scheme

The neutral diffusion scheme is based on Griffies et al. (1998) with a constant diffusivity of $600 \text{ m}^2 \text{ s}^{-1}$ and the neutral slope tapering scheme of Danabasoglu and McWilliams (1995). CM2.1 and CM3 use the rather small value of $1/500$, whereas ESM2M and CM_O1.0_C180 use $1/200$ for the maximum slope. Following the recommendations from Treguier et al. (1997), Ferrari et al. (2008), and Ferrari et al. (2010), neutral diffusion is exponentially transitioned to horizontal diffusion in those regions where the surface boundary

layer is encountered. Following from the recommendations of [Gerdes et al. \(1991\)](#), neutral diffusive fluxes are furthermore converted to horizontal diffusion next to solid walls.

The quasi-Stokes transport from mesoscale eddies is implemented using the skew flux approach of [Griffies \(1998\)](#). For CM2.1 and CM3, the quasi-Stokes streamfunction is computed via the local methods from [Gent et al. \(1995\)](#) following the upper ocean transition developed by [Treguier et al. \(1997\)](#). For ESM2M and CM_O1.0_C180, the quasi-Stokes streamfunction is computed via a boundary value problem extending across the full ocean column according to [Ferrari et al. \(2010\)](#), which contrasts fundamentally from the local approach of [Gent and McWilliams \(1990\)](#) and [Gent et al. \(1995\)](#).

The horizontal variation of the eddy diffusivity used for the quasi-Stokes transport is based on vertically averaged flow properties ([Griffies et al., 2005](#)). In ESM2M, the allowable range for the diffusivity is given by

$$100 \text{ m}^2 \text{ s}^{-1} \leq \kappa_{\text{ESM2M}} \leq 800 \text{ m}^2 \text{ s}^{-1} \quad (3.130)$$

whereas the standard settings for CM2.1 and CM3 are

$$100 \text{ m}^2 \text{ s}^{-1} \leq \kappa_{\text{CM2.1}} \leq 600 \text{ m}^2 \text{ s}^{-1}. \quad (3.131)$$

Motivated by the studies of Southern Ocean eddy variability and the impacts from eddy parameterizations considered by [Farneti et al. \(2010\)](#) and [Farneti and Gent \(2011\)](#), we choose for CM_O1.0_C180 a diffusivity bounded at the upper end by the larger value

$$100 \text{ m}^2 \text{ s}^{-1} \leq \kappa_{\text{CM_O1.0_C180}} \leq 1200 \text{ m}^2 \text{ s}^{-1}. \quad (3.132)$$

[Figure 3.12](#) shows the annual mean diffusivity from CM_O1.0_C180. Note the presence of enhanced diffusivities in regions of strong baroclinicity, which corresponds to the choice made in the [Griffies et al. \(2005\)](#) approach. Also note that the diffusivity is scaled smaller in regions approaching the equator. To achieve this scaling, we multiply the diffusivity by the following resolution function

$$\kappa = \frac{\kappa_0}{1 + (\lambda/\Delta)^2}, \quad (3.133)$$

where κ_0 is the diffusivity sans the scaling, λ is the first baroclinic Rossby radius, and

$$\Delta = \frac{2\Delta x \Delta y}{\Delta x + \Delta y} \quad (3.134)$$

is the nominal grid spacing. In regions where the first baroclinic Rossby radius is larger than the nominal grid spacing, the resolution function scales down the diffusivity. The approach follows that detailed in [Hallberg \(2013\)](#), although note that he recommends a much stronger scaling between “resolved” and “unresolved” regions, in effect using a step function.

3.13.2 Overturning from the parameterized mesoscale transport

To evaluate the overturning streamfunction when implementing the mesoscale closure using skew fluxes, we follow the approach for the submesoscale closure ([Section 3.12.4](#)), whereby we perform the following step in Ferret

$$\mathcal{T}^{(y)}(y, z, t) = \text{ty_trans_gm[i = @sum]} \quad \text{skew fluxes.} \quad (3.135)$$

We provide a derivation of this expression in [Section 4.8.5](#). The vertically integrated seawater transport from the mesoscale parameterization scheme vanishes, just as the submesoscale scheme (equation [\(3.122\)](#) and [Section 4.8.5](#)). So there is no contribution from this scheme to the column integrated volume/mass transport (see also [Section 4.8.5](#) for more discussion on this point).

[Figure 3.13](#) shows the annual mean overturning streamfunction from the mesoscale parameterization as realized in CM_O1.0_C180. The streamfunction is nontrivial only in the Southern Ocean.

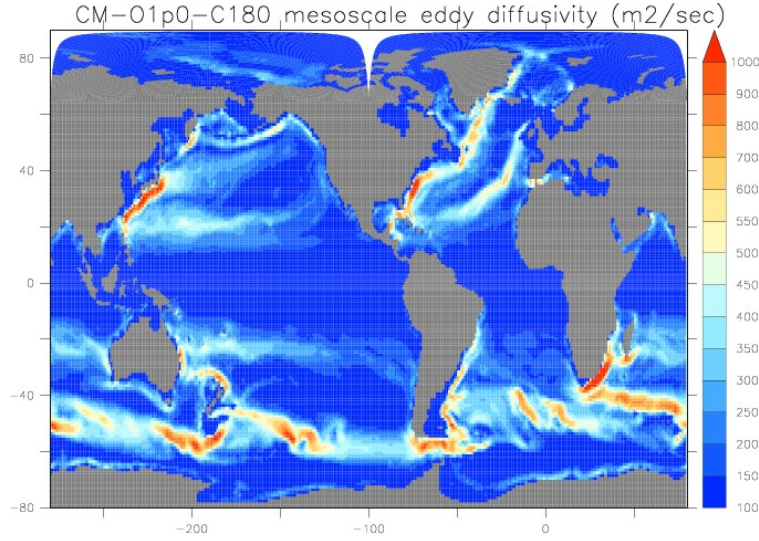


Figure 3.12: Time mean (years 101-140) mesoscale eddy diffusivity associated with the parameterized quasi-Stokes transport. The spatial structure is determined by the depth averaged baroclinicity approach of Griffies et al. (2005). We bound the diffusivity within the range $100 \text{ m}^2 \text{ s}^{-1} \leq \kappa_{\text{CM},01,0,C180} \leq 1200 \text{ m}^2 \text{ s}^{-1}$. The maximum value is motivated by the studies from Farneti et al. (2010) and Farneti and Gent (2011). It is larger than the CM2.1 value (maximum set to $600 \text{ m}^2 \text{ s}^{-1}$) and ESM2M value (maximum set to $800 \text{ m}^2 \text{ s}^{-1}$). The scaling function (3.133) is used to reduce the diffusivity in the tropics towards the minimum setting.

3.14 Ocean optics and chlorophyll dataset

The following MOM modules are directly connected to the material in this chapter:

```
ocean_core/ocean_sbc.F90
ocean_param/sources/ocean_shortwave.F90
ocean_param/sources/ocean_shortwave_gfdl.F90
```

The purpose of this section is to discuss the numerical implementation of shortwave heating in MOM5, with this material following that provided in Chapter 17 of Griffies (2004). The importance of shortwave ocean heating has been raised in many studies, with the following making use of GFDL models: Sweeney et al. (2005), Anderson et al. (2007), Anderson et al. (2009), Gnanadesikan and Anderson (2009), and Gnanadesikan et al. (2010).

3.14.1 General considerations and model implementation

Solar penetration brings solar shortwave heating downward in the ocean column, thus providing a heating at depth. The parameterization of the oceanic absorption of downward solar radiation is generally written as

$$I(x, y, z) = I_{0-}(x, y) \mathcal{F}(z), \quad (3.136)$$

where I_{0-} , in units of Wm^{-2} , is the total shortwave downwelling radiative heating per unit area incident at the earth surface, and $\mathcal{F}(z)$ is a dimensionless attenuation function. For the CM2-O suite, we use the attenuation based on Manizza et al. (2005), which follows the approach of Dunne et al. (2012) for the ESM2 suite of GFDL earth system models. Note that the total downwelling radiation I_{0-} is to be distinguished from the total shortwave heating I_0 , where $I_{0-} = (1 - \alpha) I_0$, with $\alpha \approx 0.06$ the sea surface albedo.

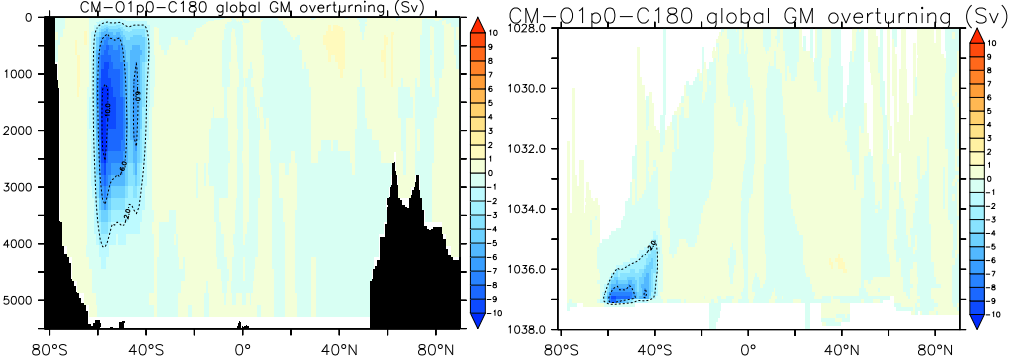


Figure 3.13: Time mean (years 101-140) overturning streamfunction from the mesoscale eddy parameterization as realized in CM_O1p0_C180 (the eddy admitting models CM2.5 and CM2.6 do not have a mesoscale parameterization). Positive values indicate clockwise circulation. We exhibit the streamfunction as a meridional-depth overturning and a meridional- σ_{2000} overturning.

Shortwave heating affects the heat budget locally according to

$$\frac{\partial(\rho\Theta)}{\partial t} = -\partial_z(\rho F^z - I/C_p^0). \quad (3.137)$$

In this equation, F^z accounts for vertical processes such as advection and diffusion, C_p^0 is the heat capacity of seawater (equation (3.2)), and ρ is the *in-situ* density which for a Boussinesq fluid is set to the Boussinesq reference density ρ_0 . Finally, Θ is the conservative temperature of [McDougall \(2003\)](#), which is approximated in the CM2-O suite by potential temperature θ .

Shortwave heating leads to the following net heat flux over a column of ocean fluid

$$\int_{-H}^{\eta} \left(\frac{\partial I}{\partial z} \right) dz = I(\eta) - I(-H). \quad (3.138)$$

For CM2-O, we assume there is no shortwave heating of the solid rock underneath the ocean fluid, so

$$I(z = -H) = 0, \quad (3.139)$$

with this boundary condition set via masks in MOM. Although the expression (3.136) suggests the upper boundary condition $I(\eta) = I_{0-}$, we must be careful to not double-count the shortwave source since it is typically carried as part of the surface temperature flux array `stf` and thus handled by the module `ocean_core/ocean_sbc.F90`. We now present the two approaches available in MOM.

The vertical convergence of penetrative shortwave radiation is incorporated into MOM's heat equation. Additionally, it is typical to include the total downwelling shortwave heating I_{0-} within the surface flux array `stf`, where other forms of heating such as those from latent, sensible, and longwave affects are also incorporated. Hence, for proper accounting of the shortwave heating, the upper boundary condition for the irradiance function must be specified as

$$I(\eta) = \begin{cases} 0 & \text{if } I_{0-} \text{ is already included in } \text{stf} \\ I_{0-}(x, y) & \text{if } I_{0-} \text{ is NOT already included in } \text{stf}. \end{cases} \quad (3.140)$$

The typical practice at GFDL is to set $I(\eta) = 0$ since I_{0-} is already included in `stf`, and this practice is followed for CM2-O. Hence, when mapping the effects from penetrative shortwave heating in the surface grid cell, one must be careful to add two terms, as discussed in Section 3.14.3.

3.14.2 Chlorophyll-a climatology

Following [Dunne et al. \(2012\)](#), the CM2-O suite uses the optical scheme of [Manizza et al. \(2005\)](#) to define the attenuation exponentials. We make use of a chlorophyll-a monthly climatology for attenuating shortwave radiation entering the ocean surface layers. The monthly mean chlorophyll climatology currently being used in the CM2.1, CM2.4, CM2.5, CM2.5_FLOR, CM2.6 and CM2.7 class models is based on SeaWiFS data from GSFC monthly mean files available from

oceandata.sci.gsfc.nasa.gov

The raw data is provided on a nine km grid, and then interpolated to a one degree grid. A nearest in time approach is then applied to fill missing ocean values. A monthly mean climatology for the period (1998–2007) is calculated, and then smoothed with a box-car routine. It is this monthly climatology that is used for the CM2-O suite. Figure 3.14 shows the annual mean for the chlorophyll-a concentration for the three ocean models in the CM2-O suite.

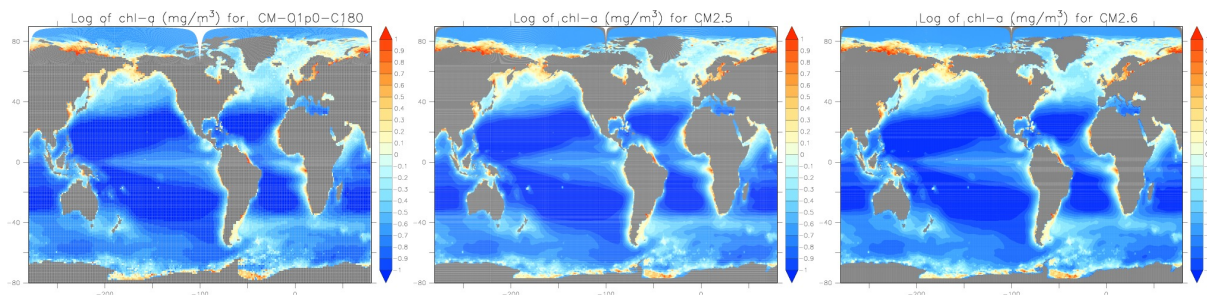


Figure 3.14: Annual mean chlorophyll-a concentration in mg m^{-3} used as an input for the CM2-O optics to attenuate shortwave radiation. Whit.Anderson@noaa.gov created this file. A global mean value is used for grid points with no satellite measurements.

3.14.3 Diagnosing the impacts of shortwave heating in MOM

It is of interest to diagnose the impacts of shortwave heating on the ocean fluid, both at the surface and beneath. As detailed here, there are two terms needed to fully diagnose the impacts of shortwave heating.

- SURFACE NET DOWNWARD SHORTWAVE FLUX: This is the surface net downward shortwave flux $I_{0-}(x, y)$ discussed in equation (3.136), and it is the shortwave heat flux entering through the top of the surface ocean model grid cell. This heat flux is handled by `ocean_core/ocean_sbc.F90`, and it contributes to the `stf` array as part of the temperature derived type.

The diagnostic table entry for $I_{0-}(x, y)$ is `swflx`, which is the surface net downward shortwave flux. If there was zero penetrative shortwave radiation through the ocean column, then this flux would represent the density and thickness weighted convergence of shortwave flux impacting the surface model grid cell. However, penetration is the norm, so there is another contribution to the net impacts of shortwave radiation on the ocean.

- DOWNWARD SHORTWAVE FLUX IN SEAWATER: This is the density and thickness weighted flux convergence (units of W m^{-2}) of shortwave heat that impacts a tracer grid cell, arising from the penetration of shortwave radiation beneath the surface grid cell. This flux convergence is computed in `ocean_shortwave.F90`.

Because MOM typically includes the surface shortwave flux $I_{0-}(x, y)$ in the treatment of surface boundary conditions ($I(\eta) = 0$ in equation (3.140)), the surface shortwave flux is excluded from

the flux convergence computed in `ocean_shortwave.F90` (equation (3.137)) in order to avoid double counting. The diagnostic `sw_heat` from `ocean_shortwave.F90` will thus have a negative flux convergence in the surface grid cell, since this convergence is computed with a zero flux crossing the top of the surface grid cell.

- **TOTAL IMPACTS OF SHORTWAVE RADIATION:** Assuming the traditional MOM approach whereby surface shortwave flux $I_{0-}(x, y)$ is included in the `ocean_core/ocean_sbc.F90` module ($I(\eta) = 0$ in equation (3.140)), to diagnose the full impacts of shortwave radiation requires the sum of two terms

$$\text{net shortwave radiation heating at } k = 1 = \text{swflx} + \text{sw_heat}(k = 1). \quad (3.141)$$

$$\text{net shortwave radiation heating at } k > 1 = \text{sw_heat}(k > 1). \quad (3.142)$$

3.15 Icebergs

As for the ESM2M simulations from [Dunne et al. \(2012\)](#), the CM2-O simulations make use of the iceberg model of [Martin and Adcroft \(2010\)](#). This model allows for the transport of calving land ice by the ocean currents, thus transporting freshwater away from the land-sea boundary. The [Martin and Adcroft \(2010\)](#) iceberg model, however, does not consider any impacts on albedos or on ocean currents. That is, the icebergs are passive Lagrangian particles floating on the ocean, impacted by ocean currents, gradients in sea level, and the Coriolis force. Their key role is in transporting land ice away from the land-sea boundary to allow for it to melt during this transport. Figure 3.15 illustrates this effect from the CM2-O suite, where we display the annual mean latent heat of fusion provided by the liquid ocean to melt icebergs.

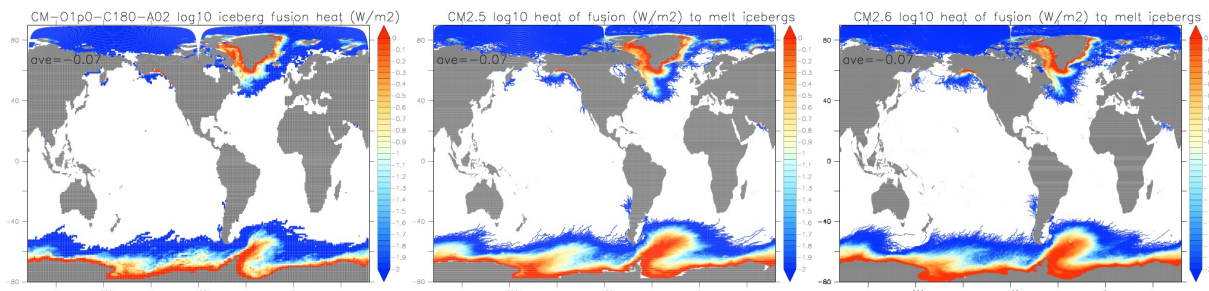


Figure 3.15: The \log_{10} of time mean (years 101-140) heat of fusion in the CM2-O suite given by the ocean to melt icebergs (heat loss for the ocean). This figure illustrates the effects of iceberg transport moving the calving land ice away from the land-sea boundary. Note the icebergs in the Arabian Sea are an artefact of the land model routing scheme, taking melting Himalayan glaciers into the ocean.

Budgets and transport

Mechanistic questions about how the ocean works can be answered, at least in part, by considering how various physical processes contribute to the budget for fields such as heat, salt, buoyancy, kinetic energy, momentum, and vorticity. This part, we present budgets for mass and tracers, starting from the formulations presented in Chapter 1. As part of a various budget analyses, one also asks questions about the transport of the associated fields by ocean currents, such as the poleward transport of heat or the mass transport through straits. We thus consider how to measure such transport in ocean models.

Seawater mass budget and transport

Contents

4.1	Mass crossing the ocean surface boundary	96
4.1.1	Air-sea mass fluxes	96
4.1.2	Land-sea and ice-sea mass fluxes	96
4.2	Global ocean mass budget	99
4.3	Seawater mass budget for a tracer grid cell	101
4.3.1	Semi-discrete mass budget for tracer grid cells	101
4.3.2	Finite volume expressions for the grid cell budget	102
4.4	Subgrid scale mass transport in ocean interior	102
4.5	MOM5 diagnostics for mass transport	103
4.6	Barotropic quasi-streamfunction	104
4.6.1	Vertically integrated transport	104
4.6.2	Barotropic quasi-streamfunction in the CM2-O suite	105
4.7	Mass transport through straits	106
4.7.1	The WGOMD-CMIP5 transports	106
4.7.2	Strait locations on the CM2-O ocean model grids	108
4.7.3	Sample time series from CM2-O simulations	108
4.8	Meridional overturning circulation	108
4.8.1	Formulation of the overturning streamfunction	110
4.8.2	A diagnostic expression for Ψ	111
4.8.3	Transport beneath an arbitrary surface	112
4.8.4	Overturning streamfunction from eddy-induced advection	113
4.8.5	Diagnosing the streamfunction in Ferret from MOM output	113
4.8.6	Global overturning streamfunction	114
4.8.7	Atlantic-Arctic overturning streamfunction	116
4.8.8	Atlantic meridional overturning circulation index	117
4.8.9	Indian-Pacific overturning streamfunction	117

As introduced in Section 1.1, the mass of a seawater parcel is conserved as it moves through the ocean. Upon encountering boundaries, the ocean mass can change through the exchange of fresh water and trace constituents with other components of the earth system. For example, freshwater is exchanged with the atmosphere as it enters through precipitation and leaves via evaporation. Freshwater and trace constituents also pass into the ocean through the flow of rivers, which generally enter at a nonzero depth. Mass also enters the ocean via the melting of sea ice and calving land ice that is generally transported

as icebergs (Section 3.15). Upon entering the ocean, ocean currents transport seawater mass, as well as other tracers such as heat, salt, and further material constituents. Establishing methods for analyzing mass balances and mass transport is useful on its own, in order to develop and understanding of the how the ocean “plumbing” works. It is also an important step towards developing the more complex analysis of heat and tracer transport.

In this chapter, we detail methods to diagnose the seawater mass budget and transport in an ocean model, with the ocean model in CM2-O providing us with working examples. As the CM2-O ocean model component is configured with the volume conserving Boussinesq approximation (see Section 1.10), the mass budget reduces to a volume budget, in which case seawater mass is equivalent to seawater volume multiplied by the constant reference density, $\rho_0 = 1035 \text{ kg m}^{-3}$. However, for generality, we formulate budgets for mass conserving non-Boussinesq fluids. The specialization to the Boussinesq case is trivially made by replacing appearances of *in situ* density, ρ , with reference density, ρ_0 .

4.1 Mass crossing the ocean surface boundary

We start our analysis of ocean mass budgets and transport by presenting maps of the mass crossing the ocean surface boundary, with Figure 4.1 presenting the net mass flux from all contributions.

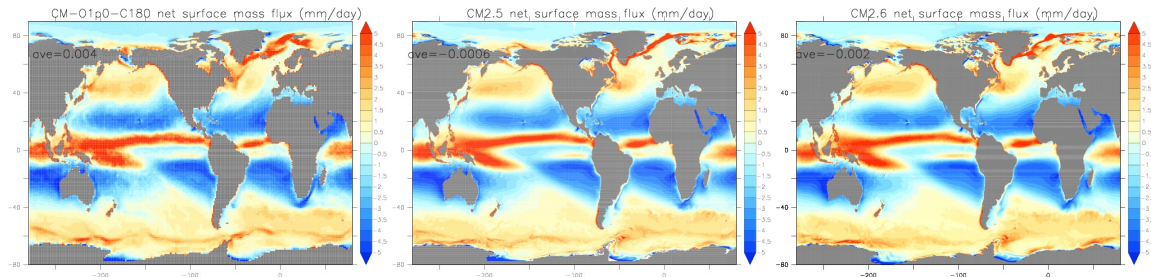


Figure 4.1: Maps of the time mean (years 101-140) net mass flux crossing the ocean surface boundary. Positive values mean mass enters the ocean. The units are mm day^{-1} , which is computed by dividing the surface mass flux in units of $\text{kg m}^{-2} \text{ s}^{-1}$ by the density $\rho_{\text{fresh}} = 1000 \text{ kg m}^{-3}$ of freshwater and then converting seconds to day. Note that the area factor is that of the ocean surface, so that multiplication of these maps by the surface area of an ocean grid cell and by the density of fresh water leads to the mass per time of water crossing the ocean surface. The global mean for the field is noted in the upper left of the map.

4.1.1 Air-sea mass fluxes

Figures 4.2 exhibits the mass flux arising from exchange across the air-sea interface arising from evaporation (mass leaves the ocean) and precipitation (liquid and frozen mass entering the ocean).

4.1.2 Land-sea and ice-sea mass fluxes

Figure 4.3 shows the mass flux arising from liquid river runoff, solid calving land ice that is transported as part of the iceberg model (Section 3.15), and sea ice melting (adds liquid to the ocean) or formation (removes liquid from the ocean).

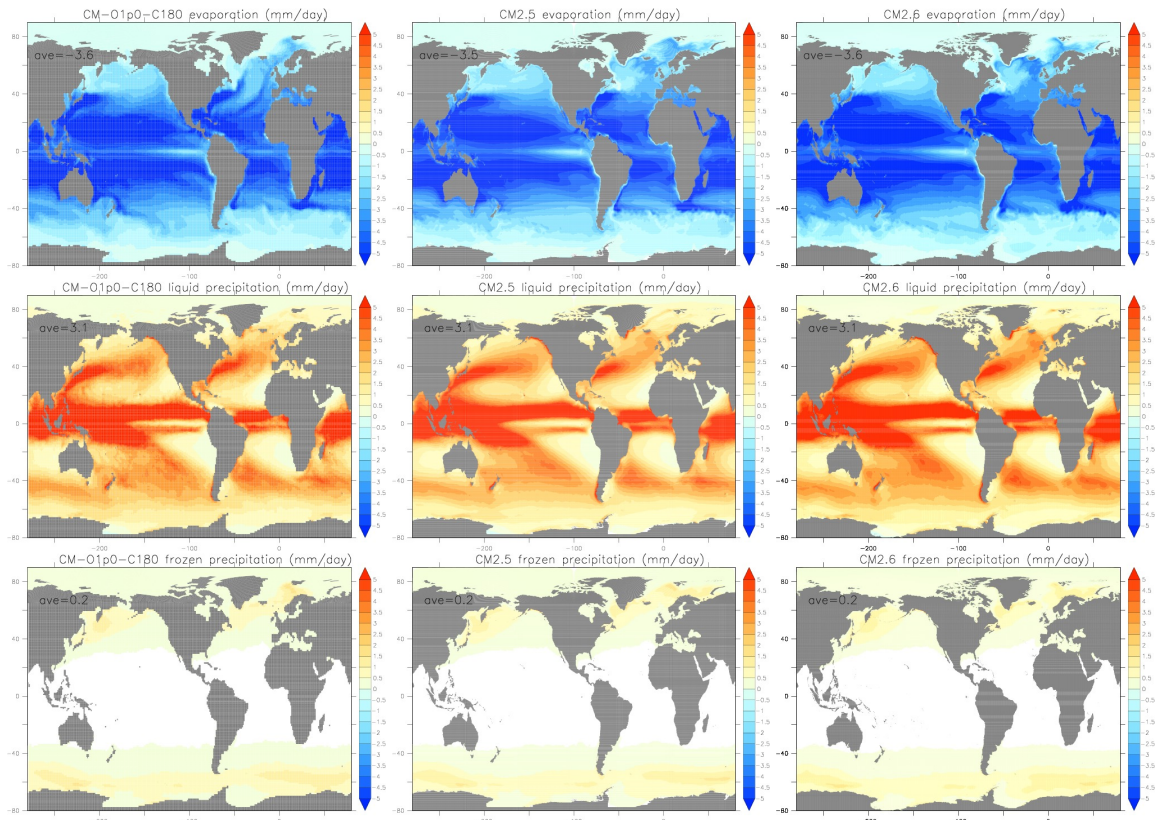


Figure 4.2: Maps of the time mean (years 101-140) mass flux crossing the ocean surface boundary through the air-sea interface from evaporation, liquid precipitation, and frozen precipitation. Positive values mean mass enters the ocean. The units are mm day^{-1} , which is computed by dividing the surface mass flux in units of $\text{kg m}^{-2} \text{s}^{-1}$ by the density $\rho_{\text{fresh}} = 1000 \text{ kg m}^{-3}$ of freshwater and then converting seconds to day. Note that the area factor is that of the ocean surface, so that multiplication of these maps by the surface area of an ocean grid cell and by the density of fresh water leads to the mass per time of water crossing the ocean surface. The global mean for the field is noted in the upper left of the map.

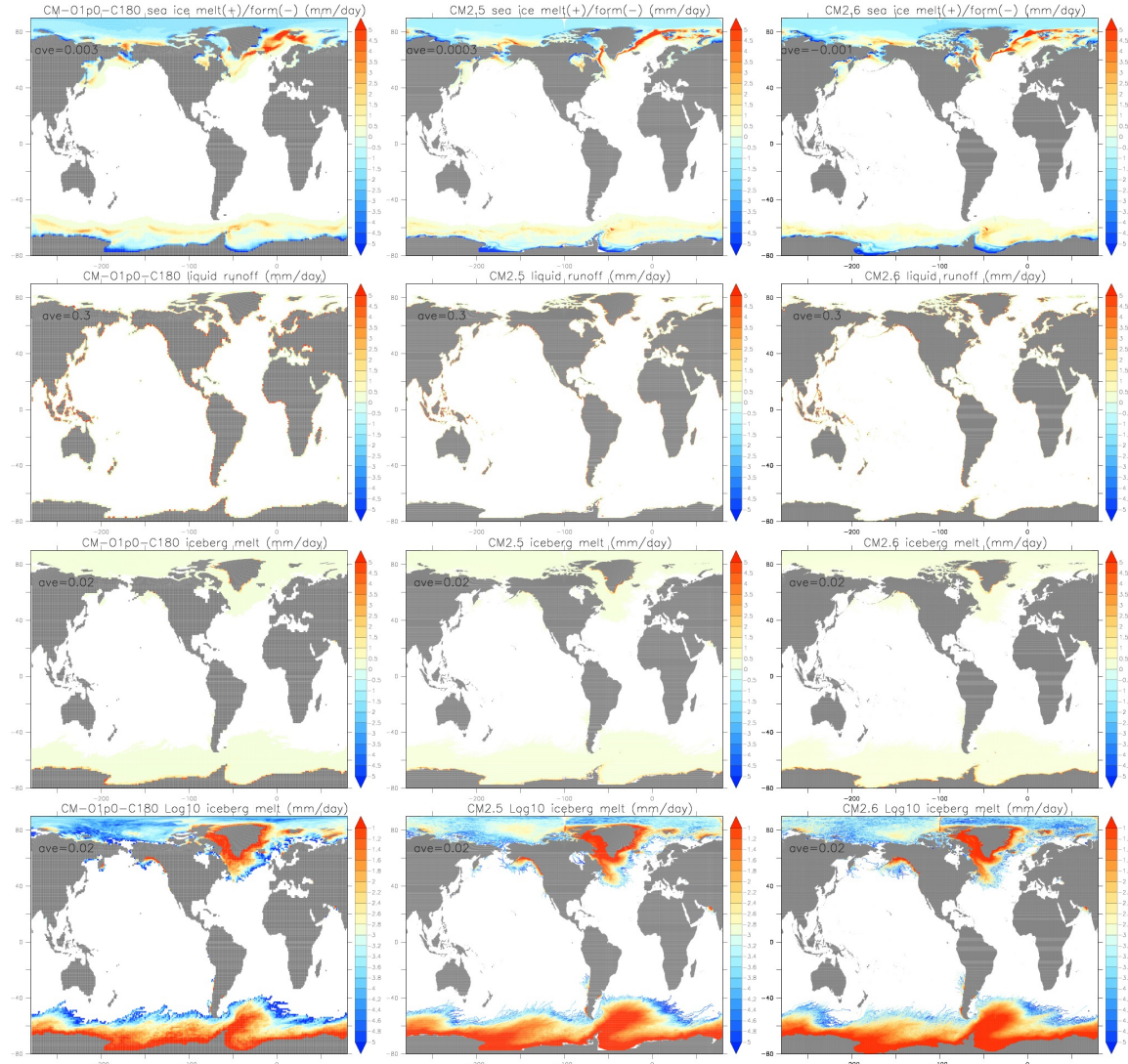


Figure 4.3: Maps of the time mean (years 101-140) mass flux crossing the surface boundary. The units are mm day^{-1} , which is computed by dividing the surface mass flux in units of $\text{kg m}^{-2} \text{s}^{-1}$ by the density $\rho_{\text{fresh}} = 1000 \text{ kg m}^{-3}$ of freshwater and then converting seconds to day. Positive values mean mass enters the ocean. The area factor is that of the ocean surface, so that multiplication of these maps by the surface area of an ocean grid cell and by the density of fresh water leads to the mass per time of water crossing the ocean surface. The global mean for the field is noted in the upper left of the map. Note the second row of the iceberg melt panels exhibits the \log_{10} to highlight the transport away from the boundaries. The log figure exposes a problem with the icebergs associated with the coordinate fold across the Arctic bipolar cap.

4.2 Global ocean mass budget

The mass of seawater in the global ocean is altered through exchanges with other components of the climate system. For a Boussinesq fluid, as used in the ocean component of the CM2-O suite of models, we are concerned with the ocean volume. Evolution of the global mean sea surface height then reflects on changes in the net ocean volume.

We formulate the above by considering the evolution equation for the Boussinesq sea level, in which case the model's prognostic sea level, η^B , evolves according to

$$\rho_o \left(\frac{\partial \eta^B}{\partial t} \right) = -\rho_o \nabla \cdot \mathbf{U} + Q^{\text{mass}}, \quad (4.1)$$

where Q^{mass} is the mass flux of water crossing the ocean surface, and

$$\mathbf{U} = \int_{-H}^{\eta^B} \mathbf{u} dz \quad (4.2)$$

is the depth integrated horizontal velocity. Since $\nabla \cdot \mathbf{U}$ vanishes when integrating globally, the global area average surface height, $\bar{\eta}^B$, satisfies the budget

$$\rho_o \left(\frac{\partial \bar{\eta}^B}{\partial t} \right) = \overline{Q^{\text{mass}}}. \quad (4.3)$$

The global area average of a field, such as the surface height, is computed by

$$\bar{\eta}^B = \frac{\int \eta^B dA}{\mathcal{A}}, \quad (4.4)$$

with

$$\mathcal{A} = \int dA = \int dx dy \quad (4.5)$$

the global wet ocean surface area. For brevity in subsequent sections, we drop the superscript on the sea surface height, since the CM2-O suite uses a Boussinesq ocean

$$\eta^B = \eta. \quad (4.6)$$

Figure 4.4 shows the global mean effective sea level in the CM2-O suite, along with the net mass flux crossing the surface boundary. We define the effective sea level according to

$$\eta_{\text{eff}} = \eta + \frac{p_a}{g \rho_o}, \quad (4.7)$$

where η is the surface height for the liquid ocean (i.e., the result of solving the ocean free surface equation), and p_a is the applied pressure at the ocean surface. In the CM2-O suite, the atmospheric pressure is *not* applied to the ocean surface. However, sea ice presses down on the ocean surface according to the inverse barometer (see Appendix C.2 in Griffies and Greatbatch (2012)). Adding back in the pressure, normalized by the gravitational acceleration and the Boussinesq reference density, removes the ice depression, rendering a sea level relevant for, say, coastal applications. The global effective sea level in each simulation remains relatively stationary, although offset from one another. The offset is of no consequence dynamically, and it arises from a slight difference in net amount of water in the coupled models.

The global net mass flux crossing the ocean surface is determined by

$$\text{surface mass transfer} = \text{precipitation} - \text{evaporation} + \text{liquid runoff} + \text{solid calving} + \text{sea ice melt}. \quad (4.8)$$

The net mass transfer crossing the ocean interface is shown in the middle panel of Figure 4.4. Each model shows a net transfer close to zero, so that the net water crossing the ocean interface is close to zero on

annual time scales. However, CM2.6 shows a systematic decrease in net water passed to the liquid ocean, as revealed by plotting the running integral

$$\overline{\eta_{\text{eff}}}(\tau) = \overline{\eta_{\text{eff}}}(\tau = 0) + \frac{\Delta\tau}{\rho_o} \sum_{\tau} \overline{Q^{\text{mass}}} \quad (4.9)$$

in the third panel to Figure 4.4, where $\Delta\tau = 1$ year for the annual mean data. The trend in the accumulated water entering the CM2.6 ocean is associated with a reduction in melting sea ice entering the ocean. However, time series for the net mass of sea ice in CM2.6 reveals no systematic trend of increasing mass. So there is a mystery as to why the ocean model has a negative trend in surface mass transport, yet neither the effective sea level nor the sea ice mass show an associated trend.

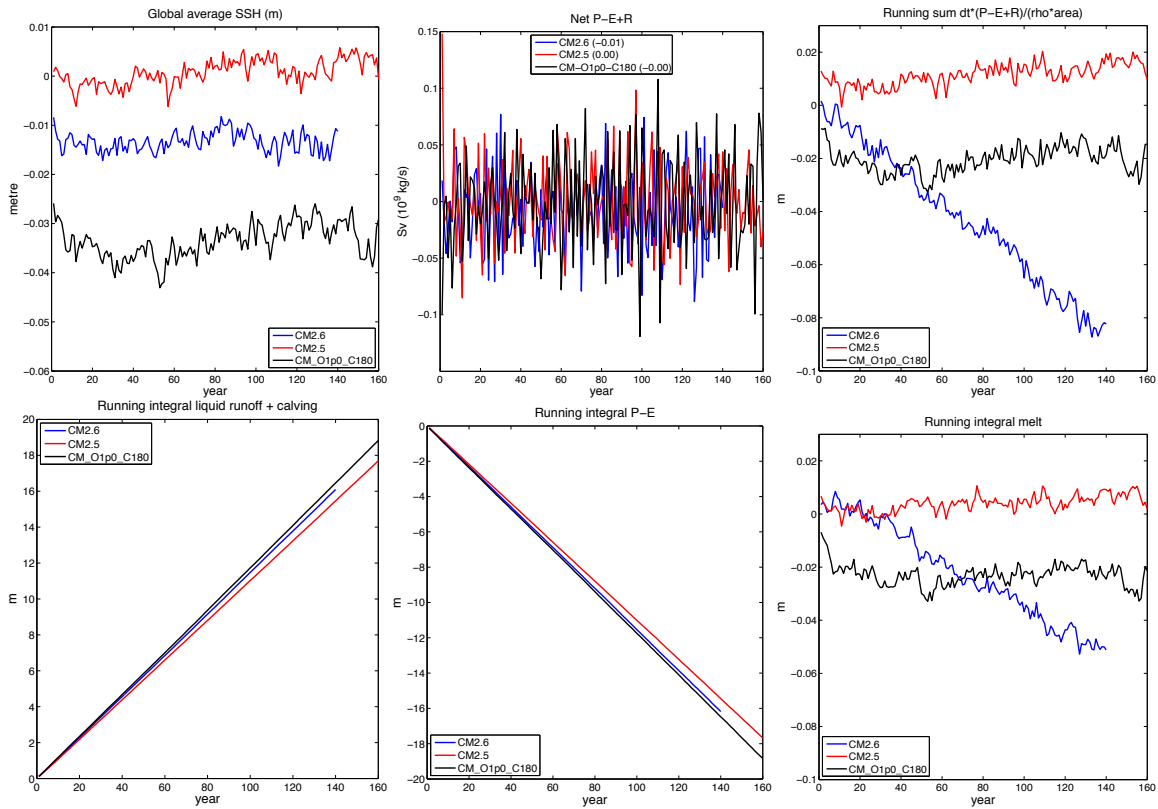


Figure 4.4: Annual mean time series for global mean SSH, global integrated surface boundary water mass flux, and running integral of the net boundary mass flux. These time series are computed by enabling the diagnostic table entries `eta_global`, `total_ocean_pme_river`, `total_ocean_melt`, `total_ocean_runoff`, `total_ocean_calving`, `total_ocean_evap`, `total_ocean_fprec`, and `total_ocean_lprec`. The black line is for CM_O1.0_C180, the red line is for CM2.5, and the blue line is for CM2.6. The second row presents the following running sums for global mean annual mean fields: Left panel: liquid river runoff plus solid calving land ice entering the ocean; Middle panel: precipitation minus evaporation; Right panel: sea ice melt. We see that the drift in the CM2.6 simulation is related to drift in the melt of sea ice towards reduced melt, leading to an increase in water contained in the sea ice field, in turn reducing the amount of precipitation reaching the liquid ocean.

4.3 Seawater mass budget for a tracer grid cell

In Section 1.6, we formulated the semi-discrete budget for seawater mass per unit horizontal area within a MOM tracer grid cell. We revisit the results of that formulation here, and express the mass budget in a form suitable for analysis.

4.3.1 Semi-discrete mass budget for tracer grid cells

The formulation from Section 1.6 renders the following budget for mass within a surface, interior, and bottom grid cell, where we assume no mass transport through the solid-earth

$$\text{surface} \quad \partial_t(\rho dz) = -\nabla_s \cdot (\mathbf{u} \rho dz) + (\rho w^{(z)})_{s=s_{k=1}} + Q_m + \mathcal{S}^{(M)} \rho dz \quad (4.10a)$$

$$\text{interior} \quad \partial_t(\rho dz) = -\nabla_s \cdot (\mathbf{u} \rho dz) - (\rho w^{(z)})_{s=s_{k-1}} + (\rho w^{(z)})_{s=s_k} + \mathcal{S}^{(M)} \rho dz \quad (4.10b)$$

$$\text{bottom} \quad \partial_t(\rho dz) = -\nabla_s \cdot (\mathbf{u} \rho dz) - (\rho w^{(z)})_{s=s_{k+1}} + \mathcal{S}^{(M)} \rho dz. \quad (4.10c)$$

To remain self-contained, we summarize the symbols in these equations, which were originally introduced in Chapter 1.

- ρdz (units of kg m^{-2}) is the mass per unit horizontal area in a grid cell, with dz the thickness and ρ the *in situ* density. Again, for the Boussinesq case used in CM2-O, we set ρ to the constant ρ_0 in these equations. However, it is important to note that the thickness of a grid cell is generally time dependent, as for the z^* vertical coordinate used in CM2-O (see equation (4.12)).
- The vertical velocity component (units of m s^{-1})

$$w^{(z)} = \left(\frac{\partial z}{\partial s} \right) \frac{ds}{dt} \quad (4.11)$$

is the transport through the generalized vertical coordinate surface s . The convention is that $w^{(z)}_{s=s_k}$ is the vertical transport through the lower face of the grid cell with vertical label k , so that $w^{(z)}_{s=s_{k-1}}$ is the vertical transport through the upper face of cell k . As detailed in Section 2.3, the CM2-O suite uses the generalized level coordinate

$$s = z^* = H \left(\frac{z - \eta}{\eta + H} \right), \quad (4.12)$$

where $z = \eta(x, y, t)$ is the ocean free surface deviation from $z = 0$, and $z = -H(x, y)$ measures the distance from $z = 0$ to the ocean bottom topography.

- Q_m is the flux (units of $\text{kg m}^{-2} \text{s}^{-1}$) of mass crossing the ocean surface, generally arising from precipitation, evaporation, runoff, and melt.
- $\mathcal{S}^{(M)} \rho dz$ (units of $\text{kg m}^{-2} \text{s}^{-1}$) is an interior mass source, which is typically zero except for those cases where mass is transferred from one interior point to another due to unresolved processes, such as cross-land mixing present in the one-degree model CM_O1.0_C180.
- Note the absence of any subgrid scale terms on the right hand side. The reason is that the eddy transport, as parameterized by Gent et al. (1995) for the mesoscale and Fox-Kemper et al. (2011) for the submesoscale, do not contribute to a net mass convergence onto any region.

4.3.2 Finite volume expressions for the grid cell budget

Use of Gauss' Law and an associated finite volume interpretation of the discrete model variables leads to the continuous-time/discrete-space seawater budget for a tracer grid cell

$$\text{surface} \quad \partial_t \mathcal{M} = -\delta_i T^x - \delta_j T^y + (T^z)_{k=1} + Q_m dA + S^{(M)} \mathcal{M} \quad (4.13a)$$

$$\text{interior} \quad \partial_t \mathcal{M} = -\delta_i T^x - \delta_j T^y - \delta_k T^z + S^{(M)} \mathcal{M} \quad (4.13b)$$

$$\text{bottom} \quad \partial_t \mathcal{M} = -\delta_i T^x - \delta_j T^y - (T^z)_{k=kmt-1} + S^{(M)} \mathcal{M}, \quad (4.13c)$$

where

$$dV = dx dy dz \quad (4.14)$$

is the volume of a tracer grid cell,

$$\mathcal{M} = \rho dV \quad (4.15)$$

is the tracer cell mass, and

$$dA = dx dy \quad (4.16)$$

is the horizontal area of the cell. We also introduced the mass transports crossing the face of a tracer cell¹

$$T^x = u \rho dz dy \quad (4.17a)$$

$$T^y = v \rho dz dx \quad (4.17b)$$

$$T^z = w \rho dx dy. \quad (4.17c)$$

We expose discrete labels only when necessary, and use the discrete notation $(T^x)_i$ to denote mass transport through the east face of a tracer cell, $(T^y)_j$ for mass transport through the north cell face, and $(T^z)_k$ for mass transport through the bottom face. Hence, the discrete difference operators are given by

$$\delta_i T^x = (T^x)_i - (T^x)_{i-1} \quad (4.18a)$$

$$\delta_j T^y = (T^y)_j - (T^y)_{j-1} \quad (4.18b)$$

$$\delta_k T^z = (T^z)_{k-1} - (T^z)_k \quad (4.18c)$$

4.4 Subgrid scale mass transport in ocean interior

Parameterized subgrid scale advection, such as from Gent et al. (1995) for the mesoscale or Fox-Kemper et al. (2008) for the submesoscale, introduces zero mass to a grid cell. Hence, it satisfies the balance

$$0 = -\delta_i T^{*x} - \delta_j T^{*y} + (T^{*z})_{k=1} \quad (4.19a)$$

$$0 = -\delta_i T^{*x} - \delta_j T^{*y} - \delta_k T^{*z} \quad (4.19b)$$

$$0 = -\delta_i T^{*x} - \delta_j T^{*y} - (T^{*z})_{k=kmt-1}, \quad (4.19c)$$

where

$$T^{*x} = u^* \rho dz dy \quad (4.20a)$$

$$T^{*y} = v^* \rho dz dx \quad (4.20b)$$

$$T^{*z} = w^* \rho dx dy \quad (4.20c)$$

are components to the mass transport arising from subgrid scale processes. As a result of introducing zero mass to each grid cell, the subgrid scale mass transport introduces zero mass over a full ocean column,

¹We omit horizontal staggering in these equations for brevity. Staggering is handled using B-grid prognostic horizontal velocity components (u, v), and C-grid mass transports.

so that the transport satisfies the column integrated constraints

$$\delta_i \left(\sum_{k=1}^{k=kmt} T^{*x} \right) + \delta_j \left(\sum_{k=1}^{k=kmt} T^{*y} \right) = 0 \quad (4.21a)$$

$$\sum_{k=1}^{k=kmt} T^{*z} = 0. \quad (4.21b)$$

In fact, to maintain these constraints for a general land-sea configuration requires the more stringent constraints

$$\sum_{k=1}^{k=kmt} T^{*x} = 0 \quad (4.22a)$$

$$\sum_{k=1}^{k=kmt} T^{*y} = 0 \quad (4.22b)$$

$$\sum_{k=1}^{k=kmt} T^{*z} = 0, \quad (4.22c)$$

which are indeed maintained by [Gent et al. \(1995\)](#) and [Fox-Kemper et al. \(2008\)](#). Hence, when measuring the vertically integrated mass transport (Sections 4.7 and 4.6), contributions from subgrid scale transport vanish. Hence, an overturning circulation associated with subgrid scale transport is fully closed (Section 4.8). That is, horizontal mass transport from subgrid scale processes that moves into a region is balanced by transport leaving the region at other depths.

4.5 MOM5 diagnostics for mass transport

The MOM5 diagnostic for mass transport by the resolved flow field is given by

$$T^x = tx_trans \quad (4.23a)$$

$$T^y = ty_trans \quad (4.23b)$$

$$T^z = tz_trans \quad (4.23c)$$

along with the vertical integrated transports of use to compute transports through choke points

$$\sum_k T^x = tx_trans_int_z \quad (4.24a)$$

$$\sum_k T^y = ty_trans_int_z. \quad (4.24b)$$

The analogous transports from the subgrid scale flow from [Gent et al. \(1995\)](#) are

$$T^{x-gm} = tx_trans_gm_adv \quad (4.25a)$$

$$T^{y-gm} = ty_trans_gm_adv \quad (4.25b)$$

$$T^{z-gm} = tz_trans_gm_adv \quad (4.25c)$$

and from [Fox-Kemper et al. \(2008\)](#) are

$$T^{x-submeso} = tx_trans_submeso_adv \quad (4.26a)$$

$$T^{y-submeso} = ty_trans_submeso_adv \quad (4.26b)$$

$$T^{z-submeso} = tz_trans_submeso_adv. \quad (4.26c)$$

Note that the suffix `adv` is present to distinguish from diagnostics computed according to the skew flux approach which is used for the parameterizations in CM2-O, and thus necessitates distinct diagnostics for computing the overturning (Section 4.8).

4.6 Barotropic quasi-streamfunction

When the vertically integrated transport is non-divergent, it may be described by a streamfunction, which is often termed the *barotropic streamfunction*. This situation generally holds for a Boussinesq rigid lid model in the absence of surface water fluxes. However, MOM5 is not a rigid lid model, so one requires both a streamfunction and stream potential to describe the vertically integrated transport. Nonetheless, for many purposes the vertically integrated transport is nearly non-divergent on annual and longer time scales, even in the presence of surface water fluxes. Hence, the *barotropic quasi-streamfunction* defined in the following is quite useful as an approximation to the vertically integrated transport.

4.6.1 Vertically integrated transport

The vertically integrated horizontal mass transport

$$\mathbf{U}^\rho = \int_{-H}^{\eta} \rho \mathbf{u} dz \quad (4.27)$$

generally has a non-zero divergence due to fluctuations of mass within the vertical column, as seen by the column integrated mass balance

$$\partial_t \left(\int_{-H}^{\eta} \rho dz \right) + \nabla \cdot \mathbf{U}^\rho = Q_m + \int_{-H}^{\eta} \rho S^{(M)} dz. \quad (4.28)$$

We ignore mass sources in the following, thus considering

$$\nabla \cdot \mathbf{U}^\rho = -\partial_t \left(\int_{-H}^{\eta} \rho dz \right) + Q_m. \quad (4.29)$$

The presence of a nonzero divergence requires both a streamfunction $\tilde{\psi}$ and a velocity potential χ

$$\mathbf{U}^\rho = \hat{\mathbf{z}} \wedge \nabla \tilde{\psi} + \nabla \chi. \quad (4.30)$$

Only for a Boussinesq rigid-lid model with zero boundary mass flux will χ vanish. Hence, to compute the precise vertically integrated mass transport passing between two points, a direct evaluation of the integral

$$T_{ab} = \int_a^b \hat{\mathbf{n}} \cdot \mathbf{U}^\rho dl \quad (4.31)$$

is given, which is just what has been prescribed for the choke point transports in Section 4.7. Although accurate and complete, this integral does not readily provide a horizontal map of transport, and so it loses much of the appeal associated with the barotropic transport streamfunction used with a rigid lid.

For many practical situations, maps of the function

$$\psi^{(U)}(x, y, t) = - \int_{y_0}^y U^\rho(x, y', t) dy' \quad (4.32)$$

are quite useful, where the lower limit y_0 is taken at the southern boundary of the domain, generally given by a solid wall along Antarctica for ocean climate models. By its definition, the meridional derivative of $\psi^{(U)}$ yields the zonal mass transport

$$\frac{\partial \psi^{(U)}}{\partial y} = U^\rho. \quad (4.33)$$

The zonal derivative, however, does not yield the meridional mass transport due to the divergent nature of the vertically integrated flow. It is for this reason that we denote $\psi^{(U)}$ a *barotropic quasi-streamfunction*.

Notably, for many cases, especially with long time averages, the divergence is small, thus allowing ψ to present a good indication of the path and intensity of the vertically integrated mass transport.

By construction, $\psi^{(U)}$ reduces to the transport streamfunction in the case of a rigid lid where $\nabla \cdot \mathbf{U} = 0$. However, this is not a unique choice and alternatives do exist. For example,

$$\psi^{(V)}(x, y, t) = \psi^{(U)}(x_o, y, t) + \int_{x_o}^x V^\rho(x', y, t) dx', \quad (4.34)$$

gives

$$\frac{\partial \psi^{(V)}}{\partial x} = V^\rho. \quad (4.35)$$

$\psi^{(V)}$ has the advantage that zonal derivatives give the exact meridional transport, yet the meridional derivative in general deviates from the zonal transport. Comparing maps of $\psi^{(U)}$ and $\psi^{(V)}$ reveals the degree to which the vertically integrated mass transport is non-divergent. For most purposes of climate modeling at GFDL, we map the streamfunction $\psi^{(U)} = -\int_{y_o}^y U^\rho dy'$, as deviations from $\psi^{(V)}$ are modest for most applications.

As mentioned in Section 4.4, the vertically integrated transport from both the Gent et al. (1995) mesoscale eddy closure and the submesoscale scheme of Fox-Kemper et al. (2008) vanish. Hence, the transport from these schemes add zero to the vertically integrated transport through any ocean column.

Finally, note that for the CM2.6 model in the CM2-O suite, the online diagnostic computation of $\psi^{(U)}$ and $\psi^{(V)}$ are problematic. We therefore must prescribe an offline calculation. The following approach is used in Ferret for this purpose.

```
let field  = tx_trans_int_z

let drake  = field[x=70w,y=80s:50s@sum]
let fieldA = if field then field else 0      ! to convert missing values to 0

let maskA  = if field ne 0 then 1 else 0
let maskB  = if field ne 0 then 1

let uhsum  = fieldA*maskA
let psiu   = -1*uhsum[ j=@rsum]*maskB + drake[1=1]*maskB
```

4.6.2 Barotropic quasi-streamfunction in the CM2-O suite

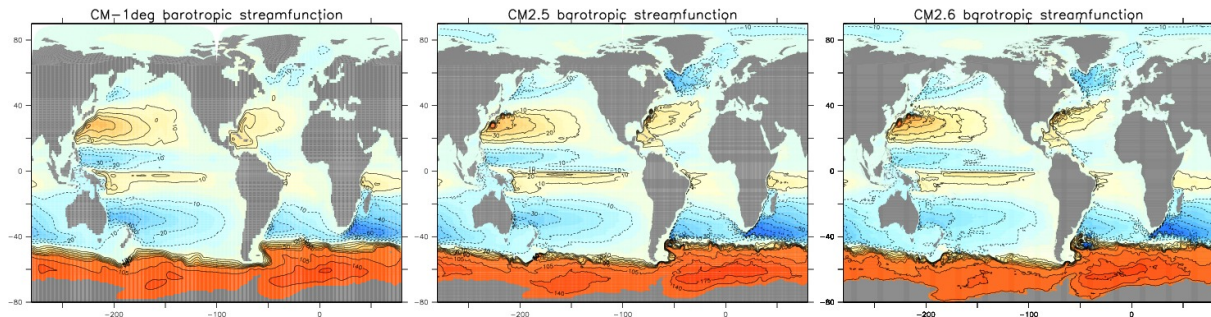


Figure 4.5: Barotropic quasi-streamfunction (Sv) for the CM2-O suite of models.

4.7 Mass transport through straits

We can measure mass transport by, for example, setting up devices to determine the flow of water between two fixed points. Monitoring such flows has occurred in various locations over many years, sometimes quasi-continuously but more often intermittently. Comparing these measurements with ocean model simulations provides a means to examine the integrity of the model “plumbing”. It is for this reason that the CLIVAR Working Group for Ocean Model Development (WGOMD) ([Griffies et al., 2009a](#)) recommended that certain of these transports be archived as part of the 5th Coupled Model Intercomparison Project ([Taylor et al., 2012](#)) model comparison. We exhibit the results from the CM2-O suite for a number of these recommended transport sections.

4.7.1 The WGOMD-CMIP5 transports

We detail here the geographic locations for the WGOMD-CMIP5 transports and provide references to observation-based measurements, where available.

1. **BARENTS OPENING:** The Barents Opening separates Spitsbergen from Norway. Vertically integrated transport through the Barents Opening occurs geographically roughly between the points

- BARENTS OPENING = $(16.8^\circ E, 76.5^\circ N)$ to $(19.2^\circ E, 70.2^\circ N)$.

Observational estimates range from 1.5-2.0 Sv northwards, with large variability, thus necessitating longer time series to get a zero order estimate.

2. **BERING STRAIT:** The Bering Strait separates Alaska from Siberia. Vertically integrated transport through the Bering Strait provides the only exchange between Pacific and Arctic waters. It is defined geographically from

- BERING STRAIT = $(171^\circ W, 66.2^\circ N)$ to $(166^\circ W, 65^\circ N)$.

An observational estimate from [Roach et al. \(1995\)](#) is 0.8Sv northward from the Pacific into the Arctic Ocean.

3. **CANADIAN ARCTIC ISLANDS:** The Canadian Archipelago refers to the wide range of Arctic islands in northern Canada. The transport through these islands connects waters of the open Arctic to the North Atlantic through the Davis Strait and into the Labrador Sea. Vertically integrated transport through the Canadian Archipelago can be defined according to the following geographic region

- CANADIAN ARCTIC ISLANDS = $(128.2^\circ W, 70.6^\circ N)$ to $(59.3^\circ W, 82.1^\circ N)$.

Observational estimates range from 0.7 to 2.0Sv southward ([Sadler, 1976](#); [Fissel et al., 1998](#); [Melling, 2000](#)).

4. **DAVIS STRAIT:** Although not part of the CMIP5 request, the Davis Strait is a useful section to record its transport. It separates Greenland from Baffin Island in Canada. We may take any convenient location for the Davis Strait transport, such as the constant latitude line

- DAVIS STRAIT = $(62^\circ W, 65^\circ N)$ to $(62^\circ W, 65^\circ N)$.

5. **DENMARK STRAIT:** The Denmark Strait separates Greenland from Iceland. Vertically integrated transport between Iceland and Greenland occurs over the following geographical region

- DENMARK STRAIT = $(37^\circ W, 66.1^\circ N)$ to $(22.5^\circ W, 66^\circ N)$.

Observational estimates are 0.8Sv for the net northward transport ([Osterhus et al., 2005](#)) and 3Sv for the net southward transport ([Olsen et al., 2008](#)).

6. **DRAKE PASSAGE:** The Drake Passage separates South America from Antarctica. It presents the narrowest constriction for the Antarctic Circumpolar Current. Vertically integrated transport in the Southern Ocean through the Drake Passage is determined by flow through the region

- DRAKE PASSAGE = $(68^{\circ}W, 54^{\circ}S)$ to $(60^{\circ}W, 64.7^{\circ}S)$.

An observational estimate from [Cunningham et al. \(2003\)](#) is an eastward transport of 135Sv.

7. **ENGLISH CHANNEL:** The English Channel separates Britain from the European continent. Vertically integrated transport in the English Channel occurs geographically through the region

- ENGLISH CHANNEL = $(1.5^{\circ}E, 51.1^{\circ}N)$ to $(1.7^{\circ}E, 51.0^{\circ}N)$.

Observational estimates from [Otto et al. \(1990\)](#) are roughly 0.1 – 0.2Sv northward.

8. **PACIFIC EQUATORIAL UNDERCURRENT:** A commonly used region to measure transport in the equatorial undercurrent is given by the region

- PACIFIC EQUATORIAL UNDERCURRENT = $(155^{\circ}W, 3^{\circ}S)$ to $(155^{\circ}W, 3^{\circ}N)$ over the depth range 0-350m.

Observational estimates range between 24Sv-36Sv in an eastward direction ([Lukas and Firing, 1984](#); [Sloyan et al., 2003](#)).

9. **FAROE-SCOTLAND CHANNEL:** The Faroe-Scotland Channel separates the Faroe Islands from Scotland. Vertically integrated transport between the Faroe Islands and Scotland occurs geographically through the region between

- FAROE-SCOTLAND CHANNEL = $(6.9^{\circ}W, 62^{\circ}N)$ to $(5^{\circ}W, 58.7^{\circ}N)$

Observational estimates are 3.8Sv for the net northward transport ([Osterhus et al., 2005](#)) and 2.1Sv for the net southward transport ([Olsen et al., 2008](#)).

10. **FLORIDA STRAIT:** The Florida Strait separates Florida from Cuba. It was not requested from CMIP5, but it is useful to measure its transport. We define this transport according to the following geographical locations

- FLORIDA STRAIT = $(80.9^{\circ}W, 23^{\circ}N)$ to $(80.9^{\circ}W, 24.9^{\circ}N)$.

11. **FLORIDA-BAHAMAS STRAIT:** Since 1982 cables have been used to measure the transport of the Florida Current between Florida and the Bahamas near 27N. We thus define this transport according to the following geographical locations

- FLORIDA-BAHAMAS STRAIT = $(78.5^{\circ}W, 26^{\circ}N)$ to $(80.5^{\circ}W, 27^{\circ}N)$.

Observational estimates range from 29Sv-35Sv ([Leaman et al., 1987](#)). Updated information is available from AOML at www.aoml.noaa.gov/phod/floridacurrent/. See also Figure 2-6 from the MERSEA project ([MERCATOR, 2006](#)).

12. **FRAM STRAIT:** The Fram Strait separates Spitsbergen from Greenland. Vertically integrated transport in the Fram Strait occurs geographically through the region

- FRAM STRAIT = $(11.5^{\circ}W, 81.3^{\circ}N)$ to $(10.5^{\circ}E, 79.6^{\circ}N)$.

Observational estimates from [Schauer et al. \(2004\)](#) are 4 ± 2 Sv southwards.

13. **ICELAND FAROE CHANNEL:** The Iceland Faroe Channel separates Iceland from the Faroe Islands. Vertically integrated transport between Iceland and the Faroe Islands occurs geographically through the region between

- ICELAND-FAROE CHANNEL = $(13.6^{\circ}W, 64.9^{\circ}N)$ to $(7.4^{\circ}W, 62.2^{\circ}N)$

Observational estimates are 3.8Sv for the net northward transport ([Osterhus et al., 2005](#)) and 1Sv for the net southward transport ([Olsen et al., 2008](#)).

14. **INDONESIAN THROUGHFLOW:** Vertically integrated transport through the Indonesian Archipelago is defined approximately by

- **INDONESIAN THROUGHFLOW** = $(100^{\circ}E, 6^{\circ}S)$ to $(140^{\circ}E, 6^{\circ}S)$.

An observational estimate from [Gordon et al. \(2003\)](#) is roughly 10Sv from the Pacific to the Indian Oceans.

15. **MOZAMBIQUE CHANNEL:** The Mozambique Channel separates Madagascar from the African continent. Vertically integrated transport through the Mozambique channel separating Madagascar from Southeast Africa is defined approximately by

- **MOZAMBIQUE CHANNEL** = $(39^{\circ}E, 16^{\circ}S)$ to $(45^{\circ}E, 18^{\circ}S)$.

16. **TAIWAN-LUZON STRAITS:** We ask here for the vertically integrated transport giving the combined inflow to the South China Sea through the Taiwan and Luzon straits. The value from observations is positive when entering the South China Sea, and [Yaremchuk et al. \(2009\)](#) present a review of observed values.

17. **WINDWARD PASSAGE:** The Windward Passage lies between the easternmost region of Cuba and the northwest of Haiti, and is defined approximately by

- **WINDWARD PASSAGE** = $(75^{\circ}W, 20.2^{\circ}N)$ to $(72.6^{\circ}W, 19.7^{\circ}N)$.

4.7.2 Strait locations on the CM2-O ocean model grids

For most of the above geographic openings, transports can be diagnosed by aligning an approximation to the section along a model grid axis, and thus identifying the (i,j) grid points that delimit the two ends to the section. In this case, it is straightforward to assign a positive sign to transports going in a pseudo-north or pseudo-east direction, and negative signs for the opposite direction. We use the term *pseudo* here as it refers to an orientation according to the model grid lines, which in general may not agree with geographical longitude and latitude lines. The only section that we cannot approximate in this manner is that which crosses the Canadian Archipelago. The difficulty with that section is that it crosses the bipolar fold ([Figure 2.2](#)), and we do not have analysis code to define a transport section across the fold. We thus omit this transport. Additionally, the one-degree model CM_O1.0.C180 does not have the English Channel or the Florida-Bahamas strait.

[Figure 4.6](#) shows a map of the transport sections as approximated for the three ocean model grids in the CM2-O suite. Note that we do not compute a transport across the Canadian Archipelago, as offline analysis has not been written to compute transport that crosses the bipolar fold on the [Murray \(1996\)](#) grid used in these models. Also note that the English Channel is not resolved by the one-degree ocean grid, so it is omitted.

4.7.3 Sample time series from CM2-O simulations

[Figure 4.7](#) shows the time series for annual mean mass transport through various of the sections listed in [Table 4.1](#). The steady decline in transport for the Drake Passage in CM2.6 is consistent with an absence of ventilation in the Weddell Sea. In contrast, the CM2.5 simulation appears to maintain a robust Drake Passage transport.

4.8 Meridional overturning circulation

A streamfunction can be defined for any non-divergent transport. For the zonally integrated mass transport, equations ([4.13a](#))–([4.13c](#)) indicate there is zero divergence if the zonal integral of the time tendency

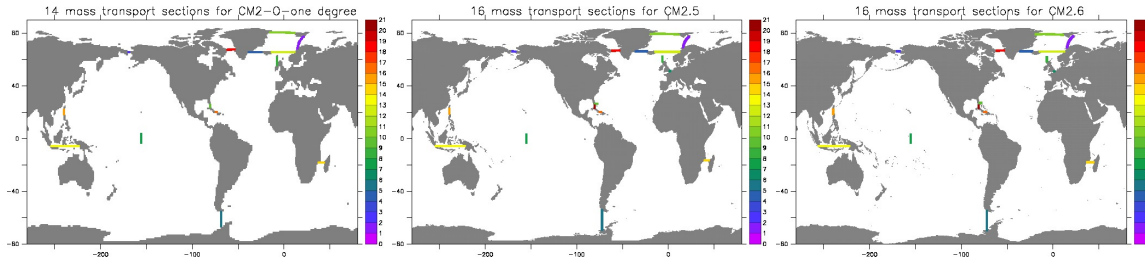


Figure 4.6: Maps of transport sections for the three ocean model grids in the CM2-O suite. These lines follow constant i-lines or j-lines on the model grid. The one-degree ocean grid omits the English Channel and Florida-Bahamas strait. The (i,j) values for the endpoints of these sections are provided in Table 4.1.

SECTION	CM_O1.0_C180	CM2.5	CM2.6
BARENTS OPENING	(295,189) (295,179)	(1183, 962) (1183, 876)	(2949,2435) (2949,2212)
BERING STRAIT	(111,176) (112,176)	(440, 844) (453, 844)	(1100,2135) (1130,2135)
CANADIAN ARCHIPELAGO	N/A	N/A	N/A
DAVIS STRAIT	(217,176) (229,176)	(875, 856) (908, 856)	(2188,2165) (2268,2165)
DENMARK STRAIT	(242,176) (256,176)	(978, 845) (1027, 845)	(2443,2137) (2571,2137)
DRAKE PASSAGE	(212,27) (212,16)	(831, 229) (831, 102)	(2081, 588) (2081, 272)
ENGLISH CHANNEL	N/A	(1126, 727) (1129, 727)	(2811,1839) (2817,1839)
PACIFIC EQUATORIAL UNDERCURRENT	(125,88) (125,105)	(500, 476) (500, 501)	(1250,1215) (1250,1276)
FAROE-SCOTLAND CHANNEL	(273,172) (273,166)	(1094, 808) (1094, 777)	(2732,2037) (2732,1967)
FLORIDA STRAIT	(200, 136) (200, 134)	(798, 592) (798, 583)	(1992,1503) (1992,1483)
FLORIDA-BAHAMAS STRAIT	N/A	(800, 598) (811, 598)	(2000,1526) (2016,1526)
FRAM STRAIT	(267, 191) (285, 191)	(1054, 970) (1143, 970)	(2634,2442) (2855,2442)
ICELAND FAROE CHANNEL	(267, 176) (272, 173)	(1066, 834) (1092, 808)	(2645,2090) (2727,2045)
INDONESIAN THROUGHFLOW	(27, 83) (57, 83)	(104, 466) (232, 466)	(248,1187) (583,1187)
MOZAMBIQUE CHANNEL	(318, 65) (324, 65)	(1279, 421) (1298, 421)	(3171,1062) (3240,1062)
TAIWAN-LUZON STRAITS	(41,132) (41, 128)	(164, 581) (164, 565)	(408,1470) (408,1435)
WINDWARD PASSAGE	(206, 130) (207, 130)	(820, 570) (826, 570)	(2052,1450) (2072,1450)

Table 4.1: Model grid (i,j) grid pairs that approximate the geographical points defining sections through which we measure seawater transport. The English Channel and Florida-Bahamas strait is not resolved by the one-degree grid, and so are omitted for this model. The Canadian Archipelago crosses the bipolar fold, and we do not have analysis code to handle this section, so it is omitted for all three models.

of mass vanishes, and there are no boundary fluxes or interior mass sources. Ignoring boundary fluxes and interior sources, a zero time tendency for mass in a cell arises if the top and bottom grid cell boundaries are set according to constant hydrostatic pressure surfaces, so that $\rho dz = -g^{-1} dp$. In this case, the mass within a cell is constant in time. Analogously, there is also a zero divergence of the volume transport for a Boussinesq fluid using geopotential vertical coordinates, in which case the volume of fluid in a cell is constant. In more general cases, however, there is no guarantee that the mass within a cell is constant. Additionally, in the presence of water crossing the ocean boundaries, mass will change, again leading to a nonzero divergence. Even with these caveats, the streamfunction defined below provides a very useful measure of the zonally integrated mass transport, thus motivating its near ubiquitous use as a model diagnostic.

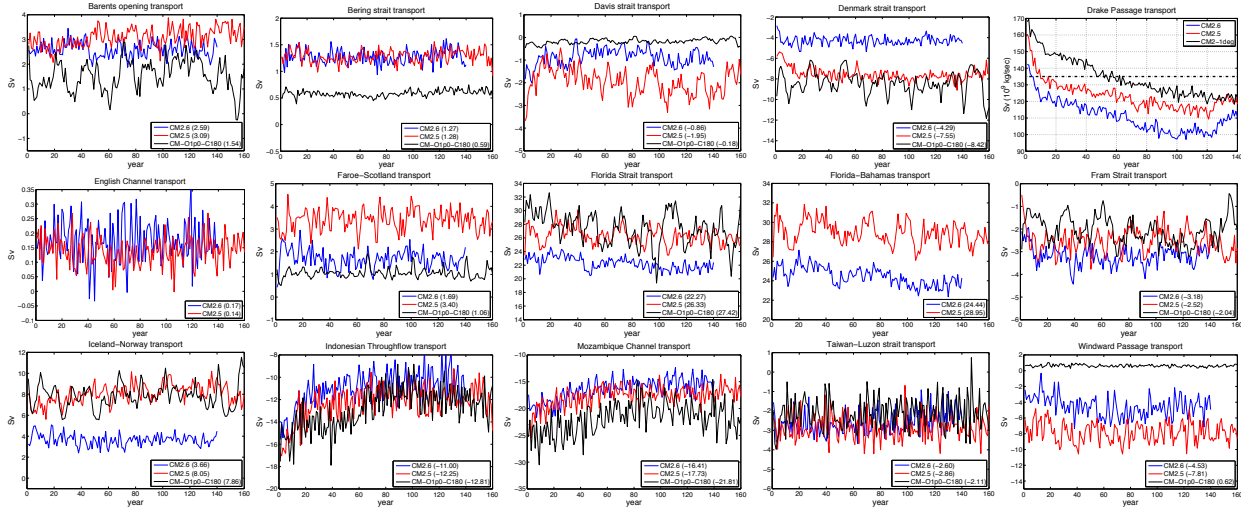


Figure 4.7: Time series for the annual mean mass transport through the CMIP5 straits as simulated in the CM2-O suite of models. These simulations are all based on 1990 radiative forcing. The time mean for each simulation is shown in the figure legend. A time mean is sensible for those transports that have reached a near steady-state, but not relevant for the Drake Passage transport as it has a centennial time scale for spin-up. The black line is for CM_O1.0_C180, the red line is for CM2.5, and the blue line is for CM2.6. Note that there is no value for the CM_O1.0_C180 transport through the Florida-Bahamas strait and English Channel, due to lack of grid resolution. Note the upturn in the Drake Passage transport for both CM2.5 and CM2.6 near year 120, with this fluctuation associated with increased ventilation in the Weddell Sea and associated retreat of sea ice.

4.8.1 Formulation of the overturning streamfunction

To formulate an expression for the vertical-meridional mass transport streamfunction, Ψ , we assume the zonally integrated flow is non-divergent, so that equations (4.13a)–(4.13c) take the form

$$\text{surface} \quad 0 = -\delta_j \mathcal{V} + \mathcal{W}_{k=1} \quad (4.36a)$$

$$\text{interior} \quad 0 = -\delta_j \mathcal{V} - \delta_k \mathcal{W} \quad (4.36b)$$

$$\text{bottom} \quad 0 = -\delta_j \mathcal{V} - \mathcal{W}_{k=k_{\text{mt}}-1}. \quad (4.36c)$$

In these equations, we dropped the zonal sum of the zonal transport by assuming either a periodic domain or solid zonal boundaries, and we wrote the zonally integrated meridional and vertical transport as

$$\mathcal{V} = \sum_i T^y \quad (4.37a)$$

$$\mathcal{W} = \sum_i T^z. \quad (4.37b)$$

We can combine the three equations (4.36a)–(4.36c) into a single equation by noting that the vertical transport is assumed to vanish at the top and bottom boundaries, so that

$$\delta_j \mathcal{V} + \delta_k \mathcal{W} = 0. \quad (4.38)$$

We now introduce a function Ψ according to²

$$\mathcal{V} = -\delta_k \Psi \quad (4.39a)$$

$$\mathcal{W} = \delta_j \Psi. \quad (4.39b)$$

To satisfy the non-divergent mass budget (4.36a)-(4.36c) requires that Ψ vanish at the top of the top cell and at the bottom topography. With these boundary conditions, the function Ψ is indeed a streamfunction for the non-divergent mass budget. The streamfunction has dimensions mass/time, with the oceanographically relevant unit given by the Sverdrup, where

$$1 \text{ Sv} = 10^9 \text{ kg sec}^{-1}. \quad (4.40)$$

4.8.2 A diagnostic expression for Ψ

A streamfunction describes the zonally integrated flow only when the flow is non-divergent. It is nonetheless conventional to call Ψ the meridional-depth overturning streamfunction even in the case of a divergent flow. We follow that nomenclature here. Recall a similar situation was encountered for the vertically integrated flow, where the barotropic quasi-streamfunction was introduced in Section 4.6, and found to be useful even when the vertically integrated flow is divergent.

The aim here is to determine a diagnostic expression for Ψ . We may start from either of the expressions (4.39a) or (4.39b). Integration and the use of boundary conditions then leads to two expressions for Ψ , with the expressions equivalent only if the zonally integrated mass transport is non-divergent. In many simulations, the meridional transport is more easily computed, and less noisy, than the vertical transport. It is thus conventional to make the specification $\mathcal{V} = -\delta_k \Psi$ the starting point. We consider two points before deriving the algorithm.

- From a finite volume perspective, the relation $\mathcal{V} = -\delta_k \Psi$ says that the discretized streamfunction should be computed at the top and bottom interfaces of grid cells, so that its vertical difference across the cells then leads to the meridional transport through the cell's vertical side walls, as shown in Figure 4.8. Correspondingly, the streamfunction is horizontally co-located with the meridional transport \mathcal{V} .³
- The relation $\mathcal{V} = -\delta_k \Psi$ remains valid if we modify Ψ by any function of horizontal position, since the vertical difference eliminates the arbitrary function.⁴ We choose to exploit this ambiguity by specifying the arbitrary function so that the streamfunction has a zero value at the ocean bottom. We are motivated to take this choice since for most oceanographic purposes, there is no mass transport considered between the liquid ocean and solid earth. Consequently, the solid earth boundary condition is time independent, and for convenience we specify that it vanishes.

Let us now develop an expression for the streamfunction by integrating the expression $\mathcal{V} = -\delta_k \Psi$ upwards starting from the ocean bottom. For the top surface of the bottom-most cell with $k = k_{\text{mt}}$, we have

$$\Psi_{k_{\text{mt}}-1} = 0 - \mathcal{V}_{k_{\text{mt}}}, \quad (4.41)$$

where $0 = \Psi_{k_{\text{mt}}}$ is inserted as a place-holder for the next iteration, and $\mathcal{V}_{k_{\text{mt}}}$ is the meridional transport leaving the vertical side walls within the bottom-most cell. For the next cell up in the column, we have

$$\begin{aligned} \Psi_{k_{\text{mt}}-2} &= \Psi_{k_{\text{mt}}-1} - \mathcal{V}_{k_{\text{mt}}-1} \\ &= -\mathcal{V}_{k_{\text{mt}}} - \mathcal{V}_{k_{\text{mt}}-1}. \end{aligned} \quad (4.42)$$

²This definition of Ψ has an associated sign convention, with the opposite convention just as valid mathematically, but chosen less frequently in practice.

³We are led to an alternative grid placement for Ψ if starting from the relation $\mathcal{W} = \delta_j \Psi$.

⁴This ambiguity represents a gauge symmetry, which can be exploited in whatever manner is most convenient.

Induction leads to the result

$$\begin{aligned}\Psi_k &= - \sum_{k=K+1}^{kmt} \mathcal{V}_k \\ &= - \sum_{k=K+1}^{kmt} \sum_i T^y.\end{aligned}\quad (4.43)$$

A continuous expression for the streamfunction is given by

$$\Psi(y, z, t) = - \int dx \int_{-H}^z v \rho dz'. \quad (4.44)$$

In the continuous expression, it is important to perform the vertical integral first, since the bottom topography $z = -H(x, y)$ is a function of horizontal position.

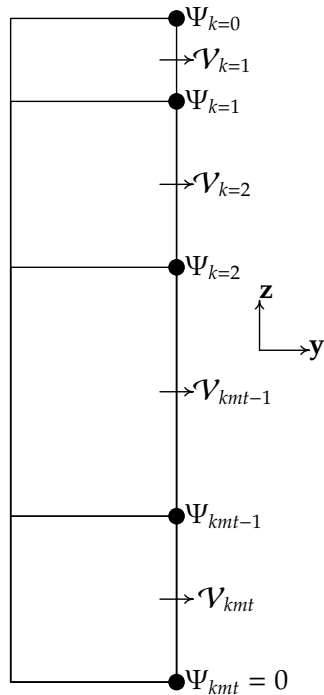


Figure 4.8: This figure illustrates the relation between the meridional-overturning streamfunction Ψ and the meridional transport \mathcal{V} , for the particular case of $kmt = 4$ vertical grid cells. The streamfunction is evaluated on the interfaces between the vertical cells, whereas the transport measures the mass leaving the cell in the meridional direction. The streamfunction vanishes at the bottom of the bottom-most cell, $\Psi_{kmt} = 0$, whereas it is generally nonzero at the top of the ocean for those cases where mass fluxes cross the ocean surface. Note the relatively thin bottom cell can arise from the use of bottom partial step representation of topography as used in MOM.

4.8.3 Transport beneath an arbitrary surface

We can extend the above considerations to the case of generalized vertical coordinates. In this case, we are concerned with the meridional transport of fluid beneath some generalized vertical coordinate surface.

It is a straightforward matter to extend the definition of the overturning streamfunction to this case, where

$$\Psi(y, s, t) = - \int_{x_a}^{x_b} dx \int_{s(-H)}^{s(z)} v \rho dz', \quad (4.45)$$

with $s = s(x, y, z, t)$ the generalized vertical coordinate (see Griffies (2004) for details). Surfaces that are physically of interest include various potential density surfaces, which are especially relevant when the flow is adiabatic.

4.8.4 Overturning streamfunction from eddy-induced advection

The mesoscale eddy parameterization of Gent and McWilliams (1990) and Gent et al. (1995) provides a volume transport in addition to the resolved scale Eulerian mean transport. The total meridional-overturning streamfunction takes the form

$$\Psi^{(tot)}(y, z, t) = - \int_{x_a}^{x_b} dx \int_{-H}^z (v + v^{gm}) \rho dz', \quad (4.46)$$

where

$$v^\dagger = v + v^{gm} \quad (4.47)$$

defines a residual-mean meridional velocity that contributes to the transport of mass and tracer. We consider now special cases for the eddy-induced velocity v^{gm} .

In the Boussinesq case as in CM2-O, the meridional eddy-induced velocity is given by

$$v^{gm} = - \left(\frac{\partial(\kappa S_y)}{\partial z} \right), \quad (4.48)$$

with S_y the neutral slope in the y -direction and $\kappa > 0$ a kinematic diffusivity. Performing the vertical integral on the GM90 piece leads to

$$\Psi^{(tot)}(y, z, t) = \Psi(y, z, t) + \Psi^{gm}(y, z, t) \quad (4.49)$$

where

$$\Psi^{gm}(y, z, t) = \rho_0 \int_{x_a}^{x_b} (\kappa S_y) dx, \quad (4.50)$$

with $\kappa S_y = 0$ at $z = -H$, and ρ_0 the reference density for the Boussinesq fluid. Hence, the Gent et al. (1995) parameterization adds a contribution that scales linearly with basin size, isopynical slope, and diffusivity

$$\Psi^{gm} \sim \rho_0 L S \kappa. \quad (4.51)$$

As an example, let $\kappa = 10^3 \text{ m}^2 \text{s}^{-1}$, $S = 10^{-3}$, and $L = 10^7 \text{ m}$, which yields $T \approx 10 \text{ Sv}$. Such transport can represent a nontrivial addition to that from the resolved scale velocity field.

4.8.5 Diagnosing the streamfunction in Ferret from MOM output

In MOM, there are two diagnostics computed on-line that should be saved in order to determine an accurate expression for the streamfunction when using a mesoscale eddy parameterization:

$$ty_trans = dx(v \rho dz) \quad (4.52)$$

$$ty_trans_gm = dx(\rho \kappa S_y) \quad (4.53)$$

Computing the Eulerian streamfunction (4.44) requires the following operations

$$\begin{aligned}
 \Psi(y, z, t) &= - \int_{x_a}^{x_b} dx \int_{-H}^z v \rho dz' \\
 &= - \int_{x_a}^{x_b} dx \int_{-H}^{\eta} v \rho dz' + \int_{x_a}^{x_b} dx \int_z^{\eta} v \rho dz' \\
 &= -\text{ty_trans}[i=@sum, k=@sum] + \text{ty_trans}[i=@sum, k=@rsum].
 \end{aligned} \tag{4.54}$$

We must compute the streamfunction in this manner since Ferret's relative sum $k=@rsum$ starts from an assumed zero value at the surface and integrates downward, whereas the streamfunction has a zero boundary condition on the ocean bottom. Hence, without subtracting the term $\text{ty_trans}[i=@sum, k=@sum]$, the diagnosed streamfunction will incorrectly have nonzero values at the bottom. A nonzero value for $\text{ty_trans}[i=@sum, k=@sum]$ arises from net vertically integrated mass transport through a section. For a rigid lid model, this net transport vanishes. However, for a model with real water fluxes, this net transport will generally be nonzero.

The GM-streamfunction is simpler to compute, whereby

$$\Psi^{\text{gm}}(y, z, t) = \text{ty_trans_gm}[i=@sum]. \tag{4.55}$$

There is no vertical sum, since the vertical integral has already been performed analytically (equations (4.50)). In particular, $\Psi^{\text{gm}}(y, z, t)$ in the ocean surface cell equals $\text{ty_trans_gm}[i=@sum, k=1]$. Since the vertical integral of the GM-streamfunction vanishes, $\text{ty_trans_gm}[i=@sum, k=0]$ is zero, by definition, although this level is not explicitly saved in the output.

In a similar manner, the streamfunction from a skew flux implementation of the submesoscale eddy parameterization of [Fox-Kemper et al. \(2008\)](#) and [Fox-Kemper et al. \(2011\)](#) (see Section 3.12) is computed as

$$\Psi^{\text{submeso}}(y, z, t) = \text{ty_trans_submeso}[i=@sum]. \tag{4.56}$$

There is no vertical sum required, since the vertical integral has already been performed analytically just as for the GM-streamfunction above. Furthermore, as for the GM-streamfunction, the submesoscale transport vanishes when integrated over the full ocean depth, so that $\text{ty_trans_submeso}[i=@sum, k=0]$ is zero, by definition, although this level is not explicitly saved in the output.

4.8.6 Global overturning streamfunction

Figure 4.9 shows the time mean overturning streamfunction from the CM2-O suite.

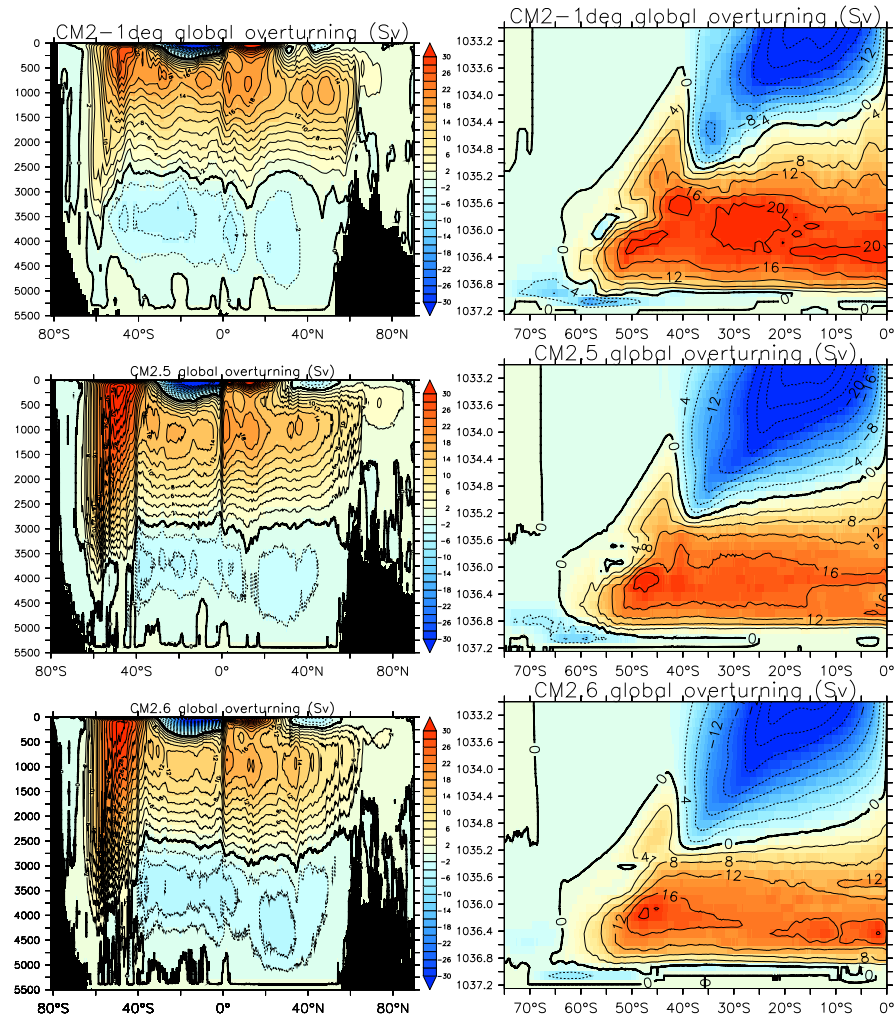


Figure 4.9: Overturning streamfunction for the global ocean as realized in the CM2-O suite of models. We exhibit the streamfunction as a meridional-depth overturning and a meridional- σ_{2000} overturning. For CM2.5 and CM2.6, the streamfunction includes contributions from the resolved flow and the parameterized submesoscale eddies. For CM_O1p0_C180, the streamfunction includes contributions from the resolved flow and parameterized mesoscale and submesoscale eddies. Note that Figure 3.11 shows the streamfunction just from the submesoscale scheme in all three models, and Figure 3.13 shows the streamfunction from the mesoscale parameterization in CM_O1p0_C180.

4.8.7 Atlantic-Arctic overturning streamfunction

Figure 4.10 shows the time mean Atlantic-Arctic overturning streamfunction from the CM2-O suite.

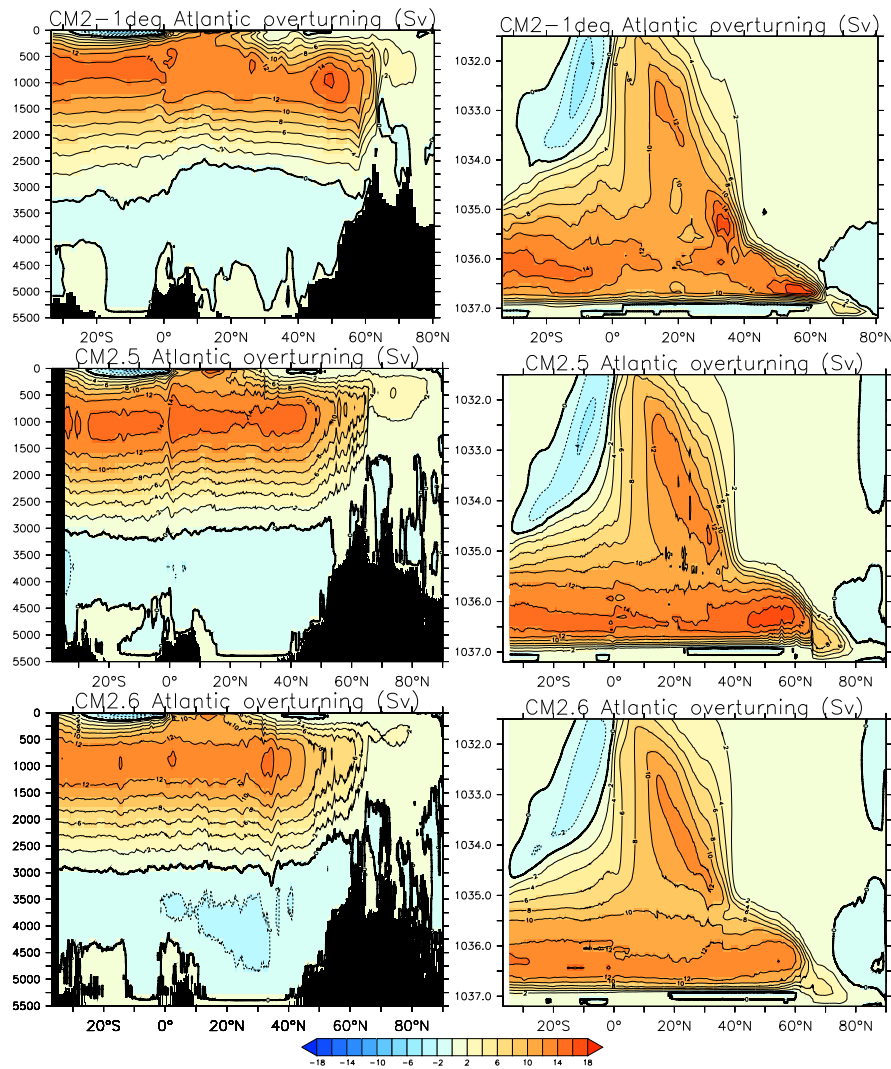


Figure 4.10: Sample overturning streamfunction for the Atlantic-Arctic ocean as realized in the CM2-O suite of models. We exhibit the streamfunction as a meridional-depth overturning and a meridional- σ_{2000} overturning. For CM2.5 and CM2.6, the streamfunction includes contributions from the resolved flow and the parameterized submesoscale eddies. For CM_O1p0_C180, the streamfunction includes contributions from the resolved flow and parameterized mesoscale and submesoscale eddies.

4.8.8 Atlantic meridional overturning circulation index

Figure 4.11 shows the time series for annual mean Atlantic meridional overturning index, computed as the maximum of the overturning streamfunction at 45°N in the Atlantic. The CM2.6 and CM2.5 streamfunctions have rather damped variability with a mean somewhat smaller in CM2.6 than in CM2.5, and both smaller in mean and variance than the CM_O1.0_C180 values.

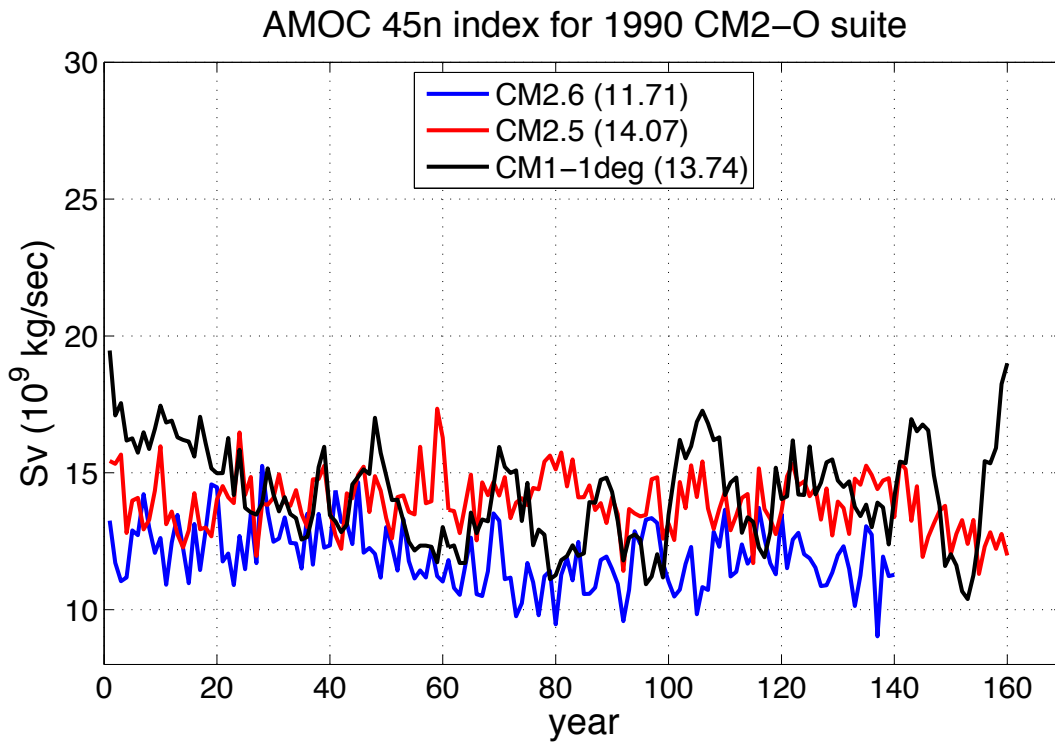


Figure 4.11: Time series for the annual mean Atlantic meridional overturning index for the CM2-O suite of simulations. The time mean is indicated in the figure legend.

4.8.9 Indian-Pacific overturning streamfunction

Figure 4.12 shows the time mean Indian-Pacific overturning streamfunction from the CM2-O suite.

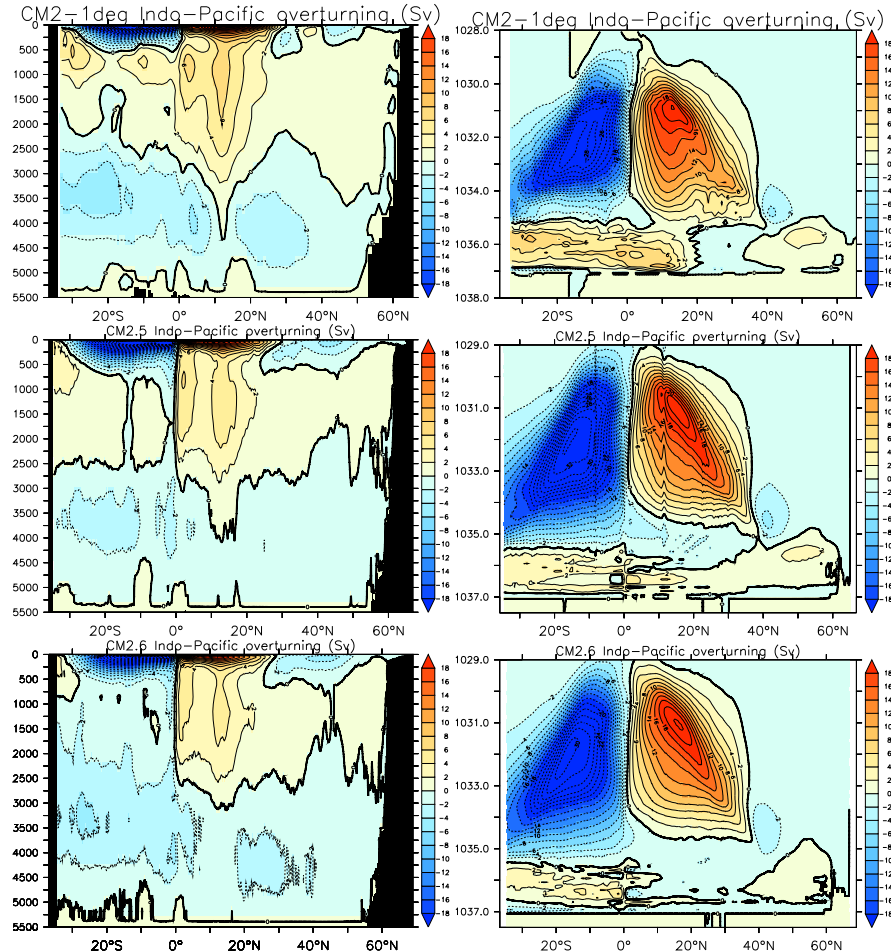


Figure 4.12: Sample overturning streamfunction for the Indian-Pacific ocean as realized in the CM2-O suite of models. We exhibit the streamfunction as a meridional-depth overturning and a meridional- σ_{2000} overturning. For CM2.5 and CM2.6, the streamfunction includes contributions from the resolved flow and the parameterized submesoscale eddies. For CM_O1p0_C180, the streamfunction includes contributions from the resolved flow and parameterized mesoscale and submesoscale eddies.

Ocean heat transport and heat budgets

Contents

5.1	Introduction	120
5.1.1	Sample bias maps	120
5.1.2	Interior temperature properties	120
5.2	Heat crossing the ocean boundaries	121
5.2.1	Boundary heat fluxes impacting the ocean	121
5.2.1.1	Non-advection surface heat fluxes	124
5.2.1.2	Advection surface heat fluxes	125
5.2.2	Diagnostics for surface heat flux	126
5.2.3	How to measure heat content associated with mass transfer	126
5.2.4	Climatological radiative heat fluxes	127
5.2.5	Climatological latent heat fluxes	128
5.2.6	Climatological sensible heat, mass heat, and frazil	129
5.2.7	Net surface ocean heat flux	130
5.3	Global ocean heat and global mean temperature	130
5.3.1	Sample model results	130
5.3.2	Some definitions	130
5.3.3	Evolution equations	132
5.4	Tracer budget for a grid cell in MOM5	133
5.5	Sample ocean heat budgets	135
5.5.1	Heat budget for an ocean grid cell in CM2.5 and CM2.6	135
5.5.1.1	Terms contributing to the heat budget	135
5.5.1.2	Summary of the CM2.5 and CM2.6 ocean heat budget	137
5.5.2	Heat budget for an ocean grid cell in CM.O1.0_C180	137
5.5.3	Heat budget for an ocean grid cell in CM2.5-FLOR	138
5.5.4	Heat budget for an ocean grid cell in ESM2M	138
5.6	Depth integrated heat budget	139
5.7	Poleward heat transport	143
5.8	Heat budget for surface ocean grid cells	147
5.8.1	Diagnostic budget terms	147
5.8.1.1	Ocean transport and surface boundary fluxes	147
5.8.1.2	Advection, mixing, and boundary processes	148
5.8.2	Global mean surface ocean temperature	149
5.8.3	Heating as sum of ocean transport and boundary fluxes	150

5.8.4	Heating as sum of advection, mixing, and boundary fluxes	151
5.8.5	Advection processes	151
5.8.6	Non-advection surface boundary fluxes plus mixing	155
5.8.7	Mixing processes	155
5.9	Zonal heat budget	157
5.9.1	Horizontally integrated heat budget	157

This chapter considers the ocean heat budget and the transport of heat across the ocean boundary and within the ocean interior. We introduce various of the physical processes that impact on the ocean heat budget, and affect its transport. We illustrate the methods by performing an analysis of the ocean model configurations in the CM2-O suite.

5.1 Introduction

Ocean heat, its movement, and its changes, are central to the ocean's role in the climate system. Assessing how heat is transported in ocean simulations, and comparing this transport to observation-based measures, is a basic element of evaluating a climate simulation.

Processes that impact ocean heat transport and heat changes are more complex than those we encountered in Chapter 4 affecting seawater mass. For example, more processes comprise the net flux of heat across the ocean boundaries. Some processes require parameterization of turbulent exchanges, such as sensible and latent heat fluxes. We require an understanding of seawater optical properties to determine how shortwave radiation penetrates beneath the surface layer. Heat is also transferred across the ocean boundary when mass through precipitation, evaporation, and river runoff enters or leaves the ocean, since this mass itself carries a heat content. And heat enters the ocean through the solid-earth lower boundary in those regions there geothermal heating is active.

The transport of heat within the ocean interior is also more complex than the transport of mass. The reason is that heat, and any other tracer, is impacted by subgrid-scale processes parameterized through a transport tensor, with symmetric and anti-symmetric elements, as well as possibly a non-local boundary layer term. We introduced in Chapter 3 the various subgrid scale processes used in the CM2-O suite. There are many more in the literature, yet those used in CM2-O are sufficient for illustrating various analysis methods.

5.1.1 Sample bias maps

As motivation to develop an analysis framework for ocean heat, we exhibit in Figure 5.1 the difference maps for sea surface temperature (SST) from six coupled climate models developed at GFDL, including the three models from the CM2-Ocean suite. These maps show where the SST deviates from the World Ocean Atlas (Locarnini et al., 2006).

5.1.2 Interior temperature properties

Figure 5.2 shows the evolution of the annual mean horizontally averaged temperature relative to the initial year of each simulation. We show results for the global ocean as well as various basins. Figure 5.3 show a map of the time mean difference at 730 m, which is near the center of the maximum in the drift seen in Figure 5.2. Note the dramatic reduction in drift found in the finest resolution model, CM2.6, relative to both CM2.5 and CM2-1deg. A similar story is told from Figure 5.4, which shows the zonal mean and time mean temperature at the end of the simulation as differenced from the first model year.

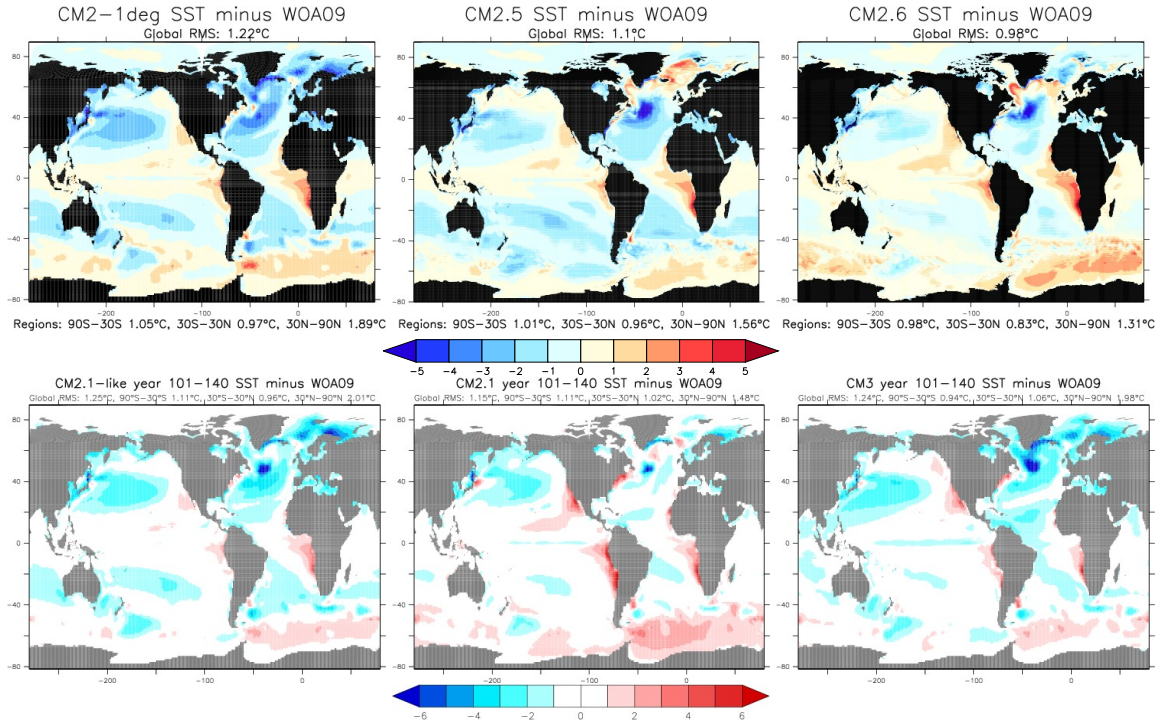


Figure 5.1: Maps of the time mean (over years 101–140) annual mean SST difference relative to the World Ocean Atlas (Locarnini et al., 2006). The first row shows results from the CM2-Ocean suite of models, starting from the one-degree on the left, CM2.5 in the middle, and CM2.6 on the right. The second row shows the analogous maps from other models built at GFDL. The first one on the left shows results from a one-degree model with an ocean configuration similar to that used in the ESM2M ocean component from Dunne et al. (2012) and with the same atmosphere and sea ice settings used in the CM2-Ocean suite, thus testing sensitivity to the ocean configuration. The middle panel on the bottom row shows results from CM2.1 documented by Delworth et al. (2006), and the right panel shows results from CM3 documented by Griffies et al. (2011). Note the different scales on the figures in the two rows.

5.2 Heat crossing the ocean boundaries

In this section, we discuss the surface ocean heat fluxes and illustrate those encountered in the CM2-O suite of simulations.

5.2.1 Boundary heat fluxes impacting the ocean

We identify here three general forms of boundary fluxes that impact on the ocean heat content.

- Ocean heat is impacted by radiative transfer, such as shortwave heat entering the ocean or longwave radiation back to the atmosphere. Shortwave radiation is special since it generally can penetrate into the ocean interior according to the optical properties of seawater (Section 3.14).
- Turbulent exchanges impact on the sensible and latent heat fluxes that alter ocean heat content.
- As matter crosses the ocean surface, it carries with it a non-zero heat content as measured with respect to an arbitrary reference, taken as 0°C for our purposes. This transfer of heat can be thought of as arising through an advective processes, whereby mass is “advected” across the ocean surface and carries with it some heat.

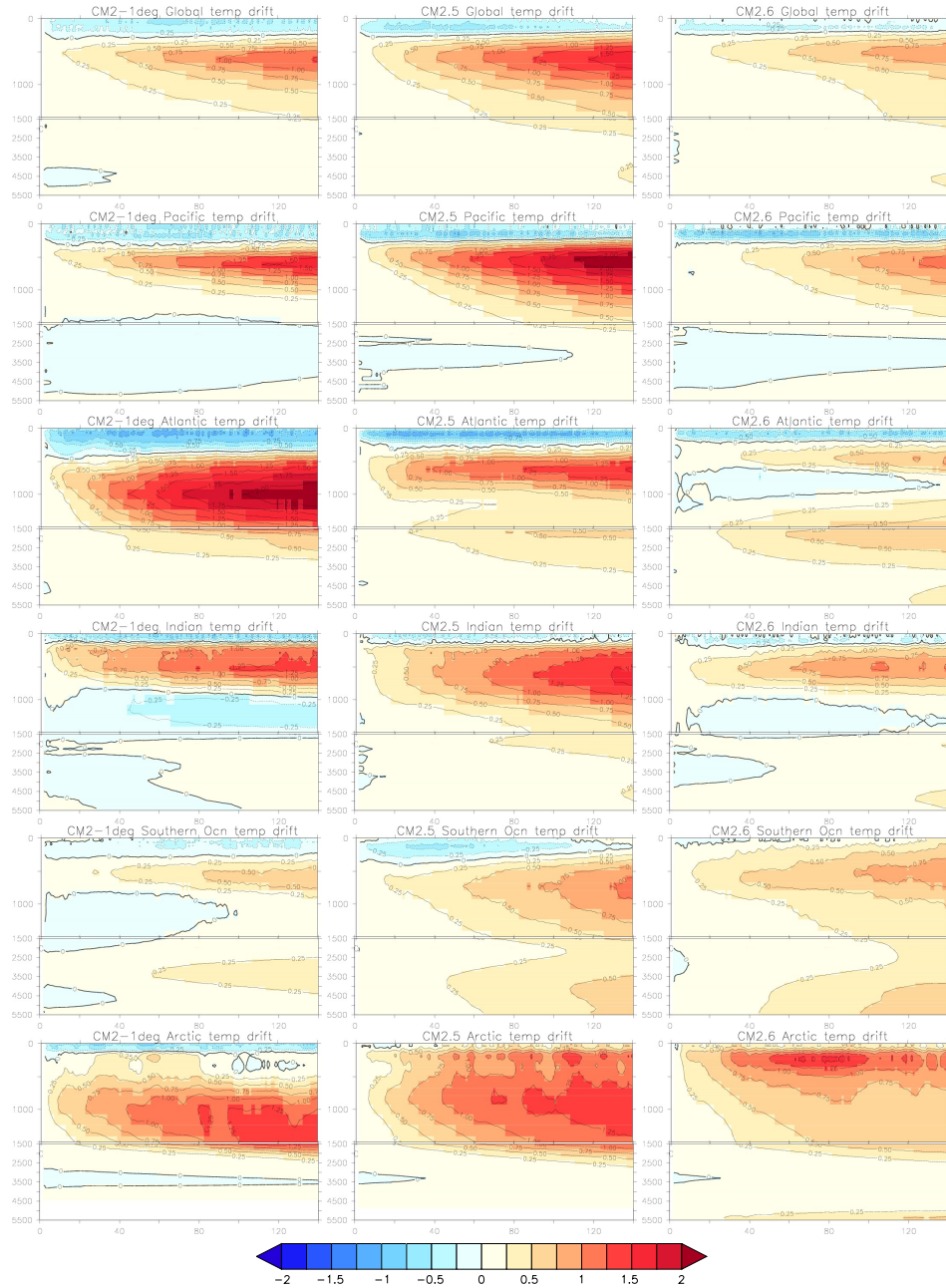


Figure 5.2: Time series for annual mean horizontally averaged temperature relative to the initial year for each of the models in the CM2-Ocean suite. Note the stretched vertical axis in the upper 1500m of the water column. This diagnostic is computed according to $\sum_{x,y} dx dy dz (\theta - \theta(\text{year} = 1)) / \sum_{x,y} dx dy dz$, where $\theta(\text{year} = 1)$ is the annual mean from the first year for the respective simulation. The use of partial bottom cells (Pacanowski and Gnanadesikan, 1998) (Section 2.5) makes it important that such horizontally averaged diagnostics incorporate variations in vertical cell thickness across a horizontal section.

We discuss these heat fluxes in the remainder of this subsection,

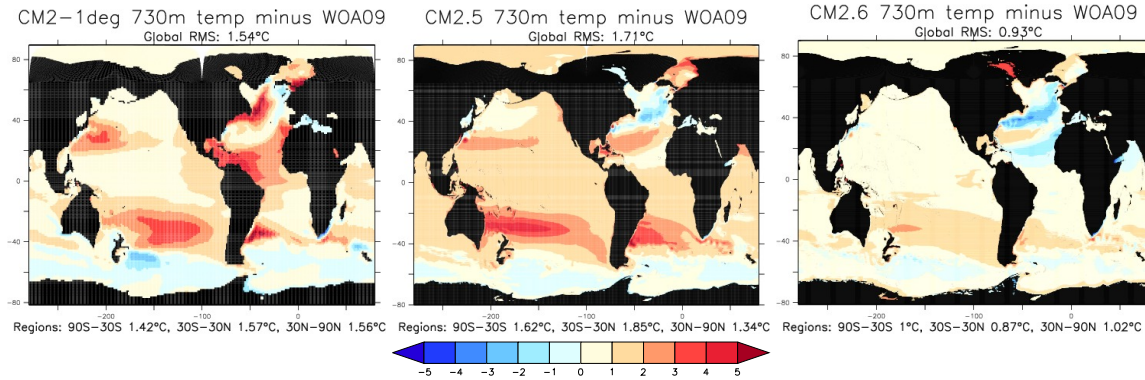


Figure 5.3: Maps of the time mean (over years 101-140) annual mean temperature at 730 m relative to the World Ocean Atlas (Locarnini et al., 2006). Results from the one-degree are shown on the left, CM2.5 in the middle, and CM2.6 on the right.

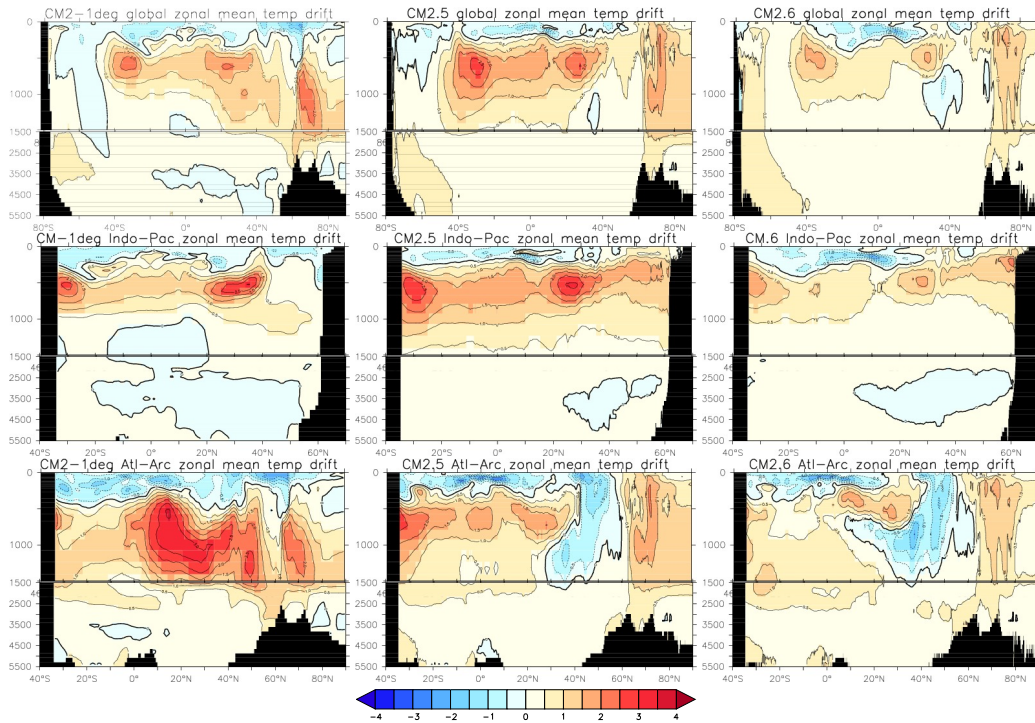


Figure 5.4: Zonal mean patterns for the difference between the ocean potential temperature averaged over years 101-140 differenced from the first year of the simulations. Shown are results for the global ocean, Pacific-Indian oceans, and Atlantic-Arctic oceans. Note the smaller biases throughout the ocean seen in CM2.6. Notably, the reduced bias in the Atlantic means that the meridional heat transport can remain large even with a modest overturning circulation.

5.2.1.1 Non-advection surface heat fluxes

We identify the following non-advection heat fluxes that cross the surface ocean boundary (generally considered in the SI units of W m^{-2}),

$$Q_{\text{non-advect}}^{\text{heat}} = Q_{\text{SW}} + Q_{\text{LW}} + Q_{\text{sens}} + Q_{\text{lat}} + Q_{\text{frazil}} \quad (5.1)$$

with a sign convention chosen so that positive fluxes add heat to the liquid seawater. Ocean models typically time step an equation for ocean temperature rather than heat content. So it is necessary to convert between heat and temperature fluxes when considering the impacts on sea level. As noted by McDougall (2003), to convert from heat fluxes to fluxes of potential temperature requires the use of a non-constant specific heat capacity, which varies by roughly 5% over the globe. In contrast, converting between heat fluxes and conservative temperature fluxes is done with a constant specific heat capacity

$$Q_{\text{surface heat flux}} = C_p^0 Q_{\text{surface}}^{(\Theta)}, \quad (5.2)$$

thus serving to further promote the use of conservative temperature. Nonetheless, as noted in Section 3.1, we ignore this distinction in the CM2-O suite, and so assume the prognostic temperature variable to be potential temperature, but take a constant heat capacity to convert between heat fluxes and temperature fluxes.

We now summarize the various heat flux contributions at the ocean surface.

- **SHORTWAVE:** The dominant heating occurs through the shortwave contribution $Q_{\text{SW}} > 0$. Shortwave radiation penetrates on the order of 10m to 100m into the ocean interior, with the distance depending on optical properties of seawater (see, e.g., Sweeney et al., 2005, and cited references).
- **LONGWAVE:** The longwave contribution Q_{LW} represents the net longwave energy that is re-radiated back to the atmosphere. Even though there are many occasions for backscattering, the net effect of longwave radiation is to cool the ocean.
- **SENSIBLE:** Sensible heating Q_{sens} arises from turbulent exchange with the atmosphere, and is generally parameterized by turbulent bulk formula. The sensible heat term typically cools the ocean surface.
- **LATENT:** Latent heating Q_{lat} cools the ocean, as it is the energy extracted from the ocean to vaporize liquid water that enters the atmosphere. Additionally, the latent heating term includes heat extracted from the ocean to melt solid runoff (i.e., calving land ice) or snow entering the liquid ocean. These latent heat terms are thus related to mass transport across the ocean surface according to

$$Q_{\text{lat}}^{\text{vapor}} = H^{\text{vapor}} Q_m^{\text{evap}} \quad (5.3)$$

$$Q_{\text{lat}}^{\text{melt}} = H^{\text{fusion}} (Q_m^{\text{calving}} + Q_m^{\text{snow}}), \quad (5.4)$$

where $H^{\text{vapor}} \approx 2.5 \times 10^6 \text{ J kg}^{-1}$ is the latent heat of vaporization, Q_m^{evap} is the evaporative mass flux in units of $\text{kg m}^{-2} \text{ s}^{-1}$, $H^{\text{fusion}} \approx 3.34 \times 10^5 \text{ J kg}^{-1}$ is the latent heat of fusion, Q_m^{calving} is the mass flux of calving land ice entering the ocean, and Q_m^{snow} is the mass flux of frozen precipitation falling on the ocean surface. Note that sea ice and frozen precipitation may enter the ocean at a temperature below the freezing point, in which case additional heat needs to be extracted from the liquid ocean to raise the frozen water to the melting point.

- **FRAZIL:** As the temperature of seawater cools to the freezing point, sea ice is formed, initially through the production of frazil. Operationally in an ocean model, liquid water can be supercooled at any particular time step through surface fluxes and transport. An adjustment process heats the liquid water back to the freezing point, with this positive heat flux Q_{frazil} extracted from the ice model as frazil sea ice is formed.

5.2.1.2 Advection surface heat fluxes

Global atmospheric models and many land models generally do not carry the heat content of their condensed moisture, either liquid or solid. Hence, ocean models with real water flux boundary conditions, such as MOM5, must make an assumption regarding the heat content of water entering or leaving the ocean. Note that the heat content of mass transferred across the ocean boundary is, by convention, computed with respect to 0°C . The question is what should we assume for the temperature of the mass that enters or leaves the ocean?

Evaporation is naively the simplest case, whereby we assume the evaporating water leaves the ocean with a temperature of the ocean surface grid cell. However, questions about bulk surface temperature versus skin temperature have not been considered, and will impact on the heat content transferred away from the ocean. Likewise, most climate models assume the liquid precipitation enters at the ocean surface temperature. This, again, is not necessarily correct, since rain may be either warmer or colder than the ocean surface temperature. But in the absence of information from an atmospheric model, setting evaporation and precipitation temperatures equal to the ocean surface grid cell temperature is the most common choice.

What about frozen precipitation (i.e., snow)? One choice is to assume it enters the ocean at the freezing point of fresh water, 0°C . If that were assumed, then snow would not contribute to the ocean heat through MASS HEAT. It would, however, affect ocean heat through the latent heat of fusion needed to melt snow, plus the heat needed to raise or lower the melted mass to the ambient ocean temperature. For example, if snow falls on an ocean with surface temperature 10°C , then the liquid ocean loses heat due to melting the snow, and loses heat in order to raise the melted snow to the ambient ocean temperature.

Rather than assume snow enters the ocean at 0°C , MOM assumes snow enters as part of the liquid precipitation, and so it carries a temperature equal to the ocean surface temperature just as the liquid precipitation. Snow therefore affects the liquid ocean heat content through the heat of fusion needed to melt the snow, and through the heat content of snow relative to 0°C . We see that this is in fact the convention by inspecting the MOM5 module ocean_core/ocean_sbc.F90, where

$$\text{MASS HEAT AIR-SEA} = C_p * \text{pme} * \text{tpme}, \quad (5.5)$$

where tpme is the temperature of the precipitation and evaporation, which is generally assumed to be the surface model temperature, and C_p is the heat capacity. The field pme is the mass per time per horizontal area of both liquid and frozen precipitation

$$\text{pme} = \text{lprec} + \text{evap} + \text{fprec}, \quad (5.6)$$

where all fields are signed so that positive indicates water entering the ocean surface. In summary, for computing MASS HEAT AIR-SEA as part of the time tendency for the temperature equation, MOM4 and MOM5 set the temperature of the frozen precipitation to the temperature of the liquid precipitation.

There is a net heat loss to the ocean system due to the heat transfer associated with precipitation minus evaporation. The reason is that evaporation tends to occur in warm regions whereas precipitation tends to occur in cooler regions. So the mass transport of warm water away from the ocean and cooler water into the ocean represents a net loss of heat to the ocean. [Delworth et al. \(2006\)](#) estimated the heat loss in CM2.1 to be roughly -0.15 W m^{-2} . As shown in Section 5.8.5 and Figure 5.21, our online diagnostic calculation yields the larger global mean value of -0.5 W m^{-2} for the CM2-O suite of simulations. As also shown in Section 5.8.5 and Figure 5.21, this value is partially offset by the 0.3 W m^{-2} of heat added to the ocean due to river runoff.

5.2.2 Diagnostics for surface heat flux

The available MOM5 diagnostics for computing surface heat fluxes are as follows (all have units of W m^{-2}):

$$\text{RADIATIVE} = \text{swflx} + \text{lw_heat} \quad (5.7\text{a})$$

$$\text{TURBULENT} = \text{sens_heat} + \text{calving_melt_heat} + \text{evap_heat} + \text{fprec_melt_heat} \quad (5.7\text{b})$$

$$\text{MASS HEAT} = \text{sfc_hflux_from_calving} + \text{sfc_hflux_from_runoff} + \text{sfc_hflux_pme} \quad (5.7\text{c})$$

$$\text{FRAZIL} = \text{frazil_2d} \quad (5.7\text{d})$$

$$\text{NET SURFACE HEAT FLUX} = \text{RADIATIVE} + \text{TURBULENT} + \text{MASS HEAT} + \text{FRAZIL}. \quad (5.7\text{e})$$

It is often the case that we are interested in the heat flux that passes through the coupler, which only includes the non-advectional fluxes, in which case

$$\text{sfc_hflux_coupler} = \text{swflx} + \text{lw_heat} + \text{sens_heat} + \text{calving_melt_heat} + \text{evap_heat} + \text{fprec_melt_heat}. \quad (5.8)$$

For the heat content associated with river water, which can in general be liquid runoff or solid calving, we have

$$\text{sfc_hflux_river} = \text{sfc_hflux_from_calving} + \text{sfc_hflux_from_runoff}. \quad (5.9)$$

Hence, we may write for the net heat flux crossing the ocean surface boundary

$$\text{NET SURFACE HEAT FLUX} = \text{sfc_hflux_coupler} + \text{sfc_hflux_river} + \text{sfc_hflux_pme} + \text{frazil_2d}. \quad (5.10)$$

5.2.3 How to measure heat content associated with mass transfer

The discussion in Section 5.2.1.2 prompts us to identify an ambiguity with MOM5 diagnostics associated with the heat content of mass crossing the ocean boundary. Namely, the diagnostic `net_sfc_hflux` is computed as¹

$$\begin{aligned} \text{net_sfc_heating} &= \text{sfc_hflux_coupler} + \text{sfc_hflux_river} \\ &\quad + \text{sfc_hflux_from_water_prec} + \text{sfc_hflux_from_water_evap}. \end{aligned} \quad (5.11)$$

However, the term `sfc_hflux_from_water_prec` is the heat content just of the liquid precipitation. It does not include that from frozen precipitation, whereas in time stepping the ocean heat content, MOM includes the heat content of both liquid and frozen precipitation as if they had the same temperature. Hence, the diagnostic `net_sfc_heating` is, unfortunately, not what the model uses for time stepping the heat content

$$\text{net_sfc_heating} \neq \text{NET SURFACE HEAT FLUX}. \quad (5.12)$$

Instead, `net_sfc_heating` is less than `NET SURFACE HEAT FLUX` by an amount equal to the mass of frozen precipitation times the ocean surface temperature. Equivalently, we have

$$\text{sfc_hflux_pme} \neq \text{sfc_hflux_from_water_prec} + \text{sfc_hflux_from_water_evap}, \quad (5.13)$$

since `sfc_hflux_pme` includes the heat content of both liquid and frozen precipitation, again by assuming frozen precipitation has the same temperature as liquid. So the bottomline is that to diagnose the net heat flux crossing the ocean surface that acts to change the heat content in MOM, we should use the expression (5.10)

$$\text{NET SURFACE HEAT FLUX} = \text{sfc_hflux_coupler} + \text{sfc_hflux_river} + \text{sfc_hflux_pme}. \quad (5.14)$$

The case of water entering through rivers is analogous to the air-sea water fluxes. However, as of 2010, the GFDL land model has been updated to carry the heat content (and tracer content) of its river water. Hence, both liquid runoff and calving land ice carry their own heat content into the ocean, computed with respect to 0°C . This more physically based approach was employed in the earth system model ESM2 documented by [Dunne et al. \(2012\)](#). Unfortunately, the land model updates were not mature when the CM2-O suite was developed. Hence, liquid runoff and solid calving are assumed in CM2-O to enter the ocean with a temperature equal to the local ocean temperature.

¹This diagnostic will be modified in mom5.0.3 to correspond to the method used for the prognostic equations, at which point the present discussion will be obsolete.

5.2.4 Climatological radiative heat fluxes

Figures 5.5 exhibits the heat flux arising from shortwave and longwave radiative fluxes across the ocean surface.

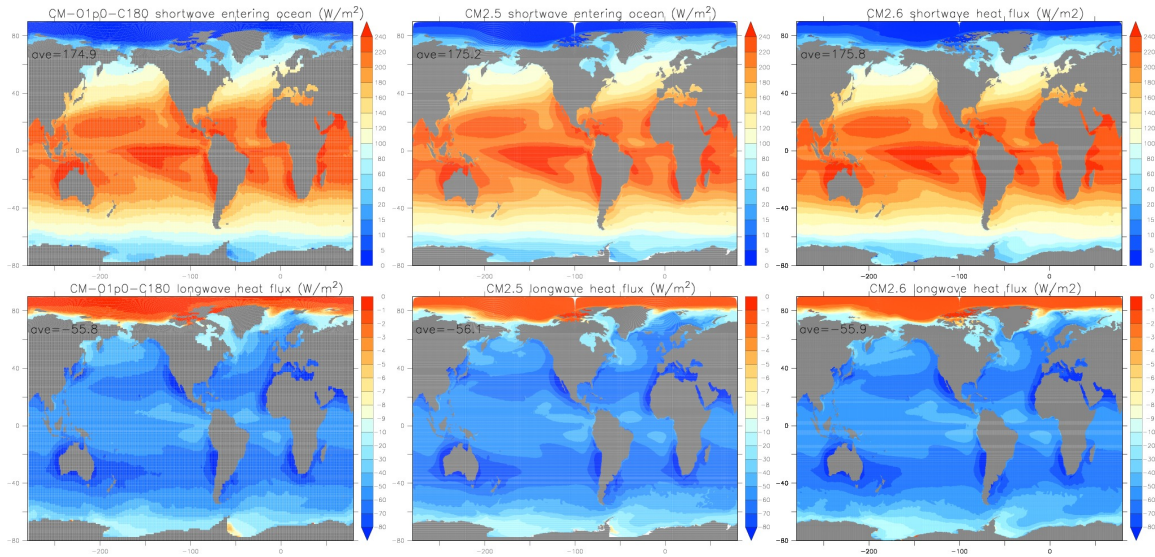


Figure 5.5: Maps of the shortwave and longwave radiative fluxes crossing the ocean boundary in the CM2-O suite, diagnosed here as a time mean over model years 101-140. The units are W m^{-2} , where the area factor is that of the ocean surface, so that multiplication of these maps by the surface area of an ocean grid cell leads to the net heat per time (Watts) crossing the ocean surface. Positive values represent heating for the ocean. The ocean area mean is noted on the top left of each panel. The colour scales are different between the shortwave and longwave figures.

5.2.5 Climatological latent heat fluxes

Figures 5.6 exhibits the heat flux arising from latent heat of vaporization and fusion. The fusion term arises from the ocean heat loss to melt snow and to melt icebergs.

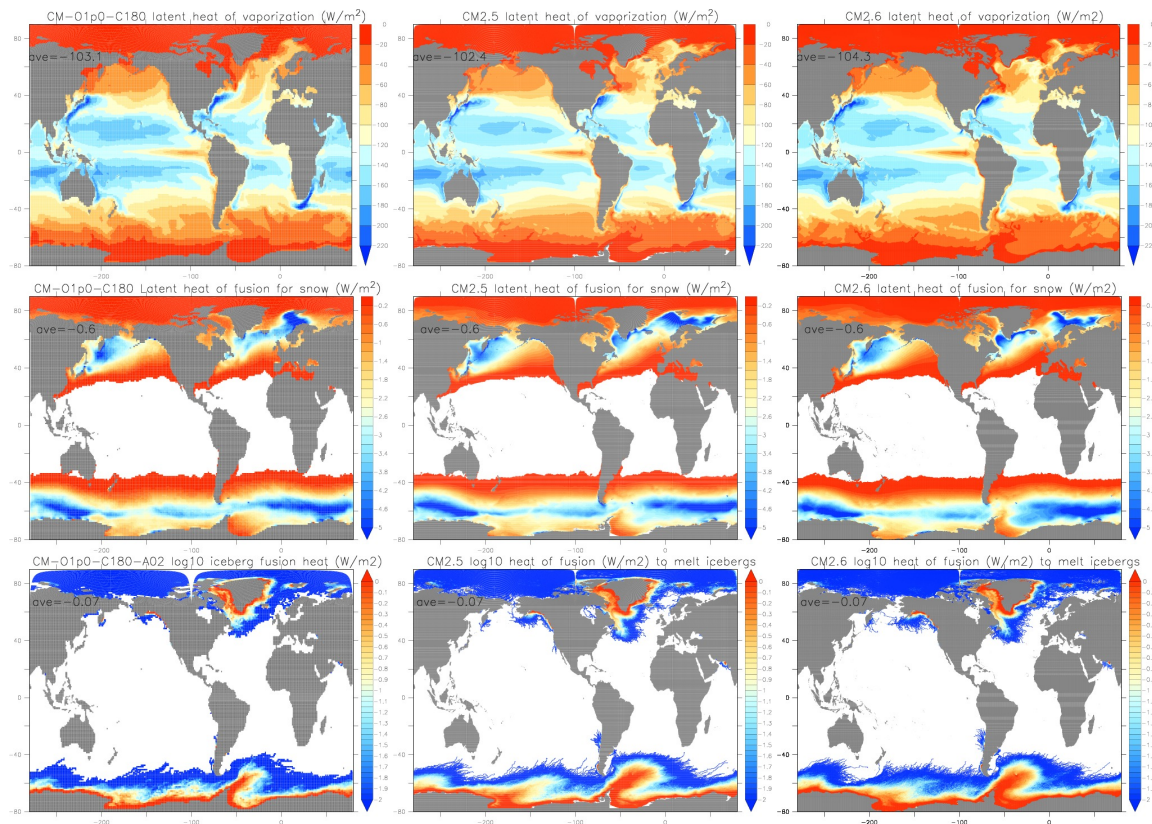


Figure 5.6: Maps of the latent heat fluxes crossing the ocean boundary in the CM2-O suite, diagnosed here as a time mean over model years 101-140. The units are W m^{-2} , where the area factor is that of the ocean surface, so that multiplication of these maps by the surface area of an ocean grid cell leads to the net heat per time (Watts) crossing the ocean surface. Positive values represent heating for the ocean. The ocean area mean is noted on the top left of each panel. The colour scales are different between the different latent heat terms.

5.2.6 Climatological sensible heat, mass heat, and frazil

Figure 5.7 shows the sensible heat flux, the heat flux associated with mass transfer, and the frazil heating.

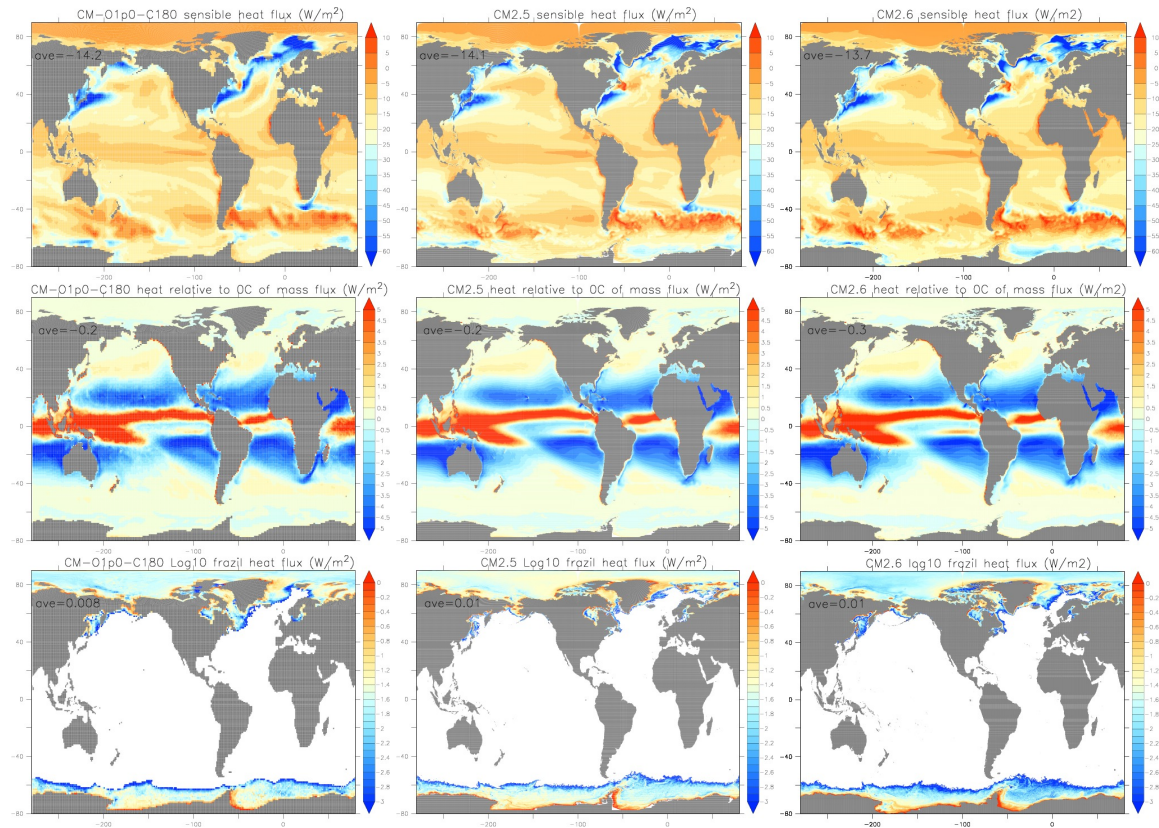


Figure 5.7: Maps of the sensible, mass heat flux, and frazil heating crossing the ocean boundary in the CM2-O suite. The units are W m^{-2} , where the area factor is that of the ocean surface, so that multiplication of these maps by the surface area of an ocean grid cell leads to the net heat per time (Watts) crossing the ocean surface. Positive values represent heating for the ocean. The ocean area mean is noted on the top left of each panel. The colour scales are different between the different heat fluxes.

5.2.7 Net surface ocean heat flux

Figure 5.8 shows the net surface ocean heat flux.

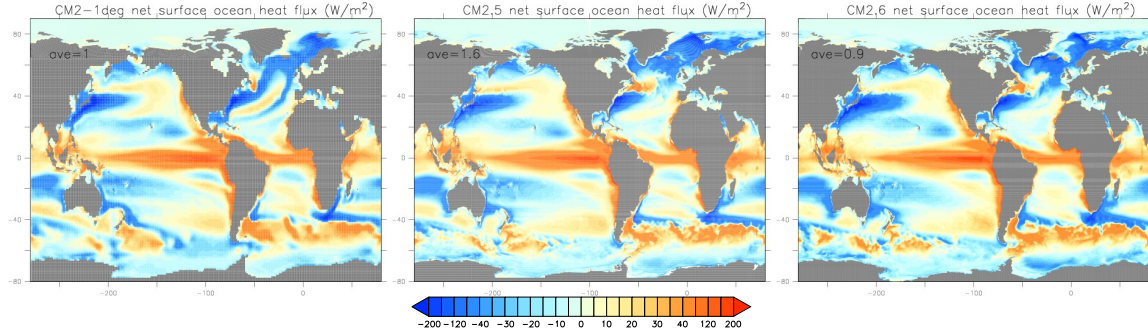


Figure 5.8: Maps of the net surface ocean heat flux crossing the ocean boundary in the CM2-O suite. The units are W m^{-2} , where the area factor is that of the ocean surface, so that multiplication of these maps by the surface area of an ocean grid cell leads to the net heat per time (Watts) crossing the ocean surface. Positive values represent heating for the ocean. The ocean area mean is noted on the top left of each panel.

5.3 Global ocean heat and global mean temperature

We consider in this section the evolution of global ocean heat and global mean conservative/potential temperature. As the ocean heat content is conserved, the total ocean heat is impacted only through the net fluxes of heat crossing the ocean boundary. We here develop the evolution equations describing the budget for global ocean heat, and correspondingly for global mean potential/conservative temperature.

5.3.1 Sample model results

We exhibit in Figure 5.9 the ocean heat content and global mean ocean potential temperature. Each of the models warm, as may be expected since the 1990 simulations represent a “committed warming” scenario. However, the rate of warming differs. As discussed in Section 5.3.3, this difference is associated with differences in net heat crossing the ocean boundaries. Explaining why the models differ in net heat requires, in part, examining the budgets in more detail, as we do in this chapter. In the remainder of this section, we explore the budgets determining the global means shown in Figure 5.9.

5.3.2 Some definitions

The mass of liquid seawater contained in the global ocean is written

$$\mathcal{M} = \int \rho dV \quad (5.15a)$$

$$= \int dA \int_{-H}^{\eta} \rho dz, \quad (5.15b)$$

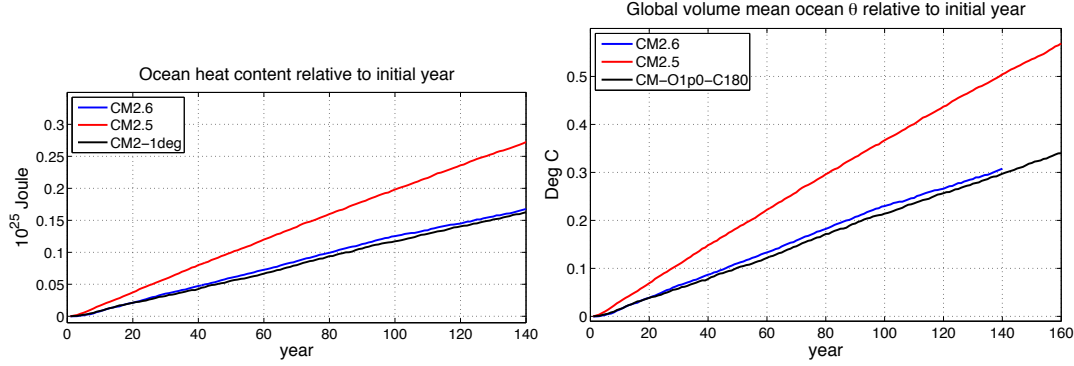


Figure 5.9: Left panel: Time series for the annual mean global ocean volume integrated heat computed relative to the first year. Right panel: Global volume averaged potential temperature computed relative to the first year. The global heat content figure has only results from the CM2-Ocean suite, with CM2.6 blue, CM2.5 red, and CM_O1p0_C180 black. The global mean temperature time series also shows results from CM3 (Griffies et al., 2011), CM2M (the physics-component from the earth system model ESM2M of Dunne et al. (2012)), and CM2.1 (Delworth et al., 2006). The MOM5 diagnostic table entries for these time series are total_ocean_heat and temp_global_ave. It is notable that CM2.5 exhibits the most rapid rate of warming, with CM3 the second most rapid, and the remaining models relatively close.

and the corresponding volume is

$$\mathcal{V} = \int dV \quad (5.16a)$$

$$= \int (H + \eta) dA. \quad (5.16b)$$

For a Boussinesq ocean, as in the CM2-O suite, the *in situ* density factors are set to the constant Boussinesq reference density ρ_0 , in which case

$$\mathcal{M}^{\text{Bouss}} = \rho_0 \mathcal{V}^{\text{Bouss}}. \quad (5.17)$$

The global mean potential temperature is defined by the density-weighed average

$$\langle \Theta \rangle^\rho = \frac{\int \rho \Theta dV}{\int \rho dV} \quad (5.18a)$$

$$= \frac{\langle \rho \Theta \rangle}{\langle \rho \rangle}, \quad (5.18b)$$

where the volume average is defined by

$$\langle \psi \rangle \equiv \frac{\int \psi dV}{\int dV}. \quad (5.19)$$

The corresponding heat content for the global ocean (units of Joules) is given by

$$\mathcal{H} = C_p^o \mathcal{V} \langle \rho \Theta \rangle = C_p^o \mathcal{M} \langle \Theta \rangle^\rho. \quad (5.20)$$

For the Boussinesq ocean, the heat content takes the form

$$\mathcal{H}^{\text{Bouss}} = C_p^o \rho_0 \mathcal{V}^{\text{Bouss}} \langle \Theta \rangle. \quad (5.21)$$

The specific heat capacity of sea water, C_p^o , is assumed constant in MOM5 as well as other ocean climate models. However, as noted by McDougall (2003) (see also IOC et al. (2010)), use of a constant specific

heat capacity is accurately justified only when the temperature variable is the conservative temperature rather than the potential temperature used in the CM2-O suite (see Section 3.1).

In addition to the global mean quantities introduced above, we also make use of area mean quantities defined by

$$\bar{\psi} = \frac{\int \psi dA}{\mathcal{A}}, \quad (5.22)$$

where

$$\mathcal{A} = \int dA \quad (5.23)$$

is the area of the surface ocean. For ocean climate modeling in the absence of changing shorelines or wetting/drying processes, the horizontal area of the ocean is constant. With this assumption, the ocean volume changes only through changes in the sea surface

$$\frac{\partial V}{\partial t} = \int \frac{\partial \eta}{\partial t} dA. \quad (5.24)$$

5.3.3 Evolution equations

It follows from the definition (5.20) that the total ocean heat changes according to changes in the mean temperature and the ocean mass

$$\frac{\partial_t \mathcal{H}}{\mathcal{H}} = \frac{\partial_t \langle \Theta \rangle^\rho}{\langle \Theta \rangle^\rho} + \frac{\partial_t \mathcal{M}}{\mathcal{M}}. \quad (5.25)$$

As heat (or more correctly potential enthalpy) is a conserved quantity in the ocean (McDougall, 2003), we know that the net ocean heat changes only via the net heat flux crossing the liquid ocean surface, in which we write

$$\partial_t \mathcal{H} = \mathcal{A} \overline{Q^{\text{heat}}}, \quad (5.26)$$

where $\mathcal{A} \overline{Q^{\text{heat}}}$ is the area integrated boundary enthalpy per time crossing the ocean (SI units of Joule/sec = Watts). This enthalpy transport arises from surface shortwave, longwave, latent, sensible heating, as well as exchanges with sea ice (see Section 3.4.1 of Griffies and Greatbatch (2012)). Some GFDL climate models also include geothermal heating (Dunne et al., 2012), but geothermal heating is not used in the CM2-O suite considered here. We term the sum of these terms the non-advectional heat flux, $Q_{\text{non-advect}}^{\text{heat}}$.

In addition to the non-advectional heat fluxes, ocean heat content changes when mass is exchanged across the ocean boundary, since the mass contains a nonzero heat. The heat content is measured with respect to a reference temperature, assumed here to be zero Celsius. This reference temperature is arbitrary, and does not impact the net heat accumulated in the ocean. But for accounting purposes, we need to make a choice. The total boundary heat flux is thus given by the sum

$$Q^{\text{heat}} = Q_{\text{non-advect}}^{\text{heat}} + Q_{\text{advect}}^{\text{heat}}. \quad (5.27)$$

As discussed in Section 5.2.3, the advective surface heat flux for the CM2-O models is computed according to

$$Q_{\text{advect}}^{\text{heat}} = C_p^0 T_{\text{sst}} (Q_{\text{liquid precip}} + Q_{\text{solid precip}} + Q_{\text{evap}}) + Q_{\text{river}}^{\text{heat}}, \quad (5.28)$$

where $Q_{\text{precip}} \geq 0$ means mass enters the ocean through precipitation, and $Q_{\text{evap}} \leq 0$ means mass leaves the ocean through evaporation. That is, the advective heat flux due to precipitation and evaporation is computed using the local ocean sea surface temperature and the seawater heat capacity. We know of no atmospheric model used for climate that carries the heat content of its water, so the computation described here of the advective heat flux associated with precipitation is generally used for models such as the CM2-O suite that uses a real water flux. In contrast, the LM3 land model carries a heat content, so it provides to the ocean the heat content of the liquid river runoff and solid calving runoff.

In the coupled model study of Delworth et al. (2006) (see their Section 3), they find $Q_{\text{advect}}^{\text{heat}} \approx -0.15 \text{ W m}^{-2}$. The net cooling arises since water tends to evaporate from warmer ocean regions and precipitate in cooler regions, thus causing a net heat loss to the ocean. As shown in Section 5.8.5 and Figure 5.21, the online diagnostic calculation yields the larger global mean value of -0.5 W m^{-2} for the CM2-O suite of simulations.

As also shown in Section 5.8.5 and Figure 5.21, this value is partially offset by the 0.3 W m^{-2} heat added to the ocean due to river runoff. As noted above, the atmospheric model used the CM2-O suite of coupled models does not carry the heat content of its condensed water. So the $Q_{\text{adve}}^{\text{heat}} < 0$ heat lost by the ocean is lost to the coupled system. That is, the coupled model does not conserve heat. It is generally believed that this non-conservation does not compromise the overall climate simulation. However, this conjecture remains untested.

Substitution of the heat budget equation (5.26) into equation (5.25) leads to an expression for the evolution of global mean ocean temperature

$$\frac{\partial_t \langle \Theta \rangle^\rho}{\langle \Theta \rangle^\rho} = \mathcal{A} \left(\overline{Q^{\text{heat}}} - \overline{Q^{\text{mass}}} \right). \quad (5.29)$$

Use of expression (5.20) for the heat content leads to

$$\frac{\partial \langle \Theta \rangle^\rho}{\partial t} = \frac{\mathcal{A}}{C_p \mathcal{M}} \left(\overline{Q^{\text{heat}}} - C_p^\rho \langle \Theta \rangle^\rho \overline{Q^{\text{mass}}} \right). \quad (5.30)$$

Finally, we substitute the advective heat flux (5.28) to render

$$\frac{\partial \langle \Theta \rangle^\rho}{\partial t} = \frac{\mathcal{A}}{C_p \mathcal{M}} \left(\overline{Q_{\text{non-adve}}^{\text{heat}}} + \overline{Q_{\text{adve}}^{\text{heat}}} - C_p^\rho \langle \Theta \rangle^\rho \overline{Q^{\text{mass}}} \right). \quad (5.31)$$

It remains very accurate for global models to set the mass term \mathcal{M} to a constant, since its relative change is tiny.

Monitoring the global mean temperature thus provides a means of monitoring the net enthalpy entering the ocean. We emphasize that the global mean temperature may reduce in those cases of a net negative enthalpy entering the ocean, yet still have global mean surface temperature increase, or vice-versa. The reason is the surface temperature is impacted by interior ocean fluxes as well as boundary fluxes. The CM2-O suite provides a clear example, in which the global mean temperature steadily rises for each of the models (Figure 5.9), yet the global mean surface temperature shown in Figure 5.17 exhibits a more complex evolution. In particular, CM2.5 and CM_O1.0_C180 show a cooling for the surface temperature for the first few decades of the simulations, whereas CM2.6 shows a nearly steady global mean surface temperature.

In a steady state, heat entering the ocean vanishes,

$$Q^{\text{heat}} = Q_{\text{non-adve}}^{\text{heat}} + Q_{\text{adve}}^{\text{heat}} = 0 \quad \text{steady state}, \quad (5.32)$$

as does the mass

$$Q^{\text{mass}} = 0 \quad \text{steady state}. \quad (5.33)$$

Thus, the following relations hold in the steady state

$$\overline{Q^{\text{heat}}} = 0 \implies \partial_t \mathcal{H} = 0 \quad (5.34a)$$

$$\overline{Q^{\text{mass}}} = 0 \implies \partial_t \mathcal{M} = 0 \quad (5.34b)$$

$$\overline{Q^{\text{heat}}} = 0 \text{ and } \overline{Q^{\text{mass}}} = 0 \implies \partial_t \langle \Theta \rangle^\rho = 0. \quad (5.34c)$$

5.4 Tracer budget for a grid cell in MOM5

In order to unwrap the information contained in the global budgets considered in Section 5.3, we need to develop equations for the tracer budgets within an ocean model grid cell. These equations were developed in Chapter 1 (see in particular Section 1.6), which resulted in the following semi-discrete equations for the surface, interior, and bottom grid cells

$$\partial_t (C \rho dz) = -\nabla_s \cdot [\rho dz (\mathbf{u} C + \mathbf{F})] + \left[\rho (w^{(s)} C + F^{(s)}) \right]_{s=s_{k-1}} + Q_{\text{adve}}^{(c)} + Q_{\text{non-adve}}^{(c)} + S^{(c)} \rho dz \quad (5.35a)$$

$$\partial_t (C \rho dz) = -\nabla_s \cdot [\rho dz (\mathbf{u} C + \mathbf{F})] - \left[\rho (w^{(s)} C + F^{(s)}) \right]_{s=s_{k-1}} + \left[\rho (w^{(s)} C + F^{(s)}) \right]_{s=s_k} + S^{(c)} \rho dz \quad (5.35b)$$

$$\partial_t (C \rho dz) = -\nabla_s \cdot [\rho dz (\mathbf{u} C + \mathbf{F})] - \left[\rho (w^{(s)} C + F^{(s)}) \right]_{s=s_{kbot-1}} + Q_{\text{(bot)}}^{(c)} + S^{(c)} \rho dz. \quad (5.35c)$$

These budgets are formulated as finite volume contributions to the tracer mass per horizontal area (or heat per area) of a grid cell. All grid cells generally have a non-constant thickness and non-constant density (Boussinesq budgets have constant density factor $\rho \rightarrow \rho_0$). The lateral convergence operator acting on a flux, $-\nabla_s \cdot \mathbf{J}$, is formulated numerically so that multiplication by the area of a grid cell leads to a difference operator acting on the lateral flux components crossing the tracer grid cell faces. That is, the numerical discretization satisfies Gauss' Law, as doing so allows us to retain the familiar finite volume budgets within the numerical model. We now detail terms in these equations.

- C is the potential (or conservative) temperature of a grid cell, or the mass of tracer (e.g., salt or DIC) per mass of seawater within the cell (i.e., tracer concentration).
- ρdz is the mass of seawater per horizontal area in a grid cell, with ρ the *in situ* density and dz the thickness. The CM2-O models as well as ESM2M make the Boussinesq approximation, so the ρ factor is replaced by a constant reference density

$$\rho_0 = 1035 \text{ kg m}^{-3}. \quad (5.36)$$

- The product $C \rho dz$ is the mass per unit horizontal area of a grid cell if C is a material tracer such as salinity. Since the horizontal area of the cell is constant in time, we may multiply by the horizontal area to recover a budget for the mass in the cell.
- The product $C \rho dz$ is the heat per horizontal area if C is potential or conservative temperature multiplied by the heat capacity. Since the horizontal area of the cell is constant in time, we may multiply by the horizontal area to recover a budget for the heat within the grid cell, in SI units of Joule.
- The generalized level vertical coordinate is denoted by s , and its discrete values s_k determine the vertical grid cell.
- The horizontal velocity component is \mathbf{u} and vertical component is $w^{(s)}$.
- The horizontal subgrid scale transport is $\rho \mathbf{F}$ and vertical component is $\rho F^{(s)}$.
- The tracer source is $S^{(c)} \rho dz$. This source is generally nonzero for biogeochemical tracers.
- Tracer flux associated with the boundary water flux is accounted for by the term $Q_{\text{advect}}^{(c)}$. It often takes the form

$$Q_{\text{advect}}^{(c)} = Q^{\text{mass}} C_m, \quad (5.37)$$

where Q^{mass} is the mass per time per horizontal area of water entering or leaving the ocean through liquid or frozen precipitation, evaporation, liquid runoff, and solid calving. The concentration C_m is that in the boundary water flux. This concentration is generally zero for salinity. For temperature, the precipitation and evaporation are assumed to have the temperature of the sea surface temperature. For the land model LM3 used in these coupled models, liquid runoff and solid calving have a heat content relative to 0°C that is transferred to the ocean, so that we do not need to assume a temperature for this water.

- $Q_{(\text{bot})}^{(c)}$ is the flux of tracer passed into the liquid ocean through the solid bottom boundary. The CM2-O suite of models does not have geothermal heating, in which case this term is zero. However, ESM2M has a non-zero geothermal heat flux (see Section 5.5.4).
- $Q_{\text{non-advect}}^{(c)}$ is the non-advection flux of tracer crossing the ocean surface boundary. The sign is defined so that a positive value represents a flux of tracer into the ocean; e.g., positive sign adds heat, salt, carbon, or other tracers to the ocean. For the heat budget, this term arises from shortwave, longwave, latent, and sensible heat fluxes.

5.5 Sample ocean heat budgets

We now identify those terms contributing to the ocean heat budget in the CM2-O ocean model components, as well as for the ocean component of ESM2M and CM2.5-FLOR. We do so by summarizing the physical processes impacting the heat within an ocean grid cell, and identifying the corresponding diagnostics available in MOM5 available for diagnosing these terms.

5.5.1 Heat budget for an ocean grid cell in CM2.5 and CM2.6

We now detail the heat budget in CM2.5 and CM2.6, with the ocean model components containing the same physical processes. The additional terms required for the nominally one-degree model CM_O1.0_C180 are given in Section 5.5.1, and the still further terms for ESM2M are detailed in Section 5.5.4.

All terms in the heat budget are multiplied by the heat capacity²

$$C_p^o \approx 3992.1 \text{ J kg}^{-1} \text{ K}^{-1}. \quad (5.38)$$

The physical units for each term are thus given by W m^{-2} . As mentioned in Section 5.4, the area normalization for each budget term corresponds to the horizontal area of the grid cell. So multiplication of any term by the tracer grid cell area yields the heat content change for that grid cell, in units of Watts.

5.5.1.1 Terms contributing to the heat budget

The following physical processes impact the heat budget within an ocean grid cell in CM2.5 and CM2.6, with these processes denoted by their diagnostic name found in the model output.

- `temp_tendency`: This is the net tendency for the temperature content (i.e., heat) in a grid cell

$$\text{temp_tendency} = \partial_t (\Theta \rho dz). \quad (5.39)$$

- `temp_advection`: This is the convergence of the three dimensional advection flux components

$$\text{temp_advection} = -\nabla_s \cdot [\rho dz \mathbf{u} \Theta] - [\rho w^{(s)} \Theta]_{s=s_{k-1}} + [\rho w^{(s)} \Theta]_{s=s_k}. \quad (5.40)$$

CM2.6 uses the multi-dimensional piecewise parabolic method for computing advection fluxes, in which case it is not convenient to split the terms into horizontal and vertical contributions. Hence, we diagnose this term as a three-dimensional convergence.

- `temp_submeso`: This is the convergence of the three dimensional subgrid scale flux components arising from the mixed-layer submesoscale parameterization scheme of Fox-Kemper et al. (2008) as implemented according to Fox-Kemper et al. (2011) and chapter 24 of Griffies (2012)

$$\text{temp_submeso} = -\nabla_s \cdot [\rho dz \mathbf{F}] - [\rho F^{(s)}]_{s=s_{k-1}} + [\rho F^{(s)}]_{s=s_k}. \quad (5.41)$$

- `temp_vdiffuse_impl`: This term contains the impacts from vertical diffusion, handled implicitly in time and including the boundary conditions

$$\text{temp_vdiffuse_impl} = \left[\rho F^{(s)} \right]_{s=s_{k-1}} + Q_{(\Theta)}^{\text{non-advect}} \quad k=1 \quad (5.42a)$$

$$\text{temp_vdiffuse_impl} = -[\rho F^{(s)}]_{s=s_{k-1}} + [\rho F^{(s)}]_{s=s_k} \quad 1 < k < k_{\text{bot}} \quad (5.42b)$$

$$\text{temp_vdiffuse_impl} = -\left[\rho F^{(s)} \right]_{s=s_{k_{\text{bot}}-1}} \quad k=k_{\text{bot}}. \quad (5.42c)$$

In these expressions, the flux component $F^{(s)}$ is that from downgradient vertical tracer diffusion. The CM2-O suite of simulations has no geothermal heating, so we set $Q_{(\text{bot})}^{(\Theta)} = 0$ (although see discussion of ESM2M in Section 5.5.4).

²The heat capacity pre-multiplier is omitted in the following for brevity, though it appears in the model code.

Note that it is often useful to separately diagnose the impacts on heat from vertical diffusion due to a vertical diffusivity, and the impacts from boundary terms. For this purpose, we have the following diagnostic identity available

$$\text{temp_vdiffuse_impl} = \text{temp_vdiffuse_sbc} + \text{temp_vdiffuse_diff_cbt}, \quad (5.43)$$

where `temp_vdiffuse_diff_cbt` arises just from a nonzero vertical diffusivity, and

$$\text{temp_vdiffuse_sbc} = Q_{(\Theta)}^{\text{non-advect}} \quad (5.44)$$

arises from the surface boundary fluxes. Another way to capture the split found in equation (5.43), without introducing a new diagnostic term, is to make use of the identity

$$\sum_{k=1}^{k_{\text{bot}}} \text{temp_vdiffuse_impl}[k] = \text{temp_vdiffuse_sbc}, \quad (5.45)$$

which follows from equations (5.42a)–(5.42c).

- `temp_nonlocal_kpp`: This term accounts for the non-local tendency arising from the KPP boundary layer parameterization. It acts to rearrange temperature in the vertical. Hence, there is no net heating involved, so that the vertical sum vanishes

$$\sum_{k=1}^{k_{\text{bot}}} \text{temp_nonlocal_kpp}[k] = 0. \quad (5.46)$$

Further details of the KPP scheme are provided in Section 3.4 as well as Chapter 18 of Griffies (2012).

- `sw_heat`: This term accounts for the penetrative heating from shortwave radiation, with details given in Chapter 17 of Griffies (2012). Note in particular the discussion in Section 17.4 that details how to avoid double counting the impacts from shortwave, with the bottomline from that discussion being

$$\text{net shortwave radiation heating at } (k=1) = \text{swflx} + \text{sw_heat}(k=1). \quad (5.47)$$

$$\text{net shortwave radiation heating at } (k>1) = \text{sw_heat}(k>1). \quad (5.48)$$

Since the penetrative radiation term `sw_heat` only acts to redistribute the radiation through the column, it has a zero vertical sum

$$\sum_{k=1}^{k_{\text{bot}}} \text{sw_heat}[k] = 0. \quad (5.49)$$

- `temp_rivermix`: This term accounts for the heating associated with the introduction of river runoff over the upper four model grid cells, with details given in Chapter 28 in Griffies (2012). Note the identity

$$\sum_{k=1}^{k_{\text{bot}}} \text{temp_rivermix}[k] = \text{sfc_hflux_runoff} + \text{sfc_hflux_calving}, \quad (5.50)$$

where `sfc_hflux_runoff` and `sfc_hflux_calving` are the heat flux, relative to 0°C, associated with the transfer of liquid runoff and solid calving.

- `sfc_hflux_pme`: This term accounts for the heating associated with the passage of precipitation and evaporation across the ocean surface, with heat flux computed relative to 0°C.
- `temp_eta_smooth`: This term accounts for the heating in the $k=1$ cell associated with smoothing the free surface to reduce the impacts from the checker-board null mode. Details are given in Chapter 31 of Griffies (2012).

- `frazil_2d`: As the temperature of seawater cools to the freezing point, sea ice is formed, initially through the production of frazil. Operationally in an ocean model, liquid water can be super-cooled at any particular time step through surface fluxes and transport. An adjustment process in the $k=1$ ocean model grid cell in CM2.6 heats the liquid water back to the freezing point, with this positive heat flux extracted from the ice model as frazil sea ice is formed. The diagnostic `frazil_2d` measures the heat impact on the ocean.

5.5.1.2 Summary of the CM2.5 and CM2.6 ocean heat budget

The following provides a diagnostic accounting of the heat budget for a grid cell in CM2.6-ocean

$$\begin{aligned} \text{temp_tendency}(k=1) = & \text{temp_advection} + \text{temp_submeso} \\ & + \text{temp_vdiffuse_diff_cbt} + \text{temp_nonlocal_KPP} + \text{sw_heat} \\ & + \text{temp_rivermix} \\ & + \text{temp_vdiffuse_sbc} + \text{sfc_hflux_pme} + \text{frazil_2d} + \text{temp_eta_smooth} \end{aligned} \quad (5.51)$$

$$\begin{aligned} \text{temp_tendency}(1 < k \leq 4) = & \text{temp_advection} + \text{temp_submeso} \\ & + \text{temp_vdiffuse_diff_cbt} + \text{temp_nonlocal_KPP} + \text{sw_heat} \\ & + \text{temp_rivermix} \end{aligned} \quad (5.52)$$

$$\begin{aligned} \text{temp_tendency}(4 < k) = & \text{temp_advection} + \text{temp_submeso} \\ & + \text{temp_vdiffuse_diff_cbt} + \text{temp_nonlocal_KPP} + \text{sw_heat}. \end{aligned} \quad (5.53)$$

In CM2.6, each of these terms are saved as annual means for the 1860 (starting around year 40) and CO₂ perturbation simulations. They are also saved in the 1990 simulation starting at year 101.

5.5.2 Heat budget for an ocean grid cell in CM_O1.0_C180

The coarse resolution ocean in CM_O1.0_C180 has a heat budget that is the same as for CM2.5 and CM2.6, but with the following added terms arising from the use of mesoscale eddy parameterization and mixing between open ocean and marginal seas

- `neutral_gm_temp`: This term arises from the convergence of the three dimensional subgrid scale flux components from the [Gent and McWilliams \(1990\)](#) scheme, with the implementation in CM_O1.0_C180 following the methods from [Ferrari et al. \(2010\)](#).
- `neutral_diffusion_temp`: This term arises from the convergence of the three dimensional subgrid scale flux components in the time-explicit portion of the neutral diffusion scheme.
- `temp_vdiffuse_k33`: This term arises from the vertical K33 portion of the neutral diffusion operator that is handled implicitly in time. Note that this term is contained already in the diagnostic `temp_vdiffuse_impl`. The following identity holds

$$\text{temp_vdiffuse_impl} = \text{temp_vdiffuse_sbc} + \text{temp_vdiffuse_diff_cbt} + \text{temp_vdiffuse_k33}. \quad (5.54)$$

It is very useful to split the `temp_vdiffuse_diff_cbt` term, arising from dianeutral mixing processes, from `temp_vdiffuse_k33`, arising from rotated neutral diffusion.

- `temp_xlandmix` and `temp_xlandinsert`: These terms arise from the exchange of volume and tracer between the open ocean and marginal seas, with details given in Chapters 29 and 30 of [Griffies \(2012\)](#).

So in summary, the new terms required for the CM_O1.0_C180 heat budget, relative to the budget for CM2.5 and CM2.6 given by equations (5.51)–(5.53), are the following:

$$\begin{aligned} \text{temp_tendency[CM_O1.0_C180]} = & \text{temp_tendency[CM.5/CM2.6]} \\ & + \text{neutral_diffusion_temp} + \text{neutral_gm_temp} + \text{temp_vdiffuse_k33} \\ & + \text{temp_xlandmix} + \text{temp_xlandinsert}. \end{aligned} \quad (5.55)$$

We also need to diagnose the contributions to the vertically integrated meridional heat transport from these two processes as available in the diagnostics

- temp_xflux_ndiffuse_int_z
- temp_yflux_ndiffuse_int_z
- temp_xflux_gm_int_z
- temp_yflux_gm_int_z.

5.5.3 Heat budget for an ocean grid cell in CM2.5-FLOR

We here document the heat budget for an ocean grid cell in CM2.5-FLOR ([Vecchi et al., 2014](#)).

$$\begin{aligned} \text{temp_tendency[CM2.5-FLOR]}(k=1) = & \text{temp_advection} + \text{temp_submeso} \\ & + \text{neutral_diffusion_temp} + \text{neutral_gm_temp} + \text{temp_vdiffuse_k33} \\ & + \text{convect_heating} + \text{temp_vdiffuse_diff_cbt} + \text{temp_nonlocal_KPP} + \text{sw_heat} \\ & + \text{temp_xlandmix} + \text{temp_xlandinsert} \\ & + \text{temp_vdiffuse_sbc} + \text{sfc_hflux_pme} + \text{frazil_2d} + \text{temp_eta_smooth} \\ & + \text{temp_rivermix} \end{aligned} \quad (5.56)$$

$$\begin{aligned} \text{temp_tendency[CM2.5-FLOR]}(1 < k \leq 4) = & \text{temp_advection} + \text{temp_submeso} \\ & + \text{neutral_diffusion_temp} + \text{neutral_gm_temp} + \text{temp_vdiffuse_k33} \\ & + \text{convect_heating} + \text{temp_vdiffuse_diff_cbt} + \text{temp_nonlocal_KPP} + \text{sw_heat} \\ & + \text{temp_xlandmix} + \text{temp_xlandinsert} \\ & + \text{temp_rivermix} \end{aligned} \quad (5.57)$$

$$\begin{aligned} \text{temp_tendency[ESM2M]}(4 < k) = & \text{temp_advection} + \text{temp_submeso} \\ & + \text{neutral_diffusion_temp} + \text{neutral_gm_temp} + \text{temp_vdiffuse_k33} \\ & + \text{convect_heating} + \text{temp_vdiffuse_diff_cbt} + \text{temp_nonlocal_KPP} + \text{sw_heat} \\ & + \text{temp_xlandmix} + \text{temp_xlandinsert}. \end{aligned} \quad (5.58)$$

5.5.4 Heat budget for an ocean grid cell in ESM2M

We now consider the heat budget for an ocean grid cell in the ESM2M earth system model documented by [Dunne et al. \(2012\)](#) and [Dunne et al. \(2013\)](#). In addition to the processes found in CM_O1.0_C180, ESM2M has the following physical processes enabled.

- mixdownslope_temp: This term arises from the convergence of the fluxes associated with the mixdownslope parameterization scheme detailed in Section 27.4 of [Griffies \(2012\)](#).
- temp_sigma_diff: This term arises from the sigma-diffusion scheme from [Beckmann and Döscher \(1997\)](#) as detailed in Section 27.2.1 of [Griffies \(2012\)](#).
- temp_runoffmix: This term arises from the contributions to the ocean heating from liquid runoff contained in the land-model.
- temp_calvingmix: This term arises from the contributions to the ocean heating from solid runoff contained in the land-model. This term is split from temp_runoffmix, whereas it is combined with temp_runoffmix in CM_O1.0_C180, CM2.5, and CM2.6.
- geo_heat: This term arises from the static geothermal heating applied to the ocean bottom. The geothermal heat flux is applied to the tracer equation as a lower boundary condition to the vertical

diffusion equation. Therefore, the identity (5.45) for the CM2-O suite of models takes the following form in ESM2M

$$\sum_{k=1}^{k\text{bot}} \text{temp_vdiffuse_impl}[k] = \text{temp_vdiffuse_sbc} + \text{geo_heat}. \quad (5.59)$$

So in summary, the new terms required for the ESM2M heat budget, relative to the budget for CM_O1.0_C180 given by equation (5.55), are the following:

$$\begin{aligned} \text{temp_tendency[ESM2M]}(k=1) &= \text{temp_advection} + \text{temp_submeso} \\ &\quad + \text{neutral_diffusion_temp} + \text{neutral_gm_temp} + \text{temp_vdiffuse_k33} \\ &\quad + \text{temp_vdiffuse_diff_cbt} + \text{temp_nonlocal_KPP} + \text{sw_heat} \\ &\quad + \text{temp_runoffmix} + \text{temp_calvingmix} \\ &\quad + \text{mixdownslope_temp} + \text{temp_sigma_diff} \\ &\quad + \text{temp_vdiffuse_sbc} + \text{sfc_hflux_pme} + \text{frazil_2d} + \text{temp_eta_smooth} \end{aligned} \quad (5.60)$$

$$\begin{aligned} \text{temp_tendency[ESM2M]}(1 < k \leq 4) &= \text{temp_advection} + \text{temp_submeso} \\ &\quad + \text{neutral_diffusion_temp} + \text{neutral_gm_temp} + \text{temp_vdiffuse_k33} \\ &\quad + \text{temp_vdiffuse_diff_cbt} + \text{temp_nonlocal_KPP} + \text{sw_heat} \\ &\quad + \text{temp_runoffmix} + \text{temp_calvingmix} \\ &\quad + \text{mixdownslope_temp} + \text{temp_sigma_diff} \\ &\quad + \text{geo_heat}[k = k\text{bot}] \end{aligned} \quad (5.61)$$

$$\begin{aligned} \text{temp_tendency[ESM2M]}(4 < k) &= \text{temp_advection} + \text{temp_submeso} \\ &\quad + \text{neutral_diffusion_temp} + \text{neutral_gm_temp} + \text{temp_vdiffuse_k33} \\ &\quad + \text{temp_vdiffuse_diff_cbt} + \text{temp_nonlocal_KPP} + \text{sw_heat} \\ &\quad + \text{mixdownslope_temp} + \text{temp_sigma_diff} \\ &\quad + \text{geo_heat}[k = k\text{bot}]. \end{aligned} \quad (5.62)$$

5.6 Depth integrated heat budget

A vertical sum of the tracer budget (5.35a)-(5.35c) over an ocean column leads to the semi-discrete depth integrated tracer budget

$$\underbrace{\partial_t \left(\sum_k C \rho dz \right)}_{\text{tendency}} = \underbrace{-\nabla_s \cdot \left(\sum_k \rho dz (\mathbf{u} C + \mathbf{F}) \right)}_{\text{transport convergence}} + \underbrace{\left(Q_{\text{advec}}^{(c)} + Q_{\text{non-advec}}^{(c)} + Q_{\text{bott}}^{(c)} \right)}_{\text{boundary fluxes}} + \underbrace{\sum_k S^{(c)} \rho dz}_{\text{sources}}. \quad (5.63)$$

As expected, the only contributions from vertical fluxes come from the top and bottom boundaries. Furthermore, by setting the tracer concentration to a uniform constant, all the subgrid scale flux terms vanish, in which case the budget reduces to the vertically integrated mass budget. Since CM2-O makes the Boussinesq approximation, the vertically integrated mass budget reduces to the volume budget for an ocean column

$$\partial_t \left(\sum_k dz \right) = -\nabla \cdot \left(\sum_k dz \mathbf{u} \right) + Q^{\text{mass}} / \rho_o, \quad (5.64)$$

where the interior mass sources, $S^{(m)}$, are zero in CM2.5 and CM2.6, though nonzero due to cross-land mixing in CM2_O1deg_C180. The vertical thickness of a column is associated with changes in the sea

surface height, η , so that we can write the volume budget in the form of the Boussinesq sea surface height equation (4.1)

$$\rho_o \left(\frac{\partial \eta}{\partial t} \right) = -\rho_o \nabla \cdot \mathbf{U} + Q^{\text{mass}}, \quad (5.65)$$

where $\mathbf{U} = \sum_k \mathbf{u} dz$ is the depth integrated horizontal velocity.

Specializing the budget (5.63) to the case of heat yields the vertically integrated heat budget

$$\underbrace{\partial_t \left(\sum_k \Theta \rho dz \right)}_{\text{tendency}} = \underbrace{-\nabla_s \cdot \left(\sum_k \rho dz (\mathbf{u} \Theta + \mathbf{F}) \right)}_{\text{transport convergence}} + \underbrace{\left(Q_{\text{advec}}^{(\Theta)} + Q_{\text{non-advec}}^{(\Theta)} + Q_{\text{bott}}^{(\Theta)} \right)}_{\text{boundary fluxes}}. \quad (5.66)$$

The CM2-O suite of simulations has no geothermal heating, in which case $Q_{\text{bott}}^{(\Theta)} = 0$, though the ESM2M simulations use geothermal heating. Figure 5.10 exhibits the heat budget (5.66) for the CM2-O suite of simulations. The time average used to compute the budget terms in this figure leads to a rather small time tendency, so that the right hand side terms nearly balance. That is, the net tendency over the time averaged period is the small residual between two large and compensating terms due to ocean transport processes, resolved and parameterized, and boundary fluxes. Note that the ocean transport processes all have a zero global integral, since they only act to redistribute heat that enters through boundary fluxes.

Figure 5.11 shows maps for the budget (5.66) in the CM2-O suite. The dominant terms are associated with resolved advection as well as parameterized submesoscale and mesoscale eddies. Recall the parameterized mesoscale contribution is only present for CM_O1p0_C180 (Section 3.13). The tendency is a small residual between the heat fluxes crossing through the ocean boundary, and ocean transport that acts to redistribute the boundary heat. Even for the one-degree model, the resolved advective transport locally provides the bulk of the ocean transport contribution to the heat budget.

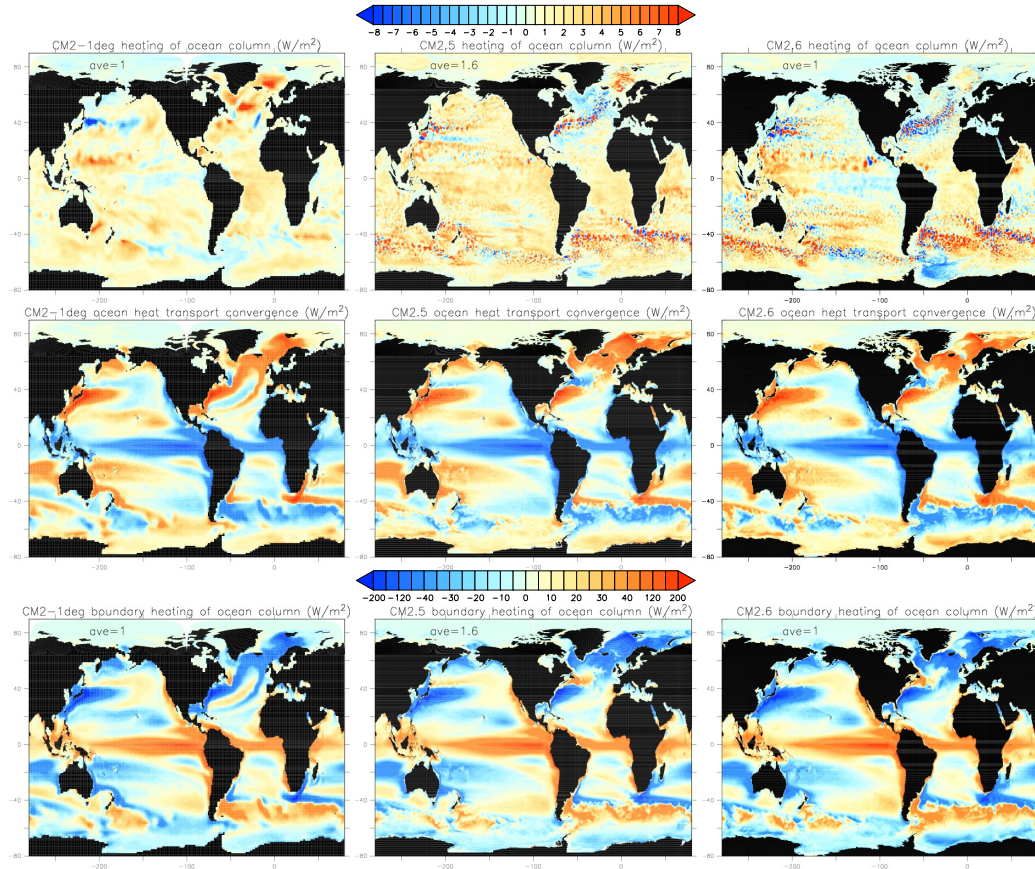


Figure 5.10: Maps of the vertically integrated heat budget (W m^{-2}) according to equation (5.66), as computed from a time mean over years 101-140. The first row shows the net heating over the ocean column. The second row shows the contribution to the heating from the convergence of ocean transport processes, both resolved and parameterized. The third row shows the net heat fluxes through the ocean surface boundary, both advective and non-advective. The net heating over the ocean column is the small residual between surface boundary fluxes and the convergence of ocean transport from advection and subgrid scale processes. Also note that ocean transport processes have a global mean of zero, since they act only to redistribute heat that enters through the boundaries.

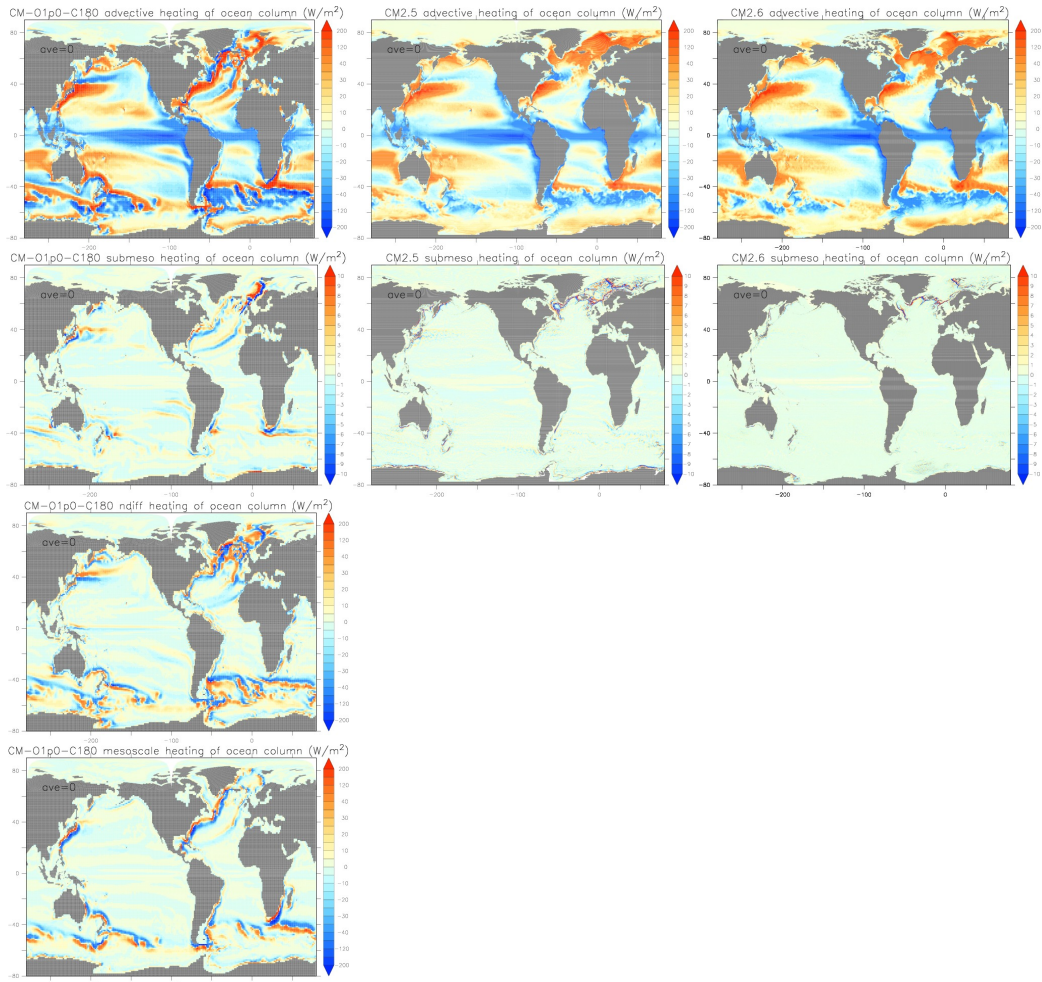


Figure 5.11: Maps of the ocean horizontal transport convergences contributing to the vertically integrated heat budget (W m^{-2}) according to equation (5.66), as computed from a time mean over years 101–140. The first row shows the contribution from resolved advective heat fluxes; the second row from parameterized submesoscale heat fluxes; the third row from parameterized neutral diffusive heat fluxes; the fourth row from parameterized mesoscale eddy induced advective heat fluxes. The neutral diffusion and mesoscale eddy advection contributions are absent in CM2.5 and CM2.6, as these models do not employ a mesoscale eddy parameterization. Heating from submesoscale closure contributes a negligible amount to CM2.5 and CM2.6, where the dominant transport arises from resolved scale advection.

5.7 Poleward heat transport

The CM2-O ocean grid is based on a tripolar layout, which includes a bipolar grid arrangement in the Arctic region poleward of 65°N. The bipolar Arctic in principle introduces some troubles when interested in obtaining poleward tracer transport diagnostics. However, for many purposes, such as heat transport, the transport north of 65°N is quite small, so the distinction between poleward and y-ward can be ignored. Here, the term “y-ward” refers to the transport along lines according to the model’s y-grid lines. In summary, we ignore the distinction between poleward and y-ward, and use the symbols “x” and “y” to refer to generalized longitude and latitude coordinates used by MOM5.

To develop an expression for the y-ward tracer transport, perform an x-ward integral of the depth integrated tracer budget (5.63) to render

$$\partial_t \left(\sum_{i,k} C \rho dx dz \right) = - \sum_i dx \frac{\partial}{\partial y} \left(\sum_k \rho dz (v C + F^{(y)}) \right) + \sum_i dx \left(Q_{\text{advect}}^{(c)} + Q_{\text{non-advect}}^{(c)} + Q_{\text{bott}}^{(c)} \right) + \sum_{i,k} S^{(c)} \rho dx dz. \quad (5.67)$$

The x-ward advective and SGS fluxes were dropped, which follows by assuming either periodicity or no-flux side boundaries. We next integrate y-ward (generalized meridional), starting from the Antarctic continent where the y-ward advective and SGS fluxes vanish, and stop at an arbitrary latitude $y = y_{jn}$ north of the southern boundary

$$\partial_t \left(\sum_{i,k,j=1}^{j=jn} C \rho dx dy dz \right) = - \sum_i dx \left(\sum_k \rho dz (v C + F^{(y)}) \right)_{y=y_n} + \sum_{i,j=1}^{j=jn} dx dy \left(Q_{\text{advect}}^{(c)} + Q_{\text{non-advect}}^{(c)} + Q_{\text{bott}}^{(c)} \right) + \sum_{i,k,j=1}^{j=jn} S^{(c)} \rho dx dy dz. \quad (5.68)$$

The y-ward advective and SGS fluxes are of particular interest, which motivates introducing the notation

$$T^{\text{merid-adv}} = \sum_i dx \sum_k v C \rho dz \quad (5.69a)$$

$$T^{\text{merid-sgs}} = \sum_i dx \sum_k F^{(y)} \rho dz, \quad (5.69b)$$

thus leading to the budget

$$\partial_t \left(\sum_{i,k,j=1}^{j=jn} C \rho dx dy dz \right) = -(T^{\text{merid-adv}} + T^{\text{merid-sgs}})_{y=y_n} + \sum_{i,j=1}^{j=jn} dx dy \left(Q_{\text{advect}}^{(c)} + Q_{\text{non-advect}}^{(c)} + Q_{\text{bott}}^{(c)} \right) + \sum_{i,k,j=1}^{j=jn} S^{(c)} \rho dx dy dz. \quad (5.70)$$

In a steady state, the y-ward transport from advection and SGS processes balance the boundary fluxes and interior source/sink terms

$$(T^{\text{merid-adv}} + T^{\text{merid-sgs}})_{y=y_n} = \sum_{i,j=1}^{j=jn} dx dy \left(Q_{\text{advect}}^{(c)} + Q_{\text{non-advect}}^{(c)} + Q_{\text{bott}}^{(c)} \right) + \sum_{i,k,j=1}^{j=jn} S^{(c)} \rho dx dy dz. \quad (5.71)$$

We now specialize the zonal and vertical integrated tracer budget (5.67) to the case of heat, in which case

$$\partial_t \left(\sum_{i,k} \Theta \rho dx dz \right) = - \sum_i dx \frac{\partial}{\partial y} \left(\sum_k \rho dz (v \Theta + F^{(y)}) \right) + \sum_i dx \left(Q_{\text{advect}}^{(\Theta)} + Q_{\text{non-advect}}^{(\Theta)} + Q_{\text{bott}}^{(\Theta)} \right), \quad (5.72)$$

where we dropped the source term, and note that $Q_{\text{bott}}^{(\Theta)} = 0$ for the CM2-O suite, but is nonzero for ESM2M. Figure 5.12 shows the contributions to the heat budget (5.72). This figure is obtained from taking the area integral of Figure 5.11, performing a zonal sum, then dividing by the area of the respective zonal strip. Figure 5.12 confirms the impression from Figure 5.11, whereby the local heating over an ocean column is

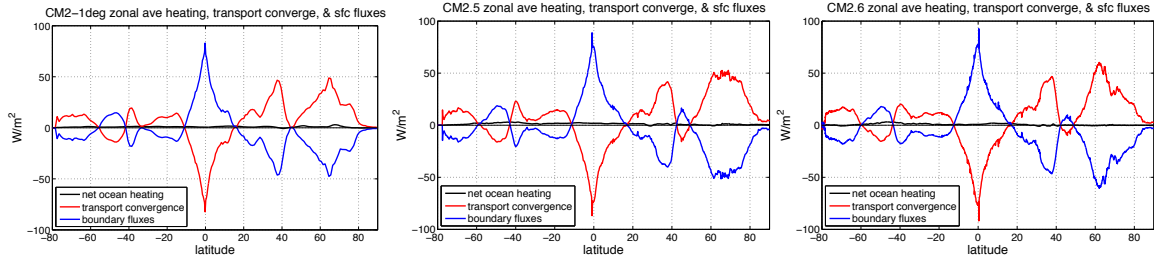


Figure 5.12: Vertical integrated and zonal averaged heat budget (W m^{-2}) according to equation (5.72) as time averaged over years 101-140. Note that the net heating over the ocean column arises from a small residual between surface fluxes and ocean transport. Also note that ocean transport processes have a global mean of zero, since they act only to redistribute heat that enters through the boundaries.

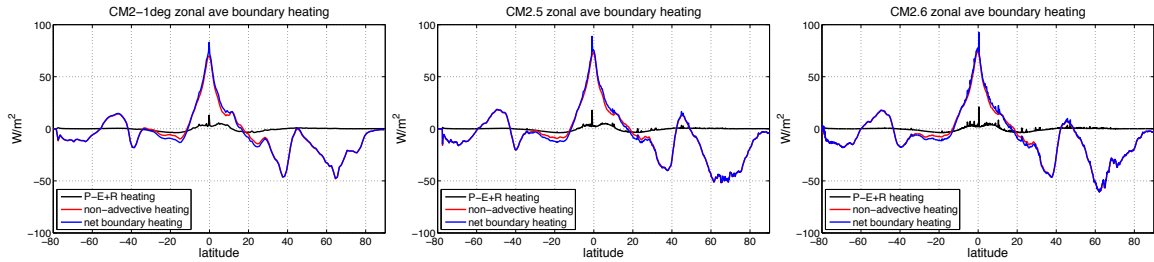


Figure 5.13: Zonal averaged boundary heat flux crossing the ocean surface (W m^{-2}). We decompose the flux into that portion due to mass fluxes (precipitation minus evaporation plus rivers), and that due to radiative and turbulent heating. Note the relatively large contribution in the tropics due to the evaporation and precipitation in this region acting on the warm surface ocean waters. I am unsure of this interpretation. The Figure 5.21 results are smooth for heating from p-e+r, so I am somewhat puzzled. I also do not understand why there are spikes in the CM2.5 and CM2.6 simulations in the northern mid-latitudes.

a residual between the surface boundary heating and ocean transport that acts to redistribute the heat. Figure 5.13 further decomposes the surface heat flux contribution into that portion arising from mass fluxes (precipitation minus evaporation plus rivers), and that due to radiative and turbulent heating.

We next perform the indefinite integral in the meridional direction, starting from the southern boundary and moving northward, resulting in the heat budget

$$\partial_t \left(\sum_{i,k,j=1}^{j=jn} \Theta \rho dx dy dz \right) = -(\mathcal{T}^{\text{merid-adv}} + \mathcal{T}^{\text{merid-sgs}})_{y=y_n} + \sum_{i,j=1}^{j=jn} dx dy \left(Q_{\text{advec}}^{(\Theta)} + Q_{\text{non-advec}}^{(\Theta)} + Q_{\text{bott}}^{(\Theta)} \right), \quad (5.73)$$

where the meridional advective and subgrid scale heat transports take the form

$$\mathcal{T}^{\text{merid-adv}} = \sum_i dx \sum_k v \Theta \rho dz \quad (5.74)$$

$$\mathcal{T}^{\text{merid-sgs}} = \sum_i dx \sum_k F^{(y)} \rho dz. \quad (5.75)$$

Contributions from the subgrid scale flux $F^{(y)}$ are generally sub-dominant to the resolved advection. However, locally there are regions where the submesoscale eddy parameterization (Section 3.12) is important, and for CM_O1p0_C180 the mesoscale eddy parameterization (Section 3.13) is particularly important in

the Southern Ocean. Figure ?? shows the resulting heat budget (5.73) for the CM2-O suite. A net ocean heating in *CM_O1p0_C180* results from a boundary heat flux that is not fully balanced by ocean transport. The imbalance is largely in the Southern Hemisphere, resulting in the accumulation of heat in the Northern Hemisphere.

Figure 5.15 shows the meridional ocean heat transport according to equations (5.74) and (5.75). Transport from the resolved advection plays a dominant role. However, in the Southern Ocean, the parameterized mesoscale eddy contribution in *CM_O1p0_C180* is important for moving heat poleward (to the south). Note that the contribution from the diffusive parameterization is larger than the advective parameterization, with this relative role not fully appreciated in the community.³

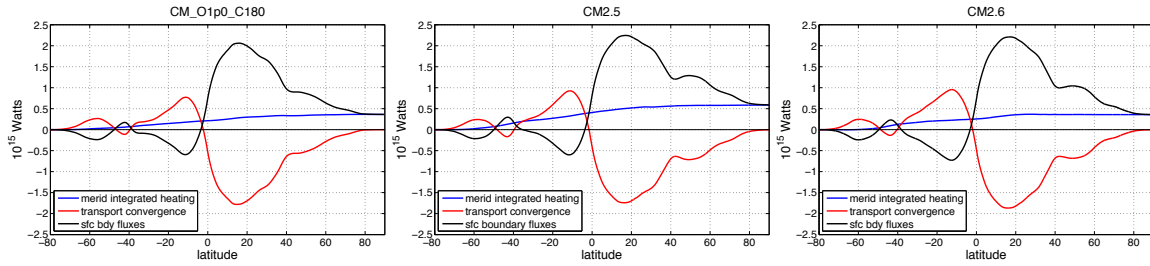


Figure 5.14: Meridional heat budget (Watts) according to equation (5.73) as time averaged over years 101-140. This figure is obtained by forming a cumulative sum in the meridional direction, starting from the southern boundary, from the tendency terms shown in Figure 5.12. Note that the residual heating results from a boundary heat flux that is not balanced by ocean transport. The imbalance is largely in the Southern Hemisphere, resulting in the accumulation of heat in the Northern Hemisphere thus leading to a nonzero trend. The residual is largest in CM2.5.

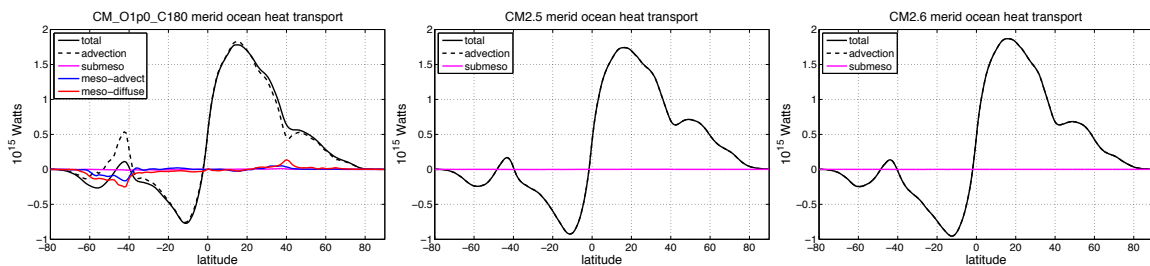


Figure 5.15: Meridional ocean heat transport (Watts) for the global ocean, according to equations (5.74) and (5.75), as computed from a time average over years 101-140.

³We should determine how much of this contribution arises from the horizontal diffusion active in the mixed layer, versus neutral diffusion in the interior.

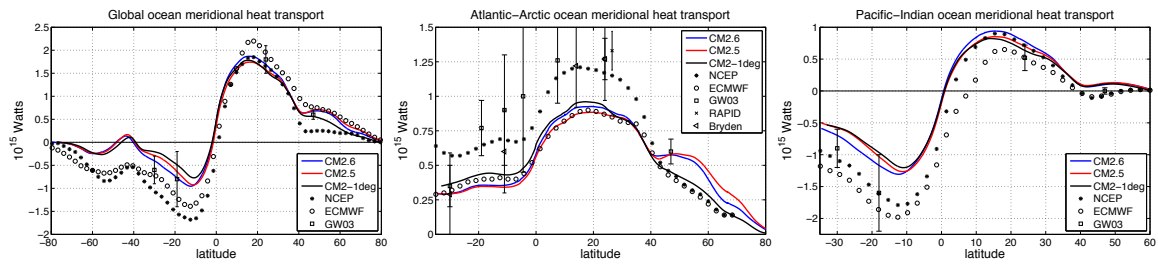


Figure 5.16: Meridional ocean heat transport (Peta-Watts) for the global ocean, Atlantic-Arctic oceans, and Pacific-Indian oceans as computed from a time average over years 101-140. Note the different vertical scales on the figures. There is a notably weak poleward transport in the Atlantic sector for CM2-1degree, with this low heat transport associated with the overly extensive sea ice coverage in the Labrador Sea. We note that this low Atlantic heat transport is associated with a larger meridional overturning in CM2-1degree than CM2.5 and CM2.6 (Figures 4.10 and 4.11). The low heat transport in CM2-1degree arises from the large warm bias in the intermediate waters of the Atlantic which reduce the vertical temperature difference relative to the CM2.5 and CM2.6 simulations.

5.8 Heat budget for surface ocean grid cells

The surface ocean directly interacts with the overlying atmosphere and cryosphere (sea ice and land ice). The heat within a surface ocean model grid cell is directly impacted by surface boundary heat fluxes as well as advective and subgrid scale transport. Surface temperature is used to determine air-sea and ice-sea heat fluxes. We consider in this section the budget for heat in a surface model grid cell for the CM2-O suite of simulations. To start our discussion, recall the SST bias maps shown in Figure 5.1.

5.8.1 Diagnostic budget terms

The semi-discrete heat budget for a surface ocean grid cell is given by specializing equation (5.35a) to temperature, in which case we have

$$\partial_t (\Theta \rho dz) = -\nabla_s \cdot [(\mathbf{u} \Theta + \mathbf{F}) \rho dz] + [\rho (w^{(s)} \Theta + F^{(s)})]_{s=s_{k=1}} + Q_{\text{advect}}^{(\Theta)} + Q_{\text{non-advect}}^{(\Theta)}, \quad (5.76)$$

where we dropped source terms. Equation (5.51) identified the diagnostic terms appropriate for the budget (5.76) in the CM2.5 and CM2.6 models

$$\begin{aligned} \text{temp_tendency}(k=1) = & \text{temp_advection} + \text{temp_submeso} \\ & + \text{temp_vdiffuse_diff_cbt} + \text{temp_nonlocal_KPP} + \text{sw_heat} \\ & + \text{temp_rivermix} + \text{sfc_hflux_pme} \\ & + \text{temp_vdiffuse_sbc} + \text{frazil_2d} + \text{temp_eta_smooth}, \end{aligned} \quad (5.77)$$

whereas equation (5.55) identified the budget terms for CM_O1.0_C180

$$\begin{aligned} \text{temp_tendency[CM_O1.0_C180]} = & \text{temp_tendency[CM.5/CM2.6]} \\ & + \text{neutral_diffusion_temp} + \text{temp_vdiffuse_k33} + \text{neutral_gm_temp} \\ & + \text{temp_xlandmix} + \text{temp_xlandinsert}. \end{aligned} \quad (5.78)$$

There are various means to organize the budget terms according to physical processes or their role as boundary versus ocean contributions. We present various methods in the following.

5.8.1.1 Ocean transport and surface boundary fluxes

The terms contributing to the budget (5.76) consist of ocean transport and boundary fluxes

$$\underbrace{\partial_t (\Theta \rho dz)}_{\text{heat tendency}} = \underbrace{-\nabla_s \cdot [(\mathbf{u} \Theta + \mathbf{F}) \rho dz] + [\rho (w^{(s)} \Theta + F^{(s)})]_{s=s_{k=1}}}_{\text{ocean transport}} + \underbrace{Q_{\text{advect}}^{(\Theta)} + Q_{\text{non-advect}}^{(\Theta)}}_{\text{boundary fluxes}}, \quad (5.79)$$

That is, we partition the total tendency into a contribution from ocean transport, either from resolved advective processes or subgrid scale processes, and a contribution from surface boundary fluxes, both advective and non-advective. Notably, the shortwave radiation input through ocean surface fluxes appears in the boundary flux contribution. However, a portion of that penetrates into the interior and thus leaves the bottom face of the surface grid cell. We consider this penetrative radiation term as part of the ocean transport term since it is a function of ocean optical properties.

We can thus organize the diagnostic expressions (5.77) and (5.78) according the decomposition proposed by equation (5.79) for the ocean transport

$$\begin{aligned} \text{ocean transport}(k=1) = & \text{temp_advection} + \text{temp_submeso} + \text{temp_vdiffuse_diff_cbt} \\ & + \text{temp_nonlocal_KPP} + \text{sw_heat} + \text{temp_eta_smooth} \\ & + \text{neutral_diffusion_temp} + \text{temp_vdiffuse_k33} + \text{neutral_gm_temp} \\ & + \text{temp_xlandmix} + \text{temp_xlandinsert}, \end{aligned} \quad (5.80)$$

and for the boundary fluxes

$$\text{boundary fluxes} = \text{temp_rivermix} + \text{sfc_hflux_pme} + \text{temp_vdiffuse_sbc} + \text{frazil_2d}. \quad (5.81)$$

5.8.1.2 Advection, mixing, and boundary processes

Another means to partition the various budget terms is according to the their role as advective transport versus mixing processes. In this case, we partition the surface heat budget according to

$$\underbrace{\partial_t(\Theta \rho dz)}_{\text{heat tendency}} = \underbrace{-\nabla_s \cdot (\mathbf{u} \Theta \rho dz) + (\rho w^{(s)} \Theta)_{s=s_k=1} + Q_{\text{advect}}^{(\Theta)} - \nabla_s \cdot (\mathbf{F}^{\text{sgs advect}} \rho dz) + (\rho F^{(s) \text{ sgs advect}})_{s=s_k=1}}_{\text{advective transport}} \\ - \underbrace{\nabla_s \cdot (\mathbf{F}^{\text{sgs mix}} \rho dz) + (\rho F^{(s) \text{ sgs mix}})_{s=s_k=1}}_{\text{mixing transport}} + \underbrace{Q_{\text{non-advect}}^{(\Theta)}}_{\text{non-advect boundary}}. \quad (5.82)$$

Note how we combined all advective related processes together, including those associated with subgrid scale transport parameterized as an advective or skew-diffusive process, as well as transport across the ocean surface boundary. We now summarize in more detail this partitioning.

- **ADVECTIVE PROCESSES:** We consider advective processes as those that arise from advection due to the resolved flow, as well as from parameterized submesoscale and mesoscale advection or skew-diffusion. We also consider the transfer of heat within mass crossing the ocean boundary to be advective in nature, albeit as realized numerically through a very diffusive first order upwind discretization. We thus define the advective processes active in the surface grid cell as

$$\text{ADVECTIVE PROCESSES} = \text{temp_advection} + \text{temp_submeso} + \text{temp_rivermix} + \text{sfc_hflux_pme} + \text{neutral_gm_temp}. \quad (5.83)$$

The `neutral_gm_temp` term is absent in the CM2.5 and CM2.6 simulations, since they do not include a mesoscale eddy parameterization.

- **NON-ADVECTIVE BOUNDARY FLUXES:** Surface boundary fluxes enter through the top face of the surface grid cell. A portion of the shortwave flux leaves through the bottom face of this cell according to the optical properties of the seawater. We consider here only those non-advective fluxes, since the advective boundary fluxes from evaporation, precipitation, and rivers are accounted for in the advective processes. We define the non-advective boundary fluxes impacting heat in the surface grid cell according to

$$\text{NON-ADVECTIVE BOUNDARY FLUXES} = \text{temp_vdiffuse_sbc} + \text{frazil_2d} + \text{sw_heat}. \quad (5.84)$$

- **MIXING:** Mixing processes arise from local diffusion, be it vertical or neutral, and non-local mixing from KPP. There are additional mixing processes associated with smoothing the sea level, and the transfer of heat across unresolved straits in CM_O1.0_C180. We thus define the mixing processes active in the surface grid cell as

$$\text{MIXING PROCESSES} = \text{temp_vdiffuse_diff_cbt} + \text{temp_nonlocal_KPP} + \text{temp_eta_smooth} + \text{neutral_diffusion_temp} + \text{temp_vdiffuse_k33} + \text{temp_xlandmix} + \text{temp_xlandinsert}. \quad (5.85)$$

The terms `neutral_diffusion_temp`, `temp_vdiffuse_k33`, `temp_xlandmix`, and `temp_xlandinsert` are absent in the CM2.5 and CM2.6 simulations.

- **MIXING + NON-ADVECTIVE BOUNDARY:** There is an implicit assumption that boundary fluxes that enter the ocean impact seawater. However, these fluxes only impact the ocean upon being mixed into

seawater through boundary mixing processes. It is therefore physically sensible to combine the processes we term “mixing” with the non-advection boundary fluxes.

$$\begin{aligned} \text{NON-ADVECTIVE BOUNDARY + MIXING} = & \text{temp_vdiffuse_sbc} + \text{frazil_2d} + \text{sw_heat} \\ & + \text{temp_vdiffuse_diff_cbt} + \text{temp_nonlocal_KPP} + \text{temp_eta_smooth} \\ & + \text{neutral_diffusion_temp} + \text{temp_vdiffuse_k33} \\ & + \text{temp_xlandmix} + \text{temp_xlandinsert}. \end{aligned} \quad (5.86)$$

Again, the terms `neutral_diffusion_temp`, `temp_vdiffuse_k33`, `temp_xlandmix`, and `temp_xlandinsert` are absent in the CM2.5 and CM2.6 simulations.

5.8.2 Global mean surface ocean temperature

We start our discussion of the surface heat budget by considering the global mean of the surface ocean temperature. Horizontally integrating equation (5.76) leads to the surface heat budget

$$\underbrace{\sum_{i,j} dA \partial_t (\Theta \rho dz)}_{\text{heat tendency}} = \underbrace{\sum_{i,j} dA [\rho(w^{(s)} \Theta + F^{(s)})]_{s=s_{k=1}}}_{\text{vertical transport}} + \underbrace{\sum_{i,j} dA (Q_{\text{advect}}^{(\Theta)} + Q_{\text{non-advect}}^{(\Theta)})}_{\text{boundary fluxes}}, \quad (5.87)$$

where we dropped the source term. Global surface ocean heat is thus impacted by vertical transport through advection and subgrid scale processes, and by boundary fluxes. This decomposition of ocean heating follows that proposed in Section 5.8.1.1.

Figure 5.17 shows the annual mean time series for the global mean temperature within the ocean surface in the CM2-O suite of simulations, with this diagnostic computed according to⁴

$$\langle \Theta \rangle^{k=1} = \frac{\int_{k=1} \Theta dA dz}{\int_{k=1} dA dz}. \quad (5.88)$$

The global volume of the surface grid cell,

$$V_{k=1} = \int_{k=1} dA dz \quad (5.89)$$

remains relatively steady in time, largely due to the use of z^* as a vertical coordinate whereby trends in sea level (Figure 4.4) are distributed throughout the full depth. Hence, variability in the averaged surface temperature (5.88) is dominated by variations in the numerator, which measures the heat within the top grid cells. It is notable that the CM2.6 simulation exhibits the least drift in Figure 5.17 from initial conditions, whereas the two coarser models generally cool during the first few decades.

Recall that the global mean temperature, averaged over the full ocean, steadily rises for each of the three models (Figure 5.9). Hence, a net uptake of heat into the ocean, thus increasing the global mean ocean temperature according to equation (5.31), does not necessarily mean the surface temperature increases (Figure 5.17). The reason is that surface boundary heating can be readily transported into the ocean interior through vertical advective and subgrid scale transfer, as per the budget shown in equation (5.87).

We illustrate this process in Figure 5.18 by showing a time series for the horizontally integrated heat accumulated in the surface ocean cells, the corresponding heat transported vertically, and the contribution from surface boundary fluxes. The net heat remaining in the surface ocean is indeed a small residual

⁴Since the top grid cell has a time-dependent thickness, this diagnostic is slightly distinct from the area averaged sea surface temperature (SST) computed without the thickness weighting. Nonetheless, the area averaged SST and grid cell averaged surface temperature exhibit very similar quantitative behaviour. The reason is that the top grid cell in a z^* model has a thickness that remains very close to the constant resting value of 10 m in the A CM2-O suite.

between that entering through the surface from boundary fluxes versus that which leaves the surface through vertical transport. When breaking down the vertical transport terms further, we find that the non-local KPP contribution adds heat to the surface ocean (see Section 3.4.9), whereas vertical advection, vertical diffusion, and penetrative shortwave radiation leaving the bottom face of the cell cool the surface cell. In the remainder of this section, we exhibit maps of the various terms contributing to the surface ocean budget, thus identifying how the various terms compare both regionally and globally.

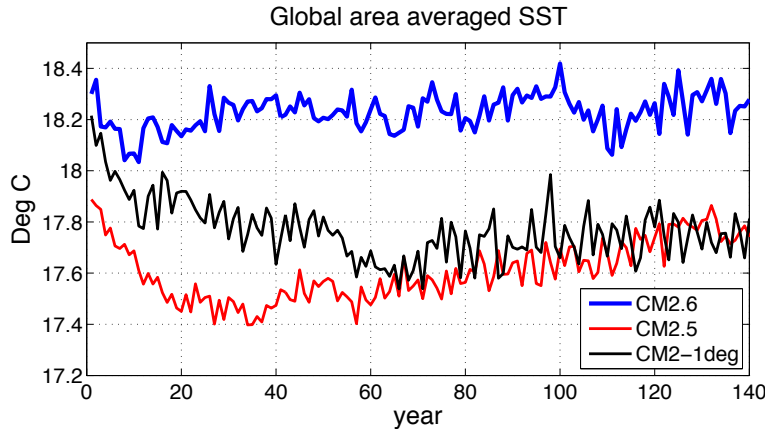


Figure 5.17: Global mean annual mean surface ocean temperature. The MOM5 diagnostic table entry for this time series is temp_surface_ave. Note the different time scales for the three models: CM2.6 reaches a near steady state within roughly 30 years; CM_O1p0_C180 reaches it within about 60 years, though somewhat cooler than CM2.6; and CM2.5 has a linear warming trend over years 40-160 and appears to not have reached a steady state.

5.8.3 Heating as sum of ocean transport and boundary fluxes

Figure 5.19 shows the net heating of the surface model grid cell, along with the heating decomposed into the contributions from ocean transport (equation (5.80)) and boundary fluxes (equation (5.81)). That is, we are showing

$$\text{NET HEATING} = \text{OCEAN TRANSPORT} + \text{SURFACE BOUNDARY FLUXES}. \quad (5.90)$$

In general, the net heating is the small residual of the two much larger terms on the right hand side. Furthermore, these terms are in turn the result of other processes that can be much larger in magnitude arising from mixing, boundary fluxes, and advective processes. We offer the following comments about these patterns.

- In general, the net surface ocean heating exhibits a less coherent pattern relative to the separate patterns for ocean transport and surface boundary fluxes.
- The tropics generally experience a warming due to surface fluxes that is partially compensated by cooling due to ocean transport (e.g., upwelling cool water). The residual yields a warming for most of the tropical regions, particularly in the Pacific.
- The western boundary currents generally experience cooling due to surface fluxes (e.g., latent and sensible) that is partially compensated by warming due to ocean transport. The residual leaves a general pattern of warming, though with less coherent structure than the individual contributing processes. The same comments are relevant for the subpolar North Atlantic.

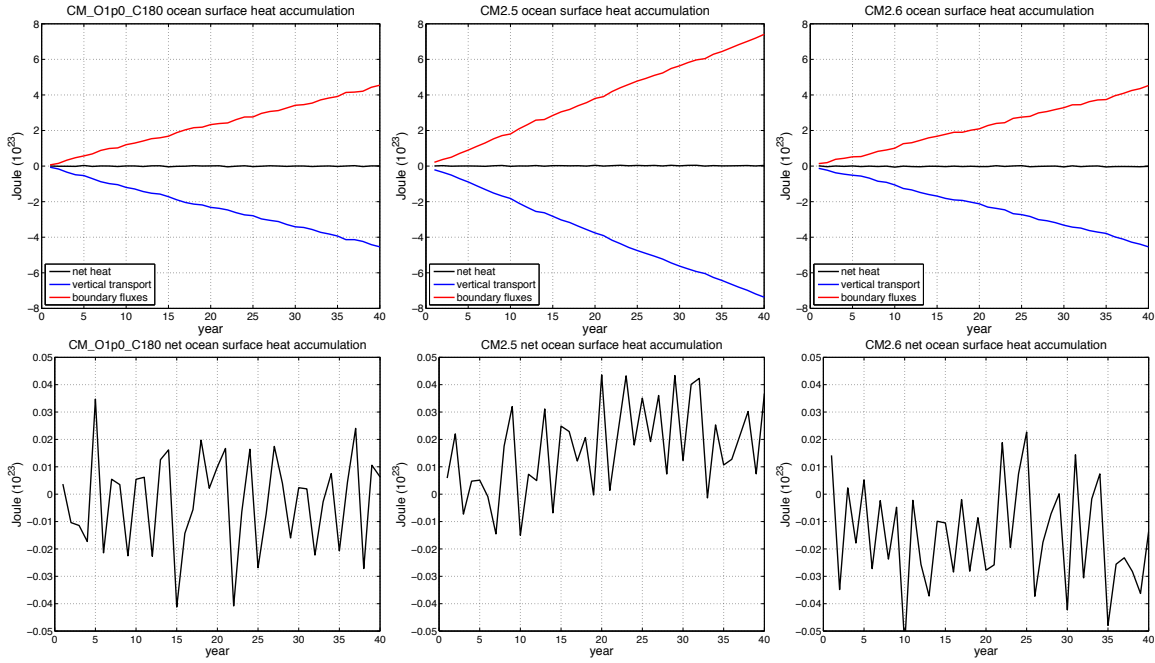


Figure 5.18: Time series for the annual mean net heat accumulated in the surface ocean grid cell relative to year 101. Contributions to the net heating are broken down into vertical transfer (moving heat vertically downward beneath the surface cell) and boundary contributions (moving heat into the surface cell from the upper boundary) according to equation (5.87).

5.8.4 Heating as sum of advection, mixing, and boundary fluxes

Figure 5.20 shows the net heating of the surface model grid cell, along with the heating decomposed into the contributions from mixing plus non-advection surface heat flux as per equation (5.86), as well as from advective processes as per equation (5.83). That is, we are showing

$$\text{NET HEATING} = (\text{NON-ADVECTIVE BOUNDARY} + \text{MIXING}) + \text{ADVECTIVE PROCESSES}. \quad (5.91)$$

In general, the net heating is the small residual of the two much larger terms on the right hand side. Furthermore, these terms are in turn the result of other processes that can be much larger in magnitude arising from mixing, boundary fluxes, and advective processes. We illustrate these further refined terms in the remainder of this section.

5.8.5 Advectional processes

Figure 5.21 shows the heating of the surface model grid cell arising from the various advective processes given by equation (5.83). We offer the following observations based on this figure.

- The dominant pattern for the net advective heating arises from the resolved advective tendency. The submesoscale and mesoscale tendencies are subdominant, as are those from the mass fluxes crossing the ocean surface.
- The resolved advection leads to a net warming of the surface ocean, with the net warming increasing as the grid resolution is refined. Note the large role played by the submesoscale parameterization. **Can the pattern of the resolved flow heating be interpreted as Ekman?**

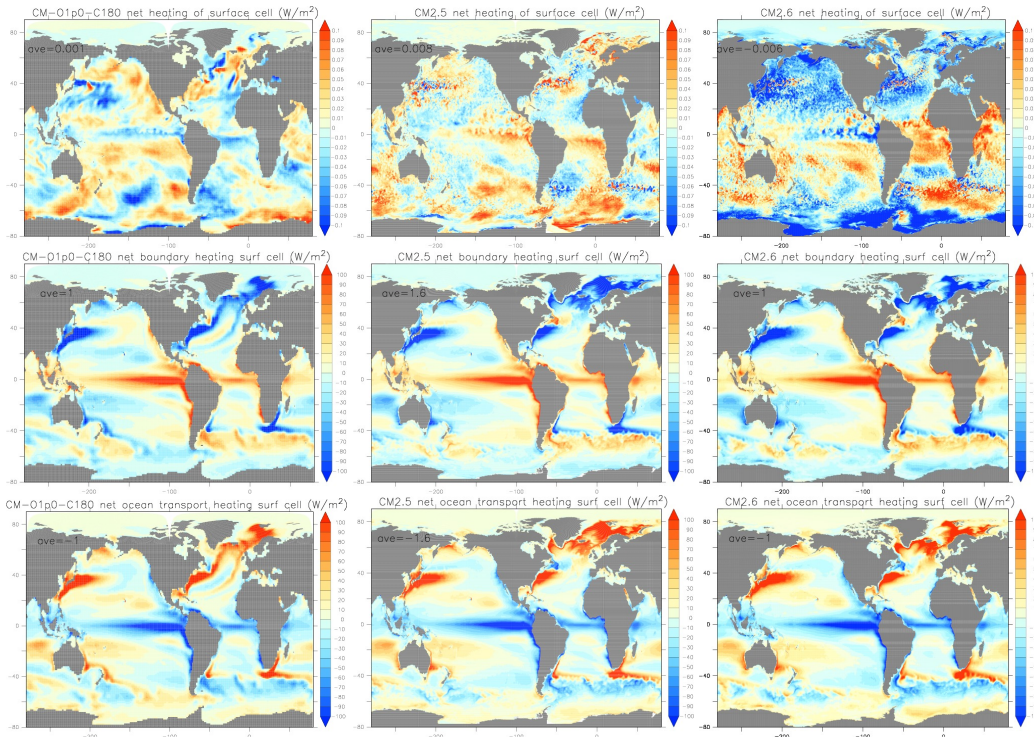


Figure 5.19: Maps of the tendency (W m^{-2}) for heat in the surface grid cell as computed as a time mean over years 101-140. The first row shows the total tendency. The second row shows the sum of the processes associated with ocean transport according to equation (5.80). The third row shows the contribution from fluxes crossing the ocean surface boundary, as per equation (5.81). The area mean tendency is noted on each panel over Siberia. The color bars on the second and third rows are distinct from the first row. Note how the total tendency in the first row is the residual between two largely compensating tendencies from the ocean transport and boundary fluxes. I am puzzled about the large differences between CM2.5 and CM2.6.

- The submesoscale tendency is regionally sub-dominant to the resolved advection, but globally it provides a net warming to the surface ocean that is larger than the net cooling from the resolved advection. The dominance of heating for the surface cell from the submesoscale scheme arises from its tendency to restratify the upper ocean, which means warming the upper portion of the mixed layer and cooling the lower portion.
- The heat contribution from precipitation minus evaporation is dominated by the tropical regions, both due to the larger mass fluxes in the tropics, and due to the warmer temperatures in that region. We note that this term is absent models with a virtual salt flux.
- The heat flux associated with river mixing can be locally quite large, on the order of 1000 W m^{-2} . For example, consider a river, such as the Amazon, that has a mass flux on the order of $0.1 \text{ Sv} = 10^8 \text{ kg sec}^{-1}$ and enters the ocean with a sea surface temperature on the order of 20°C into a grid cell with a horizontal area on the order of $5 \times 10^9 \text{ m}^2$. This mass flux corresponds to a heat flux of

$$\mathcal{H}_{\text{river}} = C_p \left(\frac{10^8 \text{ kg sec}^{-1} 20^\circ\text{C}}{5 \times 10^9 \text{ m}^2} \right) \approx 1600 \text{ W m}^{-2}. \quad (5.92)$$

This heat flux induces a large and compensating advective tendency local to the grid cell where the river water is inserted to the ocean.

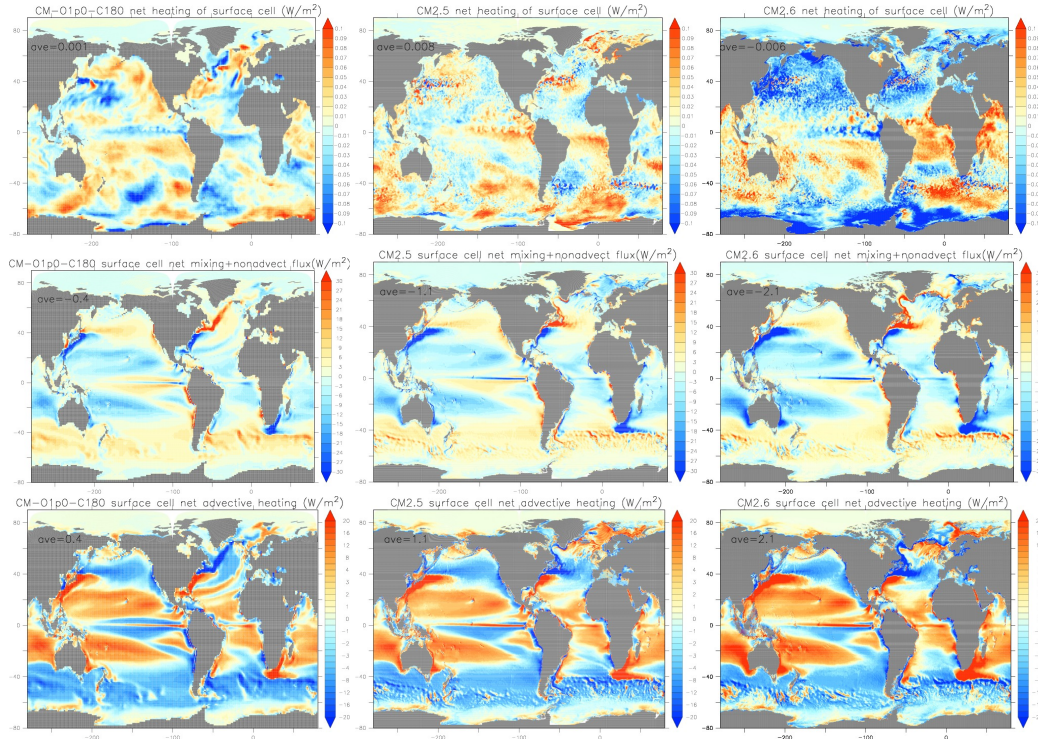


Figure 5.20: Maps of the tendency (W m^{-2}) for heat in the surface grid cell as computed as a time mean over years 101-140. The first row shows the total tendency. The second row shows the sum of the mixing plus non-advective surface heat flux as per equation (5.86). The third row shows the net advective tendency, as per equation (5.83). The area mean tendency is noted on each panel over Siberia. The color bars on the second and third rows are distinct from the first row. Note how the total tendency in the first row is the residual between two largely compensating tendencies from mixing, boundary fluxes, and advective processes.

In addition to liquid river runoff, the river term accounts for the mass transport associated with calving icebergs (Section 3.15), hence the nonzero contributions appearing far from the coastlines.

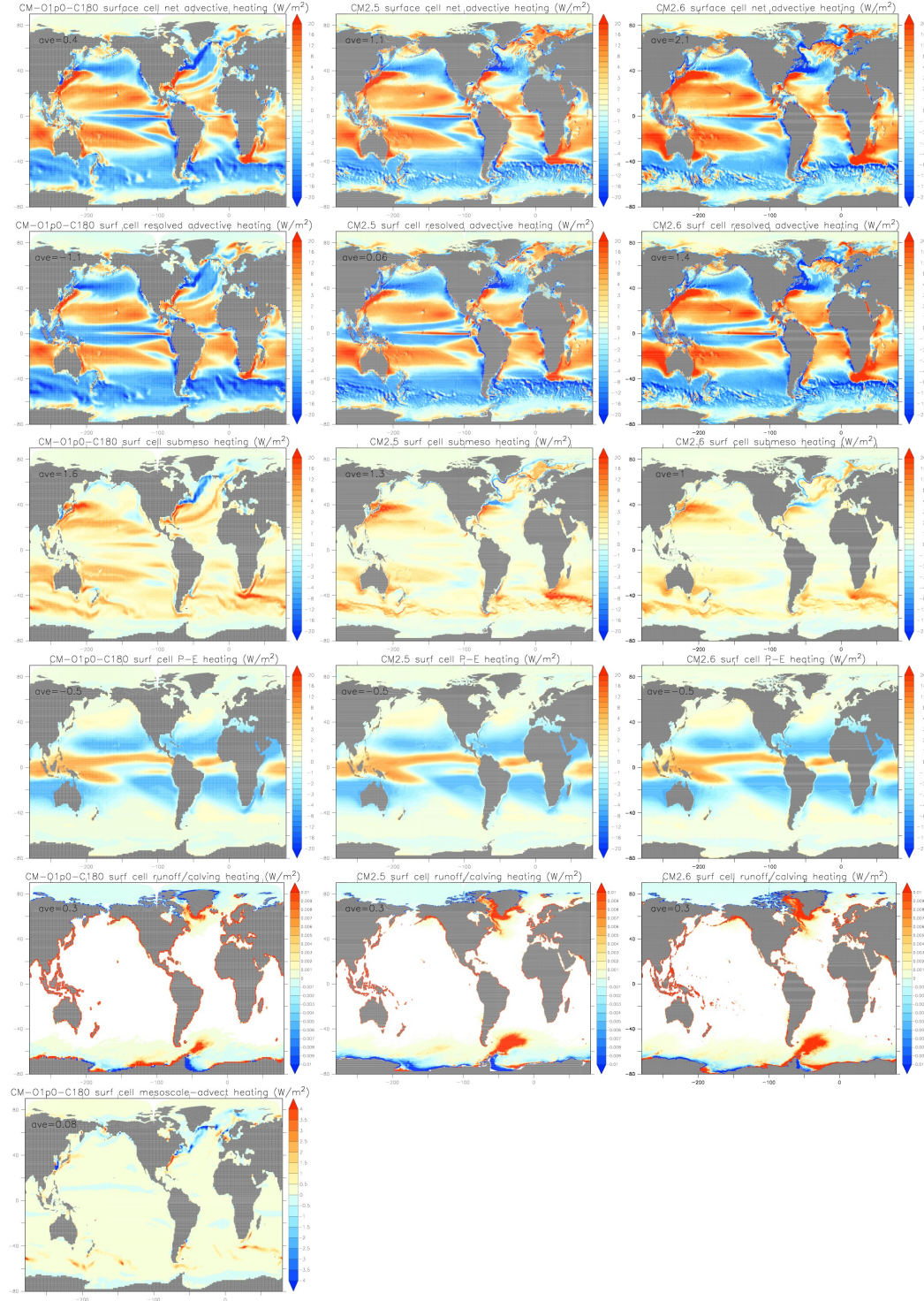


Figure 5.21: Maps of the advective tendency (W m^{-2}) for heat in the surface grid cell as time averaged over years 101-140, with the terms defined by equation (5.83). The first row is the net advective tendency that also appears in Figure 5.20. Note the different color bar ranges for the rivermix row. The area mean tendency is noted on each panel over Siberia.

5.8.6 Non-advective surface boundary fluxes plus mixing

Figure 5.22 shows the heating of the surface model grid cell arising from the non-advective surface heat processes detailed in equation (5.84), plus the mixing processes detailed in equation (5.85).

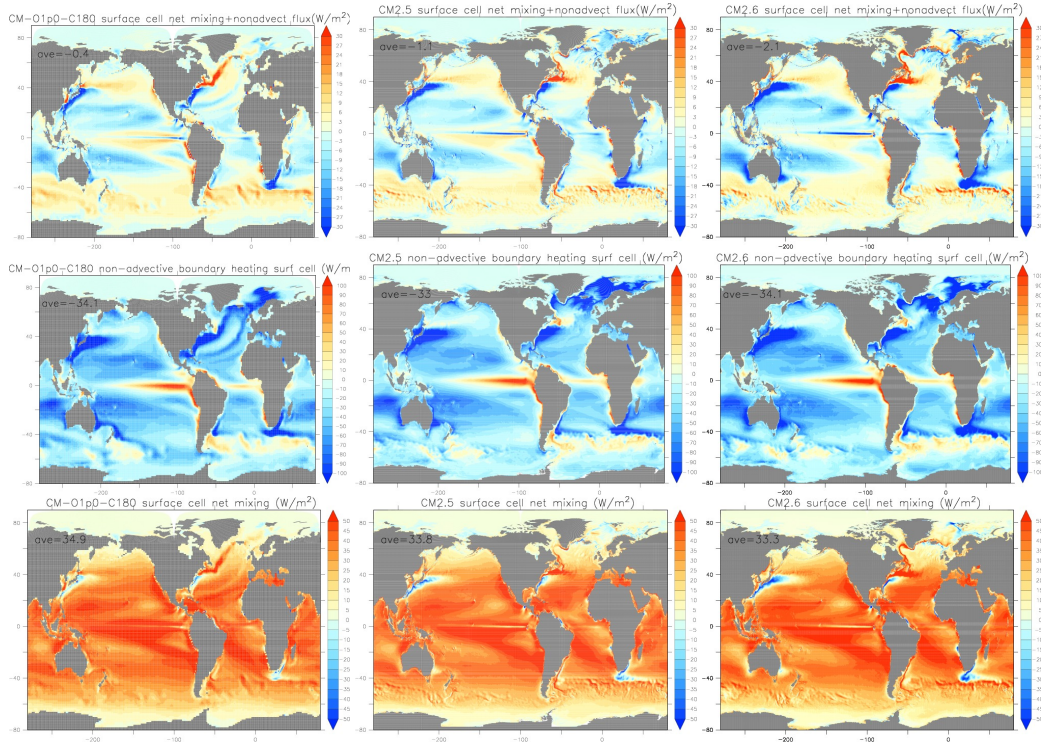


Figure 5.22: The top row shows the sum of the mixing plus non-advective surface heat flux as per equation (5.86), with these images also shown in Figure 5.20. The next row shows just the non-advective surface boundary fluxes (W m^{-2}) for heat in the surface grid cell, with the terms defined by equation (5.84). The third row shows the tendency (W m^{-2}) for heat in the surface grid cell arising from mixing processes as defined by equation (5.85). Shown here are time means over years 101–140. The area mean tendency is noted on each panel over Siberia.

5.8.7 Mixing processes

Figure 5.23 shows the heating of the surface model grid cell arising from the various mixing processes detailed in equation (5.85). We make the following observations of these figures.

- Vertical diffusion predominantly cools the surface cell. As discussed in Section 3.4.9, by assuming the upper ocean is stably stratified ($\partial_z \Theta > 0$), a downgradient diffusive flux at the bottom face of the surface cell will tend to move heat downward, thus cooling the surface cell. With the no-flux surface boundary condition applied to the local downgradient diffusive flux (equation (3.37)), we thus have a divergence of heat from the $k = 1$ cell due to the parameterized local diffusion. Hence, downgradient diffusion generally cools the surface cell.
- The non-local transport term from KPP predominantly warms the top grid cell. As discussed in Section 3.4.9, the KPP non-local transport is non-zero only for cases of negative buoyancy forcing. Assuming such forcing occurs due to a cooling surface heat flux, we already showed in Section 3.4.8

that $\gamma_\theta > 0$ for cooling (equation (3.32)). With the no-flux surface boundary condition applied to the non-local KPP term (equation (3.35)), we thus have a positive convergence of heat into the $k = 1$ cell due to the parameterized non-local flux. Hence, the parameterized non-local fluxes tend to heat the $k = 1$ cells whereas the parameterized downgradient diffusive fluxes tend to cool this cell.

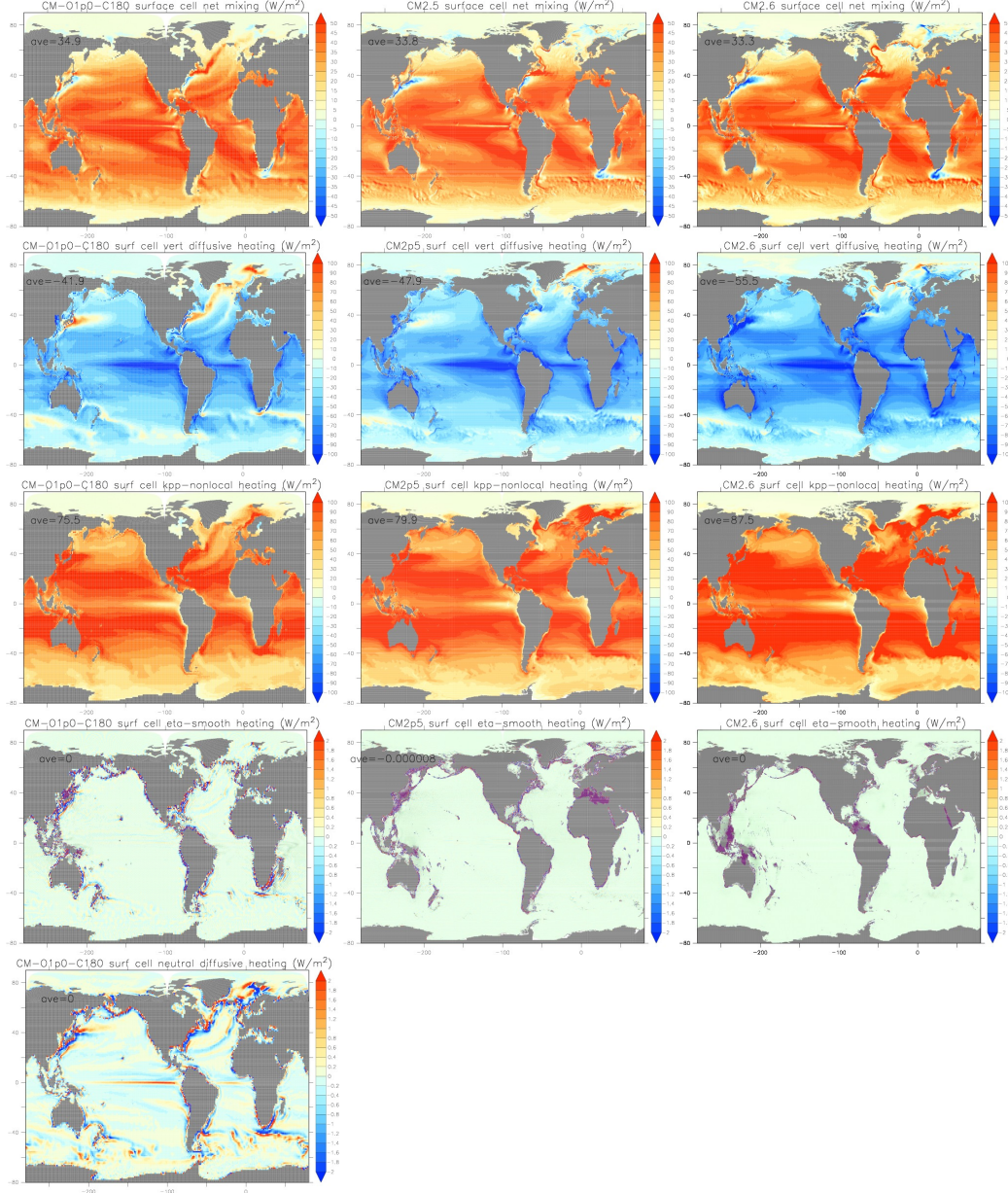


Figure 5.23: Maps of the mixing tendency (W m^{-2}) for heat in the surface grid cell, with the terms defined by equation (5.85). These maps are computed from a time mean over years 101-140. The area mean tendency is noted on each panel over Siberia. We do not show the very small term associated with cross-land mixing (used only in CM-01p0_C180).

5.9 Zonal heat budget

Figure 5.4 shows the zonal mean potential temperature drift relative to the initial year of the simulation. The pattern indicates where the water is warming or cooling relative to the initial year of the simulation. In the remainder of this section, we discuss the budget for ocean heat contributing to this drift.

5.9.1 Horizontally integrated heat budget

A horizontal integral of the tracer budget (5.35a)-(5.35c) over the full ocean domain removes the lateral convergence of advective and SGS fluxes, leaving the following budget involving the vertical transfer of tracer

$$\sum_{i,j} dA \partial_t (C \rho dz) = \sum_{i,j} dA [\rho (w^{(s)} C + F^{(s)})]_{s=s_{k=1}} + \sum_{i,j} dA (Q_{\text{advect}}^{(c)} + Q_{\text{non-advect}}^{(c)} + \mathcal{S}^{(c)} \rho dz) \quad (5.93a)$$

$$\sum_{i,j} dA \partial_t (C \rho dz) = \sum_{i,j} dA (-[\rho (w^{(s)} C + F^{(s)})]_{s=s_{k-1}} + [\rho (w^{(s)} C + F^{(s)})]_{s=s_k} + \rho dz \mathcal{S}^{(c)}) \quad (5.93b)$$

$$\sum_{i,j} dA \partial_t (C \rho dz) = \sum_{i,j} dA \left(-[\rho (w^{(s)} C + F^{(s)})]_{s=s_{kbot-1}} + Q_{(\text{bot})}^{(c)} + \rho dz \mathcal{S}^{(c)} \right). \quad (5.93c)$$

Palter et al. (2014) consider this sort of balance for the buoyancy field in a coarse resolution ESM2M control and climate change simulation, including a diagnosis of each of the many terms impacting buoyancy. A familiar case ensues when assuming a steady state and absence of internal sources/sinks, in which there is a balance between vertical advection, diffusion, and boundary fluxes

$$0 = \sum_{i,j} dx dy [\rho (w^{(s)} C + F^{(s)})]_{s=s_{k=1}} + \sum_{i,j} dx dy (Q_{\text{advect}}^{(c)} + Q_{\text{non-advect}}^{(c)}) \quad (5.94a)$$

$$0 = \sum_{i,j} dx dy (-[\rho (w^{(s)} C + F^{(s)})]_{s=s_{k-1}} + [\rho (w^{(s)} C + F^{(s)})]_{s=s_k}) \quad (5.94b)$$

$$0 = \sum_{i,j} dx dy \left(-[\rho (w^{(s)} C + F^{(s)})]_{s=s_{kbot-1}} + Q_{(\text{bot})}^{(c)} \right). \quad (5.94c)$$

Specializing to the case of temperature, we have the horizontally averaged heat budget

$$\sum_{i,j} dA \partial_t (\Theta \rho dz) = \sum_{i,j} dA [\rho (w^{(s)} \Theta + F^{(s)})]_{s=s_{k=1}} + \sum_{i,j} dA (Q_{\text{advect}}^{(\Theta)} + Q_{\text{non-advect}}^{(\Theta)}) \quad (5.95a)$$

$$\sum_{i,j} dA \partial_t (\Theta \rho dz) = \sum_{i,j} dA (-[\rho (w^{(s)} \Theta + F^{(s)})]_{s=s_{k-1}} + [\rho (w^{(s)} \Theta + F^{(s)})]_{s=s_k}) \quad (5.95b)$$

$$\sum_{i,j} dA \partial_t (\Theta \rho dz) = \sum_{i,j} dA \left(-[\rho (w^{(s)} \Theta + F^{(s)})]_{s=s_{kbot-1}} + Q_{\text{bott}}^{(\Theta)} \right), \quad (5.95c)$$

where $Q_{\text{bott}}^{(\Theta)} = 0$ for the CM2-O suite, but is nonzero in ESM2M.

Scalar budgets in the mixed layer

Contents

6.1	The mixed layer depth and mixed layer level	161
6.2	Budgets for extensive properties	161
6.2.1	A generalized vertical coordinate framework	162
6.2.2	Time evolution within an arbitrary region	162
6.2.2.1	Leibnitz's Rule	162
6.2.2.2	Transport through the moving boundaries	163
6.2.2.3	General form of the transport theorem	164
6.2.3	Finite volume evolution of extensive properties	164
6.3	Seawater mass budgets	164
6.3.1	Mass evolution for a fluid parcel	165
6.3.2	Concerning the absence of subgrid scale mass transport	165
6.3.3	Mass evolution for a fluid region	166
6.3.4	Mass evolution within the mixed layer	166
6.3.5	Steady state global balances	168
6.4	Seawater tracer budgets	168
6.4.1	Mass conservation with multiple trace constituents	168
6.4.2	The tracer equation	169
6.4.3	Tracer conservation over an arbitrary region	170
6.5	Subduction diagnostic with a continuous mixed layer base	171
6.5.1	Algorithm for subduction diagnostic	172
6.5.2	Available diagnostics	173
6.5.3	Bug in the subduction_dhdt diagnostic	173
6.6	Seawater mass and tracer budgets for a grid cell	173
6.6.1	Tracer budget for a grid cell in MOM5	174
6.6.2	Seawater mass budget for a grid cell in MOM5	175
6.7	Seawater mass and tracer budgets in the mixed layer	175
6.7.1	Distinguishing when mass enters or leaves the mixed layer	175
6.7.2	Elements of the diagnostics	176
6.7.3	Seawater mass budget in the mixed layer	177
6.7.3.1	Volume integrated total time tendency	177
6.7.3.2	Vertical transport across ocean surface	178
6.7.3.3	Vertical transport across mixed layer base (vertical subduction)	178
6.7.3.4	Zonal and meridional transport across lateral domain boundaries	178

6.7.3.5	Lateral transport through mixed layer base (lateral subduction)	179
6.7.4	Tracer mass budget in the mixed layer	180
6.7.4.1	Volume integrated terms	180
6.7.4.2	Vertical transport across ocean surface	180
6.7.4.3	Vertical transport across mixed layer base	180
6.7.4.4	Zonal and meridional transport across horizontal domain boundaries . . .	181
6.7.4.5	Lateral transport through mixed layer base	181
6.8	MOM5 mixed layer mass and tracer budgets	182
6.8.1	Surface boundary fluxes	182
6.8.2	Comments on submesoscale and KPP nonlocal transport	182
6.8.3	Total tendency for seawater mass and tracer mass	182
6.8.4	Tendency from tracer source/sinks	183
6.8.5	Vertical transport through horizontal mixed layer base	183
6.8.5.1	Resolved advective transport	183
6.8.5.2	Transport from parameterized mesoscale eddies	183
6.8.5.3	Transport from parameterized submesoscale eddies	183
6.8.5.4	Tracer transport from parameterized mixing processes	184
6.8.5.5	Heat transport from penetrative shortwave radiation	184
6.8.6	Lateral transport through boundaries of a mixed layer column	184
6.8.6.1	Transport from resolved velocity	184
6.8.6.2	Transport from advective or skew diffusive mesoscale parameterization .	185
6.8.6.3	Transport from advective or skew diffusive submesoscale parameterization	185
6.8.6.4	Diffusive transport	185
6.8.7	Lateral transport through mixed layer base	186
6.8.7.1	Transport from resolved velocity	186
6.8.7.2	Transport from parameterized mesoscale eddies	186
6.8.7.3	Transport from parameterized submesoscale eddies	187
6.8.7.4	Tracer transport from neutral diffusion	187
6.9	Sample mixed layer budget calculations	187

The ocean mixed layer experiences intimate contact with the atmosphere and sea ice. Air-sea and ice-sea exchanges of material and momentum are mediated through the mixed layer, and exchanges to the interior ocean act to sequester boundary fluxes on time scales from seasonal to longer. Studies of mixed layer processes focus on how seawater mass, and tracers such as heat and carbon, pass across the ocean surface into the mixed layer, and then further into the ocean interior.

We emphasize that the mixed layer is distinct from the surface boundary layer. For example, the boundary layer experiences rapid changes associated with the diurnal cycle, whereas the mixed layer generally evolves on a seasonal time scale. It is therefore the mixed layer that is more relevant for understanding large-scale interactions between the ocean and atmosphere.

The purpose of this chapter is to detail diagnostics in MOM5 used to compute the mixed layer depth. We also discuss budgets for seawater mass and tracer mass within the mixed layer. However, the budget analysis project was never completed within MOM5; it is hoped to be revisited in MOM6. The following MOM module is directly connected to the material in this chapter:

`ocean_diag/ocean_tracer_diag.F90`

The mixed layer budgets described in Sections 6.8 and 6.9 remain uncoded in MOM5..

6.1 The mixed layer depth and mixed layer level

The mixed layer depth is based on measuring ocean gravitational stability under a vertical displacement. To determine whether vertical transfer is favored requires a thought experiment, in which a surface ocean fluid parcel is displaced downward without changing its temperature or salinity, but feeling the local *in situ* pressure. If the density of the displaced parcel is sufficiently far from the local *in situ* density, then the displacement is not favored, and we are thus beneath the mixed layer and into the stratified interior. What determines “sufficiently far” is subjective, with convention determining the precise value.

Mathematically, we compute the difference between the following two densities

$$\rho_{\text{displaced from surface}} = \rho[S(k=1), \Theta(k=1), p(k)] \quad (6.1a)$$

$$\rho_{\text{local}} = \rho[S(k), \Theta(k), p(k)], \quad (6.1b)$$

and convert that density difference to a buoyancy difference

$$\delta B = -\left(\frac{g(\rho_{\text{displaced from surface}} - \rho_{\text{local}})}{\rho_{\text{local}}}\right). \quad (6.2)$$

This buoyancy difference is computed from the surface down to the first depth at which $\delta B > \Delta B_{\text{crit}}$, where the MOM5 default is

$$\Delta B_{\text{crit}} = 0.0003 \text{ m s}^{-2}, \quad (6.3)$$

with this value also used in [Conkright et al. \(2002\)](#). Other values may be more suitable for particular studies, such as for the Southern Ocean. The mixed layer depth, $H^{(\text{mld})}(x, y, t)$ is then approximated by interpolating between the depth where $\delta B > \Delta B_{\text{crit}}$ and the shallower depth. Note that with $g = 9.8 \text{ m s}^{-2}$ and $\rho_{\text{local}} \approx 1035 \text{ kg m}^{-3}$, then $\Delta B_{\text{crit}} = 0.0003 \text{ m s}^{-2}$ corresponds to a critical density difference of

$$\Delta \rho_{\text{crit}} = 0.03 \text{ kg m}^{-3}, \quad (6.4)$$

as used by [de Boyer Montégut et al. \(2004\)](#) in their study of ocean mixed layers. We note, however, that some studies employ the larger $\Delta \rho_{\text{crit}} = 0.125 \text{ kg m}^{-3}$, which will result in a deeper mixed layer depth due to the need to penetrate deeper into the stratified water.

For purposes of computing budgets for tracers within the mixed layer, we compute the instantaneous grid level, $K^{(\text{mld})}(x, y, t)$, that fully occupies the mixed layer depth. Doing so provides a discrete approximation to the continuous mixed layer depth, and allows us to compute precise budgets for tracers within the grid cells within this discrete mixed layer. We furthermore assume that for every wet ocean cell,

$$K^{(\text{mld})}(x, y, t) \geq 1, \quad (6.5)$$

so that at least one grid cell is contained in the mixed layer.

6.2 Budgets for extensive properties

Extensive properties scale according to the size of a system, whereas intensive properties do not (see, for example, page 10 of [Callen, 1985](#)). Mass is the canonical extensive property. It is a function of the amount of matter within a system so that the system mass equals the sum of mass within any arbitrary decomposition into sub-systems. As matter is conserved in classical physics, it is convenient mathematically and physically to focus on a mass conserving fluid parcel when developing dynamical fluid equations.

We are concerned in this chapter with budgets for extensive fluid properties, such as seawater mass, heat, and carbon, within the ocean surface mixed layer. In this section, we formulate the budget for extensive properties within an arbitrary fluid region, and then apply the general result to the mixed layer. Mathematical considerations include Leibnitz’s Theorem for differentiating an integral, Gauss’s Law, and results from differential geometry. The key result, equation (6.22), is quite intuitive, with the mathematical details leading to this equation readily skipped for the uninterested reader. Note that much of the material here revisits results from Chapter 1.

6.2.1 A generalized vertical coordinate framework

In formulating the budget for the mixed layer, we work through considerations for two special regions of interest. The first region follows material fluid parcels, so that mass does not cross the region boundaries. The transport theorem for this material region is known as Reynold's Transport Theorem and it is discussed in most treatments of fluid mechanics, such as Aris (1962). Second, we consider a region open to mass transport across its boundaries, but whose vertical side walls are static and top and bottom interfaces generally undulate and allow fluid to cross. This second region is the prototypical ocean model grid cell, which can also represent a horizontally bounded region within the mixed layer.

As a prototypical region within the ocean, we consider the top and bottom interfaces to represent the ocean top, ocean bottom, or a surface of constant generalized vertical coordinate denoted by

$$s = s(x, y, z, t). \quad (6.6)$$

For ocean models, the generalized vertical coordinate is specialized to geopotential ($s = z$), hydrostatic pressure ($s = p$), potential density ($s = \rho_p$), terrain following ($s = \sigma$), or other alternatives. For the mixed layer budget, we choose

$$s(x, y, z, t) = z + H^{(\text{mld})}(x, y, t) \quad (6.7)$$

so that the surface $s = 0$ defines the mixed layer base. We furthermore assume that the top or bottom surfaces of the region never become vertical. This assumption means there is a one-to-one relation between the geopotential depth z and the vertical coordinate s . That is, the relation between z and s is invertible, so that the Jacobian of transformation, $\partial z / \partial s$ never vanishes

$$\frac{\partial z}{\partial s} = z_s \neq 0. \quad (6.8)$$

This assumption is made in all treatments of generalized vertical coordinates used as the basis for ocean models as well as for the analysis of ocean models and observations. Note that for our mixed layer coordinate (6.7), the Jacobian is unity

$$\frac{\partial z}{\partial s} = 1 \quad \text{for } s(x, y, z, t) = z + H^{(\text{mld})}(x, y, t). \quad (6.9)$$

6.2.2 Time evolution within an arbitrary region

Consider a field, ψ , that measures an intensive property of the fluid, such as the tracer concentration C or velocity \mathbf{v} . The product of ψ times the fluid mass, $\psi \rho dV$, provides the corresponding extensive fluid property, such as seawater mass (for $\psi = 1$), tracer mass, or linear momentum. We now determine how the extensive property evolves over a finite region in a fluid.

6.2.2.1 Leibnitz's Rule

Our aim is to develop an expression for the time evolution of $\psi \rho dV$ over an arbitrary region, with focus initially on a the prototypical grid cell. We do so by examining the integral of $\partial_t (\rho \psi)$ over this region, which takes the form

$$\int \frac{\partial(\rho \psi)}{\partial t} dV = \int \frac{\partial(\rho \psi)}{\partial t} dx dy dz \quad (6.10a)$$

$$= \int dx dy \int_{z_1}^{z_2} \frac{\partial(\rho \psi)}{\partial t} dz \quad (6.10b)$$

$$= \int dx dy \left[-\frac{\partial z_2}{\partial t} (\rho \psi)_{z=z_2} + \frac{\partial z_1}{\partial t} (\rho \psi)_{z=z_1} + \frac{\partial}{\partial t} \left(\int_{z_1}^{z_2} (\rho \psi) dz \right) \right]. \quad (6.10c)$$

The second equality follows by noting that the horizontal extent of our region remains static, thus allowing for the horizontal integral to be brought outside of the time derivative. In contrast, the vertical extent has a time dependence, which necessitates the use of Leibniz's Rule.

Leibnitz's rule determines how a derivative and an integral commute when the limits of integration are not constant:

$$\frac{\partial}{\partial t} \left(\int_{\phi_1(t)}^{\phi_2(t)} F(x, t) dx \right) = F(\phi_2, t) \frac{\partial \phi_2}{\partial t} - F(\phi_1, t) \frac{\partial \phi_1}{\partial t} + \int_{\phi_1(t)}^{\phi_2(t)} \frac{\partial F(x, t)}{\partial t} dx \quad \text{Leibnitz's Rule.} \quad (6.11)$$

This rule is standard from differential calculus. We note that the result of the integration inside the brackets on the left hand side is a function only of time. Hence, we could just as well have used the symbol d/dt on the left hand side, rather than the partial derivative symbol $\partial/\partial t$. We prefer the partial derivative symbol since it clearly relates to the right hand side expressions, where the distinction between Eulerian and Lagrangian time derivatives is relevant.

6.2.2.2 Transport through the moving boundaries

The third term on the right hand side of equation (6.10c) is an expression for the time evolution of the extensive property $\psi \rho dV$ over the prototypical region. The boundary terms, however, require some interpretation, to which we now focus. For this purpose, introduce the velocity of a point on the generalized vertical coordinate surface through the identity

$$\frac{\partial s}{\partial t} + \mathbf{v}^{(s)} \cdot \nabla s = 0. \quad (6.12)$$

That is, the component of the velocity $\mathbf{v}^{(s)}$ normal to the generalized vertical coordinate surface satisfies the identity

$$\mathbf{v}^{(s)} \cdot \hat{\mathbf{n}}^{(s)} = - \left(\frac{1}{|\nabla s|} \frac{\partial s}{\partial t} \right), \quad (6.13)$$

where

$$\hat{\mathbf{n}}^{(s)} = \frac{\nabla s}{|\nabla s|} \quad (6.14)$$

is the outward normal. We now make use of triple product identity (see Section 6.5.4 in Griffies (2004))

$$\frac{\partial z}{\partial t} = - \frac{\partial s}{\partial t} \frac{\partial z}{\partial s} \quad (6.15)$$

which relates time tendencies of the depth of a generalized surface to time tendencies of the surface itself in order to write

$$\frac{\partial z}{\partial t} = \frac{\partial z}{\partial s} |\nabla s| \hat{\mathbf{n}}^{(s)} \cdot \mathbf{v}^{(s)}. \quad (6.16)$$

Finally, we make use of equation (6.58) of Griffies (2004) to relate the area element on the generalized surface to the horizontal projection $dA = dx dy$ of the surface area

$$dA^{(s)} = \left| \frac{\partial z}{\partial s} \nabla s \right| dA. \quad (6.17)$$

Introducing this area then renders

$$\left(\frac{\partial z}{\partial t} \right) dA = \hat{\mathbf{n}}^{(s)} \cdot \mathbf{v}^{(s)} dA^{(s)}. \quad (6.18)$$

This equation relates the time tendency of the depth of the generalized surface to the normal component of the velocity at a point on the surface. The two are related through the ratio of the area elements.

6.2.2.3 General form of the transport theorem

The result (6.18) is now used for the top and bottom boundary terms in relation (6.10c), which in turn yields

$$\boxed{\frac{\partial}{\partial t} \left(\int \rho \psi dV \right) = \int \frac{\partial(\rho \psi)}{\partial t} dV + \int \rho \psi \hat{\mathbf{n}}^{(s)} \cdot \mathbf{v}^{(s)} dA^{(s)}} \quad (6.19)$$

Hence, the time evolution of the extensive quantity over the fluid region equals to the domain integrated Eulerian time tendency of the density weighted intensive quantity, plus a boundary integral due to transport crossing the region boundary. This result is trivially generalized since it is written as a tensor expression. It provides us with the desired general form of a transport theorem.

6.2.3 Finite volume evolution of extensive properties

As an application of the transport theorem (6.19), consider the material evolution of ψ written in the form

$$\rho \frac{d\psi}{dt} = -\nabla \cdot \mathbf{J}^{(\psi)} + \rho \mathcal{S}^{(\psi)}, \quad (6.20)$$

where the material time derivative is modified by the convergence of a flux, $\mathbf{J}^{(\psi)}$, plus a possibly non-zero source $\mathcal{S}^{(\psi)}$. This equation can represent either the scalar tracer equation with $\mathbf{J}^{(\psi)}$ a subgrid-scale flux and $\rho \mathcal{S}^{(\psi)}$ a source. It can also represent the momentum equation where the sources are in fact body forces from gravity and Coriolis, and the flux $\mathbf{J}^{(\psi)}$ arises from contact stresses associated with pressure and subgrid-scale friction. Expanding the material time derivative and use of mass conservation leads to¹

$$\frac{\partial(\rho\psi)}{\partial t} = -\nabla \cdot (\rho\psi\mathbf{v} + \mathbf{J}^{(\psi)}) + \rho\mathcal{S}^{(\psi)}. \quad (6.21)$$

Substitution into the transport theorem (6.19), and use of Gauss's Law, leads to the canonical finite volume expression for the time derivative of an integrated quantity over a region

$$\boxed{\underbrace{\frac{\partial}{\partial t} \left(\int \rho \psi dV \right)}_{\text{time tendency}} = \underbrace{- \int (\rho \psi (\mathbf{v} - \mathbf{v}^{(s)}) + \mathbf{J}^{(\psi)}) \cdot \hat{\mathbf{n}}^{(s)} dA^{(s)}}_{\text{advective fluxes plus SGS fluxes or contact stresses}} + \underbrace{\int \mathcal{S}^{(\psi)} \rho dV}_{\text{source or body force}}} \quad (6.22)$$

Although derived for the proto-typical grid cell with fixed vertical side-walls, this result is general. It holds for an arbitrary region, \mathcal{S} , within the fluid. We refer to this result as a transport theorem, since it identifies the impact of transport across region boundaries on the amount of an extensive fluid property within the region. Equation (6.22) is the basis for all finite volume discretizations of the evolution equations for extensive fluid properties in ocean models. Additionally, it is the basis for determining the budget of seawater mass and tracer mass within the mixed layer. We thus make use of equation (6.22) in this chapter.

6.3 Seawater mass budgets

We consider in this section the implications of seawater mass conservation for an infinitesimal fluid parcel as well as for a finite fluid region. These considerations lead to the *mass continuity equation*. We consider the corresponding statements for tracer mass conservation in Section 6.4. In developing budgets for mass and tracer over a finite region, we make use of the transport theorem (6.22) derived in Section 6.2.

¹For linear momentum on the sphere, a body force is added to $\rho \mathcal{S}^{(\psi)}$ arising from advection on the spherical geometry. We consider this term in Section 1.9.1.

6.3.1 Mass evolution for a fluid parcel

Mass conservation for a seawater parcel is expressed mathematically by stating that the parcel mass, δM , remains constant following the fluid motion

$$\frac{d(\delta M)}{dt} = 0, \quad (6.23)$$

where the material or Lagrangian time derivative, d/dt , measures the temporal change following the center of mass of the fluid parcel (see equation (6.49)). It is convenient to write the mass of the parcel in terms of the *in situ* density and volume

$$\delta M = \rho \delta V, \quad (6.24)$$

in which case mass conservation (6.23) takes on the form

$$\frac{d\rho}{dt} = -\frac{\rho}{\delta V} \frac{d(\delta V)}{dt}. \quad (6.25)$$

Density for a mass conserving parcel thus increases if the parcel volume decreases. This result illustrates that density, which is an intensive property of the fluid, has its material evolution impacted by a source term, $-(\rho/\delta V) d(\delta V)/dt$. In contrast, mass is an extensive fluid property, with its evolution given by equation (6.23) involving no source. This difference between the budget for seawater mass and seawater density provides a useful, if not trivial, example of how budgets for extensive properties differ from those for intensive.

For use later in our development, we note that the identity

$$\frac{1}{\delta V} \frac{d(\delta V)}{dt} = \nabla \cdot \mathbf{v} \quad (6.26)$$

used in expression (6.25) leads to the Lagrangian form of the continuity equation

$$\frac{d\rho}{dt} = -\rho \nabla \cdot \mathbf{v}, \quad (6.27)$$

and its equivalent Eulerian form

$$\frac{\partial \rho}{\partial t} = -\nabla \cdot (\rho \mathbf{v}). \quad (6.28)$$

6.3.2 Concerning the absence of subgrid scale mass transport

Note the absence of any subgrid scale contribution to the mass continuity equation (6.28). Operationally the reason is that the parameterized eddy-advection associated with Gent et al. (1995) for the mesoscale and Fox-Kemper et al. (2011) for the submesoscale both introduce a velocity, \mathbf{v}^* , that satisfies

$$\nabla \cdot (\rho \mathbf{v}^*) = 0 \quad (6.29a)$$

$$\mathbf{v}^* \cdot \hat{\mathbf{n}} = 0, \quad (6.29b)$$

where \mathbf{n} is the outward normal to the fluid boundaries. Consequently, there is no mass convergence to a region arising from eddy-induced transport. The analogous result holds for the Boussinesq fluid, in which case $\nabla \cdot \mathbf{v}^* = 0$. We therefore formulate the mass budget for any finite region, such as the mixed layer, only in terms of the resolved velocity field. There are no contributions to the mixed layer mass from parameterized eddy-advection. This result does not hold for tracer fields, however, in which eddy-advection of tracer introduces a nontrivial contribution to mixed layer tracer budgets.

6.3.3 Mass evolution for a fluid region

Consider now an arbitrary finite fluid region, \mathcal{S} , in which the fluid mass in this region is written

$$M(\mathcal{S}) = \int_{\mathcal{S}} dM = \int_{\mathcal{S}} \rho dV. \quad (6.30)$$

We make use of the transport theorem (6.22) to determine the budget of mass for this arbitrary region, noting that seawater mass is not effected by diffusive fluxes (see equation (6.53) in Section 6.4.2), or interior sources. The theorem (6.22) thus renders the finite volume mass budget

$$\frac{\partial}{\partial t} \left(\int_{\mathcal{S}} \rho dV \right) = - \int_{\partial\mathcal{S}} \rho (\mathbf{v} - \mathbf{v}^{(\mathcal{S})}) \cdot \hat{\mathbf{n}} dA. \quad (6.31)$$

In this expression, $\partial\mathcal{S}$ is the boundary of the finite domain. The motion of the boundary is described by a velocity field, $\mathbf{v}^{(\mathcal{S})}$; and its geometry is described by a normal vector to orient the surface, $\hat{\mathbf{n}}$, and an area element, dA , to measure surface area (we used the symbol $dA^{(s)}$ in Section 6.2.2 as defined by equation (6.17)). The result (6.31) says that mass within a region changes so long as mass crosses the region boundary, $\partial\mathcal{S}$, which occurs if the fluid velocity, \mathbf{v} , is different from the boundary velocity, $\mathbf{v}^{(\mathcal{S})}$.

We find it sometimes convenient to introduce the following shorthand notation

$$w^{(\mathcal{S})} = (\mathbf{v} - \mathbf{v}^{(\mathcal{S})}) \cdot \hat{\mathbf{n}}. \quad (6.32)$$

This *dia-surface* velocity component measures the relative velocity of the surface and fluid in the direction of the surface normal. Stated alternatively, the dia-surface velocity component measures the volume per time per area of seawater crossing the moving boundary of a fluid domain. Introduction of $w^{(\mathcal{S})}$ to the mass conservation equation (6.31) then leads to

$$\frac{\partial}{\partial t} \left(\int_{\mathcal{S}} \rho dV \right) = - \int_{\partial\mathcal{S}} \rho w^{(\mathcal{S})} dA. \quad (6.33)$$

A material fluid region is defined as one that moves with the fluid, so that $\mathbf{v}^{(\mathcal{S})} = \mathbf{v}$, yielding $w^{(\mathcal{S})} = 0$. Mass within the material region thus remains constant

$$\frac{\partial}{\partial t} \left(\int_{\mathcal{S}} \rho dV \right) = 0 \quad \mathcal{S} \text{ is a material region.} \quad (6.34)$$

Our interest concerns regions that are not material, such as the mixed layer.

6.3.4 Mass evolution within the mixed layer

The mixed layer is a non-material region. Hence, there will generally be a difference between the region boundary and the velocity of a fluid parcel, thus contributing to changes in the mass of the mixed layer. There are three general types of boundaries for the mixed layer.

- The ocean surface provides the upper boundary for the mixed layer, through which mass, tracer, and heat crosses into the mixed layer.
- Lateral boundaries, such as those setup for studying a particular region of interest, provide boundaries across which mass and tracer will enter or leave.
- The mixed layer base is the lower boundary across which mass and tracer leaves or enters the mixed layer. We refer to *subduction* as the process whereby mass crosses the mixed layer base and enters the ocean interior. The opposite is *obduction*, in which fluid mass enters the mixed layer by crossing the mixed layer base.

Let us ground the discussion in a particular example of a mixed layer mass budget within a chosen lateral region. The mass budget (6.33) is thus impacted by mass crossing the ocean surface, sides, and the mixed layer base

$$\frac{\partial}{\partial t} \left(\int_{\mathcal{S}} \rho dV \right)_{\text{mixed layer}} = - \int_{\partial \mathcal{S}} \rho w^{(\mathcal{S})} dA \quad (6.35a)$$

$$= \int_{z=\eta(x,y,t)} Q^{\text{mass}} dA^{(z)} - \int_{\text{lateral boundaries}} \rho w^{(\mathcal{S})} dA - \int_{z=-H^{(\text{mld})}(x,y,t)} \rho w^{(\mathcal{S})} dA. \quad (6.35b)$$

The first term on the right hand side of the second equation measures the mass per time, $Q^{\text{mass}} dA^{(z)}$, crossing the ocean surface, where

$$dA^{(z)} = dx dy \quad (6.36)$$

is the horizontal area element. The second term represents the mass transport through the lateral boundaries. These boundaries may be vertical, as for example when considering a mixed layer budget in a region bounded by latitude-longitude lines. Alternatively, the lateral boundaries may reach all the way to the coasts, in which case they do not contribute to the mixed layer budget for those cases where mass does not enter the ocean through land-sea boundaries. The third term in equation (6.35b) represents subduction across the boundary layer base at $z + H^{(\text{mld})}(x,y,t) = 0$, and this is the term of central interest with mixed layer budgets. We write the rate of mass transport across $z = -H^{(\text{mld})}(x,y,t)$ in the following equivalent manners

$$\mathcal{S}^{(\text{subduction})} \equiv \rho w^{(\mathcal{S})} dA \quad (6.37a)$$

$$= \rho (\mathbf{v} - \mathbf{v}^{(\mathcal{S})}) \cdot \hat{\mathbf{n}} dA \quad (6.37b)$$

$$= -\rho dA^{(z)} \left| \frac{\partial z}{\partial s} \right| \frac{ds}{dt}. \quad (6.37c)$$

Derivation of the final equality follows from equation (1.31) which expresses the dia-surface velocity component for an arbitrary surface defined by isosurfaces of the generalized vertical coordinate s . The minus sign in equation (6.37c) is due to our convention in which the outward normal $\hat{\mathbf{n}}$ points downward from the mixed layer base, whereas $\hat{\mathbf{z}}$ points upward.

The expression (6.37c) says that mass transport subducted across the mixed layer base is directly proportional to the material evolution of the generalized vertical coordinate defining the mixed layer base. We write the subduction transport in a more conventional form by introducing the generalized vertical coordinate (6.7) $s(x,y,z,t) = z + H^{(\text{mld})}(x,y,t)$, which again vanishes at the mixed layer base, and which satisfies $\partial z / \partial s = 1$ (equation (6.8)). The resulting expression accords to that from (Cushman-Roisin, 1987)

$$\mathcal{S}^{(\text{subduction})} = -\rho dA^{(z)} \left(\frac{d(z + H^{(\text{mld})})}{dt} \right) \quad (6.38a)$$

$$= -\rho dA^{(z)} \left(w + \frac{\partial H^{(\text{mld})}}{\partial t} + \mathbf{u} \cdot \nabla H^{(\text{mld})} \right), \quad (6.38b)$$

where each term is evaluated at the mixed layer base $z = -H^{(\text{mld})}(x,y,t)$. The subduction transport $\mathcal{S}^{(\text{subduction})}$ (dimensions of mass per time) is positive for fluid moving downward beneath the mixed layer base into the pycnocline (subduction) and negative for water moving into the mixed layer (obduction)

$$\mathcal{S}^{(\text{subduction})} > 0 \quad \text{subduction (leave mixed layer and enter ocean interior)} \quad (6.39)$$

$$\mathcal{S}^{(\text{subduction})} < 0 \quad \text{obduction (leave interior and enter mixed layer).} \quad (6.40)$$

6.3.5 Steady state global balances

The mass budget (6.35b) can be written in terms of the subduction rate $S^{(\text{subduction})}$, so that

$$\frac{\partial}{\partial t} \left(\int_{\text{mixed layer}} \rho dV \right) = \int_{z=\eta(x,y,t)} Q^{\text{mass}} dA^{(z)} - \int_{\text{lateral boundaries}} \rho w^{(S)} dA - \int_{z=-H^{(\text{mld})}(x,y,t)} S^{(\text{subduction})}. \quad (6.41)$$

We now consider the special case of a steady state, whereby the mass within the mixed layer region remains constant. This steady state is realizable only if the mass of water crossing the ocean surface is balanced by the mass crossing the mixed layer base and crossing the lateral boundaries. Consider the special case where the lateral boundaries reach to the coasts, so they do not contribute to the mixed layer budget. A steady state global mixed layer mass budget therefore takes the form

$$\int_{z=\eta(x,y,t)} Q^{\text{mass}} dA^{(z)} = \int_{z=-H^{(\text{mld})}(x,y,t)} S^{(\text{subduction})} \quad \text{global steady state mass in mixed layer.} \quad (6.42)$$

Also note that for a steady state, the mixed layer base no longer evolves, in which case the time tendency contribution to the subduction rate, $\partial H^{(\text{mld})}/\partial t$, will be much smaller than contributions from lateral and vertical advection.

If there is a net zero surface mass flux, $\int_{z=\eta(x,y,t)} Q^{\text{mass}} dA^{(z)} = 0$, then a steady state is realized only if there is zero net water crossing the mixed layer base; i.e., the integrated obduction balances the integrated subduction.

6.4 Seawater tracer budgets

We now extend the results from Section 6.3 to tracers. The key new feature is that tracers are impacted both by advection and mixing, with mixing an important contributor to the mixed layer budget.

6.4.1 Mass conservation with multiple trace constituents

Seawater consists of many material constituents, such as freshwater, salts and biogeochemical components. We now consider mass conservation for each constituent in a seawater parcel.² The mass density of each constituent within a parcel of seawater is given by

$$\rho_n = \frac{\text{mass of component } n}{\text{volume of seawater parcel}}, \quad (6.43)$$

with the total density in a parcel given by the sum over all N constituents

$$\rho = \sum_{n=1}^N \left(\frac{\text{mass of component } n}{\text{volume of seawater parcel}} \right) \quad (6.44a)$$

$$= \sum_{n=1}^N \rho_n. \quad (6.44b)$$

Observe that the mass of a seawater parcel is the sum of individual constituent masses (numerator in equation (6.44a)), whereas the volume of the parcel is a complicated function of the temperature, pressure, and material constituents.

²The development here shares elements from Section II.2 of DeGroot and Mazur (1984), Section 8.4 of Chaikin and Lubensky (1995), and Section 3.3 of Müller (2006). See also the discussion in Warren (2009).

Consider now a material fluid parcel where the mass of each constituent remains constant. Following the derivation of seawater mass conservation considered in Section 6.3.1, we are led to the Eulerian expression of mass conservation for each constituent

$$\frac{\partial \rho_n}{\partial t} = -\nabla \cdot (\rho_n \mathbf{v}_n), \quad (6.45)$$

where \mathbf{v}_n is the velocity of material constituent n . Summing over all constituents then leads to the Eulerian expression of mass conservation for seawater given by equation (6.28)

$$\frac{\partial \rho}{\partial t} = -\nabla \cdot (\rho \mathbf{v}), \quad (6.46)$$

where

$$\mathbf{v} = \rho^{-1} \sum_{n=1}^N \rho_n \mathbf{v}_n \quad (6.47)$$

is the velocity for the center of mass of the parcel.

The density of seawater is often well approximated by

$$\rho \approx \rho_{\text{salt}} + \rho_{\text{fresh}}, \quad (6.48)$$

where ρ_{salt} is the mass of ocean “salt” per mass of seawater, and ρ_{fresh} is the mass of fresh water per mass of seawater. Other material constituents (e.g., biological matter) occur in such small concentrations that their contributions to the seawater density are generally ignored for purposes of ocean modelling. See IOC et al. (2010) for more details on how various constituents impact seawater density.

6.4.2 The tracer equation

Equation (6.45) is an expression for mass conservation for each constituent. It is an elegant means to determine the budget for the trace constituent, given the velocity, \mathbf{v}_n , of that constituent. However, for dynamical applications, we are concerned with a seawater parcel moving at the center of mass velocity \mathbf{v} (equation (6.47)). Mass conservation for each constituent is then determined by the velocity of that constituent relative to the center of mass velocity, and the resulting budget for a constituent leads to the tracer equation, which we now derive.

Introducing the center of mass material time derivative

$$\frac{d}{dt} = \frac{\partial}{\partial t} + \mathbf{v} \cdot \nabla \quad (6.49)$$

to the constituent mass balances (6.45) leads to the material budget

$$\frac{d\rho_n}{dt} = -\rho_n \nabla \cdot \mathbf{v} - \nabla \cdot [\rho_n (\mathbf{v}_n - \mathbf{v})]. \quad (6.50)$$

Now define the *relative mass flux*

$$\mathbf{J}_n = \rho_n (\mathbf{v}_n - \mathbf{v}) \quad (6.51)$$

to render an expression for the material evolution of the density for each constituent

$$\frac{d\rho_n}{dt} = -\rho_n \nabla \cdot \mathbf{v} - \nabla \cdot \mathbf{J}_n. \quad (6.52)$$

The flux \mathbf{J}_n is nonzero for those motions where the constituent n moves relative to the parcel’s center of mass. This motion can be caused by many effects, with molecular diffusion the canonical example, in which case we parameterize \mathbf{J}_n as a downgradient diffusive flux. For an ocean model, whose grid spacing is far greater than that appropriate for molecular diffusion, the relative motion of a constituent is also

affected by far larger subgrid scale processes, such as unresolved eddy advective and diffusive transport. In general, the total mass flux vanishes

$$\mathbf{J} = \sum_{n=1}^N \mathbf{J}_n = 0, \quad (6.53)$$

which follows since we choose to measure the parcel motion with respect to its center of mass. Hence, there is no subgrid scale flux for the seawater density ρ . That is, the mass conservation equation (6.46) is exact, even in the presence of subgrid scale processes.

As a final step in our development of the tracer equation, introduce the concentration of a material constituent, defined by

$$C_n = \frac{\text{mass of component } n}{\text{mass of seawater parcel}} \quad (6.54a)$$

$$= \frac{\rho_n dV}{\rho dV}. \quad (6.54b)$$

Substituting this tracer concentration into the constituent density equation (6.52) leads to the material form of the tracer equation

$$\rho \left(\frac{dC_n}{dt} \right) = -\nabla \cdot \mathbf{J}_n, \quad (6.55)$$

with the Eulerian form given by

$$\frac{\partial(\rho C_n)}{\partial t} + \nabla \cdot (\rho \mathbf{v} C_n) = -\nabla \cdot \mathbf{J}_n. \quad (6.56)$$

This is the form of the source-free tracer equation implemented in ocean models. It applies to both the material tracers considered here, such as salt, and it quite accurately approximates the evolution of the heat tracer conservative temperature McDougall (2003). Biogeochemical tracers generally have source terms associated with chemical reactions and/or biological processes, in which we write

$$\rho \left(\frac{dC_n}{dt} \right) = -\nabla \cdot \mathbf{J}_n + \rho \mathcal{S}^{(C_n)}, \quad (6.57)$$

where $\rho \mathcal{S}^{(C_n)}$ measures the rate that tracer concentration C_n is changing due to source/sink terms.

6.4.3 Tracer conservation over an arbitrary region

We now consider tracer mass conservation within an arbitrary region, with a model grid cell or the mixed layer two examples of such a region. We also set the tracer source to zero for brevity, though note that it can be readily reinserted to the formalism. For this purpose, return to the derivation in Section 6.3.3 and

introduce the constituent velocity, \mathbf{v}_n , and tracer concentration, C_n , to render

$$\frac{\partial M(\mathcal{S})}{\partial t} = \frac{\partial}{\partial t} \left(\int_{\mathcal{S}} \rho dV \right) \quad (6.58a)$$

$$= - \int_{\partial\mathcal{S}} \rho (\mathbf{v} - \mathbf{v}^{(\mathcal{S})}) \cdot \hat{\mathbf{n}} d\mathcal{S} \quad (6.58b)$$

$$= - \int_{\partial\mathcal{S}} \sum_{n=1}^N \rho_n (\mathbf{v}_n - \mathbf{v}^{(\mathcal{S})}) \cdot \hat{\mathbf{n}} d\mathcal{S} \quad (6.58c)$$

$$= - \int_{\partial\mathcal{S}} \sum_{n=1}^N \rho_n [(\mathbf{v}_n - \mathbf{v}) + (\mathbf{v} - \mathbf{v}^{(\mathcal{S})})] \cdot \hat{\mathbf{n}} d\mathcal{S} \quad (6.58d)$$

$$= - \int_{\partial\mathcal{S}} \sum_{n=1}^N \rho C_n [(\mathbf{v}_n - \mathbf{v}) + (\mathbf{v} - \mathbf{v}^{(\mathcal{S})})] \cdot \hat{\mathbf{n}} d\mathcal{S} \quad (6.58e)$$

$$= - \int_{\partial\mathcal{S}} \sum_{n=1}^N (\mathbf{J}_n \cdot \hat{\mathbf{n}} + \rho C_n w^{(\mathcal{S})}) d\mathcal{S} \quad (6.58f)$$

$$= - \int_{\partial\mathcal{S}} \rho w^{(\mathcal{S})} d\mathcal{S}. \quad (6.58g)$$

To reach the final step we made use of the property $\sum_{n=1}^N \mathbf{J}_n = 0$ (equation (6.53)) satisfied by the subgrid scale tracer fluxes. Extracting each tracer from the sum in the penultimate step yields the tracer mass conservation equation for the region

$$\frac{\partial M_n(\mathcal{S})}{\partial t} = - \int_{\partial\mathcal{S}} [\mathbf{J}_n \cdot \hat{\mathbf{n}} + \rho C_n w^{(\mathcal{S})}] d\mathcal{S}. \quad (6.59)$$

This result is a straightforward extension of that for seawater mass within an arbitrary region (equation (6.33)). It says that the mass of a trace constituent within a domain changes due to tracer fluxes crossing the domain boundary from subgrid-scale processes and advective processes. Both tracer fluxes are computed relative to the moving domain boundary. The tracer budget (6.59) is identical to that which results from application of the transport theorem (6.22) for each tracer constituent. It is useful to expose the above details in order to test self-consistency of the formalism.

Specializing our region budget to the mixed layer, we note that tracer leaving the base of the mixed layer via advective processes (the $\rho C_n w^{(\mathcal{S})}$ term) is said to be subducted into the ocean interior. The converse situation is tracer obduction. Additionally, tracer enters or leaves the mixed layer through subgrid scale transport processes, the $\mathbf{J}_n \cdot \hat{\mathbf{n}}$ term. If these subgrid scale processes are associated with mixing, then they are said to either entrain (when adding tracer to the mixed layer) or detrain (when subtracting tracer from the mixed layer). Additionally, we note that part of the subgrid scale transport may be advective in nature, such as for the mesoscale closure from Gent et al. (1995) or the submesoscale closure from Fox-Kemper et al. (2011). It is physically relevant to associate these eddy-induced advective effects with the process of subduction/obduction that arises from the resolved advection.

6.5 Subduction diagnostic with a continuous mixed layer base

We detail here the options in MOM5 for diagnosing the subduction according to a discrete approximation to the kinematic expression (6.38b).

6.5.1 Algorithm for subduction diagnostic

In brief, the algorithm consists of the following steps.

- Compute the mixed layer depth, $H^{(\text{mld})}$, based on some density increment criteria, with the increment set according to a namelist. The depth is naturally placed at the tracer point.
- Optionally smooth the diagnosed mixed layer depth. Note that smoothing is enabled via a namelist option; it incurs a trivial computational cost.
- Compute the time tendency $\partial_t H^{(\text{mld})}$ based on the discrete time step difference between mixed layer depth

$$\frac{\partial H^{(\text{mld})}}{\partial t} \approx \frac{H^{(\text{mld})}(t + \Delta t) - H^{(\text{mld})}(t)}{\Delta t}, \quad (6.60)$$

with Δt the model tracer time step.

- Compute the horizontal gradient of the mixed layer depth, $\nabla H^{(\text{mld})}$. The zonal derivative is placed on the zonal face of a tracer cell, and the meridional derivative at the meridional position.
- Horizontally interpolate the zonal velocity component to the zonal tracer cell face, and the meridional velocity component to the meridional tracer cell face, both interpolations requiring two point averages on the B-grid (see Figure 9.5 in Griffies (2012)). The result is an estimate for the horizontal C-grid velocity components

$$u_{\text{east}}(i, j, k) = \frac{u(i, j, k) \text{dun}(i, j - 1) + u(i, j - 1, k) \text{dus}(i, j)}{\text{dus}(i, j) + \text{dun}(i, j - 1)} \quad (6.61)$$

$$v_{\text{north}}(i, j, k) = \frac{v(i - 1, j, k) \text{duw}(i, j) + v(i, j, k) \text{due}(i - 1, j)}{\text{duw}(i, j) + \text{due}(i - 1, j)}. \quad (6.62)$$

- Vertically interpolate the velocity ($u_{\text{east}}, v_{\text{north}}, w$) to the mixed layer base to determine $(u_{\text{east}}^{\text{mld}}, v_{\text{north}}^{\text{mld}}, w^{\text{mld}})$. There are various conditional cases to consider.

– If $H^{(\text{mld})}(i, j) \leq \text{depth_zt}(i, j, k = 1)$, then no interpolation needed:

$$(u_{\text{east}}^{\text{mld}}, v_{\text{north}}^{\text{mld}}, w^{\text{mld}})(i, j) = (u_{\text{east}}, v_{\text{north}}, w)(i, j, k = 1) \quad \text{if } H^{(\text{mld})}(i, j) \leq \text{depth_zt}(i, j, k = 1). \quad (6.63)$$

– If $H^{(\text{mld})} = \text{depth_zt}(i, j, k)$ then no interpolation needed:

$$(u_{\text{east}}^{\text{mld}}, v_{\text{north}}^{\text{mld}}, w^{\text{mld}})(i, j) = (u_{\text{east}}, v_{\text{north}}, w)(i, j, k) \quad \text{if } H^{(\text{mld})}(i, j) \leq \text{depth_zt}(i, j, k). \quad (6.64)$$

– If $\text{depth_zt}(i, j, k - 1) < H^{(\text{mld})} < \text{depth_zt}(i, j, k)$ then vertical interpolation for each velocity component

$$\psi^{\text{mld}}(i, j) = \frac{\psi(i, j, k - 1) \text{dzup}(i, j, k) + \psi(i, j, k) \text{dztlo}(i, j, k - 1)}{\text{dzup}(i, j, k) + \text{dztlo}(i, j, k - 1)} \quad (6.65)$$

– If $H^{(\text{mld})}(i, j) \geq \text{depth_zt}(i, j, k = \text{kmt}(i, j))$, then no interpolation needed:

$$(u_{\text{east}}^{\text{mld}}, v_{\text{north}}^{\text{mld}}, w^{\text{mld}})(i, j) = (u_{\text{east}}, v_{\text{north}}, w)(i, j, k = \text{kmt}) \quad \text{if } H^{(\text{mld})}(i, j) \geq \text{depth_zt}(i, j, k = \text{kmt}). \quad (6.66)$$

- Estimate horizontal advection of the mixed layer base via

$$\mathbf{u} \cdot \nabla H^{(\text{mld})} \approx u_{\text{east}}^{\text{mld}} \left(\frac{H^{(\text{mld})}(i + 1, j) - H^{(\text{mld})}(i, j)}{\text{dxte}(i, j)} \right) + v_{\text{north}}^{\text{mld}} \left(\frac{H^{(\text{mld})}(i, j + 1) - H^{(\text{mld})}(i, j)}{\text{dytn}(i, j)} \right). \quad (6.67)$$

- Compute the subduction mass flux rate via an estimate of equation (6.38b)

$$\mathcal{S}^{(\text{subduction})}(i, j) \approx -\rho^{\text{mld}} dx_t(i, j) dy_t(i, j) \left(w^{\text{mld}} + \frac{\partial H^{(\text{mld})}}{\partial t} + \mathbf{u}^{(\text{mld})} \cdot \nabla h^{(\text{mld})} \right)(i, j), \quad (6.68)$$

where we use the estimate (6.60) for the time derivative, and equation (6.67) for the horizontal advection. The density $\rho^{\text{mld}} = \rho_0$ for a Boussinesq fluid, whereas it equals the vertically interpolated *in situ* density for a non-Boussinesq fluid.

- A final step is the optional binning of $\mathcal{S}^{(\text{subduction})}(i, j)$ according to a chosen density classification, so to record the subduction as a function of density class. This binning then allows for the diagnostic to be computed according to the recommendations of Kwon et al. (2013).

6.5.2 Available diagnostics

The following diagnostics are available related to the subduction calculation

$$\text{subduction} = \mathcal{S}^{(\text{subduction})} \quad (6.69)$$

$$\text{subduction_dhdt} = -\rho^{\text{mld}} dx_t(i, j) dy_t(i, j) \left(\frac{\partial H^{(\text{mld})}}{\partial t} \right) \quad (6.70)$$

$$\text{subduction_horz} = -\rho^{\text{mld}} dx_t(i, j) dy_t(i, j) (\mathbf{u}^{(\text{mld})} \cdot \nabla H^{\text{mld}}) \quad (6.71)$$

$$\text{subduction_vert} = -\rho^{\text{mld}} dx_t(i, j) dy_t(i, j) w^{\text{mld}}. \quad (6.72)$$

Each of these fields has a corresponding diagnostic produced according to binning into neutral density classes

$$\text{subduction_nrho} = \text{rebin_onto_rho}(\text{subduction}) \quad (6.73)$$

$$\text{subduction_dhdt_nrho} = \text{rebin_onto_rho}(\text{subduction_dhdt}) \quad (6.74)$$

$$\text{subduction_horz_nrho} = \text{rebin_onto_rho}(\text{subduction_horz}) \quad (6.75)$$

$$\text{subduction_vert_nrho} = \text{rebin_onto_rho}(\text{subduction_vert}) \quad (6.76)$$

6.5.3 Bug in the subduction_dhdt diagnostic

On 09Dec2013, a bug was found in the diagnostic `subduction_dhdt`. At the start of each segment of a simulation, the diagnostic mixed layer depth is incorrectly reset to zero. Consequently, there is a very large time tendency at the start of the diagnostic sequence, since

$$\left(\frac{\partial H^{(\text{mld})}}{\partial t} \right)_{\text{first time step}} \approx \frac{H^{(\text{mld})}(t + \Delta t) - H^{(\text{mld})}(t)}{\Delta t} \quad (6.77a)$$

$$= \frac{H^{(\text{mld})}(t + \Delta t) - 0}{\Delta t}. \quad (6.77b)$$

Furthermore, if the initial time step is January 1, then most of the northern hemisphere will be dominated by the spuriously huge obduction at the first diagnostic time step, since `subduction_dhdt` will generally be less than zero.

As a work-around, so long as the mixed layer depth is diagnosed, then one may approximate the `subduction_dhdt` diagnostic using an offline calculation with the time averaged mixed layer depths. In general, the longer the time average, the less this diagnostic term will contribute to the total subduction, in which case the diagnostic bug becomes less problematic.

6.6 Seawater mass and tracer budgets for a grid cell

In preparation for the diagnostic budget over the mixed layer, we first summarize the tracer mass budget and seawater mass budget for a grid cell in MOM5.

6.6.1 Tracer budget for a grid cell in MOM5

To get started with formulating the budget, recall results from Section 5.4, where we wrote the following semi-discrete tracer budgets for the surface, interior, and bottom grid cells

$$\partial_t(C\rho dz) = -\nabla_s \cdot [\rho dz(\mathbf{u}C + \mathbf{F})] + \left[\rho(w^{(s)}C + F^{(s)})\right]_{s=s_{k=1}} + Q_{\text{advect}}^{(c)} + Q_{\text{non-advect}}^{(c)} + S^{(c)}\rho dz \quad (6.78a)$$

$$\partial_t(C\rho dz) = -\nabla_s \cdot [\rho dz(\mathbf{u}C + \mathbf{F})] - [\rho(w^{(s)}C + F^{(s)})]_{s=s_{k-1}} + [\rho(w^{(s)}C + F^{(s)})]_{s=s_k} + S^{(c)}\rho dz \quad (6.78b)$$

$$\partial_t(C\rho dz) = -\nabla_s \cdot [\rho dz(\mathbf{u}C + \mathbf{F})] - \left[\rho(w^{(s)}C + F^{(s)})\right]_{s=s_{kbot-1}} + Q_{\text{(bot)}}^{(c)} + S^{(c)}\rho dz. \quad (6.78c)$$

These budgets are formulated as finite volume contributions to the tracer mass per horizontal area (or heat per area) of a grid cell. All grid cells generally have a non-constant thickness and non-constant density (Boussinesq budgets have constant density factor $\rho \rightarrow \rho_0$). The lateral convergence operator acting on a flux, $-\nabla_s \cdot \mathbf{J}$, is formulated numerically so that multiplication by the area of a grid cell leads to a difference operator acting on the lateral flux components crossing the tracer grid cell faces. That is, the numerical discretization satisfies Gauss' Law, as doing so allows us to retain the familiar finite volume budgets within the numerical model. We now detail terms in these equations.

- C is the potential (or conservative) temperature of a grid cell, or the mass of tracer (e.g., salt or DIC) per mass of seawater within the cell (i.e., tracer concentration).
- ρdz is the mass of seawater per horizontal area in a grid cell, with ρ the *in situ* density and dz the thickness. The CM2-O models as well as ESM2M make the Boussinesq approximation, so the ρ factor is replaced by a constant reference density

$$\rho_o = 1035 \text{ kg m}^{-3}. \quad (6.79)$$

- The product $C\rho dz$ is the mass per unit horizontal area of a grid cell if C is a material tracer such as salinity. Since the horizontal area of the cell is constant in time, we may multiply by the horizontal area to recover a budget for the mass in the cell.
- The product $C\rho dz$ is the heat per horizontal area if C is potential or conservative temperature multiplied by the heat capacity. Since the horizontal area of the cell is constant in time, we may multiply by the horizontal area to recover a budget for the heat within the grid cell, in SI units of Joule.
- The generalized level vertical coordinate is denoted by s , and its discrete values s_k determine the vertical grid cell.
- The horizontal velocity component is \mathbf{u} and vertical component is $w^{(s)}$.
- The horizontal subgrid scale transport is $\rho \mathbf{F}$ and vertical component is $\rho F^{(s)}$.
- The tracer source is $S^{(c)}\rho dz$. This source is generally nonzero for biogeochemical tracers.
- Tracer flux associated with the boundary water flux is accounted for by the term $Q_{\text{advect}}^{(c)}$. It often takes the form

$$Q_{\text{advect}}^{(c)} = Q^{\text{mass}} C_m, \quad (6.80)$$

where Q^{mass} is the mass per time per horizontal area of water entering or leaving the ocean through liquid or frozen precipitation, evaporation, liquid runoff, and solid calving. The concentration C_m is that in the boundary water flux. This concentration is generally zero for salinity. For temperature, the precipitation and evaporation are assumed to have the temperature of the sea surface temperature. For the land model LM3 used in these coupled models, liquid runoff and solid calving have a heat content relative to 0°C that is transferred to the ocean, so that we do not need to assume a temperature for this water.

- $Q_{(\text{bot})}^{(c)}$ is the flux of tracer passed into the liquid ocean through the solid bottom boundary. The CM2-O suite of models does not have geothermal heating, in which case this term is zero. However, ESM2M has a non-zero geothermal heat flux.
- $Q_{\text{non-advect}}^{(c)}$ is the non-advective flux of tracer crossing the ocean surface boundary. The sign is defined so that a positive value represents a flux of tracer into the ocean; e.g., positive sign adds heat, salt, carbon, or other tracers to the ocean. For the heat budget, this term arises from shortwave, longwave, latent, and sensible heat fluxes.

6.6.2 Seawater mass budget for a grid cell in MOM5

The seawater mass budget follows from the tracer mass budget by setting the tracer concentration to a constant, and dropping all subgrid scale transport processes. The resulting seawater mass budget was discussed in Section 4.3.1, where the following grid cell budgets were presented

$$\text{surface} \quad \partial_t (\rho dz) = -\nabla_s \cdot (\mathbf{u} \rho dz) + (\rho w^{(s)})_{s=s_{k=1}} + Q^{\text{mass}} \quad (6.81\text{a})$$

$$\text{interior} \quad \partial_t (\rho dz) = -\nabla_s \cdot (\mathbf{u} \rho dz) - (\rho w^{(s)})_{s=s_{k-1}} + (\rho w^{(z)})_{s=s_k} \quad (6.81\text{b})$$

$$\text{bottom} \quad \partial_t (\rho dz) = -\nabla_s \cdot (\mathbf{u} \rho dz) - (\rho w^{(s)})_{s=s_{kmt-1}}. \quad (6.81\text{c})$$

For purposes of diagnosing mass budgets in the mixed layer, we have dropped the mass source term $S^{(M)} \rho dz$ (see equations (4.10a)–(4.10c)), as this term is generally set to zero in applications.

6.7 Seawater mass and tracer budgets in the mixed layer

In this section, we begin our discussion of the MOM5 diagnostic that computes an online seawater mass and tracer mass budget within the mixed layer. This diagnostic calculation makes direct use of the numerical methods used for the prognostic grid cell budgets. It therefore provides a numerically exact budget over the mixed layer; i.e., exact to within computational roundoff. Analysts can use the diagnostics to make precise and detailed statements about the evolution of seawater mass and tracer mass within the simulated mixed layer.

6.7.1 Distinguishing when mass enters or leaves the mixed layer

Consider the zonal-depth slice through a mixed layer in Figure 6.1. We need an algorithm whereby a flux crossing the discrete mixed layer base is counted when it adds or subtracts from the mixed layer region, and ignored when it does not impact the mixed layer budget. Our considerations have relevance for all vector fluxes carrying seawater mass or tracer mass. According to the terminology introduced in Section 6.3.4, subduction/obduction refers to advective transport of seawater mass or tracer that crosses the mixed layer base, either via resolved advective fluxes or eddy-induced advection. Entrainment/detrainment refers to transport from mixing processes, such as diffusion and non-local KPP transport.

Upward transport (through vertical advection, diffusion, or other processes) crossing a horizontally oriented mixed layer base affects the mass and tracer content in the mixed layer region. Lateral transport is more subtle. Referring back to the continuous expression (6.38b) for the subduction rate, mass is added to the mixed layer for transport crossing the mixed layer base in the direction of a deepening mixed layer. Mass is removed for transport in the opposite sense. This result leads to the following rule for lateral transport of seawater or tracer mass crossing the vertical faces of the mixed layer base:

lateral transport across ML base towards deeper mixed layer \Rightarrow adds to mixed layer (6.82a)

lateral transport across ML base towards shallower mixed layer \Rightarrow removes from mixed layer. (6.82b)

This rule is used in the following to account for the sign of lateral transport crossing the mixed layer base.

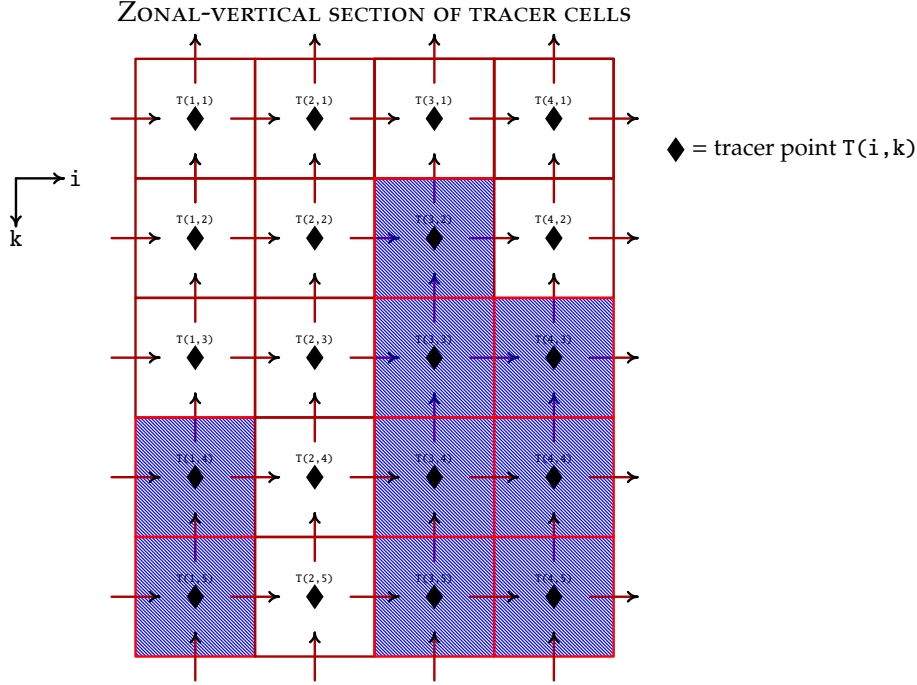


Figure 6.1: Zonal-depth schematic of tracer cells, with colored cells indicating regions beneath the mixed layer and white cells those regions within the mixed layer. The mixed layer region is separated from the interior by horizontal and vertical regions of the mixed layer base. The MOM5 diagnostic of mixed layer budgets aims to decompose the evolution of scalar budgets within this piecewise constant region. The western boundary is assumed here to have $i_s = 1$ and the eastern boundary is at $i_e = 4$. Vectors represent zonal and vertical fluxes that cross the tracer cell faces. The MOM convention is to label a zonal flux leaving the east face of cell $T(i, k)$ as $F_x(i, k)$ and crossing the west face as $F_x(i-1, k)$. The vertical fluxes crossing through the bottom of cell $T(i, k)$ is labeled $F_z(i, k)$ and leaving the top face as $F_z(i, k-1)$.

6.7.2 Elements of the diagnostics

For purposes of the mixed layer tracer budget, we define the mixed layer according to the discrete vertical level $K_{\text{ml}}(x, y)$ (see equation (6.5)). The model field carrying this information is written

$$\text{kml}(i, j) = \text{mixed layer k-level.} \quad (6.83)$$

We will also need to make use of a mask that is zero outside the mixed layer and unity within the mixed layer

$$\text{mask}(i, j, k) = \begin{cases} 0 & \text{outside mixed layer} \\ 1 & \text{inside mixed layer.} \end{cases} \quad (6.84)$$

The mask array is used to help vectorize do-loops. All budgets are computed assuming the mixed layer is comprised of full grid cell regions. This approximation facilitates the inclusion of budget terms without needing to perform potentially expensive interpolation.

As discussed in Section 6.7.1, seawater mass is added to the mixed layer when lateral transport crosses a vertically oriented mixed layer base in a direction in which the mixed layer deepens. Mass increase in the mixed layer generally is associated with a deepening of the mixed layer base. Conversely, the mixed layer shoals as mass leaves. Consider a zonal flux at the east face of the tracer cell (Figure 6.1). This flux can remove mass from the mixed layer by moving mass from the mixed layer into the ocean interior. It can conversely add mass to the mixed layer by obtaining mass from interior. Additionally, it can move mass

from one mixed layer region to another, in which the mixed layer mass is unchanged. Finally, it can move mass from one interior region to another, again leaving the mixed layer unaffected. We quantify the net effects on the mixed layer scalar budget arising from zonal transport through the following vertical sum

$$\mathcal{T}_{\text{ml base}}^x(i, j) = dy \sum_{k=1}^{k=nk} J^x(i, j, k) [\text{mask}(i+1, j, k)(1 - \text{mask}(i, j, k)) - \text{mask}(i, j, k)(1 - \text{mask}(i+1, j, k))] \quad (6.85a)$$

$$= dy \sum_{k=1}^{k=nk} J^x(i, j, k) [\text{mask}(i+1, j, k) - \text{mask}(i, j, k)], \quad (6.85b)$$

where the mass flux component, J^x , arises either from either an advective flux or subgrid scale flux. The meridional distance factor dy produces a transport with dimensions of mass per time (or heat per time). As expected, these formula contribute zero to the mixed layer budget for cases where the two adjacent masks are the same. If the adjacent mask, $\text{mask}(i+1, j, k)$, is one and $\text{mask}(i, j, k)$ is zero, we have a positive zonal mass flux (mass is added to the mixed layer into column $(i+1, j)$). Conversely, if the adjacent mask, $\text{mask}(i+1, j, k)$, is zero and $\text{mask}(i, j, k)$ is one, mass leaves the mixed layer from column (i, j) . Similar considerations lead to the meridional mass transport crossing the north face of a tracer cell

$$\mathcal{T}_{\text{ml base}}^y(i, j) = dx \sum_{k=1}^{k=nk} J^y(i, j, k) [\text{mask}(i, j+1, k) - \text{mask}(i, j, k)]. \quad (6.86)$$

In the remainder of this section, we consider a seawater and tracer budget integrated over a horizontal region of the ocean mixed layer as defined by the index range

$$is \leq i \leq ie \quad (6.87a)$$

$$js \leq j \leq je. \quad (6.87b)$$

This horizontal region could be the global ocean, a basin, a small region, or a single grid cell (if $is = ie$ and $js = je$). The tracer budget for the mixed layer is determined by integrating the grid cell tracer budgets (6.78a)–(6.78c) over the chosen horizontal region from the surface down to level $\text{kmlD}(i, j)$. The seawater mass budget for the mixed layer is computed likewise, making use of the grid cell budgets (6.81a)–(6.81c).

To perform a mixed layer budget over an arbitrary horizontal region, we diagnose the accumulated transport crossing these boundaries as they impact the mixed layer region, with these transport components taking the form

$$\mathcal{T}_{\text{ml side}}^x(i, j) = dy \sum_{k=1}^{k=nk} J^x(i, j, k) \text{mask}(i, j, k) \quad (6.88a)$$

$$\mathcal{T}_{\text{ml side}}^y(i, j) = dx \sum_{k=1}^{k=nk} J^y(i, j, k) \text{mask}(i, j, k). \quad (6.88b)$$

Again, these transports do not measure whether or not fluid crosses the mixed layer base. Instead, they measure transport crossing a horizontal boundary over any chosen region to determine the net transport entering or leaving the mixed layer within that region.

6.7.3 Seawater mass budget in the mixed layer

With reference to Figure 6.1 as guidance, we make note of the following terms that contribute to the seawater mass budget in the mixed layer. All terms have units of kg s^{-1} .

6.7.3.1 Volume integrated total time tendency

Here we consider the volume integrated total time tendency for mass within the ocean mixed layer.

- The integral of the time tendency for the seawater mass within the mixed layer domain takes the form

$$\text{mass tendency within mixed layer} = \sum_{j=js}^{je} \sum_{i=is}^{ie} dA \left(\sum_{k=1}^{k=nk} \text{mask}(i, j, k) \partial_t (\rho dz) \right) \quad (6.89)$$

where dA is the horizontal area of a tracer grid cell with units of m^2 . The net tendency (6.89) provides the “left hand side”, to which the sum of all terms on the “right hand side” must equal.

6.7.3.2 Vertical transport across ocean surface

Here we consider transport across the ocean surface due to surface boundary fluxes.

- Area integrated surface boundary fluxes of seawater mass passing into the upper ocean within the horizontal region of interest take the form

$$\text{surface boundary mass transport} = \sum_{j=js}^{je} \sum_{i=is}^{ie} dA Q^{\text{mass}}. \quad (6.90)$$

Recall that surface boundary fluxes, Q^{mass} , are positive when entering the ocean, and negative when leaving. Also recall that mixed layer has no less than one grid cell in the vertical, so that surface fluxes for all cells within the horizontal domain contribute to the mixed layer budget.

6.7.3.3 Vertical transport across mixed layer base (vertical subduction)

Here we consider vertical transport due to vertical advective fluxes crossing the mixed layer base.

- Vertical mass transport crossing the horizontal bottom face of the grid cell $\text{kmld}(i, j)$ sitting at the mixed layer base takes the form

$$\text{vertical mass transport crossing bottom of mixed layer} = \sum_{j=js}^{je} \sum_{i=is}^{ie} dA [\rho w^{(s)}]_{k=\text{kmld}(i, j)}. \quad (6.91)$$

Recall that a vertical mass flux $\rho w^{(s)}$ is positive when it moves vertically upward, and negative when downward. There is no subgrid scale term since there is no net mass change within any region due to subgrid scale processes (Section 6.3.2).

6.7.3.4 Zonal and meridional transport across lateral domain boundaries

Here we consider transport across the lateral domain boundaries delineated by $i = is, i = ie$ and $j = js, j = je$.

- The zonal mass transport crossing through the western boundary $i = is$ takes the form

$$\text{zonal mass transport crossing } i = is \text{ boundary} = \sum_{j=js}^{je} \left(\sum_{k=1}^{k=nk} \text{mask}(i = is - 1, j, k) [dy \rho dz u]_{i=is-1} \right), \quad (6.92)$$

where dy is the meridional grid spacing located at the east face of a tracer cell coincident with the location of the zonal flux. Note that the western face of the $i = is$ grid cell has a zonal flux labelled by $is - 1$. Recall that a zonal flux is positive when it moves eastward and negative when westward. There is no subgrid scale term since there is no net mass change within any region due to subgrid scale processes (Section 6.3.2).

- The zonal mass transport leaving through the eastern boundary $i = ie$ takes the form

$$\text{zonal mass transport crossing } i = ie \text{ boundary} = - \sum_{j=js}^{j=je} \left(\sum_{k=1}^{k=nk} \text{mask}(i = ie, j, k) [dy \rho dz u]_{i=ie} \right). \quad (6.93)$$

Note that the eastern face of the $i = ie$ grid cell has a zonal flux labelled by ie .

- The meridional mass transport crossing through the southern boundary $j = js$ takes the form

$$\text{meridional mass transport crossing } j = js \text{ boundary} = \sum_{i=is}^{i=ie} \left(\sum_{k=1}^{k=nk} \text{mask}(i, j = js - 1, k) [dx \rho dz v]_{j=js-1} \right), \quad (6.94)$$

where dx is the zonal grid spacing, located at the northern face of a tracer cell coincident with the meridional flux component. Note that the southern face of the $j = js$ grid cell has a meridional flux labelled by $js - 1$. Recall that a meridional flux is positive when it moves northward and negative when southward. There is no subgrid scale term since there is no net mass change within any region due to subgrid scale processes (Section 6.3.2).

- The meridional mass transport leaving through the northern boundary $j = je$ takes the form

$$\text{meridional mass transport crossing } j = je \text{ boundary} = - \sum_{i=is}^{i=ie} \left(\sum_{k=1}^{k=nk} \text{mask}(i, j = je, k) [dx \rho dz v]_{j=je} \right), \quad (6.95)$$

Note that the northern face of the $j = je$ grid cell has a meridional flux labelled by je .

6.7.3.5 Lateral transport through mixed layer base (lateral subduction)

Here we consider how to compute the subduction/obduction due to lateral seawater mass transport through the mixed layer base.

- The zonal mass transport crossing the eastern vertical face of the mixed layer base is given by

zonal mass transport across a vertical mixed layer boundary =

$$\sum_{j=js}^{j=je} \sum_{i=is}^{i=ie} \left(\sum_{k=1}^{k=nk} [\text{mask}(i + 1, j, k) - \text{mask}(i, j, k)] [dy \rho dz u]_{i,j,k} \right). \quad (6.96)$$

There is no subgrid scale term since there is no net mass change within any region due to subgrid scale processes (Section 6.3.2).

- The meridional mass transport crossing the northern vertical face of the mixed layer base is given by

meridional mass transport crossing northern vertical mixed layer boundary =

$$\sum_{j=js}^{j=je} \sum_{i=is}^{i=ie} \left(\sum_{k=1}^{k=nk} [\text{mask}(i, j + 1, k) - \text{mask}(i, j, k)] [dx \rho dz v]_{i,j,k} \right). \quad (6.97)$$

There is no subgrid scale term since there is no net mass change within any region due to subgrid scale processes (Section 6.3.2).

6.7.4 Tracer mass budget in the mixed layer

The tracer budgets follow largely from the seawater mass budgets, with additional terms associated with subgrid scale transport from mixing. We refer to such mixing-related transport processes as entrainment/detrainment, whereas advective transport processes retain the subduction/obduction terminology used for seawater mass. Each of the following terms has dimensions of tracer mass per time, or heat per time. With reference to Figure 6.1 as guidance, we make note of the following terms that contribute to the tracer mass budget in the mixed layer.

6.7.4.1 Volume integrated terms

- The integral of the time tendency for the tracer mass (or heat) within the mixed layer domain takes the form

$$\text{tracer tendency within mixed layer} = \sum_{j=js}^{j=je} \sum_{i=is}^{i=ie} dA \left(\sum_{k=1}^{k=nk} \text{mask}(i, j, k) \partial_t (\rho dz C) \right). \quad (6.98)$$

The net tendency term (6.98) provides the “left hand side”, to which the sum of all terms on the “right hand side” must equal.

- The integral of the sources or sinks for tracer mass (or heat) within the mixed layer domain takes the form

$$\text{tracer sources within mixed layer} = \sum_{j=js}^{j=je} \sum_{i=is}^{i=ie} dA \left(\sum_{k=1}^{k=nk} \text{mask}(i, j, k) S^{(c)} \rho dz \right). \quad (6.99)$$

Sources and sinks are most relevant for biogeochemical tracers.

6.7.4.2 Vertical transport across ocean surface

- Surface boundary fluxes of tracer passing into the upper ocean within the horizontal region of interest take the form

$$\text{surface boundary tracer transport} = \sum_{j=js}^{j=je} \sum_{i=is}^{i=ie} dA \left(Q_{\text{advec}}^{(c)} + Q_{\text{non-advec}}^{(c)} \right). \quad (6.100)$$

Recall that all surface boundary fluxes are assumed positive when they enter the ocean, and negative when they leave. Also recall that mixed layer has no less than one grid cell in the vertical, so that surface fluxes for all cells within the horizontal domain contribute to the mixed layer budget.

6.7.4.3 Vertical transport across mixed layer base

- Vertical tracer transport crossing the horizontal bottom face of the grid cell km1d sitting at the mixed layer base take the form

$$\text{vertical transport crossing bottom of mixed layer} = \sum_{j=js}^{j=je} \sum_{i=is}^{i=ie} dA [\rho (w^{(s)} C + F^{(s)})]_{k=\text{km1d}}. \quad (6.101)$$

Recall that a vertical flux is positive when it moves vertically upward, and negative when downward.

6.7.4.4 Zonal and meridional transport across horizontal domain boundaries

- The zonal tracer transport crossing the western boundary $i = is$ of the region takes the form

$$\text{zonal transport crossing } i = is \text{ boundary} = \sum_{j=js}^{j=je} \left(\sum_{k=1}^{k=nk} \text{mask}(i = is - 1, j, k) [dy \rho dz (u C + F^x)]_{i=is-1} \right), \quad (6.102)$$

where dy is the meridional grid spacing located at the east face of a tracer cell coincident with the location of the zonal flux. Note that the western face of the $i = is$ grid cell has a zonal flux labelled by $is - 1$. Recall that a zonal flux is positive when it moves eastward and negative when westerward.

- The zonal transport leaving through the eastern boundary $i = ie$ of the region takes the form

$$\text{zonal transport crossing } i = ie \text{ boundary} = - \sum_{j=js}^{j=je} \left(\sum_{k=1}^{k=nk} \text{mask}(i = ie, j, k) [dy \rho dz (u C + F^x)]_{i=ie} \right). \quad (6.103)$$

Note that the eastern face of the $i = ie$ grid cell has a zonal flux labelled by ie .

- The meridional transport crossing the southern boundary $j = js$ of the region takes the form

$$\text{meridional transport crossing } j = js \text{ boundary} = \sum_{i=is}^{i=ie} \left(\sum_{k=1}^{k=nk} \text{mask}(i, j = js - 1, k) [dx \rho dz (v C + F^y)]_{j=js-1} \right), \quad (6.104)$$

where dx is the zonal grid spacing, located at the northern face of a tracer cell coincident with the meridional flux component. Note that the southern face of the $j = js$ grid cell has a meridional flux labelled by $js - 1$. Recall that a meridional flux is positive when it moves northward and negative when southward.

- The meridional transport leaving through the northern boundary $j = je$ of the region takes the form

$$\text{meridional transport crossing } j = je \text{ boundary} = - \sum_{i=is}^{i=ie} \left(\sum_{k=1}^{k=nk} \text{mask}(i, j = je, k) [dx \rho dz (v C + F^y)]_{j=je} \right), \quad (6.105)$$

Note that the northern face of the $j = je$ grid cell has a meridional flux labelled by je .

6.7.4.5 Lateral transport through mixed layer base

- The zonal tracer mass transport crossing the eastern vertical face of the mixed layer base is given by

zonal tracer transport across a vertical mixed layer boundary =

$$\sum_{j=js}^{j=je} \sum_{i=is}^{i=ie} \left(\sum_{k=1}^{k=nk} [\text{mask}(i + 1, j, k) - \text{mask}(i, j, k)] [dy \rho dz (u C + F^x)]_{i,j,k} \right). \quad (6.106)$$

- The meridional tracer mass transport crossing the northern vertical face of the mixed layer base is given by

meridional mass transport crossing northern vertical mixed layer boundary =

$$\sum_{j=js}^{j=je} \sum_{i=is}^{i=ie} \left(\sum_{k=1}^{k=nk} [\text{mask}(i, j + 1, k) - \text{mask}(i, j, k)] [dx \rho dz (v C + F^y)]_{i,j,k} \right). \quad (6.107)$$

6.8 MOM5 mixed layer mass and tracer budgets

For the MOM5 mixed layer budget diagnostic, we do not presume a particular horizontal region over which the budget is to be computed. Instead, we only integrate the relevant terms vertically over the mixed layer. The mixed layer mask function `mask(i,j,k)` (equation (6.84)) is used for the mixed layer integration. Hence, all diagnostic fields are two-dimensional (i,j). Furthermore, each diagnostic is accumulated every time step when performing time averages.

6.8.1 Surface boundary fluxes

Diagnostics for the surface boundary fluxes of mass and tracer are saved as part of the usual surface boundary condition module `mom5/core/ocean_sbc.F90`. There are no separate diagnostics for the mixed layer budgets required for these terms, since all surface fluxes within a horizontal region of interest will contribute to the mixed layer budget.

6.8.2 Comments on submesoscale and KPP nonlocal transport

The mixed layer submesoscale eddy parameterization scheme from [Fox-Kemper et al. \(2011\)](#) prescribes a zero flux at the base of the mixed layer (Section 3.12). Hence, it does not contribute to fluxes crossing the mixed layer base. However, when performing regional budgets where we define a boundary at a particular longitude or latitude, the contributions from the submesoscale scheme to the region are nontrivial, and must be accounted for. We therefore include all diagnostics for this term in the following.

The KPP parameterization from [Large et al. \(1994\)](#) provides a non-local redistribution of surface fluxes within the KPP boundary layer in those cases where the surface buoyancy forcing is negative (i.e., convective buoyancy forcing). For cases where the mixed layer is as deep or deeper than the KPP boundary layer, the KPP non-local redistribution flux does not contribute to mixed layer tracer budgets. For those cases where the KPP boundary layer is deeper than the mixed layer, the non-local flux contributes to the mixed layer budget. We therefore provide diagnostics from this process for the mixed layer budget in order to verify that the term is negligible. Or if not negligible, to determine why.

6.8.3 Total tendency for seawater mass and tracer mass

The time change for the seawater mass in the mixed layer is given by

$$\text{mld_mass_tendency} = \text{dat} \left(\sum_{k=1}^{nk} \text{mask}(i, j, k) \partial_t (\rho dz) \right), \quad (6.108)$$

where `dat` is the horizontal area of a tracer grid cell with units of m^2 . To enhance vectorization of the diagnostic code, we perform the vertical sum over all vertical grid cells from $k = 1$ to $k = nk$, and apply `mask(i,j,k)` to remove contributions from terms below the mixed layer.

The time change for the tracer content in the mixed layer is given by

$$\text{mld_tracer_tendency} = \text{dat} \left(\sum_{k=1}^{nk} \text{mask}(i, j, k) \partial_t (\rho dz C) \right). \quad (6.109)$$

The name “tracer” appearing in the diagnostic is replaced by “temp”, “salt”, or another shortname for the relevant prognostic tracer concentration. To enhance vectorization of the diagnostic code, we perform the vertical sum over all vertical grid cells from $k = 1$ to $k = nk$, and apply `mask(i,j,k)` to remove contributions from terms below the mixed layer.

6.8.4 Tendency from tracer source/sinks

The tendency from sources within the mixed layer is given by

$$\text{mld_tracer_source} = \text{dat} \left(\sum_{k=1}^{nk} \text{mask}(i, j, k) \rho dz S^{(c)} \right), \quad (6.110)$$

There are no sources for seawater mass, heat, or salt, but there are sources for biogeochemical tracers. The code calling the vertical sum needs to be incorporated into the relevant TOPAZ, BLING, miniBLING code.

6.8.5 Vertical transport through horizontal mixed layer base

The following diagnostics are available for the vertical transports passed across the horizontally oriented portion of the mixed layer base.

6.8.5.1 Resolved advective transport

- The seawater mass transport from vertical advective fluxes across mixed layer base is given by

$$\text{mld_base_tz_trans} = \text{dat} \left(\rho w^{(s)} \right)_{k=\text{kmlid}(i, j)}, \quad (6.111)$$

where $\text{kmlid}(i, j)$ is the k-level where the mixed layer base sits.

- The tracer mass transport from vertical advective fluxes across mixed layer base is given by

$$\text{mld_base_tracer_zflux_adv} = \text{dat} \left(\rho w^{(s)} C \right)_{k=\text{kmlid}(i, j)}. \quad (6.112)$$

6.8.5.2 Transport from parameterized mesoscale eddies

- The tracer mass transport across mixed layer base from the vertical component to the [Gent et al. \(1995\)](#) mesoscale eddy parameterization is given by

$$\text{mld_base_tracer_zflux_gm} = \text{dat} \left(\rho F_{\text{gm}}^{(s)} \right)_{k=\text{kmlid}(i, j)}. \quad (6.113)$$

Note that we generally diagnose this term according to the skew flux ([Griffies, 1998](#)) realization of the [Gent et al. \(1995\)](#) or [Ferrari et al. \(2010\)](#) scheme. There is no corresponding subgrid scale term for the mass budget since there is no net mass change within any region due to subgrid scale processes (Section [6.3.2](#)).

6.8.5.3 Transport from parameterized submesoscale eddies

- The tracer mass transport across mixed layer base from the vertical component to the [Fox-Kemper et al. \(2011\)](#) mixed layer submesoscale eddy parameterization is given by

$$\text{mld_base_tracer_zflux_submeso} = \text{dat} \left(\rho F_{\text{submeso}}^{(s)} \right)_{k=\text{kmlid}(i, j)}. \quad (6.114)$$

This term is typically zero, since the parameterization is turned off at the base of the mixed layer. We nonetheless provide this diagnostic in order to verify the term is negligible. There is no corresponding subgrid scale term for the mass budget since there is no net mass change within any region due to subgrid scale processes (Section [6.3.2](#)).

6.8.5.4 Tracer transport from parameterized mixing processes

- The tracer mass transport across mixed layer base from vertical diffusive fluxes is given by

$$\text{mld_base_tracer_zflux_vdiff} = \text{dat} \left(\rho F_{\text{vert diff}}^{(s)} \right)_{k=\text{kmlid}(i,j)}. \quad (6.115)$$

- The tracer mass tendency across mixed layer base from KPP parameterized vertical redistribution of surface fluxes is given by

$$\text{mld_base_tracer_zflux_kpp_nonlocal} = \text{dat} \left(\rho F_{\text{kpp nonlocal}}^{(s)} \right)_{k=\text{kmlid}(i,j)}. \quad (6.116)$$

This term is zero for cases where the mixed layer is as deep or deeper than the KPP boundary layer.

- The tracer mass transport across mixed layer base from the vertical component to the neutral diffusive flux is given by

$$\text{mld_base_tracer_zflux_ndiff} = \text{dat} \left(\rho F_{\text{neutral diff}}^{(s)} \right)_{k=\text{kmlid}(i,j)}. \quad (6.117)$$

6.8.5.5 Heat transport from penetrative shortwave radiation

Shortwave heat flux is included as part of the net surface boundary heat flux. Yet a portion of the shortwave radiation penetrates into the ocean depth, within the mixed layer and possibly below. We must account for the portion of this penetrative shortwave transport that leaves the bottom of the mixed layer.

- The vertical heat transport from penetrative shortwave radiation that leaves the bottom of the mixed layer is given by

$$\text{mld_base_heat_swpen} = \text{dat} \left(\rho F_{\text{shortwave pen}}^{(s)} \right)_{k=\text{kmlid}(i,j)}. \quad (6.118)$$

6.8.6 Lateral transport through boundaries of a mixed layer column

We detail here those diagnostics needed to compute the lateral seawater mass and tracer mass transport crossing all vertical cell faces (west, east, south, and north) within the mixed layer for each (i, j) column.

6.8.6.1 Transport from resolved velocity

- Seawater mass transport from the zonal advective flux crossing the eastern face of a column in the mixed layer

$$\text{mld_tx_trans} = \sum_{k=1}^{k=nk} \text{mask}(i, j, k) [\rho dz dy u]_i. \quad (6.119)$$

- Seawater mass transport from the meridional advective flux crossing the northern face of a column in the mixed layer

$$\text{mld_ty_trans} = \sum_{k=1}^{k=nk} \text{mask}(i, j, k) [\rho dz dx v]_j. \quad (6.120)$$

- Tracer mass transport from the zonal advective flux crossing the eastern face of a column in the mixed layer

$$\text{mld_tracer_xflux_adv} = \sum_{k=1}^{k=nk} \text{mask}(i, j, k) [\rho dz dy u C]_i. \quad (6.121)$$

- Tracer mass transport from the meridional advective flux crossing the northern face of a column in the mixed layer

$$\text{mld_tracer_yflux_adv} = \sum_{k=1}^{k=nk} \text{mask}(i, j, k) [\rho dz dx v C]_j. \quad (6.122)$$

6.8.6.2 Transport from advective or skew diffusive mesoscale parameterization

The following details the diagnostics available for the mesoscale eddy parameterizations, such as those from Gent et al. (1995) or its refinement according to Ferrari et al. (2010). The tracer transport is generally implemented according to the Griffies (1998) approach.

- Tracer mass transport from the zonal parameterized mesoscale eddy flux (advective or skew diffusive) crossing the eastern face of a column in the mixed layer

$$\text{mld_tracer_xflux_gm} = \sum_{k=1}^{k=nk} \text{mask}(i, j, k) \left[\rho dz dy F_{\text{gm}}^{(x)} \right]_i. \quad (6.123)$$

- Tracer mass transport from the meridional parameterized mesoscale eddy flux (advective or skew diffusive) crossing the northern face of a column in the mixed layer

$$\text{mld_tracer_yflux_gm} = \sum_{k=1}^{k=nk} \text{mask}(i, j, k) \left[\rho dz dx F_{\text{gm}}^{(y)} \right]_j. \quad (6.124)$$

There are no corresponding subgrid scale terms for the mass budget since there is no net mass change within any region due to subgrid scale processes (Section 6.3.2).

6.8.6.3 Transport from advective or skew diffusive submesoscale parameterization

The following details the diagnostics available for the Fox-Kemper et al. (2011) scheme.

- Tracer mass transport from the zonal parameterized submesoscale eddy flux (advective or skew diffusive) crossing the eastern face of a column in the mixed layer

$$\text{mld_tracer_xflux_submeso} = \sum_{k=1}^{k=nk} \text{mask}(i, j, k) \left[\rho dz dy F_{\text{submeso}}^{(x)} \right]_i. \quad (6.125)$$

- Tracer mass transport from the meridional parameterized submesoscale eddy flux (advective or skew diffusive) crossing the northern face of a column in the mixed layer

$$\text{mld_tracer_yflux_submeso} = \sum_{k=1}^{k=nk} \text{mask}(i, j, k) \left[\rho dz dx F_{\text{submeso}}^{(y)} \right]_j. \quad (6.126)$$

There are no corresponding subgrid scale terms for the mass budget since there is no net mass change within any region due to subgrid scale processes (Section 6.3.2).

6.8.6.4 Diffusive transport

- Tracer mass transport from the zonal component of the neutral diffusive flux crossing the eastern face of a column in the mixed layer

$$\text{mld_tracer_xflux_ndiff} = \sum_{k=1}^{k=nk} \text{mask}(i, j, k) \left[\rho dz dy F_{\text{neutral diff}}^{(x)} \right]_i. \quad (6.127)$$

Note that in regions of steep neutral slope, as in the mixed layer, the neutral diffusive flux is largely oriented horizontally (Treguier et al. (1997), Ferrari et al. (2008), ?, Ferrari et al. (2010)).

- Tracer mass transport from the meridional component of the neutral diffusive flux crossing the northern face of a column in the mixed layer

$$\text{mld_tracer_yflux_ndiff} = \sum_{k=1}^{k=nk} \text{mask}(i, j, k) \left[\rho dz dx F_{\text{neutral diff}}^{(y)} \right]_j. \quad (6.128)$$

6.8.7 Lateral transport through mixed layer base

We now detail diagnostics available to compute the vertically integrated fluxes crossing the vertical faces of the mixed layer base (west, east, south, and north) that pass from or to the mixed layer from non-mixed layer cells. The resulting transports account for mass entering or leaving the base of the mixed layer through lateral processes.

6.8.7.1 Transport from resolved velocity

- Mass transport from the zonal advective flux is given by

$$\text{mld_base_tx_trans} = \sum_{k=1}^{k=nk} [\text{mask}(i+1, j, k) - \text{mask}(i, j, k)] [\rho dz dy u]_i. \quad (6.129)$$

- Mass transport from the meridional advective flux is given by

$$\text{mld_base_ty_trans} = \sum_{k=1}^{k=nk} [\text{mask}(i, j+1, k) - \text{mask}(i, j, k)] [\rho dz dx v]_j. \quad (6.130)$$

- Tracer transport from the zonal advective flux is given by

$$\text{mld_base_tracer_xflux_adv} = \sum_{k=1}^{k=nk} [\text{mask}(i+1, j, k) - \text{mask}(i, j, k)] [\rho dz dy C u]_i. \quad (6.131)$$

- Tracer transport from the meridional advective flux is given by

$$\text{mld_base_tracer_yflux_adv} = \sum_{k=1}^{k=nk} [\text{mask}(i, j+1, k) - \text{mask}(i, j, k)] [\rho dz dx C v]_j. \quad (6.132)$$

6.8.7.2 Transport from parameterized mesoscale eddies

The following details the mixed layer transport diagnostics available for the mesoscale eddy parameterizations, such as those from [Gent et al. \(1995\)](#) or its refinement according to [Ferrari et al. \(2010\)](#). The tracer transport is generally implemented according to the [Griffies \(1998\)](#) approach.

- Tracer transport from the zonal advective or skew tracer flux is given by

$$\text{mld_base_tracer_xflux_gm} = \sum_{k=1}^{k=nk} [\text{mask}(i+1, j, k) - \text{mask}(i, j, k)] [\rho dz dy F_{\text{gm}}^{(x)}]_i. \quad (6.133)$$

- Tracer transport from the meridional advective or skew tracer flux is given by

$$\text{mld_base_tracer_yflux_gm} = \sum_{k=1}^{k=nk} [\text{mask}(i, j+1, k) - \text{mask}(i, j, k)] [\rho dz dx F_{\text{gm}}^{(y)}]_j. \quad (6.134)$$

There are no corresponding subgrid scale terms for the mass budget since there is no net mass change within any region due to subgrid scale processes (Section [6.3.2](#)).

6.8.7.3 Transport from parameterized submesoscale eddies

The following details the mixed layer diagnostics available for the [Fox-Kemper et al. \(2011\)](#) scheme. As noted in Section [6.8.2](#), this scheme is generally small, if not zero, at the mixed layer base, in which case this term contributes nothing to the mixed layer mass budget. We nonetheless provide a diagnostic in order to verify the term is indeed negligible.

- Tracer transport from the meridional advective or skew tracer flux is given by

$$\text{mld_base_tracer_xflux_submeso} = \sum_{k=1}^{k=nk} [\text{mask}(i+1, j, k) - \text{mask}(i, j, k)] \left[\rho dz dy F_{\text{submeso}}^{(x)} \right]_i. \quad (6.135)$$

- Tracer transport from the meridional advective or skew tracer flux is given by

$$\text{mld_base_tracer_yflux_submeso} = \sum_{k=1}^{k=nk} [\text{mask}(i, j+1, k) - \text{mask}(i, j, k)] \left[\rho dz dx F_{\text{submeso}}^{(y)} \right]_j. \quad (6.136)$$

There are no corresponding subgrid scale terms for the mass budget since there is no net mass change within any region due to subgrid scale processes (Section [6.3.2](#)).

6.8.7.4 Tracer transport from neutral diffusion

- Tracer transport from the meridional neutral diffusive tracer flux is given by

$$\text{mld_base_tracer_xflux_ndiff} = \sum_{k=1}^{k=nk} [\text{mask}(i+1, j, k) - \text{mask}(i, j, k)] \left[\rho dz dy F_{\text{neutral diff}}^{(x)} \right]_i. \quad (6.137)$$

- Tracer transport from the meridional neutral diffusive tracer flux is given by

$$\text{mld_base_tracer_yflux_ndiff} = \sum_{k=1}^{k=nk} [\text{mask}(i, j+1, k) - \text{mask}(i, j, k)] \left[\rho dz dx F_{\text{neutral diff}}^{(y)} \right]_j. \quad (6.138)$$

6.9 Sample mixed layer budget calculations

Following the examples for heat budgets provided in Section [5.5](#), we here consider some sample mixed layer mass and tracer budgets. Seawater mass budget for the mixed layer over a horizontal region $is \leq i \leq ie$ and $js \leq j \leq je$.

$$\begin{aligned} \sum_{i,j} \text{mld_mass_tendency} &= \sum_{i,j} \text{surface_mass_transport} + \sum_{i,j} (\text{mld_base_tz_trans}) \\ &\quad + \sum_j (\text{mld_tx_trans})_{i=is-1} - \sum_j (\text{mld_tx_trans})_{i=ie} \\ &\quad + \sum_i (\text{mld_ty_trans})_{j=js-1} - \sum_i (\text{mld_ty_trans})_{j=je} \\ &\quad + \sum_{i=is, j=js}^{i=ie, j=je} (\text{mld_base_tx_trans}) + \sum_{i=is, j=js}^{i=ie, j=je-1} (\text{mld_base_ty_trans}). \end{aligned} \quad (6.139)$$

The indices are important, with Figure 6.1 providing guidance. The tracer mass budget within a horizontal regional over the full mixed layer is given by

$$\begin{aligned}
 \sum_{i,j} \text{mld_tracer_tendency} = & \sum_{i,j} (\text{boundary_tracer_transport} + \text{eta_tracer_smooth} + \text{mld_tracer_source}) \\
 & + \sum_{i,j} (\text{mld_base_tracer_zflux_adv} + \text{mld_base_tracer_zflux_gm} + \text{mld_base_tracer_zflux_submeso}) \\
 & + \sum_{i,j} (\text{mld_base_tracer_zflux_vdiff} + \text{mld_base_heat_swpen}) \\
 & + \sum_j (\text{mld_tracer_xflux_adv} + \text{mld_tracer_xflux_gm} + \text{mld_tracer_xflux_submeso} + \text{mld_tracer_xflux_ndiff})_{i=is-1} \\
 & - \sum_j (\text{mld_tracer_xflux_adv} + \text{mld_tracer_xflux_gm} + \text{mld_tracer_xflux_submeso} + \text{mld_tracer_xflux_ndiff})_{i=ie} \\
 & + \sum_j (\text{mld_tracer_yflux_adv} + \text{mld_tracer_yflux_gm} + \text{mld_tracer_yflux_submeso} + \text{mld_tracer_yflux_ndiff})_{j js-1} \\
 & - \sum_j (\text{mld_tracer_yflux_adv} + \text{mld_tracer_yflux_gm} + \text{mld_tracer_yflux_submeso} + \text{mld_tracer_yflux_ndiff})_{j=je} \\
 & + \sum_{i=is, j=js}^{i=ie-1, j=je} (\text{mld_base_tracer_xflux_adv} + \text{mld_base_tracer_xflux_gm} + \text{mld_base_tracer_xflux_submeso} + \text{mld_base_tracer_xflux_ndiff}) \\
 & + \sum_{i=is, j=js}^{i=ie, j=je-1} (\text{mld_base_tracer_yflux_adv} + \text{mld_base_tracer_yflux_gm} + \text{mld_base_tracer_yflux_submeso} + \text{mld_base_tracer_yflux_ndiff}).
 \end{aligned} \tag{6.140}$$

Eddy-mean flow decomposition

This part provides a very brief introduction to the decomposition between eddies and mean flow.

Chapter 7

Transient eddy contributions

Contents

7.1	Eddy-mean flow decomposition of tracer transport	192
7.1.1	Diagnosing time mean and transient eddy heat fluxes	193
7.1.2	MOM5 requirements to diagnose temp_advection[$\langle \mathcal{U} \rangle, \langle \mathcal{W} \rangle, \langle \Theta \rangle$]	194
7.2	Eddy decomposition with a seasonal cycle	194
7.2.1	General formulation	194
7.2.2	Seasonal decomposition for the temporal variance	195
7.2.3	Seasonal decomposition for the tracer advection operator	196
7.3	Higher moments estimated from daily output	196
7.4	Horizontally averaged heat budget with eddy-mean flow decomposition	197

The tracer budgets (5.35a)-(5.35c) contain contributions from the convergence of resolved advective transport, boundary terms, and the convergence of parameterized subgrid scale transport. In an eddying simulation such as CM2.6, we are interested in decomposing the contribution from resolved advection into a time mean and transient eddy term. The transient term is, presumably, something that is parameterized in coarser resolution models that do not admit mesoscale eddy variability. We are also interested in diagnosing the contribution from transient eddies to the kinetic energy and sea surface height in order to measure the relative contributions from mean and transient processes.

To compare impacts from the CM2.6 transient eddies to the parameterized eddies in a coarser model, it is useful to define a suitable eddy-mean flow decomposition. Details of this procedure are many and complex, with a number of methods available largely determined by the vertical coordinates, space-time scales of the eddies of interest, and style of the analyst. We pursue here one method that is readily available within MOM5, and serves our needs to garner a diagnostic representation of the impacts from transient eddies on advective tracer transport. Namely, we work within the coordinates of MOM5 and perform quasi-Eulerian time averages to decompose fields into mean and eddy. We readily acknowledge other means of performing this eddy-mean flow decomposition, such as by projecting fluxes onto neutral directions, given that these are directions preferred for mesoscale eddy fluxes. However, we work within the traditional Eulerian framework here, if only because of its simplicity and due to its being an entry point to alternative approaches. These methods are also trivially extended to the study of eddy dynamics manifesting in sea surface properties, such as SST, SSS, and SSH.

7.1 Eddy-mean flow decomposition of tracer transport

The mathematical goal is to decompose the tracer advection operator

$$\mathcal{A} \equiv -\nabla_s \cdot [\rho dz \mathbf{u} C] - [\rho w^{(s)} C]_{s=s_{k-1}} + [\rho w^{(s)} C]_{s=s_k} \quad (7.1)$$

into a term determined just by time mean fields, and a term associated with correlations between transient eddy fluctuations. For this purpose, we introduce the horizontal and vertical advective mass transports according to

$$\mathcal{U} = \mathbf{u} \rho dz \quad (7.2a)$$

$$\mathcal{W} = w^{(s)} \rho. \quad (7.2b)$$

These mass transport components are defined as part of the MOM5 algorithm for determining the tracer advection operator. For a Boussinesq ocean, such as CM2.6-ocean, the density factors reduce to constant reference density ρ_0 , in which case they can be readily dropped. With generalized level coordinates, the thickness factor dz is time dependent. For an adiabatic isopycnal model, correlations between layer thickness and lateral velocity are physically meaningful, with parameterization of these correlations the aim of such schemes as [Gent and McWilliams \(1990\)](#). However, in MOM5, the generalized level coordinates are not isopycnal, so the correlations between thickness and velocity are not of interest for an eddy parameterization. We therefore retain \mathcal{U} and \mathcal{W} as distinct objects rather than decomposing them into their more basic thickness and velocity constituents.

Introducing the horizontal and vertical mass transport components into the advection operator (7.1) leads to

$$\mathcal{A} = -\nabla_s \cdot [\mathcal{U} C] - \delta_k [\mathcal{W} C]_{s=s_{k-1}}, \quad (7.3)$$

where

$$\delta_k [\mathcal{W} C]_{s=s_{k-1}} = [\mathcal{W} C]_{s=s_{k-1}} - [\mathcal{W} C]_{s=s_k}. \quad (7.4)$$

We now decompose the mass transport and tracer concentration into time mean and transient eddy components

$$\mathcal{U} = \langle \mathcal{U} \rangle + \mathcal{U}' \quad (7.5a)$$

$$\mathcal{W} = \langle \mathcal{W} \rangle + \mathcal{W}' \quad (7.5b)$$

$$C = \langle C \rangle + C', \quad (7.5c)$$

where angle brackets denote time averaging, and transients are denoted by the prime. As so defined, a fluctuating eddy quantity is defined relative to a mean field, so that the mean of the fluctuating quantity vanishes. Hence, the familiar decomposition of the time averaged advection operator is given by

$$\langle \mathcal{A} \rangle = \mathcal{A}^{\text{mean}} + \mathcal{A}^{\text{eddy}}, \quad (7.6)$$

where

$$\mathcal{A}^{\text{mean}} = -\left(\nabla_s \cdot [\langle \mathcal{U} \rangle \langle C \rangle] + \delta_k [\langle \mathcal{W} \rangle \langle C \rangle]_{s=s_{k-1}}\right) \quad (7.7)$$

is the advection operator based on fluxes constructed with the time mean transport and time mean tracer concentration, whereas

$$\mathcal{A}^{\text{eddy}} = -\left(\nabla_s \cdot \langle \mathcal{U}' C' \rangle + \delta_k \langle \mathcal{W}' C' \rangle_{s=s_{k-1}}\right) \quad (7.8)$$

is the advection operator based on the convergence of eddy fluxes. By focusing on the convergence of advective fluxes, rather than the advective fluxes themselves, we are able to deduce the affects on the tracer tendency from transient eddies without concern for the arbitrary rotational portion of the eddy heat flux field ([Fox-Kemper et al., 2003](#)). This approach was also taken by [Bryan et al. \(1999\)](#) for similar reasons.

7.1.1 Diagnosing time mean and transient eddy heat fluxes

In MOM5, the diagnostic `temp_advection` discussed in Section 5.5 measures the impacts from the convergence of the advective temperature fluxes on the heat budget for a grid cell. Using the notation of equation (7.1), we have

$$\text{temp_advection} = \mathcal{A}. \quad (7.9)$$

Performing a time average of the diagnostic `temp_advection`, and a time average on the advective mass transports and tracer concentrations, then leads to the identity

$$\langle \text{temp_advection} \rangle = \langle \mathcal{A} \rangle \quad (7.10\text{a})$$

$$= \mathcal{A}^{\text{mean}} + \mathcal{A}^{\text{eddy}} \quad (7.10\text{b})$$

$$= \text{temp_advection}[\langle \mathcal{U} \rangle, \langle \mathcal{W} \rangle, \langle \Theta \rangle] + \mathcal{A}^{\text{eddy}}. \quad (7.10\text{c})$$

This identity holds by definition, so that it is independent of the extent of the time average. We can thus define a transient eddy contribution to the advection operator corresponding to any time scale of interest, such as the following.

- We may consider the time average over a year, so that the eddy contribution can be determined as a yearly mean for each year of the simulation.
- We may consider the time average over a month, and then take a 10 or 20 year mean of the monthly time average. Then, the climatological monthly eddy contribution can be determined. We have more to say in Section 7.2 regarding the utility of a monthly time average and associated anomalies.

The diagnostic calculation of $\text{temp_advection}[\langle \mathcal{U} \rangle, \langle \mathcal{W} \rangle, \langle \Theta \rangle]$ is only available after running the simulation, since we do not have information about the time mean when time stepping the model equations online. Upon diagnosing the advection operator using the time mean fields, we can infer the eddy contribution to advection via

$$\mathcal{A}^{\text{eddy}} = \langle \text{temp_advection} \rangle - \text{temp_advection}[\langle \mathcal{U} \rangle, \langle \mathcal{W} \rangle, \langle \Theta \rangle]. \quad (7.11)$$

Upon determining the time mean and transient eddy terms, $\mathcal{A}^{\text{mean}}$ and $\mathcal{A}^{\text{eddy}}$, we can diagnose the corresponding contributions to the tracer budget for a grid cell (Section 5.4); over a depth integrated ocean column (Section 5.6); poleward heat flux (Section 5.7); and horizontally averaged tracer budgets (Section 7.4). One potential application of this diagnostic framework is to consider the budget for horizontally integrated temperature, and determine how various terms contribute to the drift as per Figure 5.2.

In summary, diagnostics required are as follows.

- `temp_advection` to compute the affects of advection on the heat budget in a grid cell, from which the time average `temp_advection` is computed.
- The time averaged temperature, $\langle \Theta \rangle$, and the time averaged mass transport components, $(\langle \mathcal{U} \rangle, \langle \mathcal{W} \rangle)$.
- We then feed the time averaged fields into MOM5 to diagnose, over a single time step, the advection operator $\text{temp_advection}[\langle \mathcal{U} \rangle, \langle \mathcal{W} \rangle, \langle \Theta \rangle]$. This is a straightforward, yet tedious, step that must be performed offline.
- The analogous diagnostic calculation is followed for any other tracer.

Rather than the use of MOM5 to determine the operator $\text{temp_advection}[\langle \mathcal{U} \rangle, \langle \mathcal{W} \rangle, \langle \Theta \rangle]$, we may choose to estimate it using 2nd order centered difference fluxes. But this approach leads to an advective flux that differs from that computed by MOM5 in CM2.6, which uses the MDPPM scheme. The centered difference approach also requires code development, using Matlab, Python, Fortran, or another suitable language (not Ferret!) and testing, along with the associated I/O required to read in the time mean fields that are particularly large for CM2.6.

7.1.2 MOM5 requirements to diagnose $\text{temp_advection}[\langle \mathcal{U} \rangle, \langle \mathcal{W} \rangle, \langle \Theta \rangle]$

MOM5 provides a mechanism to read the climatological transport and tracer concentrations to thus diagnose the advection operator $\mathcal{A}_m^{\text{mean}}$. Necessary steps include the following.

- Fill the file INPUT/ocean_advect_velocity.nc with the following variables:
 - ★ ue = $\langle u_{\text{hrho}} \rangle_{\text{et}}$
 - ★ vn = $\langle v_{\text{hrho}} \rangle_{\text{nt}}$
 - ★ wb = $\langle w_{\text{rho}} \rangle$.
- Replace the snapshot tracer concentration in the restart file with the time averaged concentration, such as the time averaged temperature $\langle \Theta \rangle$.
- Inside the namelist ocean_advection_velocity.nml, make the following settings:


```
read_advection_transport = .true.          (7.12a)
```

```
read_advection_velocity = .false.           (7.12b)
```
- Set interpolate_tprog_to_pbott = .false. inside the namelist ocean_tracer.nml to remove the default extrapolation of tracer fields into the partial bottom cells. This extrapolation is normally done if starting from initial conditions. We do not wish to have the extrapolation performed, since we wish to have the advection operator evaluated from the precise time mean tracer fields. Set interpolate_tprog_to_pbott = .false. to eliminate the extrapolation step.
- Run the model for a single time step, and diagnose the resulting advection operator temp_advection for temperature, salt_advection for salinity, etc.

We note one minor caveat regarding this diagnostic. Namely, the history files that save the time mean tracer and time mean transport are normally accumulated using single precision, in order to save disk space. Consequently, the evaluated advection operator will have less precision than if working with full precision time averaged fields. Nonetheless, single precision should be sufficiently accurate for most purposes.

7.2 Eddy decomposition with a seasonal cycle

The CM2-Ocean model suite includes diurnal and seasonal cycles for surface ocean boundary fluxes. Diurnal forcing affects the upper ocean boundary layer. Seasonal forcing affects the boundary layer as well as the pycnocline, including deep ocean impacts for the high latitudes. Seasonal forcing impacts on mesoscale eddies through stratification via mechanical and buoyancy forcing. To explore impacts from transient mesoscale eddies in CM2-Ocean simulations, we define a transient fluctuation relative to its climatological monthly value, with statistical details given here.

7.2.1 General formulation

The CM2-Ocean suite diagnoses monthly mean values of various fields, Φ , computed by time averaging over each model time step within a particular month $m = 1, 12$

$$\overline{\Phi}^m = \frac{1}{N_m} \sum_{n=1}^{N_m} \Phi(t), \quad (7.13)$$

where N_m is the number of time steps in month m .¹ A climatological month is computed by averaging over the N years of a chosen analysis period

$$\langle \bar{\Phi}^m \rangle = \frac{1}{N} \sum_{n=1}^N \bar{\Phi}^m. \quad (7.14)$$

At any time t within a month m , the instantaneous value for a field is written as the sum of a climatological month plus a fluctuation

$$\Phi(t) = \langle \bar{\Phi}^m \rangle + \Phi'(t) \quad t \in [T_{\text{start}}^m, T_{\text{end}}^m], \quad (7.15)$$

with $[T_{\text{start}}^m, T_{\text{end}}^m]$ the time interval for a particular month m . The field, $\Phi'(t)$, measures fluctuations at time t relative to the climatological mean month, $\langle \bar{\Phi}^m \rangle$.

For any given month, the product of two anomalous fields at the same time (e.g., the anomalous transport and anomalous tracer concentration found in the eddy advection operator in equation (7.8)) is written

$$\Phi'(t) \Psi'(t) = (\Phi(t) - \langle \bar{\Phi}^m \rangle)(\Psi(t) - \langle \bar{\Psi}^m \rangle) \quad (7.16a)$$

$$= \Phi(t) \Psi(t) + \langle \bar{\Phi}^m \rangle \langle \bar{\Psi}^m \rangle - \Psi(t) \langle \bar{\Phi}^m \rangle - \Phi(t) \langle \bar{\Psi}^m \rangle. \quad (7.16b)$$

The monthly mean of this product is given by

$$\overline{\Phi' \Psi'^m} = \overline{\Phi \Psi^m} + \langle \bar{\Phi}^m \rangle \langle \bar{\Psi}^m \rangle - \overline{\Psi^m} \langle \bar{\Phi}^m \rangle - \overline{\Phi^m} \langle \bar{\Psi}^m \rangle. \quad (7.17)$$

The corresponding climatological monthly mean correlation is

$$\langle \overline{\Phi' \Psi'^m} \rangle = \langle \overline{\Phi \Psi^m} \rangle - \langle \bar{\Phi}^m \rangle \langle \bar{\Psi}^m \rangle. \quad (7.18)$$

and the climatological mean correlation over a full year is

$$\langle \overline{\Phi' \Psi'^a} \rangle = \langle \overline{\Phi \Psi^a} \rangle - \sum_{m=1}^{12} \chi_m \langle \bar{\Phi}^m \rangle \langle \bar{\Psi}^m \rangle, \quad (7.19)$$

where χ_m is the fraction of a year occupied by each month, and

$$\langle \overline{\Phi \Psi^a} \rangle = \sum_{m=1}^{12} \chi_m \langle \overline{\Phi \Psi^m} \rangle \quad (7.20a)$$

$$\langle \overline{\Phi' \Psi'^a} \rangle = \sum_{m=1}^{12} \chi_m \langle \overline{\Phi' \Psi'^m} \rangle. \quad (7.20b)$$

Note that the CM2-O suite of simulations uses a Julian calendar, in which every fourth year is a leap-year. Ignoring that detail when computing annual means produces a very small error.

7.2.2 Seasonal decomposition for the temporal variance

As an application of the formalism, consider the variance of a field such as the sea surface height, η , a tracer concentration, C , or component of the velocity field, \mathbf{v} . The climatological monthly mean correlation is given by

$$\langle \overline{\Phi' \Phi'^m} \rangle = \langle \overline{\Phi \Phi^m} \rangle - \langle \bar{\Phi}^m \rangle \langle \bar{\Phi}^m \rangle. \quad (7.21)$$

In words, the left hand side is the climatological monthly correlation between a fluctuation and itself. The first term on the right hand side is the climatological mean month for the squared field, and the second term is the square of the climatological mean monthly value of the field. Precise computation of this

¹We drop spatial dependence in this section to reduce notation clutter.

variance requires diagnosing the monthly mean for both the field Φ , and its square, Φ^2 . We use equation (7.19) to extend the monthly mean result (7.21) to a yearly mean, thus leading to

$$\langle \overline{\Phi' \Phi'^a} \rangle = \langle \overline{\Phi \Phi^a} \rangle - \sum_{m=1}^{12} \chi_m \langle \overline{\Phi^m} \rangle \langle \overline{\Phi^m} \rangle. \quad (7.22)$$

7.2.3 Seasonal decomposition for the tracer advection operator

We apply this seasonal decomposition to the advection operator decomposition (7.10b) by writing the monthly mean advection operator as

$$\langle \mathcal{A}_m \rangle = \mathcal{A}_m^{\text{mean}} + \mathcal{A}_m^{\text{eddy}}, \quad (7.23)$$

where we here drop the overline for monthly mean to reduce clutter. In this expression, the mean advection operator based on climatological monthly mean fields is given by

$$\mathcal{A}_m^{\text{mean}} = -\left(\nabla_s \cdot [\langle \mathcal{U}_m \rangle \langle C_m \rangle] + \delta_k [\langle \mathcal{W}_m \rangle \langle C_m \rangle]_{s=s_{k-1}} \right). \quad (7.24)$$

Likewise, the eddy advection operator based on climatological correlations between monthly anomalies is

$$\mathcal{A}_m^{\text{eddy}} = -\left(\nabla_s \cdot [\langle \mathcal{U}'_m C'_m \rangle] + \delta_k [\langle \mathcal{W}'_m C'_m \rangle]_{s=s_{k-1}} \right) \quad (7.25a)$$

$$= \langle \mathcal{A}_m \rangle - \mathcal{A}_m^{\text{mean}}. \quad (7.25b)$$

The eddy contribution to the full extent of the analysis is then given by the weighted sum over a year of the monthly contributions

$$\mathcal{A}^{\text{eddy}} = \sum_{m=1}^{12} \chi_m \mathcal{A}_m^{\text{eddy}}. \quad (7.26)$$

7.3 Higher moments estimated from daily output

The CM2-O simulations save the daily mean SST, SSS, and SSH within the sea ice model output, where the daily mean is computed by accumulating each model time step according to

$$\overline{\Phi^d} = \frac{1}{N_d} \sum_{n=1}^{N_d} \Phi(t), \quad (7.27)$$

where N_d is the number of time steps in a day. Absent saving triple and higher products for the surface fields, we approximate higher moments through use of daily mean fields. We are motivated by the work of [Thompson and Demirov \(2005\)](#) and [Hughes et al. \(2010\)](#) to consider such higher moments in order to compute skewness and kurtosis, where skewness is given by the dimensionless quantity

$$\mathcal{S} = \frac{\Delta^3}{(\Delta^2)^{3/2}} \quad (7.28)$$

and kurtosis, also dimensionless, is

$$\mathcal{K} = \frac{\Delta^4}{(\Delta^2)^2}, \quad (7.29)$$

with Δ the deviation from the climatological mean.

Given both the monthly mean and daily mean values for a field, Φ , we can estimate the monthly mean for the third moment by computing the monthly mean of the product

$$\overline{\Phi' \Phi' \Phi'^m} = \frac{1}{D_m} \sum_{d=1}^{D_m} \left(\overline{\Phi^d} - \langle \overline{\Phi^m} \rangle \right)^3, \quad (7.30)$$

where D_m is the number of days in month m .² Likewise, the fourth moment for a month is approximated by

$$\overline{\Phi' \Phi' \Phi' \Phi'^m} = \frac{1}{D_m} \sum_{d=1}^{D_m} (\overline{\Phi^d} - \langle \overline{\Phi^m} \rangle)^4. \quad (7.31)$$

The annual mean for these moments is computed by averaging over a year, and the climatological mean is computed as for the climatological mean and variance given in Section 7.2.1.

Expressions (7.30) and (7.31) are straightforward, yet in practice they involve a great deal of intermediate calculations. We thus find it useful to introduce some manipulations to bring them into a more suitable form. For the third moment we have the following

$$\overline{\Phi' \Phi' \Phi'^m} = \frac{1}{D_m} \sum_{d=1}^{D_m} (\overline{\Phi^d} - \langle \overline{\Phi^m} \rangle)^3 \quad (7.32a)$$

$$= \frac{1}{D_m} \sum_{d=1}^{D_m} (\overline{\Phi^d} \overline{\Phi^d} \overline{\Phi^d} - \langle \overline{\Phi^m} \rangle \langle \overline{\Phi^m} \rangle \langle \overline{\Phi^m} \rangle + 3 \overline{\Phi^d} \langle \overline{\Phi^m} \rangle \langle \overline{\Phi^m} \rangle - 3 \overline{\Phi^d} \overline{\Phi^d} \langle \overline{\Phi^m} \rangle) \quad (7.32b)$$

$$= \overline{\Phi \Phi \Phi^m} - \langle \overline{\Phi^m} \rangle \langle \overline{\Phi^m} \rangle \langle \overline{\Phi^m} \rangle + 3 \overline{\Phi^m} \langle \overline{\Phi^m} \rangle \langle \overline{\Phi^m} \rangle - 3 \overline{\Phi} \overline{\Phi^m} \langle \overline{\Phi^m} \rangle, \quad (7.32c)$$

in which case the climatological mean for the month is given by

$$\langle \overline{\Phi' \Phi' \Phi'^m} \rangle = \langle \overline{\Phi \Phi \Phi^m} \rangle + 2 \langle \overline{\Phi^m} \rangle \langle \overline{\Phi^m} \rangle \langle \overline{\Phi^m} \rangle - 3 \langle \overline{\Phi} \overline{\Phi^m} \rangle \langle \overline{\Phi^m} \rangle. \quad (7.33)$$

We may thus use the diagnosed first and second moments to evaluate equation (7.33), thus needing only to approximate the triple product $\overline{\Phi} \overline{\Phi} \overline{\Phi^m}$ using the daily means

$$\overline{\Phi \Phi \Phi^m} \approx \frac{1}{D_m} \sum_{d=1}^{D_m} \overline{\Phi^d} \overline{\Phi^d} \overline{\Phi^d}. \quad (7.34)$$

For the fourth moment we have the following

$$\overline{\Phi' \Phi' \Phi' \Phi'^m} = \frac{1}{D_m} \sum_{d=1}^{D_m} (\overline{\Phi^d} \overline{\Phi^d} - 2 \overline{\Phi^d} \langle \overline{\Phi^m} \rangle + \langle \overline{\Phi^m} \rangle \langle \overline{\Phi^m} \rangle) (\overline{\Phi^d} \overline{\Phi^d} - 2 \overline{\Phi^d} \langle \overline{\Phi^m} \rangle + \langle \overline{\Phi^m} \rangle \langle \overline{\Phi^m} \rangle) \quad (7.35a)$$

$$= \overline{\Phi \Phi \Phi \Phi^m} + \langle \overline{\Phi^m} \rangle \langle \overline{\Phi^m} \rangle \langle \overline{\Phi^m} \rangle \langle \overline{\Phi^m} \rangle - 4 \overline{\Phi} \overline{\Phi} \overline{\Phi^d} \langle \overline{\Phi^m} \rangle + 6 \overline{\Phi} \overline{\Phi^d} \langle \overline{\Phi^m} \rangle \langle \overline{\Phi^m} \rangle - 4 \overline{\Phi^d} \langle \overline{\Phi^m} \rangle \langle \overline{\Phi^m} \rangle \langle \overline{\Phi^m} \rangle, \quad (7.35b)$$

in which case the climatological mean for the month is given by

$$\langle \overline{\Phi' \Phi' \Phi' \Phi'^m} \rangle = \langle \overline{\Phi \Phi \Phi \Phi^m} \rangle - 3 \langle \overline{\Phi^m} \rangle \langle \overline{\Phi^m} \rangle \langle \overline{\Phi^m} \rangle \langle \overline{\Phi^m} \rangle - 4 \langle \overline{\Phi} \overline{\Phi} \overline{\Phi^d} \rangle \langle \overline{\Phi^m} \rangle + 6 \langle \overline{\Phi} \overline{\Phi^d} \rangle \langle \overline{\Phi^m} \rangle \langle \overline{\Phi^m} \rangle. \quad (7.36)$$

We may thus use the diagnosed first and second moments to evaluate equation (7.36), thus needing only to approximate the triple product $\overline{\Phi} \overline{\Phi} \overline{\Phi^m}$ using daily means according to equation (7.34), and the quadruple product $\overline{\Phi} \overline{\Phi} \overline{\Phi} \overline{\Phi^m}$ using daily means

$$\overline{\Phi \Phi \Phi \Phi^m} \approx \frac{1}{D_m} \sum_{d=1}^{D_m} \overline{\Phi^d} \overline{\Phi^d} \overline{\Phi^d} \overline{\Phi^d}. \quad (7.37)$$

7.4 Horizontally averaged heat budget with eddy-mean flow decomposition

We considered the horizontally averaged tracer budget here, decomposing the advective fluxes into their time mean and eddy correlation contributions. We start by rewriting equations (5.93a)–(5.93c), but drop

²CM2-O uses a Julian calendar, in which every fourth year is a leap-year (366 days, with 29 days in February). When using daily mean fields to create monthly means, the leap-year should be properly incorporated into the averaging.

the internal source/sink terms and drop the bottom geothermal heating term (CM2-O does not use geothermal heating)

$$\sum_{i,j} dx dy \partial_t (\Theta \rho dz) = \sum_{i,j} dx dy [\rho (w^{(s)} \Theta + F^{(s)})]_{s=s_{k=1}} + \sum_{i,j} dx dy (Q^{\text{mass}} \Theta_m - Q_{(\text{non-advect})}^{(\Theta)}) \quad (7.38a)$$

$$\sum_{i,j} dx dy \partial_t (\Theta \rho dz) = \sum_{i,j} dx dy (-[\rho (w^{(s)} \Theta + F^{(s)})]_{s=s_{k-1}} + [\rho (w^{(s)} \Theta + F^{(s)})]_{s=s_k}) \quad (7.38b)$$

$$\sum_{i,j} dx dy \partial_t (\Theta \rho dz) = - \sum_{i,j} dx dy [\rho (w^{(s)} \Theta + F^{(s)})]_{s=s_{kbot-1}}. \quad (7.38c)$$

MORE TO DO...

Chapter 8

KINETIC ENERGY DIAGNOSTICS

Contents

8.1	Formulation of kinetic energy diagnostics	199
8.2	Eddy-mean flow decomposition	200
8.3	Diagnostics	200

The purpose of this chapter is to present the formulation of various kinetic energy diagnostics available in MOM. The following MOM module is directly connected to the material in this chapter:

`ocean_core/ocean_velocity_diag.F90`

8.1 Formulation of kinetic energy diagnostics

The kinetic energy of the fluid in a grid cell for a discrete hydrostatic fluid is determined by the horizontal components

$$E_{\text{kinetic}} = \frac{1}{2} \rho dV \mathbf{u} \cdot \mathbf{u} \quad (8.1)$$

where $M = \rho dV$ is the mass of fluid in the grid cell. Note that the *in situ* density ρ reduces in the Boussinesq case to the constant Boussinesq reference density ρ_o . The horizontal velocity vector is written as

$$\mathbf{u} = (u, v) \quad (8.2)$$

The SI unit for kinetic energy is Joule.

We often find it useful to split the kinetic energy into that determined by the barotropic, or vertically averaged flow, and that determined by the baroclinic flow. For this purpose, define the vertically averaged velocity according to

$$\bar{\mathbf{u}}^z = \left(\frac{\sum_{k=1}^{nk} \mathbf{u} \rho dz}{\sum_{k=1}^{nk} \rho dz} \right). \quad (8.3)$$

The deviation from this vertical average approximates the baroclinic velocity

$$\hat{\mathbf{u}} = \mathbf{u} - \bar{\mathbf{u}}^z. \quad (8.4)$$

We thus introduce the baroclinic kinetic energy

$$E_{\text{clinic}} = \frac{1}{2} \rho dV \hat{\mathbf{u}} \cdot \hat{\mathbf{u}} \quad (8.5)$$

and the barotropic kinetic energy

$$E_{\text{tropic}} = \frac{1}{2} \bar{\mathbf{u}}^z \cdot \bar{\mathbf{u}}^z \left(\sum_{k=1}^{nk} \rho dV \right). \quad (8.6)$$

Note that it is only when vertically integrating that we have the identity

$$\sum_{k=1}^{nk} E_{\text{kinetic}} = E_{\text{tropic}} + \sum_{k=1}^{nk} E_{\text{clinic}}. \quad (8.7)$$

8.2 Eddy-mean flow decomposition

It is of interest to decompose the kinetic energy into its mean and eddy components, where the eddy components are defined according to a time average. For this purpose we introduce the time mean and eddy fluctuation for an arbitrary field according to (see Section 7.1 for the analogous discussion for tracer transport)

$$\psi = \langle \psi \rangle + \psi', \quad (8.8)$$

where $\langle \psi \rangle$ is a climatological mean, and ψ' is the fluctuation with respect to the mean. Introducing this decomposition leads to an expression for the kinetic energy per mass

$$\frac{2E_{\text{kinetic}}}{M} = u^2 + v^2 \quad (8.9a)$$

$$= \langle u \rangle^2 + 2\langle u \rangle u' + u' u' + \langle v \rangle^2 + 2\langle v \rangle v' + v' v', \quad (8.9b)$$

so that the climatological mean kinetic energy per mass takes the form

$$2\langle e_{\text{kinetic}} \rangle = \langle u \rangle^2 + \langle u' u' \rangle + \langle v \rangle^2 + \langle v' v' \rangle \quad (8.10a)$$

$$= 2(e_{\text{mean}} + e_{\text{eddy}}), \quad (8.10b)$$

where

$$e_{\text{kinetic}} = E_{\text{kinetic}}/M \quad (8.11a)$$

$$e_{\text{mean}} = \frac{1}{2} (\langle u \rangle^2 + \langle v \rangle^2) \quad (8.11b)$$

$$e_{\text{eddy}} = \frac{1}{2} (\langle u' u' \rangle + \langle v' v' \rangle) \quad (8.11c)$$

are, respectfully, the kinetic energy per mass for the full velocity field, the kinetic energy per mass contained in the climatological velocity field, and the kinetic energy per mass in the eddy velocity field.

8.3 Diagnostics

For the CM2-O suite, we diagnosed the kinetic energy E_{kinetic} , rather than the kinetic energy per mass, e_{kinetic} . The kinetic energy is less convenient visually, since it is weighted by the mass of a grid cell, so it is more typical to map e_{kinetic} . In order to diagnose an eddy kinetic energy, we thus need to compute

$$e_{\text{eddy}} = (E_{\text{kinetic}}/M) - e_{\text{mean}} \quad (8.12)$$

where E_{kinetic} is accumulated online each time step during the simulation; e_{mean} is computed using the climatological mean velocity fields; and the mass of a grid cell, M , is taken as a time mean. Unfortunately, this approach does not ensure that e_{eddy} is positive, given that M has a time dependence, albeit small relative to the mass of a cell. A proper eddy-mean flow decomposition of the kinetic energy per mass requires on-line diagnostics for $e_{\text{kinetic}} = (u^2 + v^2)/2$ rather than estimating it offline from E_{kinetic}/M . This is an important point to consider for new simulations with the CM2-O models.

Note that daily mean surface horizontal velocity has been saved for the full suite of simulations, thus allowing for a good approximation for the eddy and mean surface kinetic energy. Additionally, there are periods where full 3d horizontal velocity has been saved for 5day means, allowing for an estimate of the 3d eddy and mean kinetic energy.

Bibliography

- Adcroft, A., Campin, J.-M., 2004. Rescaled height coordinates for accurate representation of free-surface flows in ocean circulation models. *Ocean Modelling* 7, 269–284.
- Adcroft, A., Hallberg, R., Harrison, M., 2008. A finite volume discretization of the pressure gradient force using analytic integration. *Ocean Modelling* 22, 106–113.
- Adcroft, A., Hill, C., Marshall, J., 1997. Representation of topography by shaved cells in a height coordinate ocean model. *Monthly Weather Review* 125, 2293–2315.
- Anderson, W., Gnanadesikan, A., Hallberg, R. W., Dunne, J. P., Samuels, B. L., 2007. Impact of ocean color on the maintenance of the pacific cold tongue. *Geophysical Research Letters* 34-L11609, DOI:10.1029/2007GL030100.
- Anderson, W., Gnanadesikan, A., Wittenberg, A. T., 2009. Regional impacts of ocean color on tropical pacific variability. *Ocean Science* 5, DOI:10.5194/os-5-313–2009.
- Apel, J. R., 1987. Principles of Ocean Physics. Vol. 38 of International Geophysics Series. Academic Press, London.
- Aris, R., 1962. Vectors, Tensors and the Basic Equations of Fluid Mechanics. Dover Publishing, New York.
- Bacon, S., Fofonoff, N. P., 1996. Oceanic heat flux calculation. *Journal of Atmospheric and Oceanic Technology* 13, 1327–1329.
- Beckmann, A., Döscher, R., 1997. A method for improved representation of dense water spreading over topography in geopotential-coordinate models. *Journal of Physical Oceanography* 27, 581–591.
- Black, T. L., 1994. The new NMC mesoscale eta model: description and forecast examples. *Weather and Forecasting* 9, 265–278.
- Blumberg, A. F., Mellor, G. L., 1987. A description of a three-dimensional coastal ocean circulation model. In: Heaps, N. (Ed.), Three-Dimensional Coastal Ocean Models. Vol. 4 of Coastal and Estuarine Series. American Geophysical Union.
- Bryan, K., 1969. A numerical method for the study of the circulation of the world ocean. *Journal of Computational Physics* 4, 347–376.
- Bryan, K., Dukowicz, J. K., Smith, R. D., 1999. On the mixing coefficient in the parameterization of bolus velocity. *Journal of Physical Oceanography* 29, 2442–2456.
- Callen, H. B., 1985. Thermodynamics and an Introduction to Thermostatics. John Wiley and Sons, New York, 493 + xvi pp.
- Chaikin, P. M., Lubensky, T. C., 1995. Principles of Condensed Matter Physics. Cambridge University Press, Cambridge, United Kingdom.

- Chang, Y. S., Xu, X., Özgökmen, T. M., Chassignet, E. P., Peters, H., Fischer, P. F., 2005. Comparison of gravity current mixing parameterizations and calibration using a high-resolution 3d nonhydrostatic spectral element model. *Ocean Modelling* 3-4, 342–368.
- Chassignet, E. P., Verron, J., 2005. *Ocean Weather Forecasting: an Integrated View of Oceanography*. Springer Publishers.
- Conkright, M., Antonov, J., Baranova, O., Boyer, T., Garcia, H., Gelfeld, F., Johnson, D., Locarnini, R., Murphy, P., O'Brien, T., Smolyar, I., Stephens, C., 2002. *World Ocean Database 2001, Volume 1: Introduction*. NOAA Atlas NESDIS 42, U.S. Government Printing Office 13, NOAA, Washington, D.C., 167 pp.
- Cox, M. D., 1984. A Primitive Equation, 3-Dimensional Model of the Ocean. NOAA/Geophysical Fluid Dynamics Laboratory, Princeton, USA.
- Cunningham, S., Alderson, S., King, B., Brandon, M., 2003. Transport and variability of the Antarctic Circumpolar Current in Drake Passage. *Journal of Geophysical Research* 108, Art. 8084.
- Cushmin-Roisin, B., 1987. Subduction. In: *Dynamics of the oceanic surface mixed-layer*. Hawaii Institute of Geophysical Special Publications, pp. 181–196.
- Danabasoglu, G., Large, W. G., Tribbia, J. J., Gent, P. R., Briegleb, B. P., McWilliams, J. C., 2006. Diurnal coupling in the tropical oceans of CCSM3. *Journal of Climate* 19, 2347–2365.
- Danabasoglu, G., McWilliams, J. C., 1995. Sensitivity of the global ocean circulation to parameterizations of mesoscale tracer transports. *Journal of Climate* 8, 2967–2987.
- de Boyer Montégut, C., Madec, G., Fischer, A., Lazar, A., Ludicone, D., 2004. Mixed layer depth over the global ocean: An examination of profile data and a profile based climatology. *Journal of Geophysical Research* 109, doi:10.1029/2004JC002378.
- DeGroot, S. R., Mazur, P., 1984. *Non-Equilibrium Thermodynamics*. Dover Publications, New York, 510 pp.
- Delworth, T. L., Broccoli, A. J., Rosati, A., Stouffer, R. J., Balaji, V., Beesley, J. A., Cooke, W. F., Dixon, K. W., Dunne, J., Dunne, K. A., Durachta, J. W., Findell, K. L., Ginoux, P., Gnanadesikan, A., Gordon, C., Griffies, S. M., Gudgel, R., Harrison, M. J., Held, I. M., Hemler, R. S., Horowitz, L. W., Klein, S. A., Knutson, T. R., Kushner, P. J., Langenhorst, A. L., Lee, H.-C., Lin, S., Lu, L., Malyshev, S. L., Milly, P., Ramaswamy, V., Russell, J., Schwarzkopf, M. D., Shevliakova, E., Sirutis, J., Spelman, M., Stern, W. F., Winton, M., Wittenberg, A. T., Wyman, B., Zeng, F., Zhang, R., 2006. GFDL's CM2 global coupled climate models - Part 1: Formulation and simulation characteristics. *Journal of Climate* 19, 643–674.
- Delworth, T. L., Rosati, A., Anderson, W., Adcroft, A. J., Balaji, V., Benson, R., Dixon, K., Griffies, S. M., Lee, H.-C., Pacanowski, R. C., Vecchi, G. A., Wittenberg, A. T., Zeng, F., Zhang, R., 2012. Simulated climate and climate change in the GFDL CM2.5 high-resolution coupled climate model. *Journal of Climate* 25, 2755–2781.
- Donner, L. J., Wyman, B. L., Hemler, R. S., Horowitz, L. W., Ming, Y., Zhao, M., Golaz, J.-C., Ginoux, P., Lin, S.-J., Schwarzkopf, M. D., Austin, J., Alaka, G., Cooke, W. F., Delworth, T. L., Freidenreich, S. M., Gordon, C. T., Griffies, S. M., Held, I. M., Hurlin, W. J., Klein, S. A., Knutson, T. R., Langenhorst, A. R., Lee, H.-C., Lin, Y., Magi, B. I., Malyshev, S. L., Milly, P., Naik, V., Nath, M. J., Pincus, R., Ploschay, J. J., Ramaswamy, V., Seman, C. J., Shevliakova, E., Sirutis, J. J., Stern, W. F., Stouffer, R. J., Wilson, R. J., Winton, M., Wittenberg, A. T., Zeng, F., 2011. The dynamical core, physical parameterizations, and basic simulation characteristics of the atmospheric component of the GFDL global coupled model CM3. *Journal of Climate* 24, 3484–3519.
- Dunne, J. P., John, J. G., Hallberg, R. W., Griffies, S. M., Shevliakova, E. N., Stouffer, R. J., Krasting, J. P., Sentman, L. A., Milly, P. C. D., Malyshev, S. L., Adcroft, A. J., Cooke, W., Dunne, K. A., Harrison, M. J., Levy, H., Samuels, B. L., Spelman, M., Winton, M., Wittenberg, A. T., Phillips, P. J., Zadeh, N., 2012. GFDLs ESM2 global coupled climate-carbon Earth System Models Part I: Physical formulation and baseline simulation characteristics. *Journal of Climate* 25, 6646–6665.

- Dunne, J. P., John, J. G., Hallberg, R. W., Griffies, S. M., Shevliakova, E. N., Stouffer, R. J., Krasting, J. P., Sentman, L. A., Milly, P. C. D., Malyshev, S. L., Adcroft, A. J., Cooke, W., Dunne, K. A., Harrison, M. J., Levy, H., Wittenberg, A., Phillips, P., Zadeh, N., 2013. GFDLs ESM2 global coupled climate-carbon Earth System Models Part II: Carbon system formulation and baseline simulation characteristics. *Journal of Climate* 26, 2247–2267.
- Durran, D. R., 1999. Numerical Methods for Wave Equations in Geophysical Fluid Dynamics. Springer Verlag, Berlin, 470 pp.
- Durski, S. M., Glenn, S. M., Haidvogel, D. B., 2004. Vertical mixing schemes in the coastal ocean: Comparison of the level 2.5 Mellor-Yamada scheme with an enhanced version of the K profile parameterization. *Journal of Geophysical Research* 109, doi:10.1029/2002JC001702.
- Egbert, G., Bennett, A., Foreman, M., 1994. TOPEX/POSEIDON tides estimated using a global inverse model. *Journal of Geophysical Research* 99, 24821–24852.
- Egbert, G., Erofeeva, S., 2002. Efficient inverse modeling of barotropic ocean tides. *Journal of Atmospheric and Oceanic Technology* 19, 183–204.
- England, M. H., 1995. The age of water and ventilation timescales in a global ocean model. *Journal of Physical Oceanography* 25, 2756–2777.
- Farneti, R., Delworth, T., Rosati, A., Griffies, S. M., Zeng, F., 2010. The role of mesoscale eddies in the rectification of the Southern Ocean response to climate change. *Journal of Physical Oceanography* 40, 1539–1557.
- Farneti, R., Gent, P., 2011. The effects of the eddy-induced advection coefficient in a coarse-resolution coupled climate model. *Ocean Modelling* 39, 135–145.
- Ferrari, R., Griffies, S. M., Nurser, A. J. G., Vallis, G. K., 2010. A boundary-value problem for the parameterized mesoscale eddy transport. *Ocean Modelling* 32, 143–156.
- Ferrari, R., McWilliams, J. C., Canuto, V. M., Dubovikov, M., 2008. Parameterization of eddy fluxes near oceanic boundaries. *Journal of Climate* 21, 2770–2789.
- Fissel, D., Birch, J., Melling, H., Lake, R., 1998. Non-tidal flows in the Northwest Passage. In: Canadian Technical Report of Hydrography and Ocean Sciences. Institute of Ocean Sciences, Sidney, Canada, p. 142pp.
- Fofonoff, N. P., 1962. Physical properties of seawater. In: Hill, M. N. (Ed.), *The Sea*. Vol. 1. Wiley-Interscience, pp. 3–30.
- Fox-Kemper, B., Danabasoglu, G., Ferrari, R., Griffies, S. M., Hallberg, R. W., Holland, M., Peacock, S., Samuels, B., 2011. Parameterization of mixed layer eddies. III: Global implementation and impact on ocean climate simulations. *Ocean Modelling* 39, 61–78.
- Fox-Kemper, B., Ferrari, R., Hallberg, R., 2008. Parameterization of mixed layer eddies. I: Theory and diagnosis. *Journal of Physical Oceanography* 38, 1145–1165.
- Fox-Kemper, B., Ferrari, R., Pedlosky, J., 2003. A note on the indeterminacy of rotational and divergent eddy fluxes. *Journal of Physical Oceanography* 33, 478–483.
- Gent, P., Bryan, F., Danabasoglu, G., Doney, S., Holland, W., Large, W., McWilliams, J., 1998. The NCAR climate system model global ocean component. *Journal of Climate* 11, 1287–1306.
- Gent, P. R., McWilliams, J. C., 1990. Isopycnal mixing in ocean circulation models. *Journal of Physical Oceanography* 20, 150–155.
- Gent, P. R., Willebrand, J., McDougall, T. J., McWilliams, J. C., 1995. Parameterizing eddy-induced tracer transports in ocean circulation models. *Journal of Physical Oceanography* 25, 463–474.

- Gerdes, R., Köberle, C., Willebrand, J., 1991. The influence of numerical advection schemes on the results of ocean general circulation models. *Climate Dynamics* 5, 211–226.
- Gill, A., 1982. *Atmosphere-Ocean Dynamics*. Vol. 30 of International Geophysics Series. Academic Press, London, 662 + xv pp.
- Gille, S. T., Yale, M. M., Sandwell, D. T., 2000. Global correlation of mesoscale ocean variability with seafloor roughness from satellite altimetry. *Geophysical Research Letters* 27, 1251–1254.
- Gnanadesikan, A., Anderson, W., 2009. Ocean water clarity and the ocean general circulation in a coupled climate model. *Journal of Physical Oceanography* 39, DOI:10.1175/2008JPO3935.1.
- Gnanadesikan, A., Emanuel, K. A., Vecchi, G. A., Anderson, W., Hallberg, R., 2010. How ocean color can steer Pacific tropical cyclones. *Geophysical Research Letters* 37-L18802, DOI:10.1029/2010GL044514.
- Goff, J., Arbic, B., 2010. Global prediction of abyssal hill roughness statistics for use in ocean models from digital maps of paleo-spreading rate, paleo-ridge orientation, and sediment thickness. *Ocean Modelling* 32, 36–43.
- Gordon, A., Susanto, R., Vranes, K., 2003. Cool indonesian throughflow as a consequence of restricted surface layer flow. *Nature* 425, 824–828.
- Griffies, S. M., 1998. The Gent-McWilliams skew-flux. *Journal of Physical Oceanography* 28, 831–841.
- Griffies, S. M., 2004. *Fundamentals of Ocean Climate Models*. Princeton University Press, Princeton, USA, 518+xxxiv pages.
- Griffies, S. M., 2005. Some ocean model fundamentals. In: Chassignet, E. P., Verron, J. (Eds.), GODAE Summer School. Springer/Kluwer, pp. 19–74.
- Griffies, S. M., 2012. Elements of the Modular Ocean Model (MOM): 2013 release (GFDL Ocean Group Technical Report No. 7). NOAA/Geophysical Fluid Dynamics Laboratory, Princeton, USA, 614 + xiii pages.
- Griffies, S. M., Adcroft, A. J., 2008. Formulating the equations for ocean models. In: Hecht, M., Hasumi, H. (Eds.), *Ocean Modeling in an Eddying Regime*. Geophysical Monograph 177. American Geophysical Union, pp. 281–317.
- Griffies, S. M., Adcroft, A. J., Aiki, H., Balaji, V., Bentson, M., Bryan, F., Danabasoglu, G., Denvil, S., Drange, H., England, M., Gregory, J., Hallberg, R., Legg, S., Martin, T., McDougall, T. J., Pirani, A., Schmidt, G., Stevens, D., Taylor, K., Tsujino, H., 2009a. Sampling physical ocean fields in WCRP CMIP5 simulations. Vol. available from <http://www-pcmdi.llnl.gov>. ICPO Publication Series 137, WCRP Informal Report No. 3/2009.
- Griffies, S. M., Biastoch, A., Böning, C. W., Bryan, F., Danabasoglu, G., Chassignet, E., England, M. H., Gerdes, R., Haak, H., Hallberg, R. W., Hazeleger, W., Jungclaus, J., Large, W. G., Madec, G., Pirani, A., Samuels, B. L., Scheinert, M., Gupta, A. S., Severijns, C. A., Simmons, H. L., Treguier, A. M., Winton, M., Yeager, S., Yin, J., 2009b. Coordinated Ocean-ice Reference Experiments (COREs). *Ocean Modelling* 26, 1–46.
- Griffies, S. M., Böning, C. W., Bryan, F. O., Chassignet, E. P., Gerdes, R., Hasumi, H., Hirst, A., Treguier, A.-M., Webb, D., 2000. Developments in ocean climate modelling. *Ocean Modelling* 2, 123–192.
- Griffies, S. M., Gnanadesikan, A., Dixon, K. W., Dunne, J. P., Gerdes, R., Harrison, M. J., Rosati, A., Russell, J., Samuels, B. L., Spelman, M. J., Winton, M., Zhang, R., 2005. Formulation of an ocean model for global climate simulations. *Ocean Science* 1, 45–79.
- Griffies, S. M., Gnanadesikan, A., Pacanowski, R. C., Larichev, V., Dukowicz, J. K., Smith, R. D., 1998. Isoneutral diffusion in a z-coordinate ocean model. *Journal of Physical Oceanography* 28, 805–830.
- Griffies, S. M., Greatbatch, R. J., 2012. Physical processes that impact the evolution of global mean sea level in ocean climate models. *Ocean Modelling* 51, 37–72.

- Griffies, S. M., Hallberg, R. W., 2000. Biharmonic friction with a Smagorinsky viscosity for use in large-scale eddy-permitting ocean models. *Monthly Weather Review* 128, 2935–2946.
- Griffies, S. M., Harrison, M. J., Pacanowski, R. C., Rosati, A., 2004. A Technical Guide to MOM4. NOAA/Geophysical Fluid Dynamics Laboratory, Princeton, USA, 337 pp.
- Griffies, S. M., Pacanowski, R., Schmidt, M., Balaji, V., 2001. Tracer conservation with an explicit free surface method for z-coordinate ocean models. *Monthly Weather Review* 129, 1081–1098.
- Griffies, S. M., Winton, M., Anderson, W. G., Benson, R., Delworth, T. L., Dufour, C., Dunne, J. P., Goddard, P., Morrison, A. K., Rosati, A., Wittenberg, A. T., Yin, J., 2015. Impacts on ocean heat from transient mesoscale eddies in a hierarchy of climate models. *Journal of Climate* 28, 952–977.
- Griffies, S. M., Winton, M., Donner, L. J., Downes, S. M., Farneti, R., Gnanadesikan, A., Horowitz, L. W., Hurlin, W. J., Lee, H.-C., Liang, Z., Palter, J. B., Samuels, B. L., Wittenberg, A. T., Wyman, B. L., Yin, J., Zadeh, N. T., 2011. GFDL's CM3 coupled climate model: Characteristics of the ocean and sea ice simulations. *Journal of Climate* 24, 3520–3544.
- Hallberg, R. W., 2013. Using a resolution function to regulate parameterizations of oceanic mesoscale eddy effects. *Ocean Modelling* 72, 92–103.
- Hill, C., Ferreira, D., Campin, J.-M., Marshall, J., Abernathey, R., Barrier, N., 2012. Controlling spurious diapycnal mixing in eddy-resolving height-coordinate ocean models—insights from virtual deliberate tracer release experiments. *Ocean Modelling* 45–46, 14–26.
- Hirsch, C., 1988. Numerical Computation of Internal and External Flows. John Wiley and Sons.
- Holland, W., Chow, J., Bryan, F., 1998. Application of a third-order upwind scheme in the NCAR ocean model. *Journal of Climate* 11, 1487–1493.
- Holloway, G., 1999. Moments of probable seas: statistical dynamics of Planet Ocean. *Physica D* 133, 199–214.
- Huang, R. X., 1993. Real freshwater flux as a natural boundary condition for the salinity balance and thermohaline circulation forced by evaporation and precipitation. *Journal of Physical Oceanography* 23, 2428–2446.
- Hughes, C., Thompson, A., Wilson, C., 2010. Identification of jets and mixing barriers from sea level and vorticity measurements using simple statistics. *Ocean Modelling* 32, 44–57.
- Hundsdorfer, W., Trompert, R., 1994. Method of lines and direct discretization: a comparison for linear advection. *Applied Numerical Mathematics*, 469–490.
- IOC, SCOR, IAPSO, 2010. The international thermodynamic equation of seawater-2010: calculation and use of thermodynamic properties. Intergovernmental Oceanographic Commission, Manuals and Guides No. 56, UNESCO, available from <http://www.TEOS-10.org>, 196pp.
- Jackett, D. R., McDougall, T. J., Feistel, R., Wright, D. G., Griffies, S. M., 2006. Algorithms for density, potential temperature, conservative temperature, and freezing temperature of seawater. *Journal of Atmospheric and Oceanic Technology* 23, 1709–1728.
- Jackson, L., Hallberg, R., Legg, S., 2008. A parameterization of shear-driven turbulence for ocean climate models. *Journal of Physical Oceanography* 38, 1033–1053.
- Jayne, S., 2009. The impact of abyssal mixing parameterizations in an ocean general circulation model. *Journal of Physical Oceanography* 39, 1756–1775.
- Jayne, S., St.Laurent, L. C., 2001. Parameterizing tidal dissipation over rough topography. *Geophysical Research Letters* 28, 811–814.

- Jochum, M., 2009. Impact of latitudinal variations in vertical diffusivity on climate simulations. *Journal of Geophysical Research* 114 C01010, doi:10.1029/2008JC005030.
- Klinger, B. A., Marshall, J., Send, U., 1996. Representation of convective plumes by vertical adjustment. *Journal of Geophysical Research* 101, 18175–18182.
- Klymak, J., Moum, J., Nash, J., Kunze, E., Girton, J., Carter, G., Lee, C., Sanford, T., Gregg, M., 2005. An estimate of tidal energy lost to turbulence at the hawaiian ridge. *Journal of Physical Oceanography* submitted.
- Kopp, R. E., Mitrovica, J. X., Griffies, S. M., Yin, J., Hay, C. C., Stouffer, R. J., 2010. The impact of Greenland melt on regional sea level: a preliminary comparison of dynamic and static equilibrium effects. *Climatic Change Letters* 103, 619–625.
- Kwon, E., Downes, S., Sarmiento, J., Farneti, R., Deutsch, C., 2013. Role of the seasonal cycle in the subduction rates of Upper-Southern Ocean mode waters. *Journal of Physical Oceanography* 43, 1096–1113.
- Landau, L. D., Lifshitz, E. M., 1976. Mechanics. Pergamon Press, Oxford, UK, 170 pp.
- Large, W., 1998. Modeling the oceanic boundary layer. In: Chassignet, E. P., Verron, J. (Eds.), *Ocean Modeling and Parameterization*. Vol. 516 of NATO ASI Mathematical and Physical Sciences Series. Kluwer, pp. 81–120.
- Large, W., Gent, P., 1999. Validation of vertical mixing in an equatorial ocean model using large eddy simulations and observations. *Journal of Physical Oceanography* 29, 449–464.
- Large, W., McWilliams, J., Doney, S., 1994. Oceanic vertical mixing: a review and a model with a nonlocal boundary layer parameterization. *Reviews of Geophysics* 32, 363–403.
- Large, W. G., 2012. An ocean climate modeling perspective on buoyancy-driven flows. In: Chassignet, E. P., Cenedese, C., Verron, J. (Eds.), *Buoyancy-driven flows*. Cambridge, pp. 240–280.
- Large, W. G., Danabasoglu, G., Doney, S. C., McWilliams, J. C., 1997. Sensitivity to surface forcing and boundary layer mixing in a global ocean model: annual-mean climatology. *Journal of Physical Oceanography* 27, 2418–2447.
- Laurent, L. C. S., Schmitt, R., 1999. The contribution of salt fingers to vertical mixing in the north atlantic tracer release experiment. *Journal of Physical Oceanography* 29, 1404–1424.
- Leaman, K., Molinari, R., Vertes, P., 1987. Structure and variability of the Florida Current at 27N: April 1982–July 1984. *Journal of Physical Oceanography* 17, 565–583.
- Ledwell, J. R., Watson, A. J., Law, C. S., 1993. Evidence for slow mixing across the pycnocline from an open-ocean tracer-release experiment. *Nature* 364, 701–703.
- Lee, H.-C., Rosati, A., Spelman, M., 2006. Barotropic tidal mixing effects in a coupled climate model: Oceanic conditions in the northern Atlantic. *Ocean Modelling* 3-4, 464–477.
- Leonard, B. P., 1979. A stable and accurate convective modelling procedure based on quadratic upstream interpolation. *Computer Methods in Applied Mechanics and Engineering* 19, 59–98.
- Li, X., Chao, Y., McWilliams, J. C., Fu, L. L., 2001. A comparison of two vertical-mixing schemes in a Pacific ocean general circulation model. *Journal of Climate* 14, 1377–1398.
- Lin, S. J., 1997. A finite volume integration method for computing pressure gradient force in general vertical coordinates. *Quarterly Journal of the Royal Meteorological Society* 123, 1749–1762.
- Lin, S.-J., 2004. A vertically lagrangian finite-volume dynamical core for global models. *Monthly Weather Review*, 2293–2307.

- Locarnini, R., Mishonov, A., Antonov, J., Boyer, T., Garcia, H., 2006. World Ocean Atlas 2005, volume 1: Temperature. U.S. Government Printing Office 61, NOAA Atlas NESDIS, Washington, D.C., 182 pp.
- Lukas, R., Firing, E., 1984. The geostrophic balance of the Pacific equatorial undercurrent. Deep-Sea Research 31, 61–66.
- Machenhauer, B., Kaas, E., Lauritzen, P., 2009. Finite-volume methods in meteorology. In: Temam, R., Tribbia, J. (Eds.), Computational Methods for the Atmosphere and the Oceans. Elsevier, Amsterdam, p. 761.
- MacKinnon, J., Alford, M., Bouruet-Aubertot, P., Bindoff, N., Elipot, S., Gille, S., Girton, J., Gregg, M., Kunze, E., Naveira Garabato, A., Phillips, H., Pinkel, R., Polzin, K., Sanford, T., Simmons, H., Speer, K., 2010. Using global arrays to investigate internal-waves and mixing. In: Hall, J., Harrison, D., Stammer, D. (Eds.), Proceedings of the OceanObs09 Conference: Sustained Ocean Observations and Information for Society, Venice, Italy, 21-25 September 2009. Vol. 2. ESA Publication WPP-306.
- Manizza, M., Le Quere, C., Watson, A., Buitenhuis, E., 2005. Bio-optical feedbacks among phytoplankton, upper ocean physics and sea-ice in a global model. Geophysical Research Letters 32, doi:10.1029/2004GL020778.
- Marion, J. B., Thornton, S. T., 1988. Classical Dynamics of Particles and Systems. Harcourt Brace Johnson, San Diego, USA, 602 pp.
- Marshall, J., Hill, C., Perelman, L., Adcroft, A., 1997. Hydrostatic, quasi-hydrostatic, and nonhydrostatic ocean modeling. Journal of Geophysical Research 102, 5733–5752.
- Marshall, J., Schott, F., 1999. Open-ocean convection: observations, theory, and models. Reviews of Geophysics 37, 1–64.
- Martin, T., Adcroft, A., 2010. Parameterizing the fresh-water flux from land ice to ocean with interactive icebergs in a coupled climate model. Ocean Modelling 34, 111–124.
- McDougall, T. J., 1995. The influence of ocean mixing on the absolute velocity vector. Journal of Physical Oceanography 25, 705–725.
- McDougall, T. J., 2003. Potential enthalpy: a conservative oceanic variable for evaluating heat content and heat fluxes. Journal of Physical Oceanography 33, 945–963.
- McDougall, T. J., Greatbatch, R., Lu, Y., 2002. On conservation equations in oceanography: How accurate are Boussinesq ocean models? Journal of Physical Oceanography 32, 1574–1584.
- McDougall, T. J., McIntosh, P. C., 2001. The temporal-residual-mean velocity. Part II: isopycnal interpretation and the tracer and momentum equations. Journal of Physical Oceanography 31, 1222–1246.
- Meehl, G., Gent, P. R., Arblaster, J., Otto-Bliesner, B., Brady, E., Craig, A., 2001. Factors that affect the amplitude of El Niño in global coupled climate models. Climate Dynamics 17, 515–526.
- Melet, A., Hallberg, R., Legg, S., Polzin, K., 2013. Sensitivity of the Pacific Ocean state to the vertical distribution of internal-tide driven mixing. Journal of Physical Oceanography 43, 602–615.
- Melling, H., 2000. Exchanges of freshwater through the shallow straits of the North American Arctic. In: The freshwater budget of the Arctic Ocean. Kluwer Academic Publisher, pp. 472–523.
- MERCATOR, 2006. List of internal metrics for the mersea-godae global ocean: Specification for implementation. In: Integrated System Design and Assessment. France.
- Merryfield, W. J., Holloway, G., 2003. Application of an accurate advection algorithm to sea-ice modelling. Ocean Modelling 5, 1–15.
- Miles, J., 1961. On the stability of heterogeneous shear flows. Journal of Fluid Mechanics 10, 496–508.

- Moum, J., Caldwell, D., Nash, J., Gunderson, G., 2002. Observations of boundary mixing over the continental slope. *Journal of Physical Oceanography* 32, 2113–2130.
- Müller, P., 2006. The Equations of Oceanic Motions, 1st Edition. Cambridge University Press, Cambridge, 302pp.
- Munk, W., Anderson, E., 1948. Notes on a theory of the thermocline. *Journal of Marine Research* 3, 276–295.
- Murray, R., 1996. Explicit generation of orthogonal grids for ocean models. *Journal of Computational Physics* 126, 251–273.
- Olsen, S., Hansen, B., Quadfasel, D., Osterhus, S., 2008. Observed and modelled stability of overflow across the Greenland-Scotland ridge. *Nature* 455, doi:10.1038/nature07302.
- Osborn, T. R., 1980. Estimates of the local rate of vertical diffusion from dissipation measurements. *Journal of Physical Oceanography* 10, 83–89.
- Osterhus, S., Turrell, W., Jonsson, S., Hansen, B., 2005. Measured volume, heat, and salt fluxes from the Atlantic to the Arctic Mediterranean. *Geophysical Research Letters* 32, doi:10.1029/2004GL022188.
- Otto, L., Zimmerman, J., Furnes, G., Mork, M., Saetre, R., Becker, G., 1990. Review of the physical oceanography of the North Sea. *Netherlands Journal of Sea Research* 26, 161–238.
- Pacanowski, R. C., Gnanadesikan, A., 1998. Transient response in a z -level ocean model that resolves topography with partial-cells. *Monthly Weather Review* 126, 3248–3270.
- Pacanowski, R. C., Griffies, S. M., 1999. The MOM3 Manual. NOAA/Geophysical Fluid Dynamics Laboratory, Princeton, USA, 680 pp.
- Pacanowski, R. C., Philander, G., 1981. Parameterization of vertical mixing in numerical models of the tropical ocean. *Journal of Physical Oceanography* 11, 1442–1451.
- Palter, J. B., Griffies, S. M., Galbraith, E. D., Gnanadesikan, A., Samuels, B. L., Klocker, A., 2014. The deep ocean buoyancy budget and its temporal variability. *Journal of Climate* 27, 551–573.
- Prather, M., 1986. Numerical advection by conservation of second-order moments. *Journal of Geophysical Research* 91, 6671–6681.
- Rahmstorf, S., 1993. A fast and complete convection scheme for ocean models. *Ocean Modelling* 101, 9–11.
- Roach, A., Aagard, K., Pease, C., Salo, S., Weingartner, T., Pavlov, V., Kulakov, M., 1995. Direct measurements of transport and water properties through Bering Strait. *Journal of Geophysical Research* 100, 18443–18457.
- Rosati, A., Miyakoda, K., 1988. A general circulation model for upper ocean simulation. *Journal of Physical Oceanography* 18, 1601–1626.
- Sadler, H., 1976. Water, heat and salt transports through Nares Strait, Ellesmere Island. *Fisheries Research Board of Canada* 33, 22862295.
- Schauer, U., Fahrbach, E., Osterhus, S., Rohardt, G., 2004. Arctic warming through the Fram Strait: Oceanic heat transport from 3 years of measurements. *Journal of Geophysical Research* 109, doi:10.1029/2003JC001823.
- Schmitt, R. W., 1994. Double diffusion in oceanography. *Annual Review of Fluid Mechanics* 26, 255–285.
- Simmons, H. L., Jayne, S. R., St.Laurent, L. C., Weaver, A. J., 2004. Tidally driven mixing in a numerical model of the ocean general circulation. *Ocean Modelling* 6, 245–263.

- Sloyan, B., Johnson, G., Kessler, W., 2003. The Pacific Cold Tongue: A pathway for interhemispheric exchange. *Journal of Physical Oceanography* 33, 1027–1043.
- Smith, W. H. F., Sandwell, D. T., 1997. Global seafloor topography from satellite altimetry and ship depth soundings. *Science* 277, 1956–1962.
- Smyth, G. C. W. D., Skillingstad, E. D., Wijesekera, H., 2002. Nonlocal fluxes and Stokes drift effects in the K-profile parameterization. *Ocean Dynamics* 52, 104–115.
- Stacey, M. W., Pond, S., Nowak, Z. P., 1995. A numerical model of the circulation in Knight Inlet, British Columbia, Canada. *Journal of Physical Oceanography* 25, 1037–1062.
- St.Laurent, L. C., Simmons, H., Jayne, S., 2002. Estimating tidally driven energy in the deep ocean. *Geophysical Research Letters* 29, 2106–2110.
- St.Laurent, L. C., Stringer, S., Garrett, C., Perrault-Joncas, D., 2003. The generation of internal tides at abrupt topography. *Deep-Sea Research* 50, 987–1003.
- St.Laurent, L. C., Toole, J., Schmitt, R., 2001. Buoyancy forcing by turbulence above rough topography in the abyssal Brazil basin. *Journal of Physical Oceanography* 31, 3476–3495.
- Stouffer, R. J., Dixon, K., Spelman, M., Hurlin, W., Yin, J., Gregory, J., Weaver, A., Eby, M., Flato, G., Robitaille, D., Hasumi, H., Oka, A., Hu, A., Jungclaus, J., Kamenkovich, I., Levermann, A., Montoya, M., Murakami, S., Nawrath, S., Peltier, W., Vettoretti, G., Sokolov, A., Weber, S., 2006. Investigating the causes of the response of the thermohaline circulation to past and future climate changes. *Journal of Climate* 19, 1365–1387.
- Suresh, A., Huynh, H. T., 1997. Accurate monotonicity-preserving schemes with Runge-Kutta time stepping. *Journal of Computational Physics* 136, 83–99.
- Sweby, P., 1984. High-resolution schemes using flux limiters for hyperbolic conservation-laws. *SIAM Journal of Numerical Analysis* 21, 995–1011.
- Sweeney, C., Gnanadesikan, A., Griffies, S. M., Harrison, M., Rosati, A., Samuels, B., 2005. Impacts of shortwave penetration depth on large-scale ocean circulation and heat transport. *Journal of Physical Oceanography* 35, 1103–1119.
- Taylor, K., Stouffer, R., Meehl, G., 2012. An overview of CMIP5 and the experiment design. *Bulletin of the American Meteorological Society* 93, 485–498.
- Thiele, G., Sarmiento, J. L., 1990. Tracer dating and ocean ventilation. *Journal of Geophysical Research* 95, 9377–9391.
- Thompson, K., Demirov, E., 2005. Skewness of sea level variability of the world's oceans. *Journal of Geophysical Research* 111, C05005.
- Treguier, A. M., Held, I. M., Larichev, V. D., 1997. On the parameterization of quasi-geostrophic eddies in primitive equation ocean models. *Journal of Physical Oceanography* 27, 567–580.
- Umlauf, L., Burchard, H., Bolding, K., 2005. GOTM: source code and test case documentation: version 3.2. 231pp.
- Vecchi, G., Delworth, T., Gudgel, R., Kapnick, S., Rosati, A., Wittenberg, A., Zeng, F., Anderson, W., Balaji, V., Dixon, K., Jia, L., Kim, H.-S., Krishnamurthy, L., Msadek, R., Stern, W., Underwood, S., Villarini, G., Yang, X., Zhang, S., 2014. On the seasonal forecasting of regional tropical cyclone activity. *Journal of Climate*, submitted.
- Warren, B., 2009. Note on the vertical velocity and diffusive salt flux induced by evaporation and precipitation. *Journal of Physical Oceanography* 39, 2680–2682.

- Webb, D. J., Coward, A. C., de Cuevas, B. A., Gwilliam, C. S., 1998. The first main run of the OCCAM global ocean model. Internal Document No. 34. Southampton Oceanography Centre, Southampton, England.
- Yaremchuk, M., McCreary, J., Yu, Z., Furue, R., 2009. The South China Sea throughow retrieved from climatological data. *Journal of Physical Oceanography* 39, 753–767.
- Yin, J., Stouffer, R., Spelman, M. J., Griffies, S. M., 2010. Evaluating the uncertainty induced by the virtual salt flux assumption in climate simulations and future projections. *Journal of Climate* 23, 80–96.

Index

- Adcroft and Campin (2004), 45, 203
Adcroft et al. (1997), 22, 48, 203
Adcroft et al. (2008), 32, 35, 203
Anderson et al. (2007), 88, 203
Anderson et al. (2009), 88, 203
Apel (1987), 18, 203
Aris (1962), 162, 203
Bacon and Fofonoff (1996), 18, 203
Beckmann and Döscher (1997), 138, 203
Black (1994), 46, 203
Blumberg and Mellor (1987), 46, 203
Bryan et al. (1999), 192, 203
Bryan (1969), 35, 36, 50, 57, 203
Callen (1985), 12, 161, 203
Chaikin and Lubensky (1995), 15, 168, 203
Chang et al. (2005), 58, 203
Chassignet and Verron (2005), 4, 204
Conkright et al. (2002), 161, 204
Cox (1984), 57, 204
Cunningham et al. (2003), 107, 204
Cushmin-Roisin (1987), 167, 204
Danabasoglu and McWilliams (1995), 86, 204
Danabasoglu et al. (2006), 65, 204
DeGroot and Mazur (1984), 15, 168, 204
Delworth et al. (2006), 49, 121, 125, 131, 132, 204
Delworth et al. (2012), ii, 204
Donner et al. (2011), 46, 56, 204
Dunne et al. (2012), ii, 46, 53, 56, 57, 79, 88, 90, 91, 121, 126, 131, 132, 138, 204
Dunne et al. (2013), 46, 53, 56, 138, 204
Durran (1999), 50, 205
Durski et al. (2004), 58, 60, 205
Egbert and Erofeeva (2002), 73, 205
Egbert et al. (1994), 73, 205
England (1995), 30, 205
Farneti and Gent (2011), 87, 88, 205
Farneti et al. (2010), 87, 88, 205
Ferrari et al. (2008), 86, 185, 205
Ferrari et al. (2010), 86, 87, 137, 183, 185, 186, 205
Fissel et al. (1998), 106, 205
Fofonoff (1962), 19, 205
Fox-Kemper et al. (2003), 192, 205
Fox-Kemper et al. (2008), 82–84, 102, 103, 105, 114, 135, 205
Fox-Kemper et al. (2011), 82, 101, 114, 135, 165, 171, 182, 183, 185, 187, 205
Gent and McWilliams (1990), 82, 87, 113, 137, 192, 205
Gent et al. (1995), 83–87, 101–103, 105, 113, 165, 171, 183, 185, 186, 205
Gent et al. (1998), 58, 205
Gerdes et al. (1991), 87, 205
Gille et al. (2000), 70, 206
Gill (1982), 40, 206
Gnanadesikan and Anderson (2009), 88, 206
Gnanadesikan et al. (2010), 88, 206
Goff and Arbic (2010), 71, 206
Gordon et al. (2003), 108, 206
Griffies and Adcroft (2008), 4, 206
Griffies and Greatbatch (2012), 99, 132, 206
Griffies and Hallberg (2000), 79, 206
Griffies et al. (1998), 86, 206
Griffies et al. (2000), 36, 46, 206
Griffies et al. (2001), 30, 49, 50, 207
Griffies et al. (2004), 45, 207
Griffies et al. (2005), 5, 45, 49, 50, 87, 88, 206
Griffies et al. (2009a), 106, 206
Griffies et al. (2009b), 51, 206
Griffies et al. (2011), 46, 56, 121, 131, 207
Griffies et al. (2015), ii, 207
Griffies (1998), 87, 183, 185, 186, 206
Griffies (2004), 4, 5, 9, 11, 12, 14, 18–20, 24, 26, 37, 40, 50, 79–81, 88, 113, 163, 206
Griffies (2005), 4, 206
Griffies (2012), 4, 35, 43–45, 50, 51, 57, 58, 69, 78, 83, 135–138, 172, 206
Hallberg (2013), 87, 207
Hill et al. (2012), 52, 53, 207
Hirsch (1988), 22, 32, 207
Holland et al. (1998), 52, 58, 207
Holloway (1999), 39, 207
Huang (1993), 49, 50, 207
Hughes et al. (2010), 196, 207
Hundsdorfer and Trompert (1994), 52, 207

- Jackett et al. (2006), 56, 207
Jackson et al. (2008), 64, 207
Jayne and St.Laurent (2001), 69, 70, 207
Jayne (2009), 75, 207
Jochum (2009), 57, 207
Klinger et al. (1996), 57, 208
Klymak et al. (2005), 74, 208
Kopp et al. (2010), 46, 50, 208
Kwon et al. (2013), 173, 208
Landau and Lifshitz (1976), 5, 208
Large and Gent (1999), 64, 208
Large et al. (1994), 57–59, 61, 62, 64, 65, 75, 182, 208
Large et al. (1997), 58, 208
Large (1998), 58, 59, 208
Large (2012), 58, 208
Laurent and Schmitt (1999), 65, 208
Leaman et al. (1987), 107, 208
Ledwell et al. (1993), 57, 75, 208
Lee et al. (2006), 69, 70, 78, 208
Leonard (1979), 52, 208
Li et al. (2001), 58, 208
Lin (1997), 32, 35, 208
Lin (2004), 53, 208
Locarnini et al. (2006), 120, 121, 123, 208
Lukas and Firing (1984), 107, 209
MERCATOR (2006), 107, 209
Müller (2006), 15, 168, 210
MacKinnon et al. (2010), 57, 209
Machenhauer et al. (2009), 22, 209
Manizza et al. (2005), 88, 90, 209
Marion and Thornton (1988), 5, 209
Marshall and Schott (1999), 5, 209
Marshall et al. (1997), 57, 209
Martin and Adcroft (2010), 91, 209
McDougall and McIntosh (2001), 84, 209
McDougall et al. (2002), 40, 209
McDougall (1995), 10, 209
McDougall (2003), 18–20, 24, 56, 89, 124, 131, 132, 170, 209
Meehl et al. (2001), 57, 209
Melet et al. (2013), 74, 209
Melling (2000), 106, 209
Merryfield and Holloway (2003), 52, 209
Miles (1961), 64, 209
Moum et al. (2002), 75, 209
Munk and Anderson (1948), 78, 210
Murray (1996), 44, 45, 108, 210
Olsen et al. (2008), 106–108, 210
Osborn (1980), 74, 210
Osterhus et al. (2005), 106–108, 210
Otto et al. (1990), 107, 210
Pacanowski and Gnanadesikan (1998), 46, 48, 122, 210
Pacanowski and Griffies (1999), 44, 52, 210
Pacanowski and Philander (1981), 57, 64, 210
Palter et al. (2014), 157, 210
Prather (1986), 52, 210
Rahmstorf (1993), 57, 210
Roach et al. (1995), 106, 210
Rosati and Miyakoda (1988), 46, 210
Sadler (1976), 106, 210
Schauer et al. (2004), 107, 210
Schmitt (1994), 64, 210
Simmons et al. (2004), 69, 70, 73–75, 78, 210
Sloyan et al. (2003), 107, 210
Smith and Sandwell (1997), 70, 72, 211
Smyth et al. (2002), 58, 61, 62, 211
St.Laurent et al. (2001), 75, 211
St.Laurent et al. (2002), 74, 211
St.Laurent et al. (2003), 74, 211
Stacey et al. (1995), 45, 211
Stouffer et al. (2006), 46, 211
Suresh and Huynh (1997), 51, 53, 211
Sweby (1984), 52, 211
Sweeney et al. (2005), 88, 124, 211
Taylor et al. (2012), 106, 211
Thiele and Sarmiento (1990), 30, 211
Thompson and Demirov (2005), 196, 211
Treguier et al. (1997), 86, 87, 185, 211
Umlauf et al. (2005), 58, 211
Vecchi et al. (2014), 138, 211
Warren (2009), 15, 168, 211
Webb et al. (1998), 80, 211
Yaremchuk et al. (2009), 108, 212
Yin et al. (2010), 46, 49, 212
IOC et al. (2010), 20, 56, 131, 169, 207
de Boyer Montégut et al. (2004), 161, 204